This page intentionally left blank


OLYMPUS

Geological Observations of Lava-Dome Growth

Seismic unrest at Mount St. Helens that started in September 2004 evolved into a dome-building eruption whose first new lava erupted 18 days later, on October 11. The dome grew as a series of spines within the existing 1980 crater. Each spine impinged upon the 1980–86 lava dome, on older parts of the new dome, and, in some cases, on the adjacent crater wall. Invariably, the stress of pushing caused the active spine to shear off, override previously extruded rock, and ultimately disintegrate. The numbered spines marked sequential growth episodes, whereas the vent itself never varied in location.

Crater Glacier, which was born in the deep shadows of the 1980 Mount St. Helens crater and grew in the years thereafter, was riven into two arms by the new dome, forced aside, doubled in thickness, and accelerated downslope. The glacier provided little resistance to the extruding lava. By being pushed away, the glacier was spared substantial melting—it lost only 10 percent of its volume despite years-long proximity to hot rock in its upslope reach.

On-the-ground field work within the crater was rarely undertaken in 2004–5, because of the persistent threat of small explosions. Consequently, most geologic monitoring was done through photography and periodic dredging of samples by helicopter. Some photographs were taken during helicopter overflights, others by fixed cameras (some of which transmitted images in near-real time), and overhead aerial photographs were taken from airplanes.

Through photogrammetry, the overhead aerial photographs provided digital elevation models of the new dome. From these digital data came the popular hillshade relief maps, deformation maps, and interpretive geologic maps and cross sections that illustrated the sequence of spine growth and decay. Successive digital elevation models also allowed the calculation of changing dome volumes and extrusion rates.

View east on October 12, 2004, to the first spine of the 2004 dome sequence soon after it breached the Crater Glacier and crater-floor debris. Spine is light-gray feature mostly encased in steam. USGS photo by J.C. Wynn.

A Volcano Rekindled: The Renewed Eruption of Mount St. Helens, 2004–2006
Edited by David R. Sherrod, William E. Scott, and Peter H. Stauffer
U.S. Geological Survey Professional Paper 1750, 2008

Chapter 8

Use of Digital Aerophotogrammetry to Determine Rates of Lava Dome Growth, Mount St. Helens, Washington, 2004–2005

By Steve P. Schilling[1], Ren A. Thompson[2], James A. Messerich[2], and Eugene Y. Iwatsubo[1]

Abstract

Beginning in October 2004, a new lava dome grew on the glacier-covered crater floor of Mount St. Helens, Washington, immediately south of the 1980s lava dome. Seventeen digital elevation models (DEMs) constructed from vertical aerial photographs have provided quantitative estimates of extruded lava volumes and total volume change. To extract volumetric changes and calculate volumetric extrusion rates (magma discharge rates), each DEM surface was compared to preeruption DEM reference surfaces from 1986 and 2003. Early in the 2004–5 eruption, DEMs documented deforming glacier ice and crater floor that formed a prominent "welt" having a volume of 10×10^6 m^3 and a growth rate of 8.9 m^3/s before dacite lava first appeared at the surface on October 11, 2004. Afterward, the rate was initially 5.9 m^3/s but slowed to 2.5 m^3/s by the beginning of January 2005. During 2005, the extrusion rate declined gradually to about 0.7 m^3/s. By December 15, 2005, the new dome complex was about 900 m long and 625 m wide and reached 190 m above the 2003 surface. More than 73×10^6 m^3 of dacite lava had extruded onto the crater floor.

Successful application of aerophotogrammetry was possible during the critical earliest parts of the eruption because we had baseline data and photogrammetric infrastructure in place before the eruption began. The vertical aerial photographs, including the DEMs and calculations derived from them, were one of the most widely used data sets collected during the 2004–5 eruption, as evidenced in numerous contributions to this volume. These data were used to construct photogeologic maps, deformation vector fields, and profiles of the evolving dome and glacier. Extruded volumes and rates proved to be critical parameters to constrain models and hypotheses of eruption dynamics and thus helped to assess volcano hazards.

Introduction

The volume of a growing lava dome and its extrusion rate are primary measurements that may be compared with other traditional volcano-monitoring data from ground deformation, gas geochemistry, and seismicity for the purpose of monitoring and studying erupting volcanoes. Such comparisons have been made for some recent dome-building eruptions, including Santiaguito, Guatemala (Harris and others, 2003); Unzen, Japan (Nakada and others, 1999); Redoubt, Alaska (Miller, 1994); and Soufrière Hills, Montserrat (Sparks and others, 1998). In addition to their value as a fundamental dataset, volumetric data are needed to explore such linkages as extrusion rate thresholds for transition to explosive activity and volume thresholds for initiation of large-scale dome collapse. In this paper, we describe a new application of traditional photogrammetric techniques to track the growth of the 2004–5 Mount St. Helens lava dome.

In October 2004, a new period of dome growth began at Mount St. Helens that changed the topography of the 1980 crater dramatically (fig. 1). Between October 2004 and December 2005, more than 73×10^6 m^3 of solid dacite lava extruded onto the crater floor immediately south of the lava dome that had formed in the 1980s. The new dome grew as a succession of large spines (Vallance and others, this volume, chap. 9). Dome growth intensely deformed and divided Crater Glacier, which had developed from a small debris-covered snowbank in 1985 into a glacier covering about 1 km^2 by 2001 (Schilling and others, 2004). We use the informal names "west

[1] U.S. Geological Survey, 1300 SE Cardinal Court, Vancouver, WA 98683

[2] U.S. Geological Survey, Box 25046, Denver Federal Center, Denver, CO 80225

Crater Glacier" and "east Crater Glacier" for the two ice bodies remaining within the crater. The growing dome compressed the east Crater Glacier against the east crater wall, resulting in spectacular thickening. Compression and thickening created crevasses and rapid advance of the terminus, about 185 m in two years, followed by similar effects on the west Crater Glacier (Walder and others, this volume, chap. 13).

The extruded volume and extrusion rate of lava associated with this protracted dome eruption are critical parameters used to constrain models of the magmatic system (Mastin and others, this volume, chap. 22) and eruption dynamics (Iverson, this volume, chap. 21), to determine how the magmatic system relates to surface measurements of magmatic gases (Gerlach and others, this volume, chap. 26) and seismicity (for example, to determine if extrusion rate correlates with size and rate of occurrence of volcano-related earthquakes; Moran and others, this volume, chap. 2), and to constrain calculations that address loading effects of the growing dome on surface deformation (Lisowski and others, this volume, chap. 15).

Photogrammetry based on vertical aerial photographs has been used previously to monitor, model, map, and measure surface change and deformation at volcanoes (Achilli and others, 1998; Baldi and others, 2000, 2005; Zlotnicki and others, 1990). A recent photogrammetric study of the Mount St. Helens crater (Schilling and others, 2004) tied a block of overlapping vertical aerial photographs to a network of global positioning system (GPS) stations on the volcano's flanks, dome, and crater floor (fig. 2*A*) resulting in a digital elevation model (DEM) of the volcanic edifice and entire crater configuration in October 2000.

The 2000 DEM has served as a baseline for comparison with past DEMs. Comparison of the 2000 surface with post-May 18, 1980, and 1990 DEMs, both derived from existing topographic contour maps, produced volume estimates of

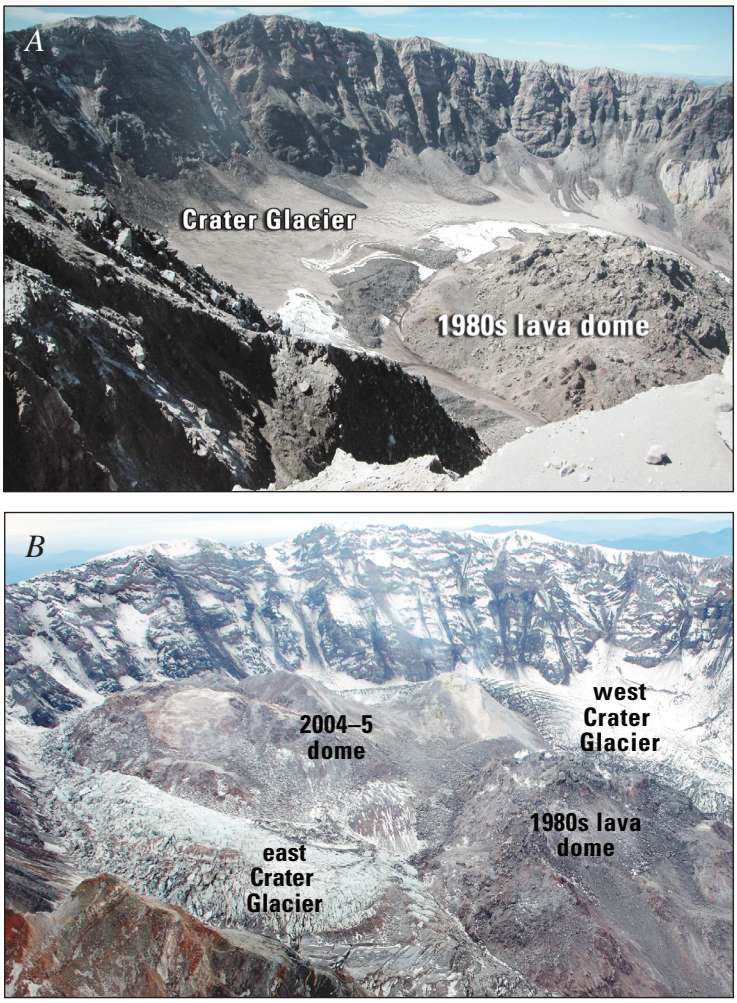

Figure 1. Oblique photographs of Mount St. Helens crater from east rim; views to southwest. *A*, Preeruption crater on August 30, 2004, showing 1980s lava dome and Crater Glacier (mostly coated with rock debris). *B*, Crater on October 12, 2005, showing new lava dome dividing and deforming glacier. USGS photographs by S.P. Schilling.

glacier ice and talus accumulation, as well as crater-wall erosion (Thompson and Schilling, 2007). Near the beginning of the 2004–5 eruption, two other craterwide DEMs were constructed to estimate volume change. One was created from digital, photogrammetrically derived contours that depicted the crater in November 1986, and another was constructed from lidar data (Queija and others, 2005) obtained September 20–22, 2003, using the same network of GPS sites for ground control that was used for photogrammetric monitoring.

Throughout the 2004–5 eruption, we used analytical photogrammetry and a softcopy (that is, digital image) system to provide stereo imaging and accurate measurement of the rapidly changing crater morphology. Seventeen DEMs have been constructed from vertical aerial photographs (Messerich and others, 2008), collected approximately every three weeks, in order to quantify volumetric changes associated with dome growth and collapse as well as deformation of Crater Glacier (Walder and others, this volume, chap. 13). Each new DEM was compared to preeruption reference surfaces of the crater in 1986 and 2003 to extract volumetric changes. For viewing purposes, each DEM was also converted to a hillshade-relief map, in the form of digital raster images (tagged image file format) and corresponding georeferenced world files (ASCII format). These raster maps are found in appendix 1, which is available in the DVD that accompanies this volume and in online versions of this chapter.

Methods

Acquiring low-altitude aerial photographs in inclement weather over mountainous terrain presents logistical challenges, and taking them over an erupting composite volcano such as Mount St. Helens, where rapid turnaround of data is needed to evaluate hazards, adds urgency. These problems were simplified by taking advantage of photogrammetric infrastructure set up during previous work at the volcano (Schilling and others, 2004). When the 2004–5 eruption began, however, some established flight-planning procedures required modification, such as selection of new ground control sites and design of flight lines for appropriate photograph scale

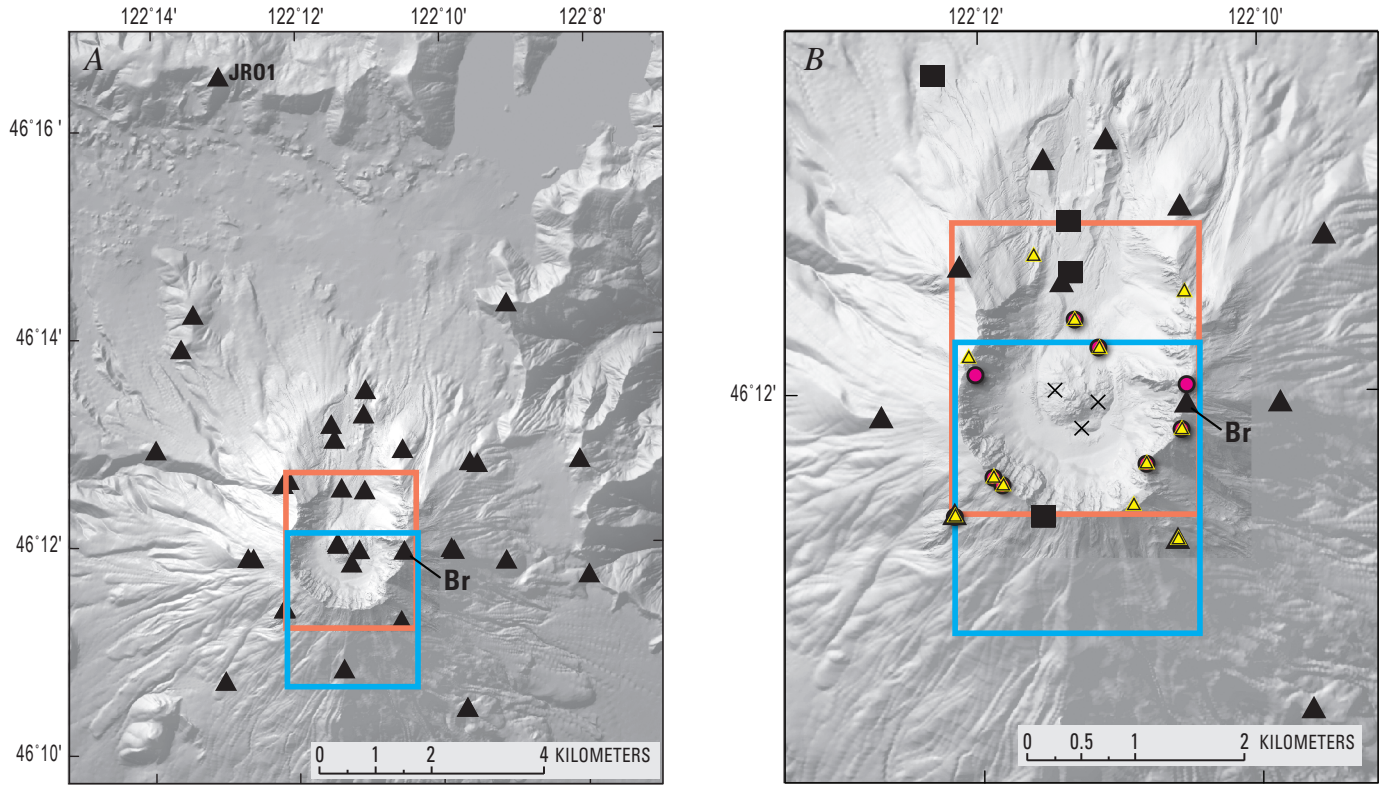

Figure 2. Shaded-relief maps of preeruption surface of Mount St. Helens (2003 DEM). Red and blue boxes show approximate areas covered by two overlapping, 1:12,000-scale vertical aerial photographs. *A*, Broad GPS ground control network (black triangles) used for aerotriangulation of block of photographs to extract coordinates for construction of 2000 DEM and to serve as control for 2003 lidar-based DEM. Br, Brutus control point on east rim. *B*, Ground control points for vertical aerial photographs obtained during 2004–5 eruption. Black X's, ground control points destroyed early in eruption. Red dots, photoidentified control points transferred from 2000 aerotriangulation for use early in eruption. Black squares, new, and black triangles, existing ground control points measured in summer 2005. Yellow triangles, photoidentified control points transferred from August 2005 aerotriangulation solution to serve as ground control for December 2005 aerotriangulation.

and overlap. Early in the eruption, having procedures already established meant that DEMs were constructed rapidly, at times within a few days of obtaining the aerial photographs.

Digital photogrammetry refers to photogrammetric systems that have been adapted from hardcopy (film) aerial photographs mounted on optical-mechanical stereo plotters to softcopy (scanned, digital) aerial photographs imported into a desktop computer workstation. Hardware for our softcopy system includes a fast central processing unit, abundant memory, two display screens (one for stereo images and one for control menus), polarizing spectacles for viewing onscreen images in stereo, and a customized mouse to control three-dimensional (3D) cursor movement. Socet Set software includes spatial resection and spatial intersection algorithms to calculate X, Y, and Z ground coordinates of features observed in stereo aerial photographs; it requires precise camera calibration parameters, carefully measured photograph coordinates, and accurate GPS ground control (Wolf and Dewitt, 2000; Thompson and Schilling, 2007). The softcopy system automates many standard photogrammetric tasks, such as inner and relative orientations of stereo models. However, the critical task of exterior orientation, which ties photographs to ground control, requires a skilled operator to maintain precision. Assuming minimal operator error, the accuracy of the final model solution is constrained by flight height, which determines scale, and by scanning resolution, which determines the minimum feature size that the operator can discern in the aerial photographs.

After considering many factors, such as safety and size of features to be measured, we selected a flying height of 3,900 m (12,800 ft), yielding a nominal photo scale of 1:12,000 with a 153.681-mm lens and 9×9-inch film format. Thus, 1 mm on the photograph at nominal scale represents 12 m on the ground. This nominal scale applies at about the altitude of the Crater Glacier surface immediately south of the 1980s lava dome, roughly midway through the range of relief within the Mount St. Helens crater—from about 2,540 m (8,330 ft) on the crater rim to about 1,815 m (5,955 ft) near the base of the 1980s dome. The variation in altitude corresponds to a variation in scale, often within a single photograph, from 1:8,964 at the rim to 1:13,726 at the base of the 1980s lava dome.

Each aerial photographic negative was scanned at 12 μm resolution, generating a graytone digital image roughly 350 megabytes in size. Owing to the scale variation within a photograph, each cell in the image may represent a different distance on the ground, from 0.108 to 0.165 m.

Global Positioning System (GPS) Control Network

Accurate ground control is equally as important as high-resolution scanning. About 30 GPS sites on the outer flanks, 1980s lava dome, and crater floor of Mount St. Helens (fig. 2*A*) form a network of ground control points for photogrammetric surveys. The sites were selected to accommodate the geometry needed for the exterior orientation (linking world and photograph coordinate systems) of blocks of overlapping photographs (multiple stereopairs along and between adjacent flight lines); each site was also accessible by helicopter. Most of the sites are part of a geodetic network established in 2000 (Dzurisin, 2003). Many are located near 3-m-high steel towers constructed after the 1980 eruption and used for electronic distance meter (EDM) surveys (Swanson and others, 1981). These towers or their shadows are relatively easy to find in the diapositive (film positives) rendering of aerial photographs used to help locate ground-control sites in the digital images. Using a helicopter and two crews, we were able to measure and place photo-targets at all of the stations in 1–2 days.

Measuring GPS locations in the field for ground control at Mount St. Helens is a straightforward task. We deploy a GPS receiver at each site, centering the antenna over a specific tower leg, piece of rebar, or benchmark. GPS receivers collect data at each site for about 1 hour. Before moving to the next site, three or four large plastic rectangular panels are placed radially about each GPS point to facilitate locating the control point in aerial photographs. The receiver data are downloaded and processed using Ashtech Office Suite for Survey ® (AOSS) software. The reference station for differential GPS processing is JRO1 (fig. 2*A*), which at the start of the eruption was the nearest continuous GPS station (approximately 9 km north of the crater). Altitudes from AOSS are converted to orthometric heights using the National Geodetic Survey (NGS) program GEOID03. The U.S. Army Corps of Engineer program CORPSCON is used to calculate X, Y, and Z coordinates using a horizontal datum of NAD83 and a vertical datum of NAVD88. The GPS data yield position accuracies of 2 to 3 cm in X and Y (horizontal) coordinates and 6 to 7 cm in the Z (vertical) coordinate.

Control points were remeasured annually from 2000 to 2004 before taking aerial photographs of the entire volcano. Repeated measurement improved and validated the positional accuracy of most sites. However, the landscape evolves quickly at Mount St. Helens, and site positions change, at times dramatically. For example, in 2002 the photo panels and rebar of the Brutus site on the east crater rim (fig. 2, station Br) were buried beneath about 20 cm of wind-blown pumice. The following year, the site toppled into the crater and had to be replaced.

New Ground Control Based on GPS Data and Photo-Identified Points

When the 2004–5 eruption began, four established flight lines used in previous studies to capture aerial photography of most of the volcano were abandoned in favor of a single, south-to-north flight line centered over the crater. A single flight line offered advantages of safety, simplicity, speed, and economy. However, it eliminated use of ground control points on the east and west outer flanks of the volcano and

forced reliance on control points on the crater rim, floor, outer south flank, and 1980s lava dome. Unfortunately, explosions early in the eruption eliminated three critical ground control sites on the 1980s lava dome (fig. 2*B*). Several of the remaining control points were outside the stereo coverage of the single flight line.

Rather than increase the number of flight lines and incorporate the ground control on the volcano flanks in an aerotriangulated block or replace the ground control in the crater's potentially dangerous environment, we transferred control points from the stored orientation solution (aerotriangulation) of the 2000 block of aerial photographs. Photoidentifiable, measured points (fig. 2*B*), such as distinct boulders or topographic prominences, were carefully selected and passed from the aerotriangulated solution of 2000 models to the 2004 aerial photographs as ground control. These points or a subset of them provided control for successive sets of photographs obtained throughout the winter of 2004–5. The resulting ground-control accuracy was reduced from a few centimeters, based solely on GPS data, to a few decimeters using photogrammetrically transferred control points.

In July 2005 we remeasured and repaneled the network of existing ground-control points on the crater rim and flanks. In addition, we reestablished one of the points on the west side of the 1980s lava dome and added points on the crater floor north of the 1980s lava dome and a site on the south crater rim (fig. 2*B*).

Aerotriangulation

Aerotriangulation provided a means of transferring accurate control from earlier photogrammetric work at Mount St. Helens, rather than establishing new control in hazardous areas as the eruption progressed. Aerotriangulation refers to solving relative orientation equations for overlapping aerial photographs (stereo model), identifying common points (pass points) between adjacent models to form continuous strips or blocks of stereomodels, and solving simultaneous equations to adjust mathematically the strips or block of photographs to ground control. A series of nonlinear expressions with many unknowns are truncated by Taylor's theorem into a series of linear equations that are solved simultaneously by the method of least squares (Wolf and Dewitt, 2000). Our 2000 benchmark DEM was created from an aerotriangulation solution for a block of aerial photographs. The block comprised four adjacent, overlapping strips of photos; each strip was formed from seven or eight overlapping photographs. Point coordinates extracted from the 2000 stereomodels and aerotriangulation were used as control points for successive stereomodels and for aerotriangulation solutions during the early part of the 2004–5 eruption. The resulting root-mean-squared (RMS) residual error for the early aerotriangulation solutions was a few decimeters. New and remeasured GPS ground-control points in the aerial photographs taken in the summer and fall of 2005 resulted in an aerotriangulation RMS residual error of several millimeters to several centimeters. The average RMS error from all aerotriangulation solutions was 0.17 m in the X, Y, and Z coordinates. Extending that error over the area that has been affected by the eruption (about 1 km^2) gives rise to a volume of uncertainty of 1.7×10^5 m^3. This error is about 4 percent of the typical monthly extruded volume (4×10^6 m^3) estimated from comparison of the series of DEMs (Iverson and others, 2006, Supplementary Notes).

Digital Elevation Model (DEM) Construction

We used spatial resection calculations to derive an aerotriangulation solution and then used spatial triangulation algorithms to extract three-dimensional coordinates and construct a DEM that defines the crater surface. Two techniques were used for obtaining X, Y, and Z coordinates from the stereomodels.

The first method was a manual technique that relies on the skill of the operator. The operator examined one or more stereomodels and identified the area being deformed and the features to be measured. For each feature, the operator carefully placed a floating mark on the feature, stored the Z (elevation) coordinate, and triangulated and stored the X and Y (planimetric) coordinates. Points were collected individually or as a stream as the operator moved the floating mark along the terrain.

The second method was an automated technique in which Socet Set software used coplanarity equations to derive a plane intersecting three points: (1) an object in one image; (2) the same object in the overlapping area of a second, adjacent image; and (3) the triangulated position of the object on the ground. The software used the line formed where the plane intersected the two adjacent photographs to guide its search for matching cell patterns. When the X and Y coordinates of matching cell patterns were identified, the software calculated the corresponding Z coordinate. The operator defined an area and density of points for the automated calculations. The automated method did not work well in steep terrain but did work in the relatively flat-lying, glacier-covered parts of the crater, provided there was enough contrast (such as a dusting of ash) in the photographs to provide unique cell patterns. The automated technique identified, calculated, and stored X, Y, and Z coordinates for many locations relatively quickly. This technique was used sparingly, however, because it can be labor intensive. Automatically generated points must be checked by the operator, either individually or by generating contours of groups of collected points, to correct any errors.

Using these two techniques, individual points or streams of points marking breaks in slope (breaklines) were collected to better define topographic inflections, enabling intervening surfaces on the growing dome and deforming glacier to be represented by significantly fewer data points. The resulting three-dimensional surface is an array of triangular

facets referred to as a triangulated irregular network (TIN), in which interpolated surfaces are triangles having measured points at each vertex. A TIN surface was checked for systematic errors or random operator error in a few seconds by generating digital contours for the surface. The operator easily located and repaired errors, such as points that caused contours to cross, and recalculated the TIN surface.

After error checking and visually determining that the TIN was an accurate representation of the three-dimensional surface depicted in the aerial photographs, the TIN data structure was stored and converted to a DEM. The DEM differs from the TIN in that the former is a regular array of square cells (or rasters), where each cell represents an area of the Earth's surface (X, Y) with a specific altitude value (Z). During this conversion process, the cell size or resolution did not dictate the accuracy of an altitude value. Rather, the resolution dictated how closely the DEM represents the TIN model. The accuracy of altitudes and horizontal positions was determined by the combined photogrammetric orientations, operator's skill, and in particular by the accuracy of the ground control.

Sources of error in the DEM construction included aerial camera calibration, film processing, flight parameters, ground control points, conversion of photos to digital form, stereomodel orientation (interior, relative, absolute), aerotriangulation, image-matching algorithms, operator bias, and random factors (Daniel and Tennant, 2001, p. 402–403). We estimated the uncertainty of any volume measurement to be a function of the area of the growing dome multiplied by the average RMS residual error (0.17 m). Thus, as the volume continued to increase, so did the estimated uncertainty of the volume calculation. However, the resulting uncertainty in volume-change calculations was about 4 percent—small compared to the ambiguity introduced by the unknown subsurface configuration of the lava dome (the lower part of the new dome masked by Crater Glacier).

Surface Depiction Using DEMs

The DEMs were imported into an ArcInfo Geographic Information System (GIS) for viewing and analysis after conversion to an ASCII text file in the softcopy system. This file, which was formatted for import to ArcInfo software, included a header containing the number of columns, number of rows, cell size, and X and Y coordinates of the lower left corner of the DEM, followed by a sequence in row-major order (top row first, bottom row last) of all the Z (elevation) values. The file was imported into the ArcInfo grid module as a high-resolution (2 m) grid (raster data structure).

Perhaps the most significant and primary use of any photogrammetrically constructed DEM is to examine the surface, either singly or in sequence with previous DEMs. Such a succession of DEMs for Mount St. Helens shows, qualitatively, the changing position, dimensions, and size of the growing dome and deforming glacier over time. The DEMs are difficult to examine or interpret directly. A hillshade algorithm was used to position an artificial "sun" at an arbitrary azimuth and altitude to render a gray-scale shaded-relief view of the changing dome and glacier. This rendition of the topography is free of potentially distracting details seen in the aerial photographs, such as steam, snow, or ash, and allows consistent and simplified viewing to study geomorphic change and compare cell alignment among DEMs.

The areal extent of the dome complex and deformed glacier increased throughout the 2004–5 eruption, forcing a corresponding increase in the extent of DEMs to document the change. To ensure proper alignment (registration) of the DEMs, they are cast within the same projection, same horizontal datum, and same vertical datum. We selected the Universal Transverse Mercator (UTM) projection's zone 10, which extends from 120° to 126° west longitude, the 1988 North American Vertical Datum (NAVD 88), and the 1983 North American horizontal datum (NAD 83). Previous DEMs derived from contours having a 1927 horizontal datum (NAD 27) were converted to NAD 83. In addition, a regional vertical correction of 1.25 m (Zilkoski and others, 1992) was applied to convert the 1929 vertical datum (NAGD 29) to NAVD 88. We confirmed this regional correction by calculating the difference between GPS control points stored in NAGD 29 and NAVD 88.

The extent of each DEM was varied in order to capture dome growth. Dome growth and the DEMs depicting the growth were bounded on the north by the relatively fixed 1980s lava dome and eventually bounded on the south by the south crater wall. The DEM edges on the east and west (as well as the south early in the eruption) were delineated visually to capture observed deformation, using the softcopy system. These results were confirmed by using GIS software to compare any current DEM to earlier DEMs. If we found that any of the DEMs had inadequate extent to represent the entire deformation field, the boundary could be extended using the scanned aerial photographs and aerotriangulation stored within the softcopy system.

Initially, the 2000 DEM was used as the baseline data set for all comparisons in order to keep the construction method consistent. However, the craterwide 2000 DEM had a cell size of 10 m, whereas DEMs constructed for the 2004–5 eruption had cell sizes of 2 m. The difference in cell size meant that each of the newer DEMs would have to be resampled to give a 10-m cell size. The error introduced by resampling outweighed the benefit of using consistent production methods; therefore, we later selected the craterwide 2003 DEM derived from lidar, and a 1986 DEM derived from contours, each having a 2-m cell size, for comparison with all subsequent DEMs.

Volume Calculation Methods

Although a single DEM surface offers a quick, synoptic portrayal of ongoing surface deformation, the comparison of successive DEM surfaces can yield estimates of erupted vol-

ume and average extrusion rate. We wrote software that uses GIS functions to subtract one DEM surface from another and generates a third, isoline surface showing net elevation change. The isoline surface stores the calculated difference between its two parent surfaces, retaining their 2-m cell size. In this manner, each cell of the isoline grid stores a positive, zero, or negative value resulting from the subtraction of the two corresponding parent cells. After the subtraction, the software sums values of all cells having a negative value (melting, erosion, or subsidence) and of all cells having a positive value (extrusion, deposition, or uplift) separately, and it also multiplies each total positive or total negative value by the area of a single cell (4 m^2). The software writes the resulting volumes to a text file and generates two additional grids, one showing the location of the positive and another showing the location of the negative results.

The potentially straightforward task of determining extruded volume from total-volume changes was complicated by the presence of Crater Glacier, in some places more than 150 m thick (greater than 200 m thick when including subglacial 1980–86 crater-floor deposits), which was displaced and severely disrupted as the eruption progressed. Two questions arose: (1) Does extrusion begin at the preexisting crater floor or at the glacier surface; and (2) how best to calculate erupted volume as a function of time? One approach (fig. 3*A*) is to difference each new DEM with the 2003 preeruption DEM and to use the total surface-volume change as a proxy for erupted volume. For example, 1 m^2 of glacier ice rising 2 m represents 2 m^3 of lava extruded beneath it or laterally displacing it. This approach has the advantage of accounting for all material that rose above the crater floor, some of which remains obscured by ice, and the method is simple and straightforward. Three disadvantages of this total volume-change technique are the unknown total amount of dilatation caused by ice deformation (though the largest crevasses are captured during DEM construction), volume gain by winter snow accumulation, and volume loss by melting.

Another approach (fig. 3*B*) is to assume that lava extends from the lava-ice contact at the surface vertically downward to the 1986 crater floor. This is a reasonable approach for three reasons: (1) field examples of ice-contact lava flows have steep sides that formed as they flowed against steep ice walls (Lescinsky and Fink, 2000); (2) where observed around the Mount St. Helens dome, ice-lava contacts are nearly vertical; and (3) this method is also simple and straightforward. One disadvantage is that this method ignores observed rising crater-floor material or glacier, especially early in the eruption, which probably deform in response to endogenous or subglacial lava emplacement.

Our solution was to use both approaches to track volume estimates. The first approach provided measurements of extruded rock independent of whether rock broke through the glacier surface. As the eruption proceeded, the dome grew larger and the impact of the glacier became proportionally smaller. The discrepancy between the two approaches therefore decreased over time.

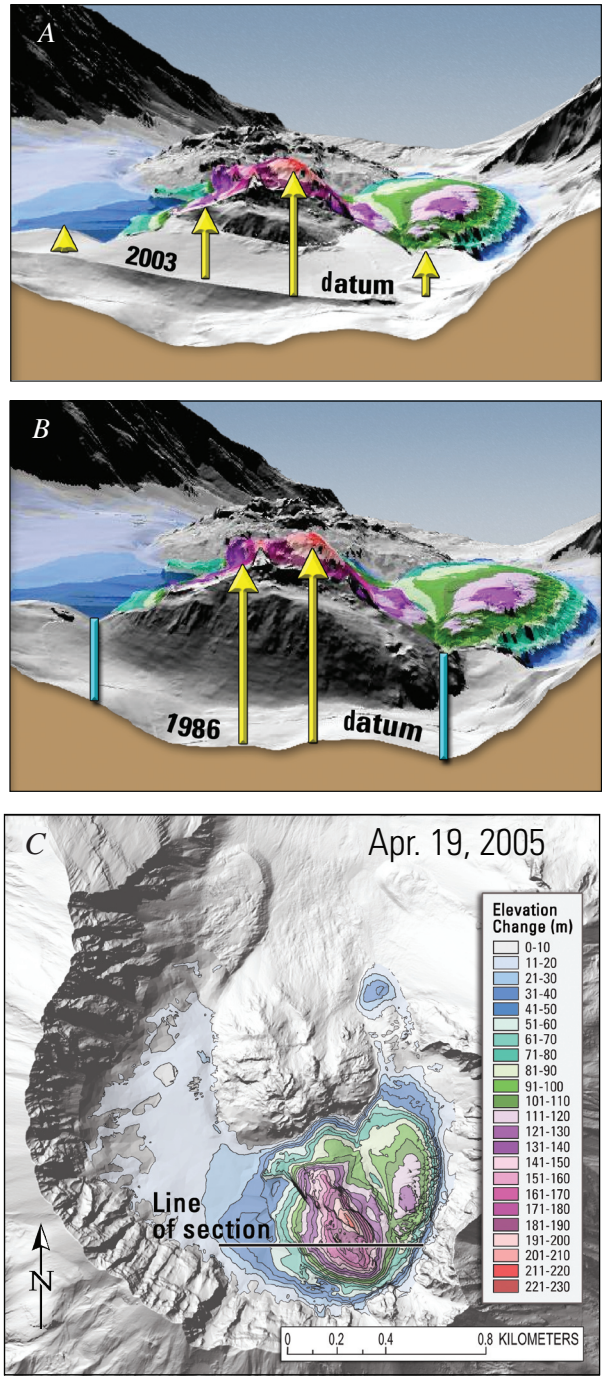

Figure 3. Diagrams (*A, B*) illustrating DEM differencing for volume-change calculations. Semitransparent oblique cutaway of surface defined by April 19, 2005, isolines (colored bands) draped on DEM showing 1986 ground topography and 2003 glacier surface. Yellow arrows, examples of local elevation changes. View to north-northwest. *A*, Total volume change. Note that differencing includes marginal areas, unlikely to be underlain by lava, that are composed of deformed glacier. *B*, Extruded-lava volume. Blue bars define inferred steep margins of extrusion. *C*, DEM and differencing surface of April 19, 2005. The DEM and differencing surface south of the line of section were removed to produce oblique views *A* and *B*.

Results

A sequence of 17 pairs of images derived from DEMs of October 4, 2004, through December 15, 2005, document lava dome growth and glacier deformation during the 2004–5 eruption (figs. 4, 6–8). For each pair, the left image is a shaded-relief map. Beginning with the October 13, 2004, map, a red line marks the approximate boundary of extruded lava on the surface that was extended vertically to the 1986 crater floor to calculate the extruded-lava volume. The right image is an isoline map draped over the shaded-relief image. Each 10-m interval of the isoline map is assigned a unique color to illustrate better the magnitude and location of elevation change relative to the 2003 crater surface. All isoline cells having an elevation difference equal to or greater than 10 m were summed to calculate total volume change. Some of the shaded-relief images, such as that for October 11, 2004 (fig. 4*E*), have triangular facets that portray areas where a

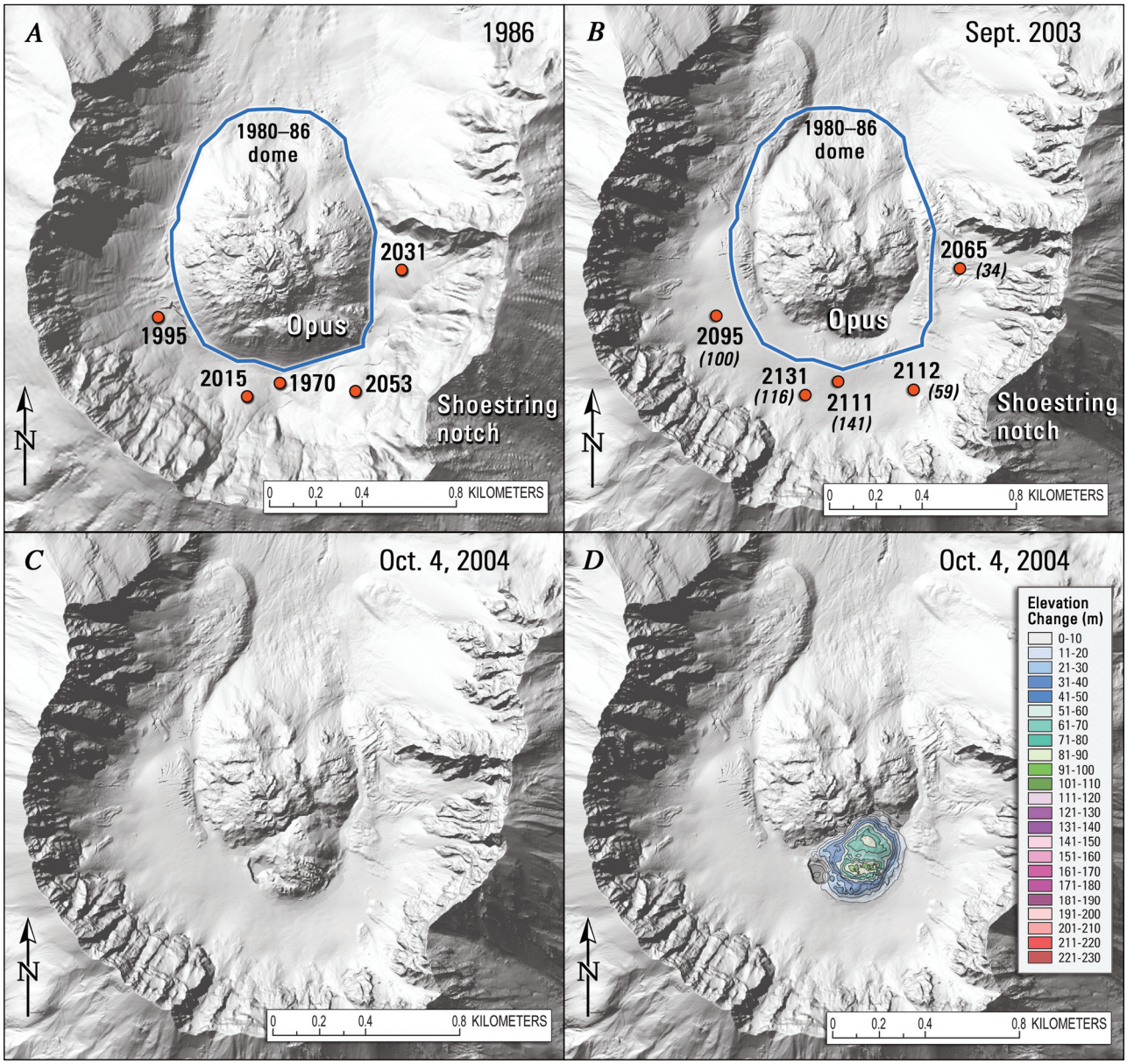

Figure 4. Shaded-relief images showing preeruption crater surface and growth of welt and initial lava extrusion (red outline in *G*). *A*, 1986 and *B*, 2003. Blue line, approximate boundary of 1980s lava dome. Red dots show altitude, in meters, of points on crater floor. Increases (in parentheses) caused by growth of Crater Glacier and deposits eroded from crater walls. Area labeled Opus is part of the 1980s lava dome involved in uplift in late September and early October 2004. *C–H*, sequence of three pairs of images from October 2004. Left image is shaded relief map; right image has 10-m isolines showing topographic changes relative to September 2003 (shown in *B*).

condensed steam plume in the aerial photographs prevented detailed coordinate collection.

Also shown for reference in figure 4 are shaded-relief images of the craterwide datum surfaces from 1986 (fig. 4*A*) and 2003 (fig. 4*B*). The shaded-relief map of the 1986 crater shows the configuration of crater walls, talus fans and other deposits on the crater floor, and the 1980s lava dome. The 2003 shaded-relief map also shows the newly formed glacier, which buries some margins of the 1980s lava dome. Spot altitudes show the magnitude of surface-elevation change from 1986 to 2003.

As the new lava dome grew, questions about the volume of the 1980s lava dome arose. We differenced DEMs to estimate a volume of 92×10^6 m^3 for the 1980s lava dome (Thompson and Schilling, 2007), which is larger than the 74×10^6 m^3 estimate of Swanson and Holcomb (1990) but is in agreement with volume calculations of Mills (1992). The difference in volume estimates may result from (1) differences in measurement methods, (2) exclusion by Swanson and Holcomb (1990) of crater-wall debris that was incorporated into the dome as it grew (Mills, 1992), and (3) different configurations for the base of the lava dome as a horizontal versus sloping surface.

The following discussion of the DEMs focuses on four time intervals and highlights key events related to dome building and deformation of Crater Glacier: (1) Growth of the so-called welt (Dzurisin and others, 2005), south of the 1980s lava dome, and its migration southward in late September and early October 2004 involved uplift of a part of the 1980s lava dome (area labeled Opus on figs. 4*A*, 4*B*),

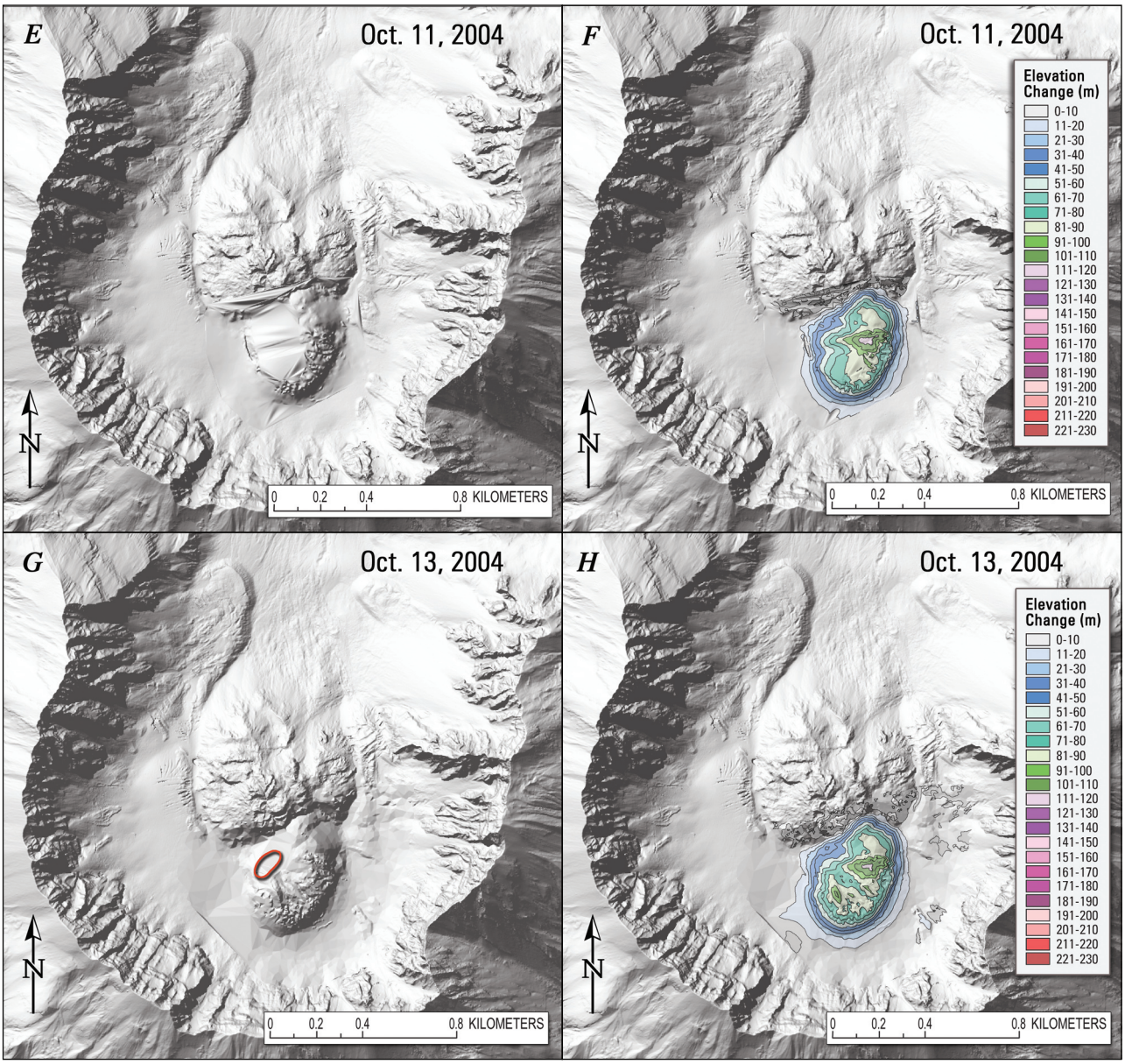

Figure 4—Continued.

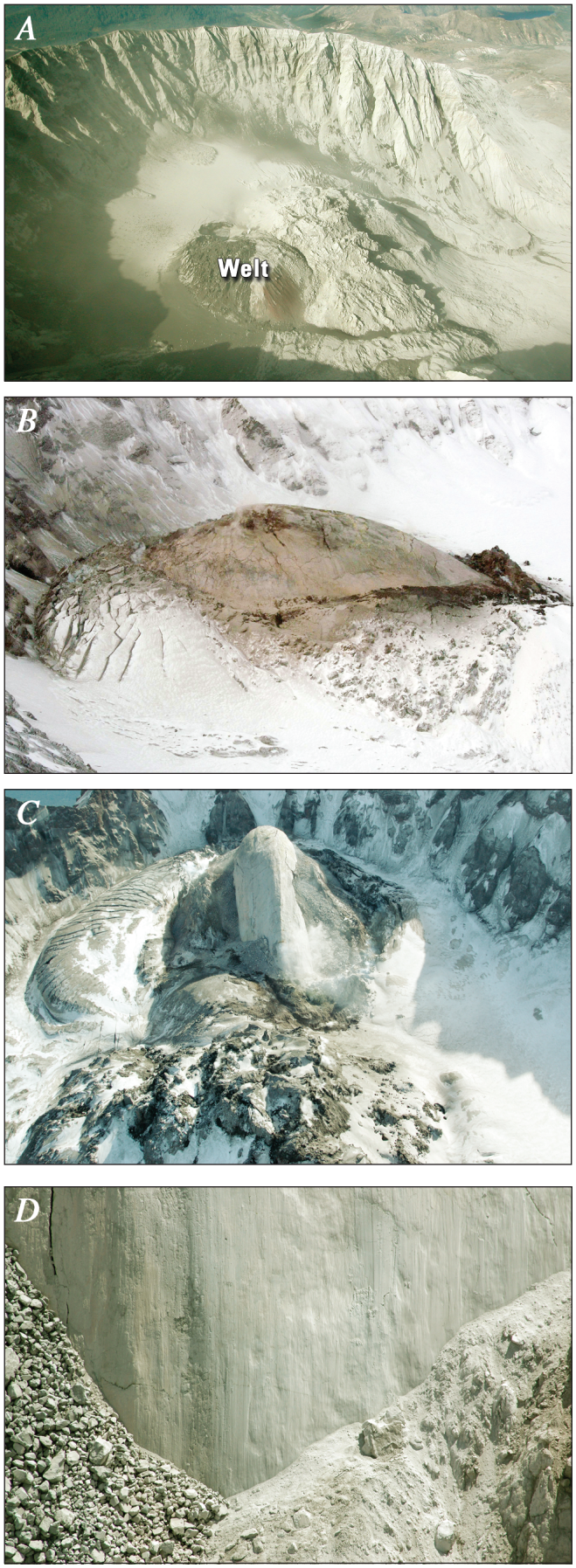

crater-floor debris, and glacier ice. Initial lava spines 1 and 2 (see Vallance and others, this volume, chap. 9, for description of the lava-spine numbering scheme) rose through the northern part of the welt near the end of this interval. (2) From late October 2004 through mid-April 2005, extrusion, growth to the south and migration east, and breakup of curvilinear, smooth-surfaced spines 3 and 4, known as whalebacks, drove extraordinary deformation of the east Crater Glacier. The first evidence of lateral movement of the spines came from the DEMs. For example, the extrusion axis, a horizontal line oriented parallel to the direction of extrusion along the approximate center of a whaleback, initially moved southward, then shifted eastward from October 2004 through April 2005 (approximately 4° horizontal rotation of the whaleback axis towards the east occurred between November and December 2004 and about 6° between February and March 2005), as successive whalebacks emerged from the vent area, displacing older parts of the growing dome. (3) Between mid-April and late July 2005, smooth-surfaced spine 5 grew at a much steeper angle than had the previous whalebacks and began a trend toward west-directed movement. (4) In August 2005 spine 6 began to grow and migrate westward, followed by penetration of its eastern part by spine 7 in early October. Both spines moved west, which compressed and thickened west Crater Glacier. For a complete description of the geologic interpretation of dome growth, see Vallance and others (this volume, chap. 9). For a complete description of glacier deformation, refer to Walder and others (this volume, chap. 13).

October 4 Through October 13, 2004

Recognition of the welt (Dzurisin and others, this volume, chap. 14) a few days after seismic unrest began on September 23, 2004 (Moran and others, this volume, chap. 2), prompted efforts to obtain DEMs of the crater. The first group of images (figs. 4*C–H*) shows the remarkably rapid

Figure 5. Photographs of 2004–5 dome. *A*, View of crater after explosion of October 5, 2004. Welt formed of uplifted glacier, crater-floor debris, and southeast part of 1980s lava dome. Light-gray ash covers most of crater. View to west. *B*, Recumbent spine 3 on November 29, 2004, after impinging upon southeast crater wall. Its smooth carapace and leading wave of deformed glacier ice inspired the descriptive term, whaleback. View to southwest. *C*, Crater on February 22, 2005, showing spine 4 flanked by talus and, to left, remains of spine 3. Highly deformed east Crater Glacier prominent in left part of photograph. View to south. *D*, Close-up view about 5 m across of gouge-covered spine 4 extruding from vent, May 12, 2005. Striations parallel the direction of motion. Talus flanking spine is covered by dust from rockfalls and sloughing of gouge on right. View to south. USGS photographs by S.P. Schilling (*A, C, D*) and S. Konfal (*B*).

Table 1. Total volume change, extruded lava volume, and rates of change during 2004–2005 eruption of Mount St. Helens.

[Extruded lava did not appear at the surface until October 11, 2004. Rates are calculated from the volume changes since the previous measurement.]

Date of photography	Total volume change (x 10^6 m^3)	Total volume change rate (m^3/s)	Extruded lava volume (x 10^6 m^3)	Lava extrusion rate (m^3/s)
10/4/2004	5 [1]	-- [1]	-- [2]	-- [2]
10/11/2004	10	8.9	-- [3]	-- [3]
10/13/2004	11	6.4	0.54 [4]	-- [4]
11/4/2004	20	4.6	12	5.9
11/29/2004	27	3.0	21	4.4
12/11/2004	30	3.4	26	4.1
1/3/2005	35	2.4	31	2.5
2/1/2005	40	1.9	35	1.8
2/21/2005	43	1.8	39	2.4
3/10/2005	45	1.5	42	1.8
4/19/2005	55	3.0	47	1.5
6/15/2005	59	0.8	54	1.4
7/14/2005	59	-0.2	57	1.3
8/10/2005	60	0.4	62	2.0
9/20/2005	62	0.7	67	1.6
10/24/2005	66	1.3	70	0.9
12/15/2005	75	1.9	73	0.7

[1] Volume is the welt, obtained by method of differencing from topographic surface of September 2003. Start date for growth of welt is imprecisely known, so no rate offered.

[2] Eruption has not begun; no extruded lava.

[3] Too steamy to confidently discern limits of new extrusion.

[4] Steamy; extruded lava volume is crude estimate, and no rate is offered.

changes that occurred in 10 days as the welt grew rapidly upward and southward, deforming parts of the 1980s lava dome, crater-floor material, and Crater Glacier (fig. 5*A*). By October 11 the welt had grown to about 425 m in width, 475 m in length, and 105 m in height (2,209 m altitude) above the 2003 glacier surface. (Length of welt and dome is measured along the approximate longest dimension of each shape, and width is measured along a line roughly perpendicular to the length.) The welt attained a volume of 10×10^6 m^3 (table 1) as lava spine 1 emerged on October 11 (Vallance and others, this volume, chap. 9; Pallister and others, this volume, chap. 30). Presumably the volume of the welt approximated the volume of lava emplaced onto the subglacial crater floor.

November 4, 2004, Through April 19, 2005

Nine image pairs (fig. 6*A*–*P*) show the sequential growth of lava spines 3 and 4, which shared a similar history in terms of form, growth, and demise. These two striated, gouge-covered, curvilinear, whaleback-shaped spines (figs. 5*B*, 5*C*, 5*D*) grew south-southeast from the vent. The southern ends were pushed eastward over time and broke apart after impinging upon the south crater wall. Both whalebacks were surrounded by talus aprons on the west, south, and east. Initially the disrupted glacier adjacent to the talus aprons formed a crevassed ridge that, in map view, looked like the bow wave of a ship (figs. 6*A*, 6*C*). West of the growing dome, the talus apron, gently flexed ice, and intervening depression formed a relatively stable configuration throughout this period.

The November 29, 2004, image (fig. 6*C*) shows that lava spine 3 had a wide center with tapering ends. It was about 145 m wide, 350 m long, and at its highest point 150 m above the 2003 surface (altitude 2,282 m). The December 11, 2004, image (fig. 6*E*) shows that a longitudinal fracture had formed and broken the whaleback into two parts. By January 3, 2005, prominent longitudinal and oblique transverse, northwest and north-northeast-striking fractures had broken spine 3 into many blocks, presumably as a result of the spine impinging on the south crater wall (Vallance and others, this volume, chap. 9). The resulting 31×10^6 m^3 dome was about 500 m long by 200 m wide and reached 184 m above the 2003 crater surface (altitude 2,293 m). East Crater Glacier was squeezed between the grow-

ing dome and the southeast crater wall (figs. 6*C*–*H*), becoming severely disrupted as it thickened more than 120 m into a conical form by December 11, 2004 (figs. 6*E*, 6*F*). The highest area of disrupted ice shifted about 100 m to the northeast by January 3, 2005 (figs. 6*G*, 6*H*). The west Crater Glacier experienced broad uplift of about 10 m near the 1980s lava dome and near the south crater wall (figs. 6*D*, 6*F*, 6*H*).

A second whaleback (spine 4) began forming in early January 2005 from the severed stump of spine 3. By February 1 it was 145 m wide, 320 m long, and 210 m above the 2003 surface (altitude 2,331 m) (elevation of corresponding point on 2003 surface varies slightly as location of high point of whalebacks changes) (figs. 6*I*, 6*J*). These dimensions are similar to those of spine 3 on November 29, 2004. Spine 4 grew south-southeastward to about 450 m in length, 150 m in width, and 210 m (altitude 2,343 m) above the 2003 surface on March 10, 2005 (figs. 6*M*, 6*N*). As with spine 3, longitudinal fractures cut the southwest edge of spine 4 (fig. 6*M*). In April 2005, longitudinal, northwest-striking fractures and oblique transverse, northeast-striking fractures broke spine 4 as it impinged on the south crater wall, forming rubble and several megablocks (fig. 6*O*).

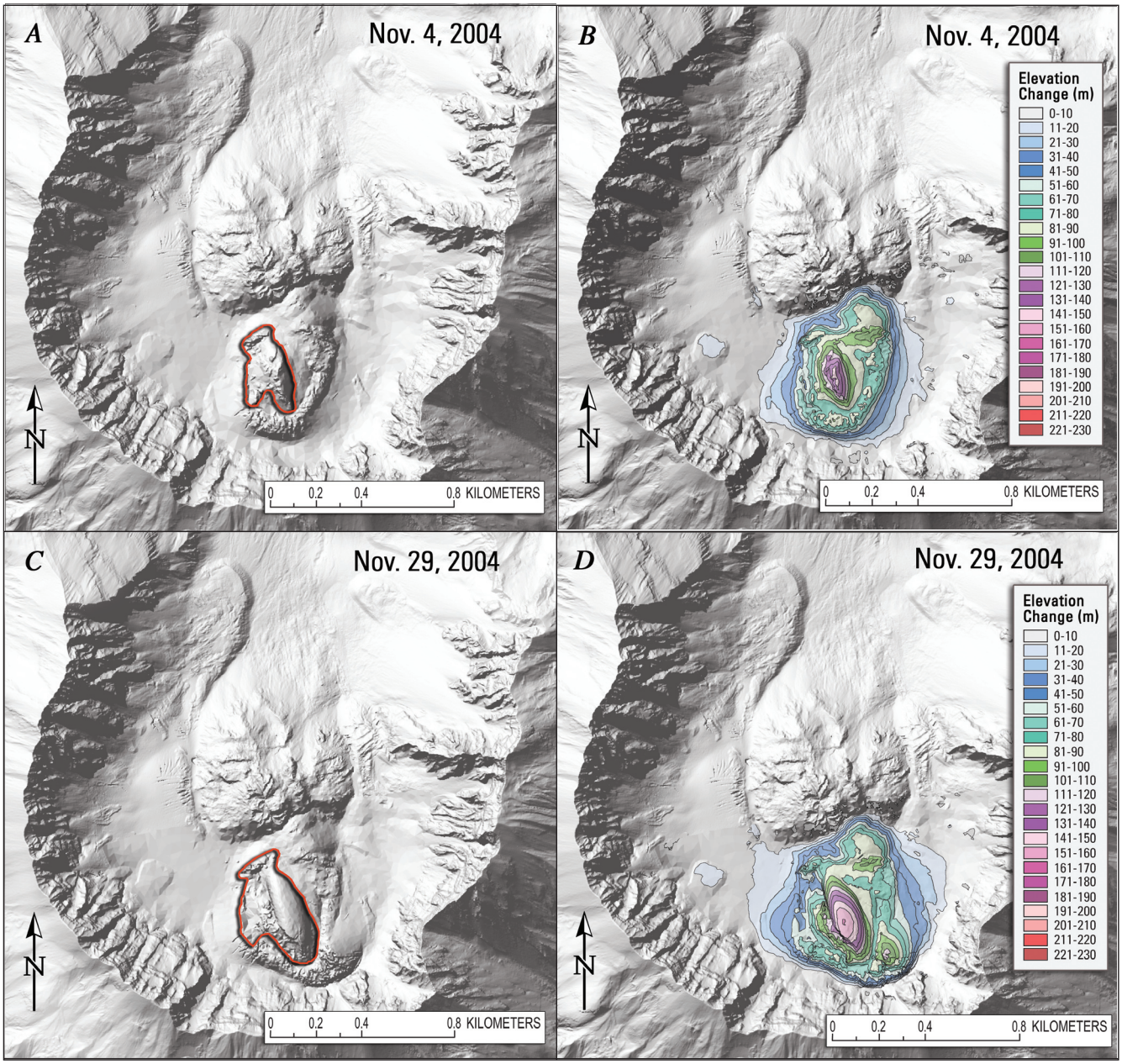

Figure 6. Sequence of eight pairs of shaded-relief images (*A*–*P*) showing growth of lava dome complex (red outline) and deformation of Crater Glacier from November 2004 to April 2005. Arrows (panel I) shows prominent, arcuate step on east Crater Glacier. For full explanation, see figure 3 and text.

The corresponding isoline maps for this time period show the response of the glacier to the growing dome (figs. 6*J*, 6*L*, 6*N*, 6*P*) as an increasing number of en echelon, east-trending, transverse crevasses cut east Crater Glacier. Apparent counterclockwise rotation and thickening of the glacier west of Shoestring notch to more than 110 m above its former surface in 2003 was in response to the dome-glacier margin moving eastward. In March 2005, a second small area of glacier ice had reached a similar height (fig. 6*N*) and, by April, an area about 100 by 50 m had attained a height of more than 120 m above the 2003 surface (fig. 6*P*).

Between late February and April, new crevasses oblique and perpendicular to the existing crevasses cut the southern part of the glacier into blocks (fig. 6*O*). A prominent east-west, arcuate, steplike feature (figs. 6*I–P*; highlighted by arrows on fig. 6*I*) about 30 m high formed at the glacier surface east of the 1980s lava dome (see discussion in Walder and others, this volume, chap. 13). This ice step was cut by short radial crevasses. The broad thickening of west Crater Glacier continued primarily along the southwest edge of the 1980s lava dome. For example, the 20-m isoline lay about 130 m farther northwest in April than in February (figs. 6*J*, 6*P*).

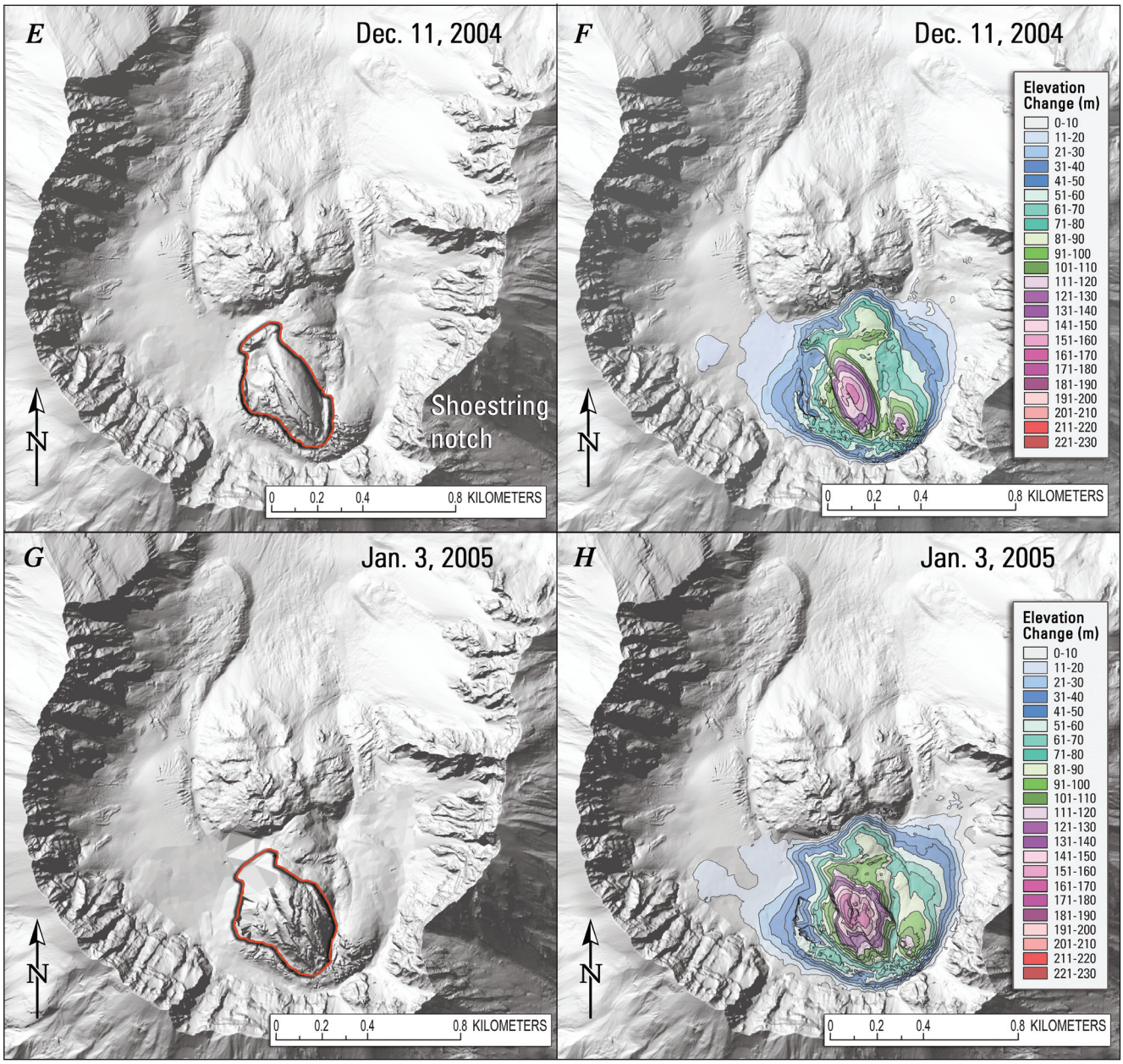

Figure 6—Continued.

June 15 Through August 10, 2005

The third group of image pairs (fig. 7*A*–*F*) shows that dome growth began to migrate west from its previous locus in the southeastern part of the crater. Though it is obscured in the June image (fig. 7*A*), the July image (fig. 7*C*) shows spine 5 was shorter (145 m in length), narrower (100 m across at the base), and higher (altitude 2,352 m, 250 m above the 2003 glacier surface) than the previous two spines, and it sloped steeply (about 60°) in all directions (see Vallance and others, this volume, chap. 9). Talus filled the substantial trough between west Crater Glacier and the dome that had existed for more than six months, eventually spilling onto the glacier surface. The slope angle of the talus on the northwest part of the new dome was about 32°. In July, spine 5 attained a height of 260 m (altitude 2,368 m) above the 2003 surface—the highest measured so far and within 2 m of the altitude of Shoestring notch, the lowest point on the crater rim. In August the dome was about 700 m in length and 600 m in width, with a volume of 62×10^6 m^3. Throughout the summer, crevasses continued to increase in number, disrupting the east Crater Glacier surface south of the prominent step, and they appeared in the elongate terminus of the glacier for the first time (fig.

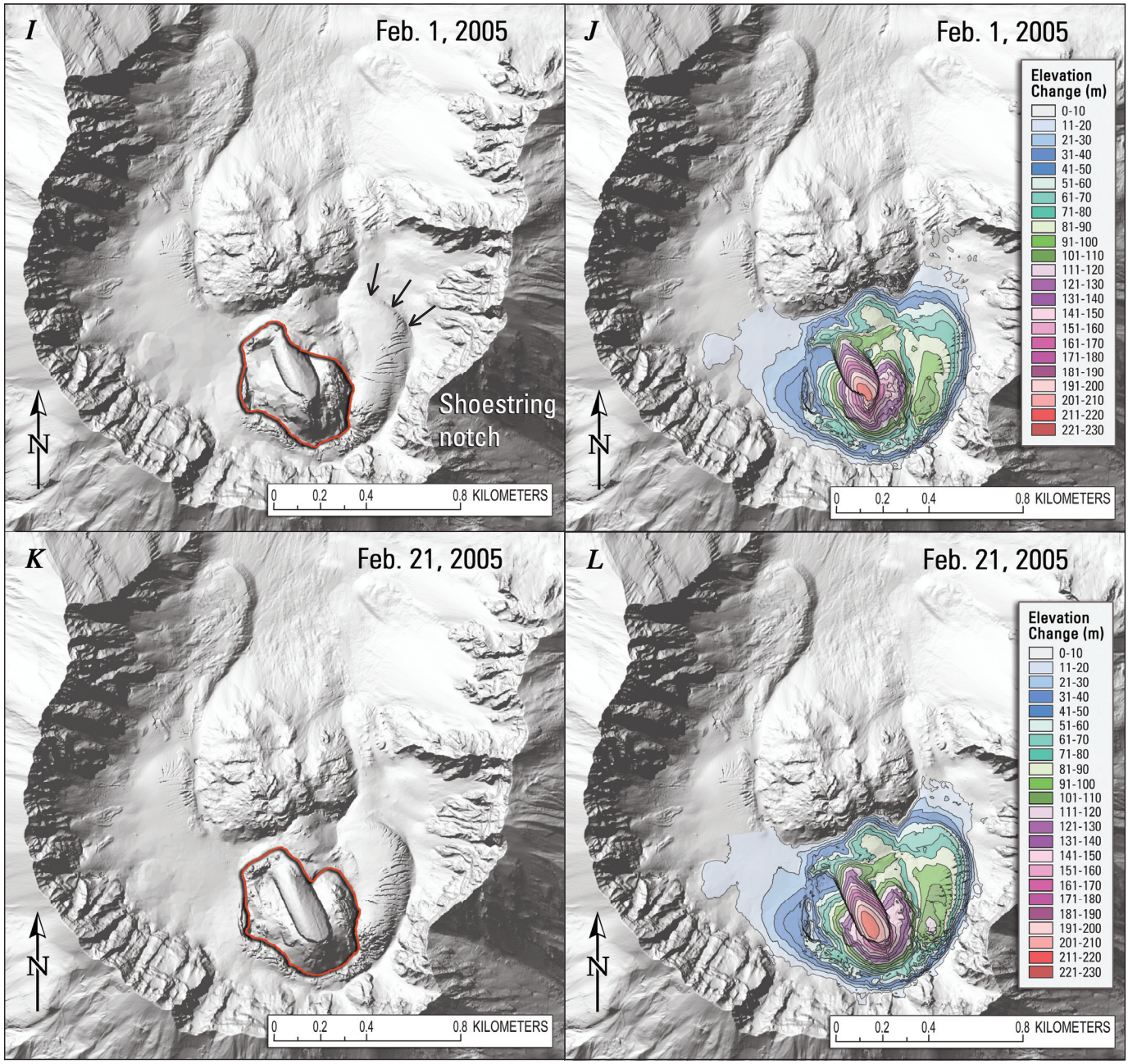

Figure 6—Continued.

7*A*–*F*). The effect of the northward advance of east Crater Glacier's terminus was to create an island of increased elevation shown by a series of closed isolines (for example, fig. 7*B*) (Walder and others, this volume, chap. 13). The isolines on west Crater Glacier indicate that thickening had slowed. However, subtracting the June 14 glacier surface from the July 15 glacier surface yields a negative change in volume (-1.5×10^6 m^3), likely a result of glacier melting. The west Crater Glacier-dome contact migrated about 60 m west between March and August, and radial and circumferential crevasses formed along the southeastern edge of the west glacier.

September 20 Through December 15, 2005

The fourth group of image pairs, (fig. 8*A*–*F*) shows that the locus of new dome growth migrated about 200 m west between August 10 and September 20, 2005. Part of spine 5 had decreased in elevation by about 75 m, forming a depression. Between September and December, spines 6 and 7 continued to grow westward, and the depression became a well-defined trough separating the newest growth from earlier spines. Spine 6 is difficult to distinguish within its flanking talus (fig. 8*A*), but it extruded on the northeast end of an elongate, arcuate ridge trending southwest along

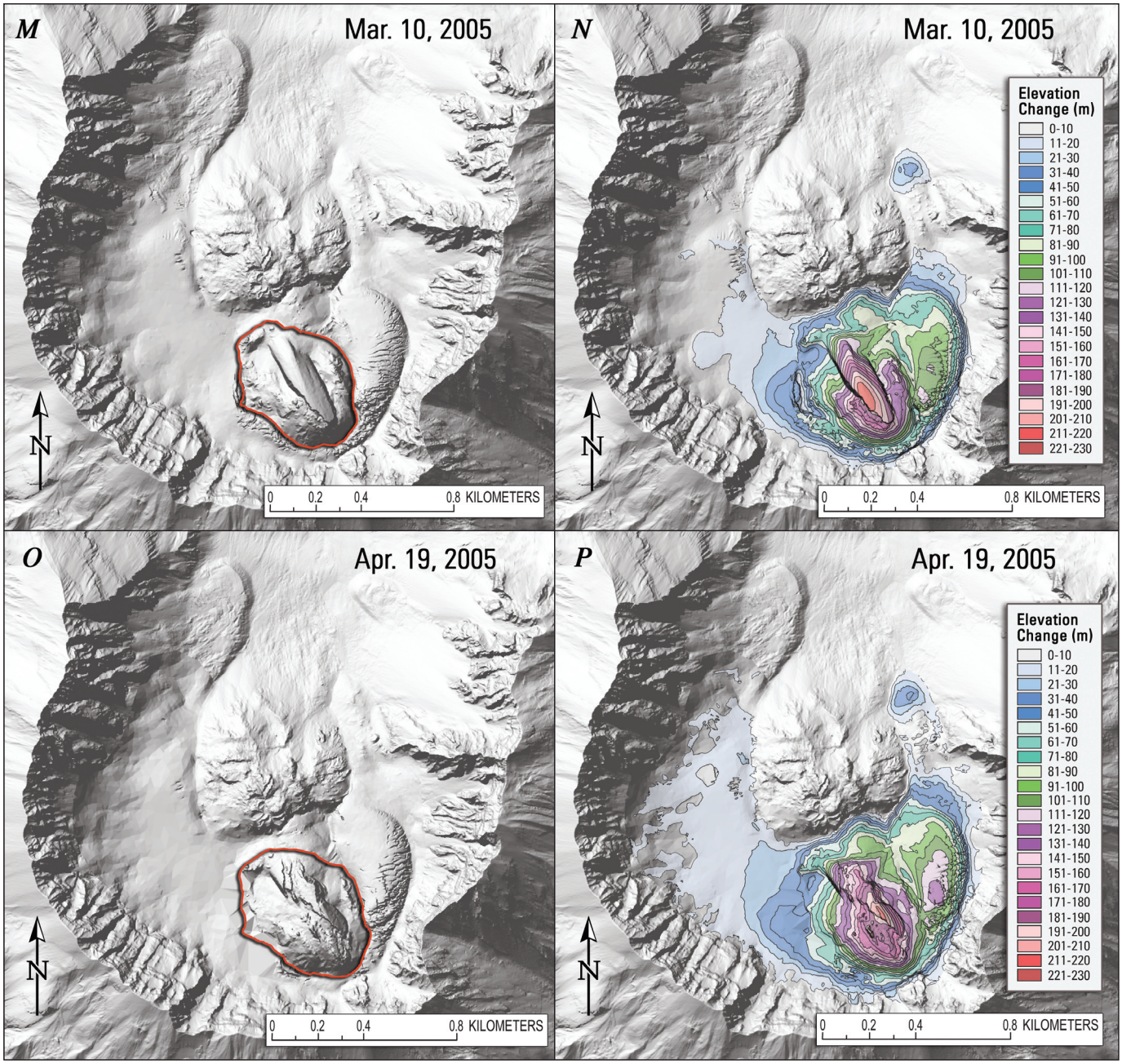

Figure 6—Continued.

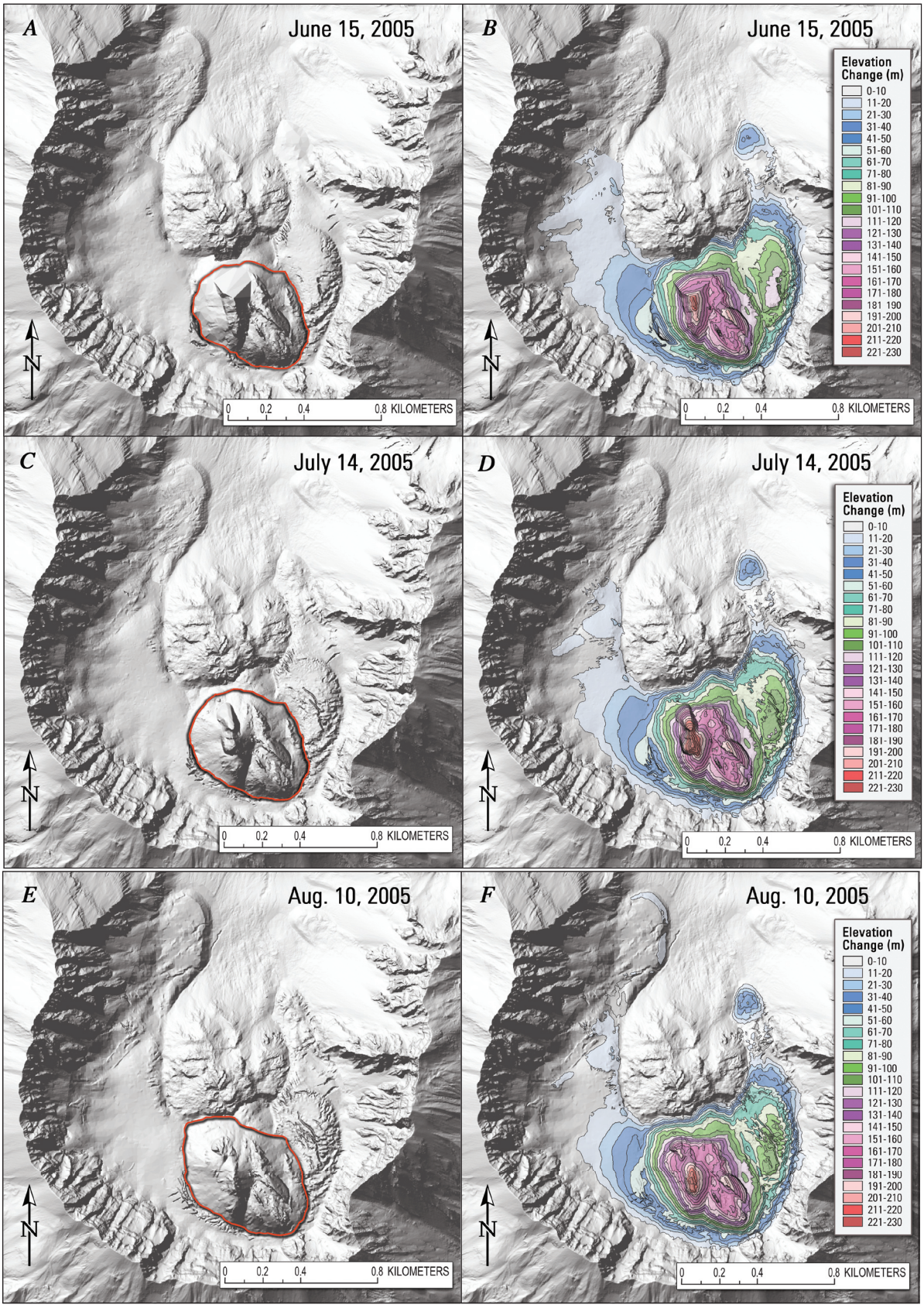

Figure 7. Sequence of three pairs of shaded-relief images (*A*–*F*) showing growth of lava dome complex (red outline) and deformation of Crater Glacier from June to August 2005. For full explanation, see figure 3 and text.

the top of the talus. In September, this newest part of the dome was about 420 m long, 285 m wide, and about 170 m (2,274 m altitude) above the 2003 glacier surface. By October, the highest point of spine 6 had migrated about 85 m west. Between October and December, spine 7 penetrated the eastern side of spine 6 and extruded upward and westward, bounded by a well-defined, nearly planar, gouge-covered surface striking approximately north-south. The nearly circular mass of talus and spines 6 and 7 was 430 m in length, 425 m in width, and about 180 m (altitude 2,280 m) above the 2003 surface. By December 2005, the entire dome complex was about 900 m long, 625 m wide, and 190 m (altitude 2,316 m) above the 2003 surface. Its volume, 73×10^6 m^3, was nearly equal to the 74×10^6 m^3 volume estimate of erupted lava for the 1980s lava dome (Swanson and Holcomb, 1990). East Crater Glacier was severely disrupted by both crevasses and summer ablation. The west glacier-dome contact migrated about 100 m west between September and December. Large crevasses formed on the west glacier, most likely in response to westward dome growth (Walder and others, this volume, chap. 13). Radial and circumferential crevasses increased in both size and number between September and December until the part of the glacier adjacent to the new dome took on the appearance of the disrupted east glacier. A prominent linear step, similar to the one on the east glacier, had migrated about 100 m north, and a broad area immediately south of the step had risen about 40 m.

Discussion

DEMs constructed from vertical aerial photographs provided an effective means to track and quantify dome growth and to calculate average magma-discharge rates of the 2004–5 lava dome at Mount St. Helens, as well as to gauge deformation of Crater Glacier. The DEMs met commonly identified needs in being (1) accurate—satisfying the appeal for precise, high-quality measurements at growing domes (Newhall and Melson, 1983); (2) safe—"acquired at low risk, and consequently * * * an important element in monitoring future activity of potentially explosive volcanoes" (Moore and Albee, 1981, p. 127); and (3) relatively inexpensive—acquisition costs of vertical aerial photographs and high-resolution scans are about 5 to 10 percent of those of other technologies such as lidar. Below we highlight suggestions for use of this technique at future eruptions, point out how DEMs and extruded-volume and extrusion-rate data were used in other studies, and draw a few brief comparisons between this and other dome-building eruptions.

Importance of Preparation and Suggestions for Improvements

Accurate measurements of the dome and glacier at Mount St. Helens were possible during even the critical earliest part of the 2004–5 eruption because we had baseline data and photogrammetric infrastructure in place before the eruption began. An earlier study of Crater Glacier (Schilling and others, 2004) had (1) identified an experienced photogrammetric contractor that ensured accuracy in camera calibration, film processing and scanning, and critical flight parameters such as altitude; (2) developed skills using aerotriangulation to orient blocks of photogrammetric stereomodels and to collect breaklines and points to create DEM surfaces with minimal operator bias and error; and (3) most importantly, established a network of ground control points on the flanks and crater floor of Mount St. Helens, validated by repeated measurements, with locational accuracy of a few centimeters. Hazards in the crater and uncertainty about the course of the eruption during late September and early October 2004 would have limited our ability to establish ground control. In retrospect, a greater number of control points in the crater area would have been useful, both to replace sites that were destroyed by explosions early in the eruption and to establish a set of points that could be remeasured to evaluate the accuracy of successive DEMs.

We spent days to weeks constructing each detailed DEM presented in this report, but, especially early in the eruption, a two-stage approach would have been advantageous to balance the need for rapid measurements for hazard-assessment purposes versus a greater level of detail for in-depth studies. Initial work would capture the minimal detail needed to obtain preliminary volume and extrusion-rate measurements. Later, as time allowed, we could add greater detail and improve accuracy.

Average Extrusion Rates

Plots of volume through time, whether comparing new crater-surface topography to the relatively uniform 2003 glacier surface (total volume change) or lava-dome volume as defined by the vertical projection of the dome outline to the 1986 crater floor (extruded volume), show that volume increased quickly early in the eruption and more slowly thereafter (fig. 9; table 1). Early in the eruption, measurements of total volume change document the deformation of glacier ice and existing crater floor to form a prominent welt (Dzurisin and others, 2005) having a volume of 10×10^6 m^3 and a growth rate of 8.9 m^3/s before lava first appeared at the surface on October 11, 2004. This volume estimate may be a minimum, because steam obscured some of the vent area. After the appearance of dacite lava at the surface, lava extrusion rates were initially 5.9 m^3/s, slowing to 2.5 m^3/s by the beginning of January 2005. After early 2005, the extrusion rate gradually declined to about 0.7 m^3/s, with a minor increase in rate during late summer 2005, and the total extruded volume gradually increased to 73×10^6 m^3 near the end of 2005.

For much of the eruption, the extruded-lava volume derived from the DEMs was the most appropriate measure of dome growth. However, especially early in the eruption, the unique situation of a lava dome erupting through a glacier required a second method, which included a measure of the total volume of surface deformation. This value was the sum of extruded volume and other surface volume change owing

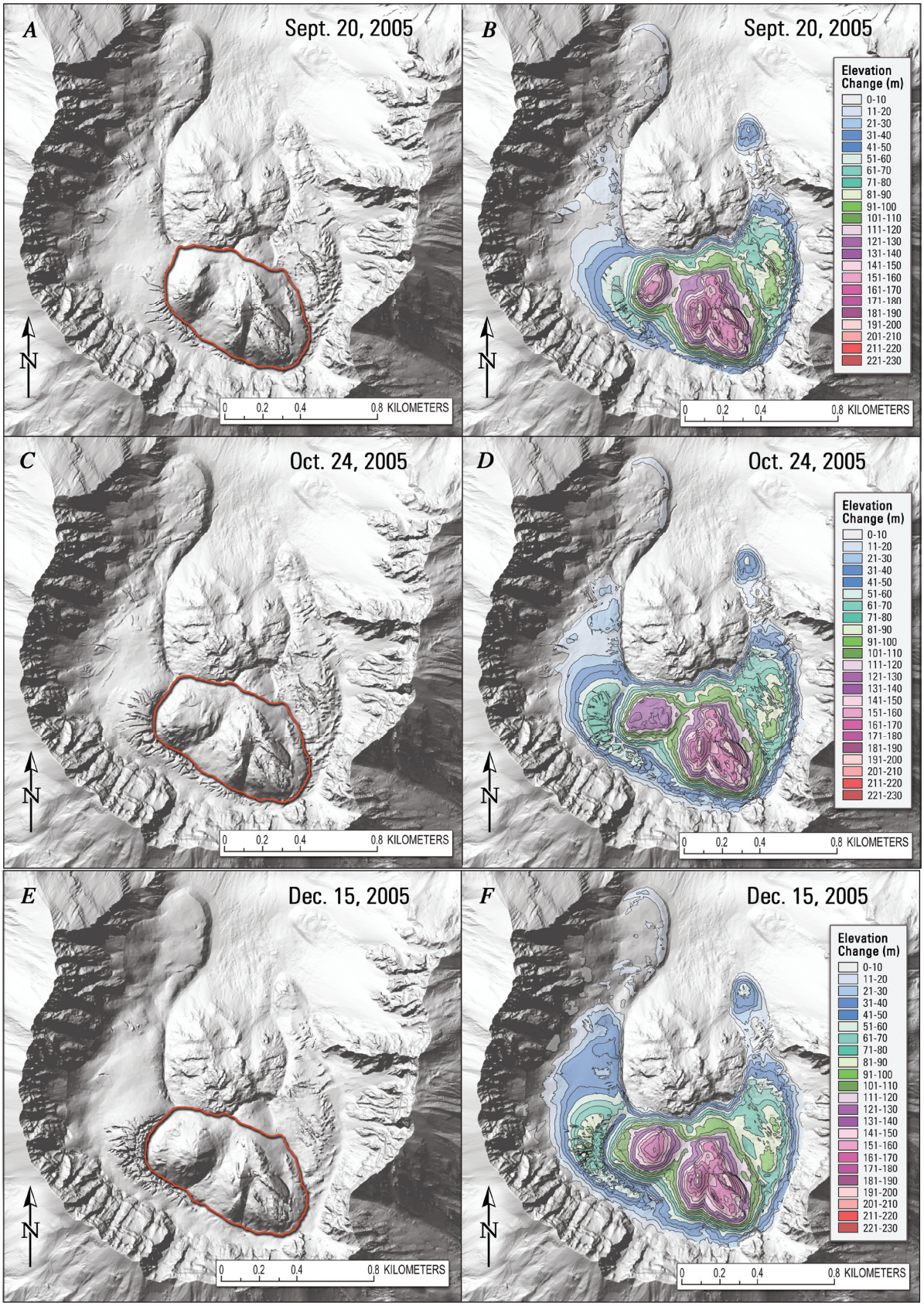

Figure 8. Sequence of three pairs of shaded-relief images (*A* –*F*) showing growth of lava dome complex (red outline) and deformation of Crater Glacier from September to December 2005. For full explanation, see figure 3 and text.

to deformation, snow and ice removal or accumulation, and addition of new talus from the crater walls. As the eruption continued, we used the extruded-lava volume to track dome growth and used the total volume change mainly to track changes in the glacier. Differences between the two rates resulted from factors unrelated to lava extrusion. For example, a prominent increase in the volume change rate in April 2005 (fig. 9*B*) coincided with including a larger part of west Crater Glacier in the April DEM, which resulted in adding more thickened glacier and seasonal snowfall to the total volume. A notable decrease of total volume change during a period of low extrusion rate during the summer of July 2005 likely reflects summer snowmelt and glacier ablation. The apparent slight increase in the extruded-lava rate in August 2005 is likely real.

Use of DEMs and Volume and Extrusion-Rate Data in Studies of the 2004–2005 Eruption

Vertical aerial photographs and the DEMs derived from them constitute one of the most widely used data sets collected during the 2004–5 eruption of Mount St. Helens. Scanned versions of the vertical aerial photographs provided a consistent base for interpretation and construction of photogeologic maps (Herriott and others, this volume, chap. 10). The DEMs provided numerical constraints to solve equations needed to estimate linear extrusion rates from a single remote camera (Major and others, this volume, chap. 12). Coupling the aerial photographic documentation with fields of deformation vectors and profiles of the dome derived from the DEMs yielded evidence to interpret the mechanics of dome growth (Vallance and others, this volume, chap. 9). Measurements and profiles from the DEMs helped to track the remarkable deformation of east and west Crater Glacier and showed that relatively little ice has been melted by dome growth (Walder and others, this volume, chap. 13).

Measurements of dome volume and extrusion rate were combined with other data sets such as seismology, gas geochemistry, and ground deformation to better understand eruptive processes. As the eruption continued, the extrusion rate remained relatively constant, even though the character of seismicity varied, suggesting that earthquakes were controlled more by changes in extrusion mechanics than by changes in extrusion rate (Moran and others, this volume, chap. 2). The

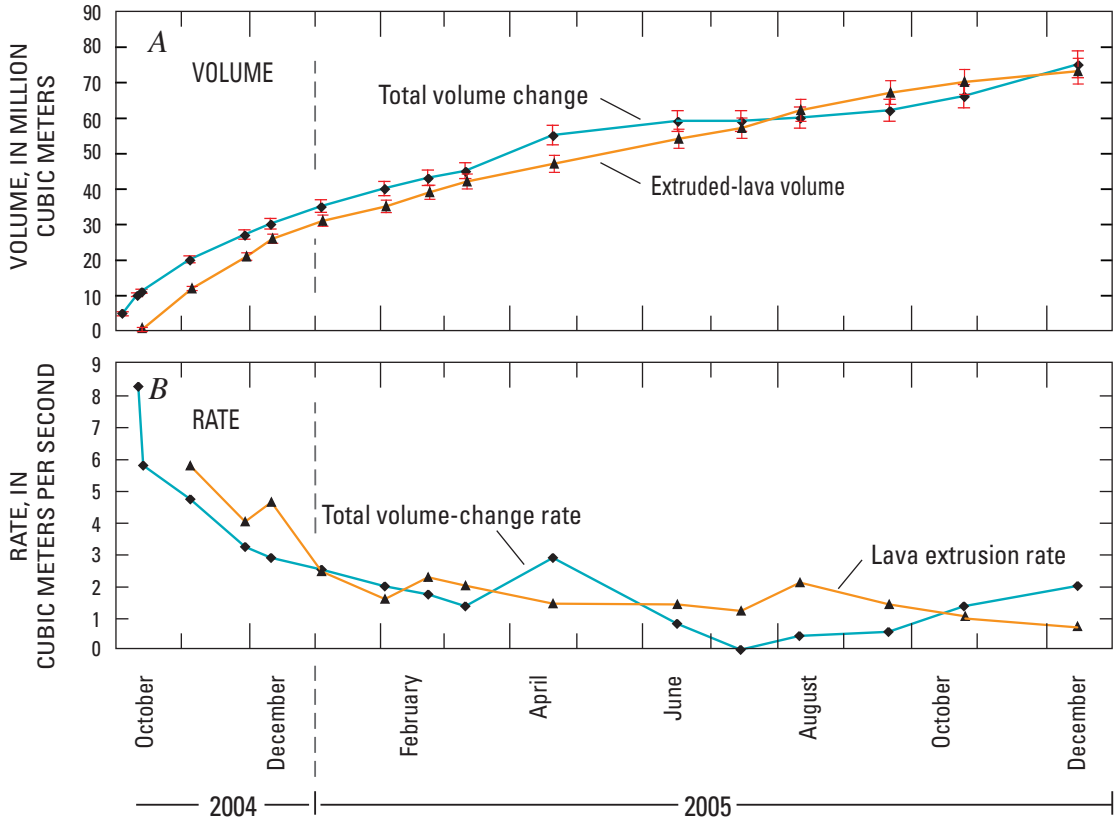

Figure 9. Time-series plots of dome growth at Mount St. Helens from start of eruption through December 2005. *A*, Total volume change (blue line) and extruded-lava volume (orange line) versus time. *B*, Total volume change rate (blue line) and volumetric extrusion rate (orange line) versus time. Early in eruption, all surface deformation likely resulted from extrusion or shallow intrusion of lava into glacier, and total volume change therefore would approximate lava extrusion rate.

nearly constant extrusion rate was also a key observation incorporated into a mechanistic model of extrusion driven by a nearly constant influx of magma from depth and resisted by a plug of solidified magma that slipped incrementally against the walls of the conduit (Iverson and others, 2006; Iverson, this volume, chap. 21). Models from GPS (Lisowski and others, this volume, chap. 15) and InSAR data (Poland and Lu, this volume, chap. 18) yield estimates of reservoir volume loss of $15–30\times10^6$ m^3, compared with a volume of $70–80\times10^6$ m^3 for the lava dome. This disparity most likely reflects a combination of expansion of magmatic volatiles and recharge (Mastin and others, this volume, chap. 22). However, erupted volumes and total volatile output for the 2004–5 eruption were used to estimate the volatile content of magma at 8.6-km depth. Gerlach and others (this volume, chap. 26) conclude that the magma was nearly depleted in excess volatiles, suggesting that new gas-rich magma has not been added into the reservoir during the months just before or during the eruption.

Volume measurements of the growing lava dome and derived extrusion rates help to place the 2004–5 eruption in context with those of other dome-building volcanoes (fig. 10) and within the growth history of Mount St. Helens since 1980. The average rate of growth of the current dome, about 2 m^3/s through the end of 2005, is an order of magnitude above the long-term (1980–present) eruption rate of Mount St. Helens (Iverson, this volume, chap. 21). However, when compared to other dome-growth episodes at Mount St. Helens and elsewhere the current growth rate is fairly typical (fig. 10).

Conclusions

Vertical aerial photographs, taken at time intervals ranging from successive days to every few weeks, and the digital elevation models (DEMs) constructed from them have been critical tools to document the remarkable growth history of the 2004–5 lava dome at Mount St. Helens, especially in providing estimates of volume and volumetric extrusion rate. Single DEMs provided length and width measurements of the dome and glacier; sequential DEMs recorded temporal and spatial changes. Moreover, measurements of volume and volumetric extrusion rate proved to be critical parameters. When combined with other primary data sets, they helped to form models and hypotheses that illuminated the mechanics and dynamics of the eruption, and thus helped to assess volcano hazards. The successful application of aerophotogrammetry to monitor this eruption was possible largely because baseline data and photogrammetric infrastructure were in place before the onset of activity. The aerial photos and DEMs obtained in this study are an enduring resource for addressing basic questions about the eruption, including many raised in other papers in this collection and, we suspect, others yet to be asked.

Acknowledgments

We thank Richard Iverson, Richard Herd, and Dan Dzurisin for their insightful and helpful reviews. Dan Dzuri-

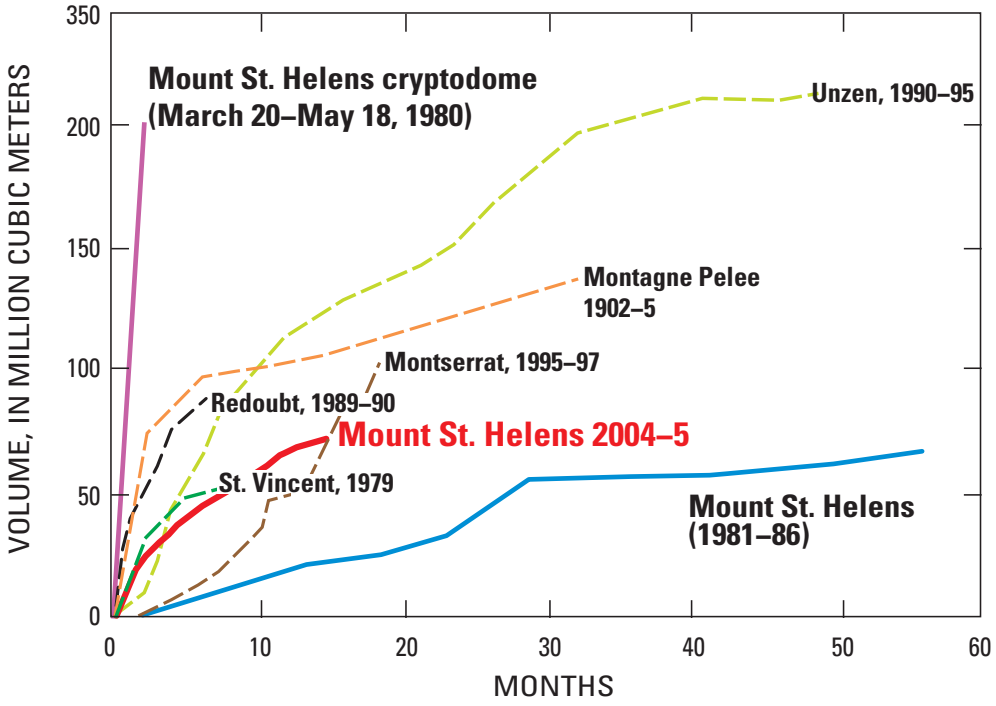

Figure 10. Mount St. Helens 2004–2005 growth rate curve compared with other historical lava domes (modified from Nakada and others, 1999; Tanguy, 2004).

sin also contributed insightful and helpful discussions. Bergman Photographic Services, including Larry and Bruce Bergman, Travis Marshall, Trevor Gray, Steve Tank, Kyla Dorsey, and John Hogl, have all contributed their expertise to ensure that we acquired excellent aerial photographs and scans. We are indebted to Jeff Linscott and the folks at JL Aviation for outstanding helicopter work, especially landing us gently in difficult places on the mountain for ground control work. Frank Trusdell, Mike Poland, Julie Griswold, Chris Harpel, Dave Ramsey, Joel Robinson, Stephanie Konfal, Angie Diefenbach, Sarah Thompson, and Susanne Ettinger helped with ground control work and offered insightful discussions. Last, but perhaps most important, we thank Bobbie Myers, who watched over us remotely, tracked our safety, and allowed us to focus on field tasks.

References Cited

Achilli, V., Baldi, P., Baratin, L., Bonini, C., Ercolani, E., Gandolfi, S., Anzidei, M., and Riguzzi, F., 1998, Digital photogrammetric survey on the island of Vulcano: Acta Vulcanologica, v. 10, no. 1, p. 1–5.

Baldi, P., Bonvalot, S., Briole, P., and Marsella, M., 2000, Digital photogrammetry and kinematic GPS applied to the monitoring of Vulcano Island, Aeolian arc, Italy: Geophysics Journal International, v. 142, no. 3, p. 801–811.

Baldi, P., Fabris, M., Marsella, M., and Monticelli, R., 2005, Monitoring the morphological evolution of the Sciara del Fuoco during the 2002–2003 Stromboli eruption using multi-temporal photogrammetry: ISPRS Journal of Photogrammetry and Remote Sensing, v. 59, no. 4, p. 199–211.

Daniel, C., and Tennant, K., 2001, DEM quality assessment, *in* Maune, D., ed., Digital elevation model technologies and applications; the DEM users manual: Town, Maryland, American Society of Photogrammetry and Remote Sensing, 539 p.

Dzurisin, D., 2003, A comprehensive approach to monitoring volcano deformation as a window on the eruption cycle: Reviews of Geophysics, v. 41, no. 1, 29 p., doi:10.1029/2001RG000107.

Dzurisin, D., Vallance, J.W., Gerlach, T.M., Moran, S.C., and Malone, S.D., 2005, Mount St. Helens reawakens: Eos (American Geophysical Union Transactions), v. 86, no. 3, p. 25, 29.

Dzurisin, D., Lisowski, M., Poland, M.P., Sherrod, D.R., and LaHusen, R.G., 2008, Constraints and conundrums resulting from ground-deformation measurements made during the 2004–2005 dome-building eruption of Mount St. Helens, Washington, chap. 14 *of* Sherrod, D.R., Scott, W.E., and Stauffer, P.H., eds., A volcano rekindled; the renewed eruption of Mount St. Helens, 2004–2006: U.S. Geological Survey Professional Paper 1750 (this volume).

Gerlach, T.M., McGee, K.A., and Doukas, M.P., 2008, Emission rates of CO_2, SO_2, and H_2S, scrubbing, and preeruption excess volatiles at Mount St. Helens, 2004–2005, chap. 26 *of* Sherrod, D.R., Scott, W.E., and Stauffer, P.H., eds., A volcano rekindled; the renewed eruption of Mount St. Helens, 2004–2006: U.S. Geological Survey Professional Paper 1750 (this volume).

Harris, A.J.L., Rose, W.I., and Flynn, L.P., 2003, Temporal trends in lava dome extrusion at Santiaguito 1922–2000: Bulletin of Volcanology, v. 65, p. 77–89.

Herriott, T.M., Sherrod, D.R., Pallister, J.S., and Vallance, J.W., 2008, Photogeologic maps of the 2004–2005 Mount St. Helens eruption, chap. 10 *of* Sherrod, D.R., Scott, W.E., and Stauffer, P.H., eds., A volcano rekindled; the renewed eruption of Mount St. Helens, 2004–2006: U.S. Geological Survey Professional Paper 1750 (this volume).

Iverson, R.M., 2008, Dynamics of seismogenic volcanic extrusion resisted by a solid surface plug, Mount St. Helens, 2004–2005, chap. 21 *of* Sherrod, D.R., Scott, W.E., and Stauffer, P.H., eds., A volcano rekindled; the renewed eruption of Mount St. Helens, 2004–2006: U.S. Geological Survey Professional Paper 1750 (this volume).

Iverson, R.M., Dzurisin, D., Gardner, C.A., Gerlach, T.M., LaHusen, R.G., Lisowski, M., Major, J.J., Malone, S.D., Messerich, J.A., Moran, S.C., Pallister, J.S., Qamar, A.I., Schilling, S.P., and Vallance, J.W., 2006, Dynamics of seismogenic volcanic extrusion at Mount St. Helens in 2004–2005: Nature, v. 444, no. 7118, p. 439–443, doi:10.1038/nature05322.

Lescinsky, D.T., and Fink, J.H., 2000, Lava and ice interaction at stratovolcanoes; use of characteristic features to determine past glacial extents and future volcanic hazards: Journal of Geophysical Research, v. 105, no. B10, p. 23711–23726.

Lisowski, M., Dzurisin, D., Denlinger, R.P., and Iwatsubo, E.Y., 2008, Analysis of GPS-measured deformation associated with the 2004–2006 dome-building eruption of Mount St. Helens, Washington, chap. 15 *of* Sherrod, D.R., Scott, W.E., and Stauffer, P.H., eds., A volcano rekindled; the renewed eruption of Mount St. Helens, 2004–2006: U.S. Geological Survey Professional Paper 1750 (this volume).

Major, J.J., Kingsbury, C.G., Poland, M.P., and LaHusen, R.G., 2008, Extrusion rate of the Mount St. Helens lava dome estimated from terrestrial imagery, November 2004–December 2005, chap. 12 *of* Sherrod, D.R., Scott, W.E., and Stauffer, P.H., eds., A volcano rekindled; the renewed eruption of Mount St. Helens, 2004–2006: U.S. Geological Survey Professional Paper 1750 (this volume).

Mastin, L.G., Roeloffs, E., Beeler, N.M., and Quick, J.E., 2008, Constraints on the size, overpressure, and volatile content of the Mount St. Helens magma system from geodetic and dome-growth measurements during the 2004–2006+ eruption, chap. 22 *of* Sherrod, D.R., Scott, W.E., and Stauffer, P.H., eds., A volcano rekindled; the renewed eruption of Mount St. Helens, 2004–2006: U.S. Geological Survey Professional Paper 1750 (this volume).

Messerich, J.A., Schilling, S.P., and Thompson, R.A., 2008, Digital elevation models of the pre-eruption 2000 crater and 2004–07 dome-building eruption at Mount St. Helens, Washington, U.S.A.: U.S. Geological Survey Open-File Report 2008–1169, 2 p., with digital database. [http://pubs.usgs.gov/of/2008/1169, last accessed July 15, 2008].

Miller, T.P., 1994, Dome growth and destruction during the 1989–1990 eruption of Redoubt Volcano: Journal of Volcanology and Geothermal Research, v. 62, nos. 1–4, p. 197–212.

Mills, H.H., 1992, Post-eruption erosion and deposition in the 1980 crater of Mount St. Helens, Washington, determined from digital maps: Earth Surface Processes and Landforms, v. 17, no. 8, p. 739–754.

Moore, J.G., and Albee, W.C., 1981, Topographic and structural changes, March–July 1980—photogrammetric data, *in* Lipman, P.W., and Mullineaux, D.R., eds,, The 1980 eruptions of Mount St. Helens, Washington: U.S. Geological Survey Professional Paper 1250, p. 123–134.

Moran, S.C., Malone, S.D., Qamar, A.I., Thelen, W.A., Wright, A.K., and Caplan-Auerbach, J., 2008, Seismicity associated with renewed dome building at Mount St. Helens, 2004–2005, chap. 2 *of* Sherrod, D.R., Scott, W.E., and Stauffer, P.H., eds., A volcano rekindled; the renewed eruption of Mount St. Helens, 2004–2006: U.S. Geological Survey Professional Paper 1750 (this volume).

Nakada, S., Shimizu, H., and Ohta, K., 1999, Overview of the 1990–1995 eruption at Unzen Volcano: Journal of Volcanology and Geothermal Research, v. 89, nos. 1–4, p. 1–22, doi:10.1016/S0377-0273(98)00118-8.

Newhall, C.G., and Melson, W.G., 1983, Explosive activity associated with the growth of volcanic domes: Journal of Volcanology and Geothermal Research, v. 17, p. 111–131.

Pallister, J.S., Thornber, C.R., Cashman, K.V., Clynne, M.A., Lowers, H.A., Mandeville, C.W., Brownfield, I.K., and Meeker, G.P., 2008, Petrology of the 2004–2006 Mount St. Helens lava dome—implications for magmatic plumbing and eruption triggering, chap. 30 *of* Sherrod, D.R., Scott, W.E., and Stauffer, P.H., eds., A volcano rekindled; the renewed eruption of Mount St. Helens, 2004–2006: U.S. Geological Survey Professional Paper 1750 (this volume).

Poland, M.P., and Lu, Z., 2008, Radar interferometry observations of surface displacements during pre- and coeruptive periods at Mount St. Helens, Washington, 1992–2005, chap. 18 *of* Sherrod, D.R., Scott, W.E., and Stauffer, P.H., eds., A volcano rekindled; the renewed eruption of Mount St. Helens, 2004–2006: U.S. Geological Survey Professional Paper 1750 (this volume).

Queija, V.R., Stoker, J.M., and Kosovich, J.J., 2005, Recent U.S. Geological Survey applications of Lidar: Photogrammetric Engineering and Remote Sensing, v. 71, no. 1, p. 5–9.

Schilling, S.P., Carrara, P.E., Thompson, R.A., and Iwatsubo, E.Y., 2004, Posteruption glacier development within the crater of Mount St. Helens, Washington, USA: Quaternary Research, v. 61, p. 325–329.

Sparks, R.S.J., Young, S.R., Barclay, J., Calder, E.S., Cole, P., Darroux, B., Davies, M.A., Druitt, T.H., Harford, C., Herd, R., James, M., Lejeune, A.M., Norton, G., Skerrit, G., Stasiuk, M.V., Stevens, N.S., Toothill, J., Wadge, G., and Watts, R., 1998, Magma production and growth of the lava dome of the Soufriere Hills Volcano, Montserrat, West Indies; November 1995 to December 1997: Geophysical Research Letters, v. 25, no. 18, p. 3421–3424.

Swanson, D.A., and Holcomb, R.T., 1990, Regularities in growth of the Mount St. Helens dacite dome, 1980–1986, *in* Fink, J.H., ed., Lava flows and domes, emplacement mechanisms and hazard implications: Berlin, Springer-Verlag, International Association of Volcanology and Chemistry of the Earth's Interior, Proceedings in Volcanology 2, p. 3–24.

Swanson, D.A., Lipman, P.W., Moore, J.G., Heliker, C.C., and Yamashita, K.M., 1981, Geodetic monitoring after the May 18 eruption, *in* Lipman, P.W., and Mullineaux, D.R., eds., The 1980 eruptions of Mount St. Helens, Washington: U.S. Geological Survey Professional Paper 1250, p. 157–168.

Tanguy, J.-C., 2004, Rapid dome growth at Montagne Pelée during the early stages of the 1902–1905 eruption; a reconstruction from Lacroix's data: Bulletin of Volcanology, v. 66, no. 7, p. 615–621, doi:10.1007/s00445-004-0344-z.

Thompson, R.A., and Schilling, S.P., 2007, Photogrammetry, *in* Dzurisin, D., ed., Volcano deformation—geodetic monitoring techniques: Berlin, Springer, Springer-Praxis Books in Geophysical Sciences, p. 195–221.

Vallance, J.W., Schneider, D.J., and Schilling, S.P., 2008, Growth of the 2004–2006 lava-dome complex at Mount St. Helens, Washington, chap. 9 *of* Sherrod, D.R., Scott, W.E., and Stauffer, P.H., eds., A volcano rekindled; the renewed eruption of Mount St. Helens, 2004–2006: U.S. Geological Survey Professional Paper 1750 (this volume).

Walder, J.S., Schilling, S.P., Vallance, J.W., and LaHusen, R.G., 2008, Effects of lava-dome growth on the Crater Glacier of Mount St. Helens, Washington, chap. 13 *of* Sherrod, D.R., Scott, W.E., and Stauffer, P.H., eds., A volcano

rekindled; the renewed eruption of Mount St. Helens, 2004–2006: U.S. Geological Survey Professional Paper 1750 (this volume).

Wolf, P.R., and Dewitt, B.A., 2000, Elements of photogrammetry with applications in GIS (3d ed.): Boston, McGraw-Hill, 608 p.

Zilkoski, D.B., Richards, J.H., and Young, G.M., 1992, Special report—results of the general adjustment of the North American Vertical Datum of 1988: Surveying and Land Information Systems, v. 52, p. 133–149.

Zlotnicki, J., Ruegg, J.C., Bachelery, P., and Blum, P.A., 1990, Eruptive mechanism on Piton de la Fournaise volcano associated with the December 4, 1983, and January 18, 1984 eruptions from ground deformation monitoring and photogrammetric surveys: Journal of Volcanology and Geothermal Research, v. 40, no. 3, p. 197–217, doi:10.1016/0377-0273(90)90121-U.

Appendix 1. Hillslope Shaded-Relief Maps

[This appendix appears only in the digital versions of this work—in the DVD that accompanies the printed volume and as a separate file accompanying this chapter on the Web at: http://pubs.usgs.gov/pp/1750.]

The appendix contains 17 raster images in Tagged Image File Format (filename extension is “tif”), one for each of the hillshade relief maps used in figures 4, 6, 7, and 8. The filename contains the date (year-month-day) of the map. Corresponding ASCII world files (filename extension “tfw”) for georeferencing the raster maps by GIS software are included, each using the Universal Transverse Mercator projection, zone 10, North American Datum 1983. A separate metadata file summarizes the pertinent details of image processing.

This page intentionally left blank

A Volcano Rekindled: The Renewed Eruption of Mount St. Helens, 2004–2006
Edited by David R. Sherrod, William E. Scott, and Peter H. Stauffer
U.S. Geological Survey Professional Paper 1750, 2008

Chapter 9

Growth of the 2004–2006 Lava-Dome Complex at Mount St. Helens, Washington

By James W. Vallance[1], David J. Schneider[2], and Steve P. Schilling[1]

Abstract

The eruption of Mount St. Helens from 2004 to 2006 has comprised extrusion of solid lava spines whose growth patterns were shaped by a large space south of the 1980–86 dome that was occupied by the unique combination of glacial ice, concealed subglacial slopes, the crater walls, and relics of previous spines. The eruption beginning September 2004 can be divided (as of April 2006) into five phases: (1) pre-dome deformation and phreatic activity, (2) initial extrusion of spines, (3) recumbent spine growth and repeated breakup, (4) southward extrusion across previous dome debris, and (5) normal faulting of the phase 4 dome to form a depression, a shift to westward extrusion and overthrusting of earlier phase 5 products. Overall, steady spine extrusion gradually slowed from 6 m^3/s in November 2004 to 0.6 m^3/s in February 2006.

Thermal camera data show that phase 1 activity included low-temperature thermal features, such as fumaroles, fractures, and ground warming related to rapid uplift, as well as deformation in the south moat of the crater. The relatively cold (<160°C) phreatic eruptions of early October heralded activity at a subglacial vent situated along the south-sloping margin of the 1980–86 dome. Thermal infrared imagery, documenting increased heat flow, presaged phase 2 extrusion of the October 11–15, 2004, lava spine. The thermal images of the extruding spine revealed a hot basal margin and highest temperatures of 600–730°C.

During phase 3, a recumbent whaleback-shaped spine with a low-temperature shroud of fault gouge and a hot, U-shaped basal margin extruded. This spine pushed southward along the bed of the glacier until it encountered the south wall of the 1980 crater, whereupon it broke up, decoupled, and regrew. Continued southward growth of the recumbent spine pushed cold deformed rock, hot dome rubble, and glacier ice eastward at a rate of 2 m/d. In April 2005, breakup of the whaleback and growth of a lava spine across previous dome rubble heralded phase 4 spine thrusting over previous spine remnants. During phase 4, the active spine pushed southward with an increasingly vertical component and increasing incidence of large rockfalls. In late July, the spine decoupled from its source, the vent reorganized, and a new spine began to grow westward at right angles to the previous growth direction, defining phase 5. Dome migration again plowed glacier ice out of the way at a rate of about 2 m/d, this time westward. In early October, the spine buckled near the vent and thrust over the previous one. A massive spine monolith had been constructed by December 2005, and growth of spines with increasingly steep slopes characterized activity through April 2006.

The chief near-surface controls on spine extrusion during 2004–6 have been vent location, relict topographic surfaces from the 1980s, and spine remnants emplaced previously during the present eruption. In contrast, glacier ice has had minimal influence on spine growth. Ice as thick as 150 m has prevented formation of marginal angle-of-repose talus fans but has not provided sufficient resistance to stop spine growth or slow it appreciably. Spines initially emerged along a relict south-facing slope as steep as 40° on the 1980s dome. The open space of the moat between that dome and the crater walls permitted initial southward migration of recumbent spines. An initial spine impinged on the opposing slopes of the crater and stopped; in contrast, recumbent whaleback spines of phase 3 impinged on opposing walls of the crater at oblique angles and rotated eastward before breaking up. Once spine remnants occupied all available open space to the south, spines thrust over previous remnants. Finally, with south and east portions of the moat filled, spine growth proceeded westward. Although Crater Glacier had only a small influence on the growing spines, spine growth affected the glacier dramatically, initially dividing it into two arms and then bulldozing it hundreds of meters, first east and then west, and heaping it more than 100 m higher than its original altitude.

[1] U.S. Geological Survey, 1300 SE Cardinal Court, Vancouver, WA 98683

[2] U.S. Geological Survey, Alaska Volcano Observatory, 4200 University Drive, Anchorage, AK 99508

Introduction

Continuous, steady extrusion of gas-poor, solidified dacitic magma through glacier ice has characterized the 2004–6 eruption of Mount St. Helens. Dome emplacement has been influenced by the geometry of the 1980 crater, an amphitheater ~2 km across, 500 m deep, and open to the north (fig. 1). In the exact middle of the amphitheater, the 1980–86 dome grew to a volume of about 77×10^6 m^3, attaining dimensions of 860 by 1,060 m in plan and reaching a height of 270 m above the flat-floored amphitheater (fig. 1*A*) (Swanson and Holcomb, 1990). By fall 2004, the north-facing aspect and steep walls, prolific annual snowfall, and frequent winter avalanches in the 1980 crater had given rise to a rapidly growing glacier, as thick as 150 m and with a volume of about 80×10^6 m^3, that wrapped the 1980s dome like a U (fig. 1*B*) (Schilling and others, 2004).

During initial volcanic unrest between September 23 and October 10, 2004, uplift and deformation along the southern part of the 1980s dome and glaciated areas to the south formed a welt more than 100 m high. Deformation of the 1980–86 dome, crater-floor debris, and glacier ice south of the 1980–86 dome has continued throughout the eruption. However, during subsequent dome growth, the locus of deformation has shifted southward, then alternately eastward and westward, as actively growing spines plowed old rocks, recently emplaced but inactive spines, and glacier ice out of their way (Dzurisin and others, 2005).

Following unrest that began on September 23, 2004, and culminated with phreatic eruptions 8–12 days later, intrusion and extrusion of solid magma has typified the eruption. The magma is unusually gas poor (Gerlach and others, this volume, chap. 26) and crystal rich (Pallister and others, this volume, chap. 30). Several meters of pulverized, variably sintered rock (Cashman and others, this volume, chap. 19) has commonly coated emergent lava spines, lending them a smooth appearance. Other spines have broken apart to become surrounded by hot talus fans.

Terminology used in this paper is as follows. A single lava dome was extruded at Mount St, Helens from 1980 to 1986 and a second from October 11, 2004, through the time of this writing. Because of their solid-state character, individual extrusions of the current dome-building eruption are termed "spines," not lobes. The term "recumbent" implies that the horizontal component of extrusion is greater than the vertical component. The term "whaleback" describes a form of smooth-surfaced recumbent spine. Several spines include upthrusted deformed rock of previous crumbled spines and older rock from the 1980–86 dome. Such spines are termed "compound" following Blake (1990) and distinguished from individual growing spines, which are typically monolithic rather than rubbly.

Spine morphologies of the current eruption are variants of Blake's (1990) upheaved plugs and peléean domes but do not include the more fluid, low lava domes and coulees. As of April 2006, the growing dome has included seven spines (figs. 2, 3) but no surface flowage features or extruded silicic lava flows. Spine shapes have included steeply inclined fins, broken blocky forms, and whalebacks (fig. 2). Four of the spines have grown recumbently, and five of them have pushed through thick glacial ice.

Thermal infrared imagery, petrography, and seismology all suggest that extrusion of these solid spines occurred at temperatures below the rock's solidus temperature. Rock samples that are porphyritic, microlite rich, and glass poor are consistent with subsolidus eruption (Pallister and others, this volume, chap. 30). Shallow seismic signals that locate within about 1 km of the surface and an absence of deeper signals (Moran and others, this volume, chap. 2; Thelen and others, this volume, chap. 4) suggest a possible viscous-to-solid transition of the magma at that depth. The hottest recorded temperatures of the extruding spines, culled from >10,000

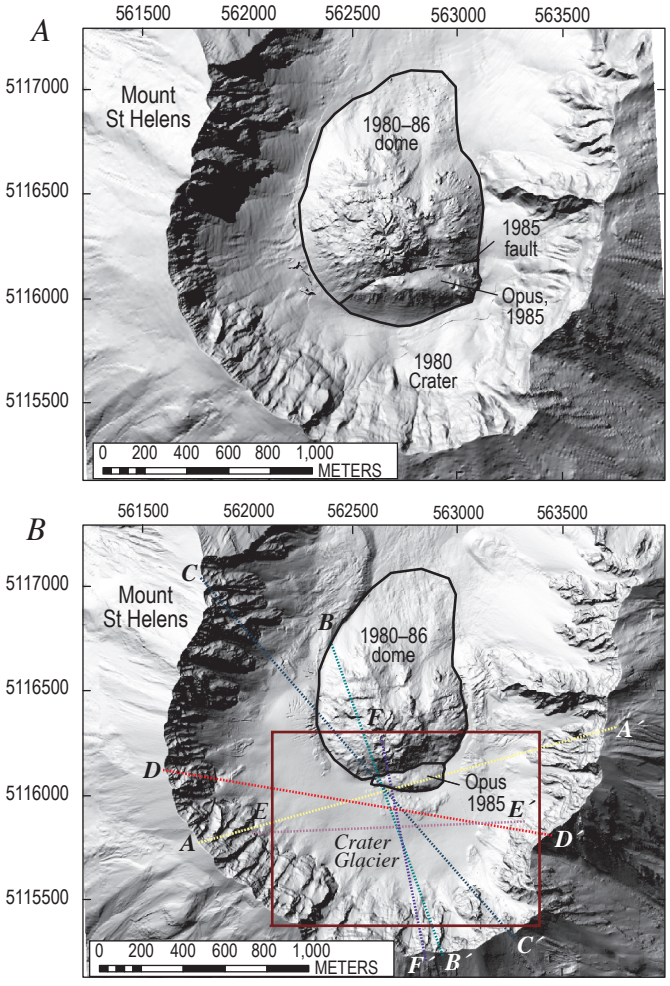

Figure 1. Digital elevation models (DEMs) of Mount St. Helens showing 1980 crater, 1980–86 dome, Opus, and Crater Glacier. Coordinate system is North American Datum 1927 Universal Transverse Mercator, zone 10N, in this and subsequent map figures. *A*, 1986 DEM. *B*, 2003 DEM. Solid rectangle locates DEMs in subsequent figures, and dashed lines locate cross sections illustrated in subsequent figures.

images collected during 37 missions, cluster where cracks and avalanches expose fresh interior surfaces and fall between 700°C and 730°C. These measurements provide a minimum limit for the temperature of extruded spines that is much lower than the solidus temperature of 920–960°C for the dacite of spines 1–7 (Pallister and others, this volume, chap. 30).

The purpose of this report is to document the characteristics of spine growth at Mount St. Helens, the dramatic near-field deformation that accompanied it, and the impact of dome growth on Crater Glacier. To achieve this we examined and analyzed oblique and vertical aerial photography, digital elevation models (DEMs), and thermal infrared imagery. In particular, we used DEMs and aerial photographs to document growth of spines and nearby deformation as a function of time. To illustrate how the dome has grown and how that growth has affected surrounding areas, we generated surface deformation maps and interpretive cross sections. As supporting evidence we considered results reported elsewhere in this volume, such as geologic mapping (Herriott and others, chap. 10), GPS instrumentation (LaHusen and others, chap. 16), and repeat photography from fixed sites (Major and others, chap. 12; Dzursin and others, chap. 14; Poland and others, chap. 11).

Deformation Within the Crater

Methods and Assumptions

During a period of about 18 months, repeated visual observations, oblique aerial photography, thermal infrared imagery, lidar, and high-resolution aerial photography delineated evolution of the 2004–6 dome at Mount St. Helens and deformation of nearby features in response to that growth. Frequent aerial reconnaissance allowed observations and oblique aerial photography as weather permitted. Cascades Volcano Observatory (CVO) staff collected such data almost daily in the period from September 27, 2004, until October 15, 2004. Thereafter, observations were less frequent, with repeat intervals increasing from a few days to as long as eight weeks.

Thermal Infrared Imagery

Thermal infrared (TIR) images allowed estimation of pixel-integrated temperatures for exposed dome-rock surfaces, fumaroles, and other features. More generally TIR surveys showed how surface areas were heated before the appearance of spines at the surface, allowed differentiation of individual spines, showed thermal structures within spines, and revealed how spines evolved and cooled once extruded (fig. 3). We conducted 37 TIR surveys of the deformed area and the growing dome between October 1, 2004, and April 30, 2006.

The instrument used, a FLIR Systems ThermaCAM™ PM595 infrared camera, mounted on a helicopter, is a microbolometer that measures brightness in the 7.5–13 μm waveband to detect temperatures in the range from –40°C to 1,500°C. It collects TIR images as frequently as once per second and can acquire both TIR and standard video (Schneider and others, this volume, chap. 17). Conversions to temperature depend on emissivity, atmospheric temperature, humidity, distance, viewing angle, steam, and gas (Ball and Pinkerton, 2006; Harris and others, 2005). We can independently measure atmospheric temperature, humidity, and distance well enough that resultant errors are about ±10°C; if emissivity is 0.96±0.1, additional errors would be ±5 percent (Schneider and others, this volume, chap. 17). We can only minimize errors owing to the other parameters by repeating measurements at multiple viewing angles and reporting temperature values for conditions with minimal gas and steam. Images from a TIR survey at a distance of about 1 km yield a horizontal field of view of about 210 m and a pixel resolution of about 1.5 m. Integration of brightness within individual pixels means that hottest reported temperatures could be averaged across areas less than 2 m^2 (Schneider and others, this volume, chap. 17).

Repeat Aerial Photographs, Lidar, and DEMs

A sequence of aerial photographs and lidar converted to DEMs provided vertical and planimetric control at intervals of 1 to 55 days during the 18-month study period. Lidar data from November 2003 (Queija and others, 2005) provided initial datum control, and DEMs generated from topographic maps provided control for the 1980 and 1986 surfaces (fig. 1). Three DEMs were derived from lidar surveys made early in the eruption between October 4 and November 20, 2004, (U.S. Geological Survey and National Aeronautics and Space Administration, unpub. data). In addition, Schilling and others (this volume, chap. 8) created 18 DEMs from vertical aerial photography taken between October 4, 2004, and February 9, 2006. The DEMs of October 4 and 13, 2004, (Schilling and others, this volume, chap. 8) provided a check of lidar DEMs collected October 4 and 14.

Identification and Tracking of Features

During the study period, we used aerial photographs and DEMs to identify and track primary and secondary features. Primary features could be located three dimensionally in two or more DEMs and included points at distinctive topographic crests or, less commonly, troughs and intersections of linear features. Examples of point features include distinctive spine formations (for example, fig. 2, point c), megablocks, stranded ice blocks, the toes of avalanches from the 1980 crater walls (fig. 2, points a and i), and seracs. Intersection features include crack networks on the growing dome (fig. 2, point h) and crevasses on Crater Glacier. In many cases, primary features formed of ice and snow persisted only from October 2004 through March 2005. Secondary features are those that we could track approximately in plan view but for which vertical control was difficult or impossible to obtain (fig. 2, features d, e, f, g). Secondary features included margins of actively

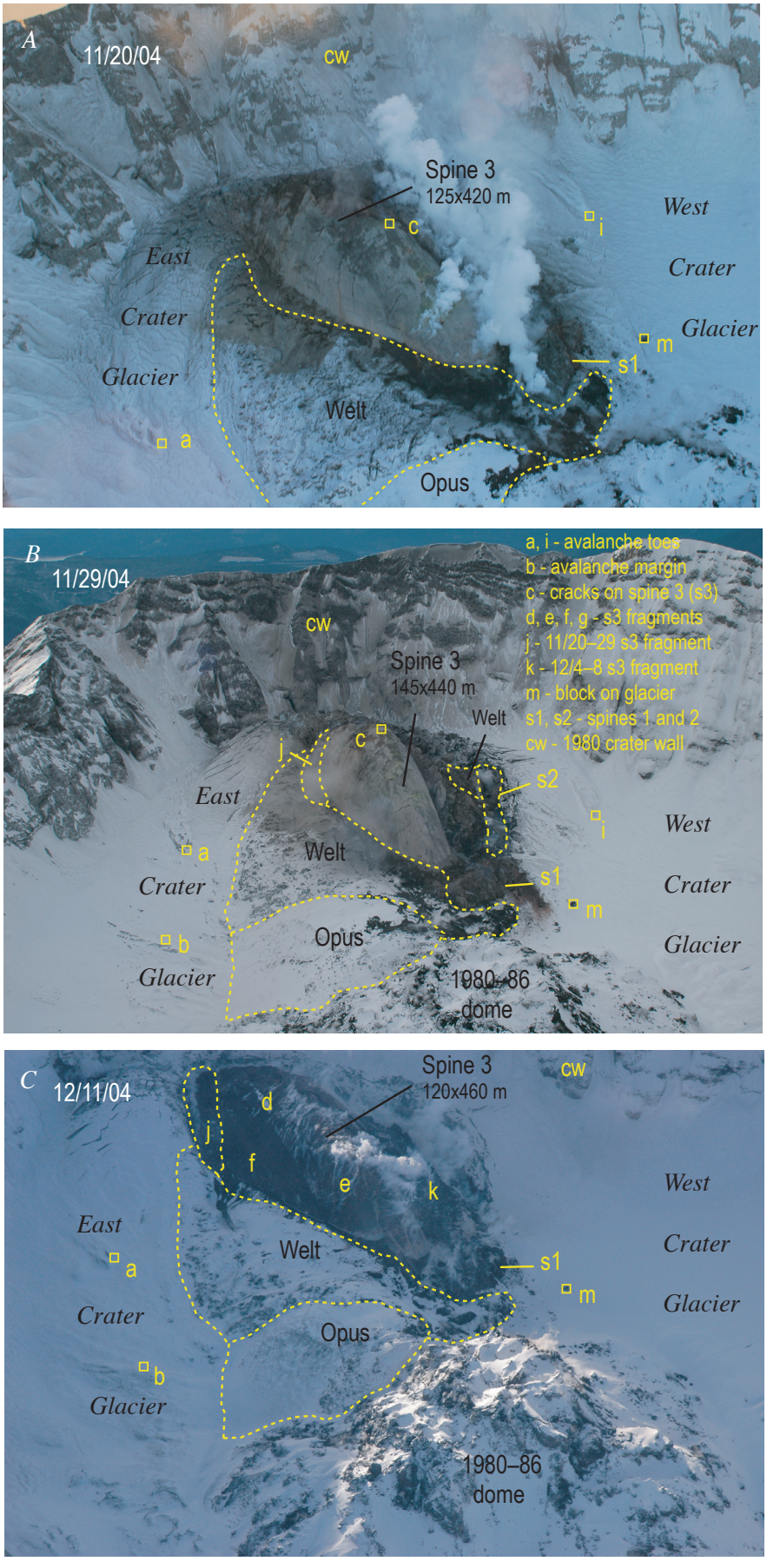

Figure 2. Photographs of Mount St. Helens crater and whaleback-form spines 3 and 4 taken looking south-southwest and illustrating primary and secondary features as they evolved during spine growth and deformation. Features denoted with squares are primary "point" features, and others are secondary features. *A*, November 20, 2004; USGS photo by J.N. Marso. *B*, November 29, 2004; USGS photo by M. Logan. *C*, December 11, 2004; USGS photo by J.S. Pallister. *D*, December 28, 2004; USGS photo by S. Konfal. *E*, January 3, 2005; USGS photo by M. Logan. *F*, January 14, 2005; USGS photo by M. Logan.

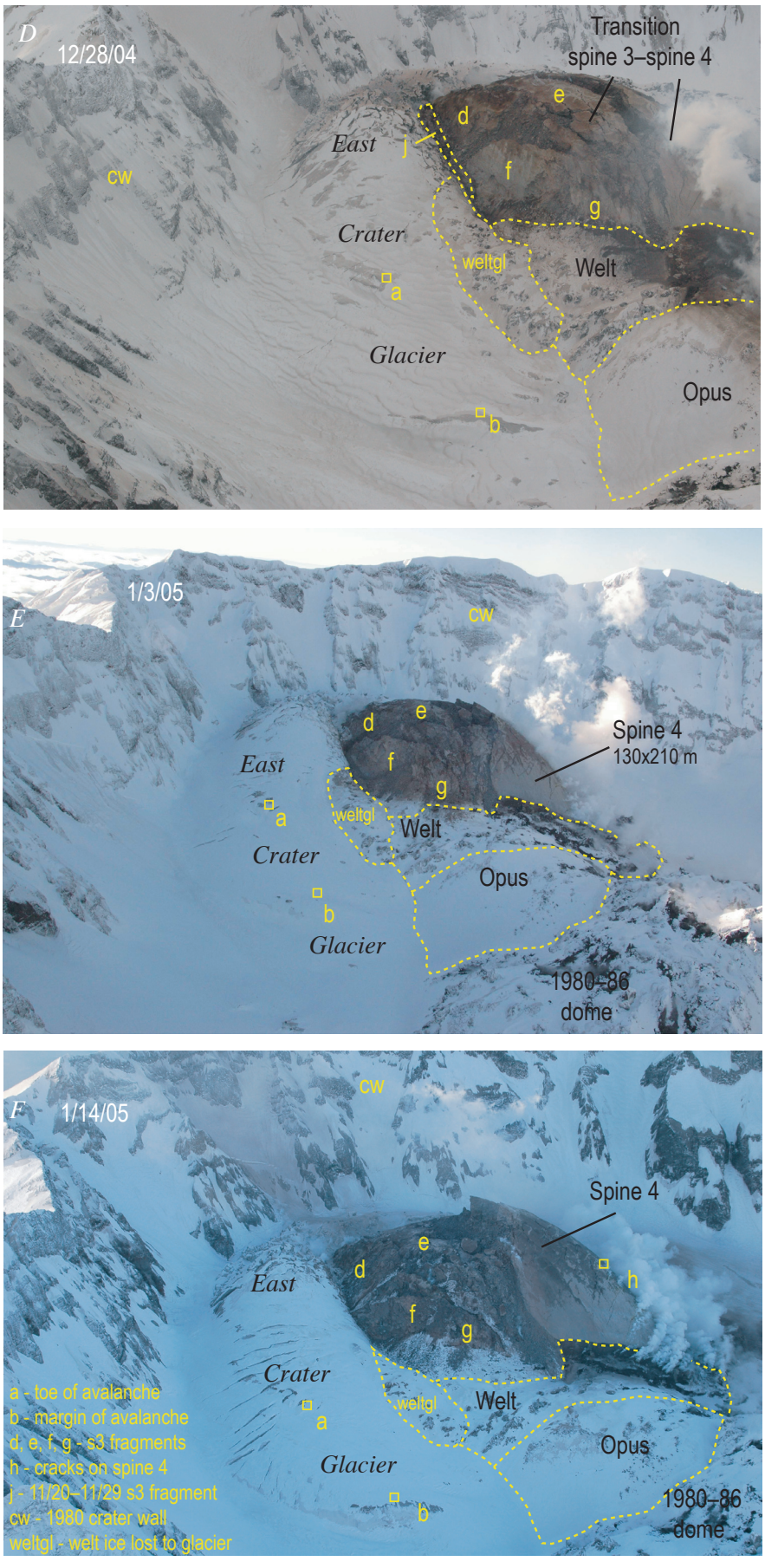

Figure 2—Continued.

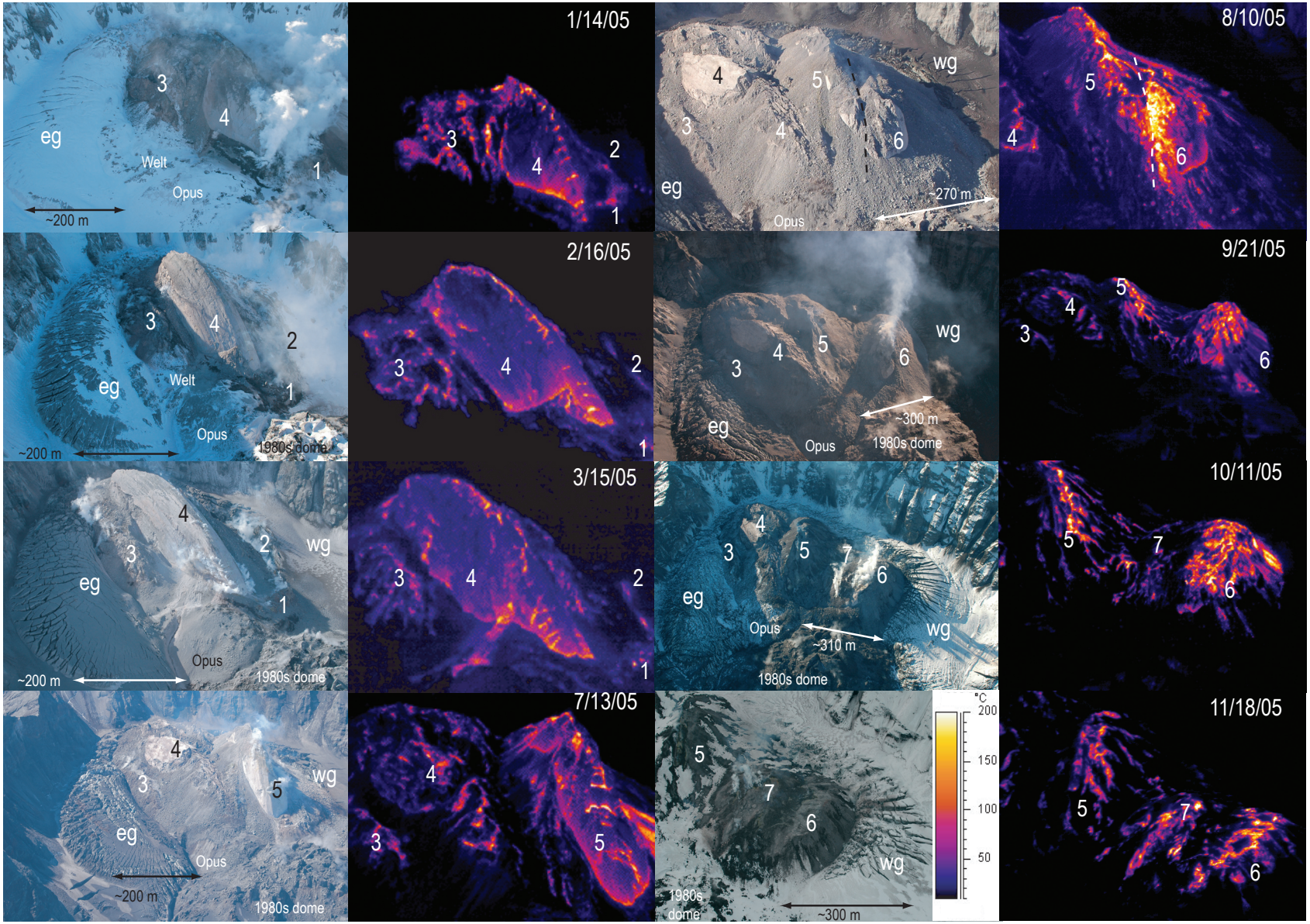

Figure 3. Photograph and thermal-infrared image pairs from Mount St. Helens, views from north-northeast (Jan. 14–Sep. 21, 2005), north (Oct. 11, 2005), and northwest (Nov. 18, 2005), illustrating evolution of the 2004–6 dome. Numbers designate spines 1–7; eg and wg designate east and west Crater Glacier. Dashed line in photograph of Aug. 10, 2005, is trace of fault developing between spines 5 and 6. USGS photos of Jan. 14, March 15, July 11, and Nov. 18, 2005, by J.W. Vallance; those of Feb. 16 and Sep. 21, 2005, by J.W. Ewert; those of Aug. 10 and Oct. 11, 2005, by C.A. Gardner and C. Fox-Lent. Thermal images of Feb. 16 and Sep. 21, 2005, by J.W. Vallance; the remainder by M. Logan.

growing spines, the contact of the 1980–86 dome with the new dome, the contacts of the glacier with the new dome and crater wall, and glacier snouts. Such secondary features provided useful constraints on deformation but could not be used to measure that deformation directly.

Sources of error in locating primary features included accuracy of DEMs, accuracy of repeating a location in a single DEM, identification and location of features in consecutive DEMs, deformation of features with time, melting or addition of snow to features, and misidentification of features in successive DEMs. Precision of DEMs is a few centimeters to about a decimeter (Schilling and others, this volume, chap. 8). On individual DEMs, distinctive features could be relocated to within ±2 m horizontally and ±1 m vertically.

Features were identified and relocated on successive DEMs with some certainty unless the features were obscured by snow, shadows, steam, or clouds or were so deformed during the interval between DEMs as to become difficult to recognize. Fresh snow and ablation may have affected relocation and ultimately even recognition of primary features, but some areas on or near the active dome were windswept or remained warm year-round; features in such areas were not subject to relocation errors related to melting or snowfall. Comparison of relative motion of groups of neighboring objects provided a check on correlations. We eliminated correlations that yielded results greatly at variance with those of neighboring objects.

Generally, error in locating primary features in successive DEMs is between ±2 m and ±5 m in the horizontal and vertical dimensions. Features subject to the most deformation—those on or near the actively growing dome—tend to be those with the greatest errors in relocation. Features away from the locus of deformation may have small absolute location errors but may not move far enough to register significant motion, given the magnitude of error in locating them.

Generation of Surface-Deformation Vectors

Primary features that can be located in two or more successive DEMs allow estimation of vector components from one time to another. This allows calculation of average rates of deformation (for example, points a, b, c, and h in fig. 2). As we know of no systematic source of error in locating primary features, errors should not tend to accumulate for features that can be located in three or more successive DEMs. Repeated locations of primary features indicated in figures by solid arrows thus allow generation of surface-deformation vectors within our stated error limits.

Successive locations of secondary features give a sense of magnitude and direction of deformation but do not yield true vectors. In such cases, the vertical component of deformation may be poorly known or unknown. Despite poor constraints on vertical position, plan-view locations of some secondary features are as accurate as those of primary features. Examples include features located in rectified aerial photographs for which no DEM exists and features that crumble as they move laterally yet still can be identified. Crumbling features are common on or near active spines. Relocations of such features can be accurate in plan; but vertical changes, if given, are minimum values. Relocations of secondary features such as the contact between the glacier and active dome give minimum constraints on deformation in both horizontal and vertical directions.

Vector Fields

Vector fields were derived from simultaneous tracking of numerous primary features on successive DEMs. Vector fields were used to delineate growth of active spines, deformation of inactive parts of the dome and its surroundings, and deformation of the glacier in locations where motion exceeded a threshold of about 4 m in the time between successive DEMs. Because DEMs were produced at intervals of 9–55 days and vertical and horizontal precision were ~5 m, detection limits for time-averaged deformation rates range from 0.6 to 0.09 m/d.

Comparison with GPS Data

During certain intervals, portable GPS receivers that provided nearly continuous measurement of deformation (LaHusen and others, this volume, chap. 16) were located near features tracked during this study using DEMs, thereby providing a check on our results. The GPS deformation measurements compared well with those of this study. For example, a GPS receiver placed on the spine during November 21–29, 2004, gave a vector almost identical in magnitude and direction (10.3 m/d, S. 19° E., up 6°) to that of a nearby feature 30 m east that we tracked November 20–29 (10.4 m/d, S. 21° E., up 8°).

Our deformation measurements have advantages and disadvantages compared with those derived from GPS receivers. The chief advantage of our approach is that we can track numerous features simultaneously and thus obtain a complete picture of dome growth and nearby deformation patterns. GPS sensors are advantageous in that their data streams can be sampled frequently and transmitted back to the observatory. Such real-time acquisition permits the use of GPS data in monitoring. In contrast, our measurements are values averaged over intervals between successive DEMs and have no application in real-time monitoring because of the additional time required to prepare DEMs.

Volume and Flux Calculations

All reported volumes assume the 1986 topographic surface as a datum and subtract it from DEMs of various dates over pertinent areas (hot-rock volumes given in Schilling and others, this volume, chap. 8). Because thick glacial ice overlay the 1986 debris fill of the moat by 2004, we chose the 1986 surface as a datum for volume calculations rather than the more recent ice-mantled surface of 2003–4. To facilitate calculations, we assumed that bounding surfaces between the datum and the areal extent of hot rock on any subsequent DEM were

vertical. The assumption of vertical bounding surfaces dictates that calculated volumes are minimum values in cases where natural surfaces differ substantially from vertical. A steep, near-vertical contact between the extruding dome and glacier ice is probably a reasonable assumption for two reasons. First, visible upper parts of glacier contacts with hot rock were steep and nearly vertical. Second, relict ice-hot rock contacts exposed in other volcanic areas are commonly nearly vertical because the ice cools and buttresses the rock margin, preventing avalanches and rockfall that tend to form slopes more closely approaching the angle of repose.

Time-averaged volumetric extrusion rates for individual spines are derived by comparing volumes from one DEM to the next and dividing by the time between them. In many cases, volumetric rates are the same as the hot-rock extrusion rates of Schilling and others (this volume, chap. 8). Well-constrained growth intervals of certain spines allow more precise calculation of their volumetric extrusion rates.

Cross Sections

Cross sections were constructed from DEMs sampled at horizontal intervals of 10 m, are presented with no vertical exaggeration, and include both simple representations of successive surfaces and interpretive relations among units at depth. Our guiding philosophy in the construction of cross sections was not to extend geologic interpretation below levels for which we have no constraints. Therefore none is extended below our lowermost control surface, that of summer 1980.

Phases of Dome Growth at Mount St. Helens

Between the onset of unrest on September 23, 2004, and April 2006, the eruption developed in a manner that is divisible into five distinct phases, each with characteristic rate and pattern of eruption (table 1). An initial brief vent-clearing phase included seismic unrest, spectacular deformation features, and phreatic explosions developed in the moat between the 1980s dome and the 1980 crater walls. Initial spine extrusion began October 11, 2004. As extrusion continued, the locus of spine growth shifted, spines grew and stagnated, and new ones formed in their stead (table 1). As of April 2006, a total of seven discrete spines have erupted that we have grouped on the basis of similar growth patterns into four additional phases (table 1).

Phase 1, Precursory Vent Clearing, September 23–October 10, 2004: Phreatic Explosions and Deformation

The first indications of an impending eruption included a week of intensifying seismicity beginning September 23, 2004, deformation-induced surficial cracks in glacier ice south of the 1980–86 dome that began to appear by September 29 (Dzursin and others, this volume, chap. 14), and four phreatic explosions between October 1 and 5 (Moran and others, this volume, chap. 6). The phreatic explosions formed a vent at the west edge of deformed ice. Thermal IR images show that the explosions of early October had temperatures of no more than 160°C (Schneider and others, this volume, chap. 17). On the basis of these low temperatures, we infer that the explosions were phreatic rather than magmatic. However, the explosions did indicate interaction of hot rock with the shallow hydrothermal system, thus suggesting rise of magma to near the surface.

During early October, a zone of highly fractured ice developed and expanded southward as subsurface intrusion fractured and thrust the part of the 1980–86 dome called Opus, which had formed in 1985, and adjacent crater-floor debris upward to form a feature named “the welt” (fig. 4). This shallow intrusion of magma caused surface uplift in excess of 70 m (figs. 5, 6). Uplift was greatest along a north-south axis about 200 m east of the October vent (fig. 5) and diminished rapidly away from that axis.

The welt expanded southward, but motion of recognizable features through October 4 was upward and northward along a reverse fault with a strike of ~N. 80° E. and located between Opus and the remainder of the 1980–86 dome to the north (fig. 5). This faulting apparently reactivated a normal fault of 1985 that bounded the north margin of the Opus feature (fig. 1*A*). Surface deformation vectors south of the fault trace show motion of 25–30 m north and 50–70 m up. If deformation indicated motion along the fault, then its dip was ~60° south.

During October 4–14 the locus of deformation migrated south from Opus, and the sense of motion at the surface was radial, away from the most intense deformation. Motion on Opus was undetectable to barely detectable at ~5 m east and up (figs. 5, 6). On glacier surfaces, ballistic impact sites and distinctive avalanche toes near the periphery of the welt moved 5–15 m away from the welt (southwest to east) and up (fig. 5). The few traceable points on the eastern and central parts of the actively deforming welt moved 30–80 m eastward away from the axis of the welt (fig. 5).

The DEMs of October 13 and 14 recorded displacement in the range of 5–30 m along the surface of the expanding welt (fig. 5). Points along the deformation axis, which coincided with the axis of spine 3 when it later emerged in November, moved 15–30 m S. 10° E. along the axis and rose 6–8 m in one day. Nearby features to the east moved laterally 12–15 m S. 20° E. to S. 45° E., with little vertical motion. Features on fractured ice to the east also moved away from the growing welt, whereas those on Opus showed no detectable motion.

Phase 2, October 11–24, 2004: Spines 1 and 2

Initial Spine Growth

Spines 1 and 2 each extruded rapidly within a few days and thereafter remained inactive, though each was affected

Table 1. Timing, extrusion rates, character of dome growth, deformation within crater, and impact on glacier during each of five eruptive phases from September 2004 to April 2006, Mount St. Helens, Washington.

[Estimates of extrusion rates are derived from comparing DEMs from one date to the next (Schilling and others, this volume, chap. 8; and this chapter). Estimates of linear advance are obtained from tracking features in DEMs or aerial photographs (this chapter), from repeat photos from fixed positions (Major and others, this volume, chap. 12), and from portable GPS stations (LaHusen and others, this volume, chap. 16).]

Phase	Spine	Time period	Growth rate	Nature of eruptive activity	Deformation within 1980 crater	Effect on glacier
1—Precursory vent clearing	Pre-dome	Sept. 23 –Oct. 10, 2004	Not applicable	Vent clearing and phreatic explosions. Ascent of solid spine to surface.	Uplift of 1980–86 dome, and crater floor to north of 1980–86 dome to form welt. By Oct. 4, 2004, total volume of deformed area (welt) is ~5×10^6 m^3.	Disruption and uplift of Crater Glacier.
2—Initial spines	Spine 1	Oct. 11–15, 2004	2–3 m^3/s; 15–20 m/d	Near-vertical spine growth.	Continuing uplift of crater floor to south of 1980s dome; Volume of deformed welt increases, 5×10^6–11×10^6 m^3, Oct. 4–13, 2004.	Continuing uplift and disruption of glacier but no appreciable melting.
	Spine 2	Oct. 15– ~Oct. 24, 2004	3 m^3/s; 25 m/d	Advance of spine 2 to the south; probable subterranean and subglacial intrusion of spine 3.	Locus of deformation shifts southward and eastward; formation of roof pendant over intruding spine.	
3—Recumbent growth of whaleback spines	Spine 3	Oct. 25– Dec. 18, 2004	4–6 m^3/s; 8–11 m/d	Recumbent growth of spine 3 toward south crater wall; spine 3 begins pushing against south crater wall ~Nov. 12, 2004.	Emerging spine displaces older rocks to east and south; roof pendant is transported to south end of spine 3; spine 2 subsides.	Growth of spine 3 divides Crater Glacier into east and west arms. Spines 3 and 4 plow east Crater Glacier eastward and thereby thicken it as much as 100 m; crevasses form parallel to maximum principal-strain direction (~east–west) but no appreciable melting.
	Transition	Dec. 18, 2004–Jan. 3, 2005	No data	Spine 3 deflects off south crater wall, fractures, breaks up, and decouples from source.		
	Spine 4	Jan. 3–Apr. 9, 2005	1.5–2.5 m^3/s; 5–8 m/d	Continuing extrusion forms spine 4, which continues pushing to the south.	Southward growth of spine 4 tilts and pushes spine 3 to east; deformed 1980–86 debris migrates eastward; remnants of spines 1–3 to west are static	
4—Spine thrusts over previous spines	Transition	Apr. 10–19, 2005	No data	Spine 4 encounters south crater wall, fractures, and decouples from source.		East Crater Glacier deformation slows, then stops; glacier responds to thickening caused by previous deformation by accelerating downslope to north. West Crater Glacier is pushed west.
	Spine 5	Apr. 19-July 18, 2005	1–1.5 m^3/s; 3–6 m/d	Spine 5 thrusts over spine remnants west of spine 4. Smooth surface forms at north end of spine and gradually steepens. In June, spine fractures to the south and disintegrates.	Deformation to east is greatest near vent and diminishes south. This deformation slows and stops. Deformation to west is moderate and continual. Rockfall from spine 5 buries spine 2, then 1.	
		July 19–31, 2005		Spine 5 crumbles to feed rockfall avalanches and slumping events.		
5—Spines grow to west, then thrust over one another	Transition	Aug. 1–5, 2005	No data	Spine 5 fractures near its source and begins to slump.		West Crater Glacier thickens and cracks owing to westward migration of spines 6 and 7; cracks radiate westward along maximum principal-strain axes.
	Spine 6	Aug. 6– Oct. 9, 2005	1.5–2 m^3/s; 3–4 m/d	Sag depression grows owing to slumping of spine 5 and westward migration of spine 6; spine growth is chiefly recumbent and endogenous.	Deformation to west; east part of 2004–5 dome complex is stagnant.	
	Spine 7	Oct. 9, 2005 –Apr. 2006	0.5–1 m^3/s; 1–2 m/d	Endogenous growth followed by exogenous spine growth in depression.	Spine 7 pushes spine 6 to west and begins thrusting over elements both of itself and of spine 6.	

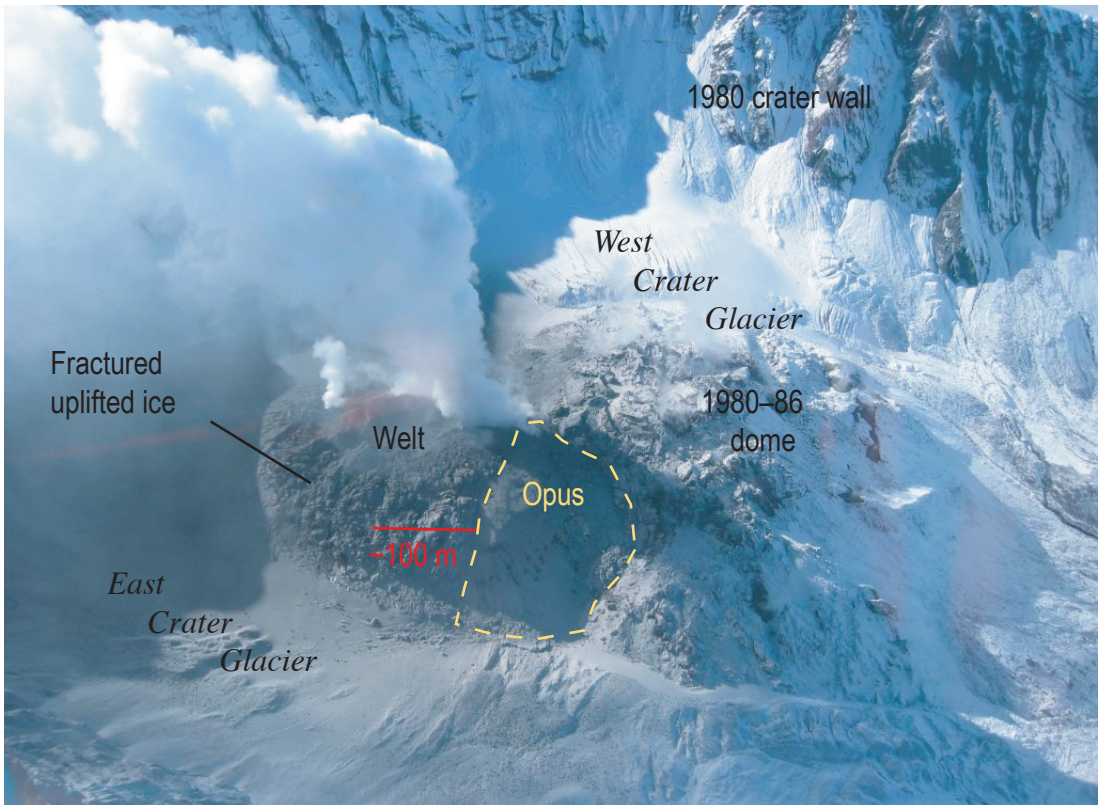

Figure 4. View of Mount St. Helens crater from north-northeast on October 10, 2004, illustrating welt, Opus, 1980–86 dome, crater wall, and Crater Glacier. USGS photo by R. Wessels.

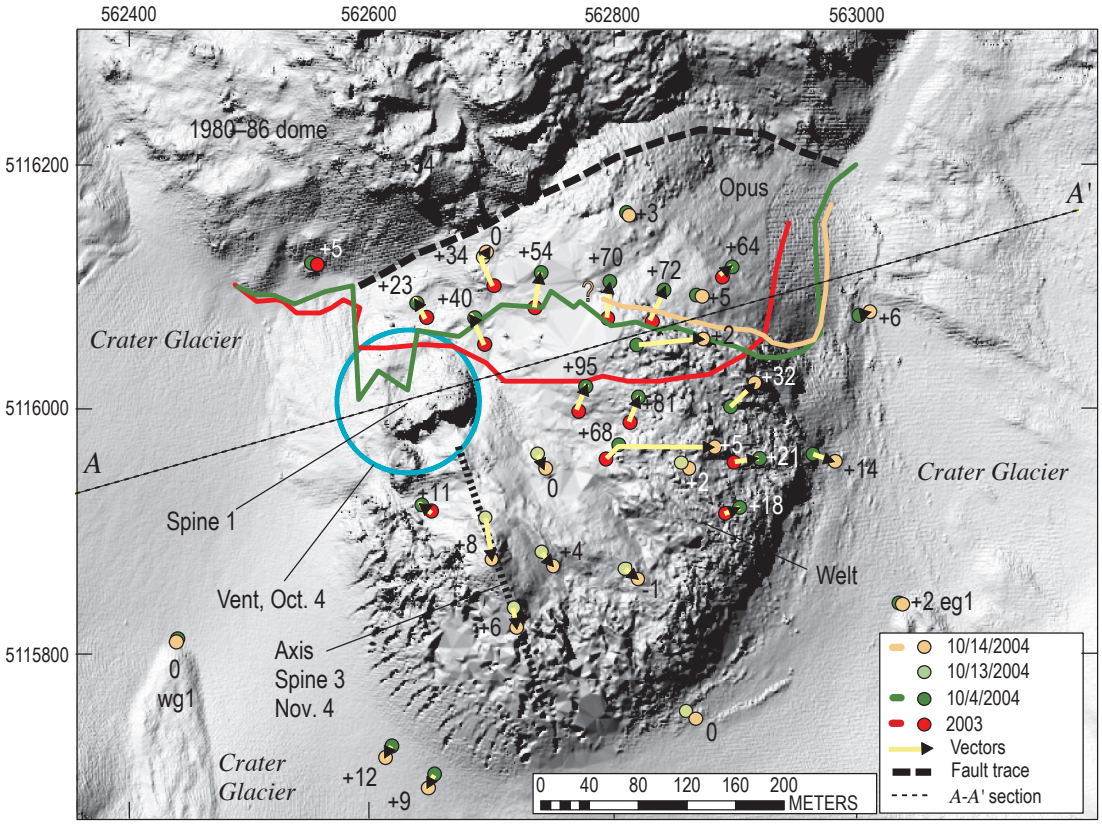

Figure 5. DEM of October 14, 2004, locating vent of October 4, 2004, and illustrating initial extrusion of spine 1 and locations of welt, Opus, 1980–86 dome, Crater Glacier, and cross section *A*–*A*´ shown in figure 6. Dots indicate features tracked, and solid lines indicate changes in fractured ice margin for dates identified by color in key. Arrows show surface deformation vectors; numbers show vertical component of vectors in meters.

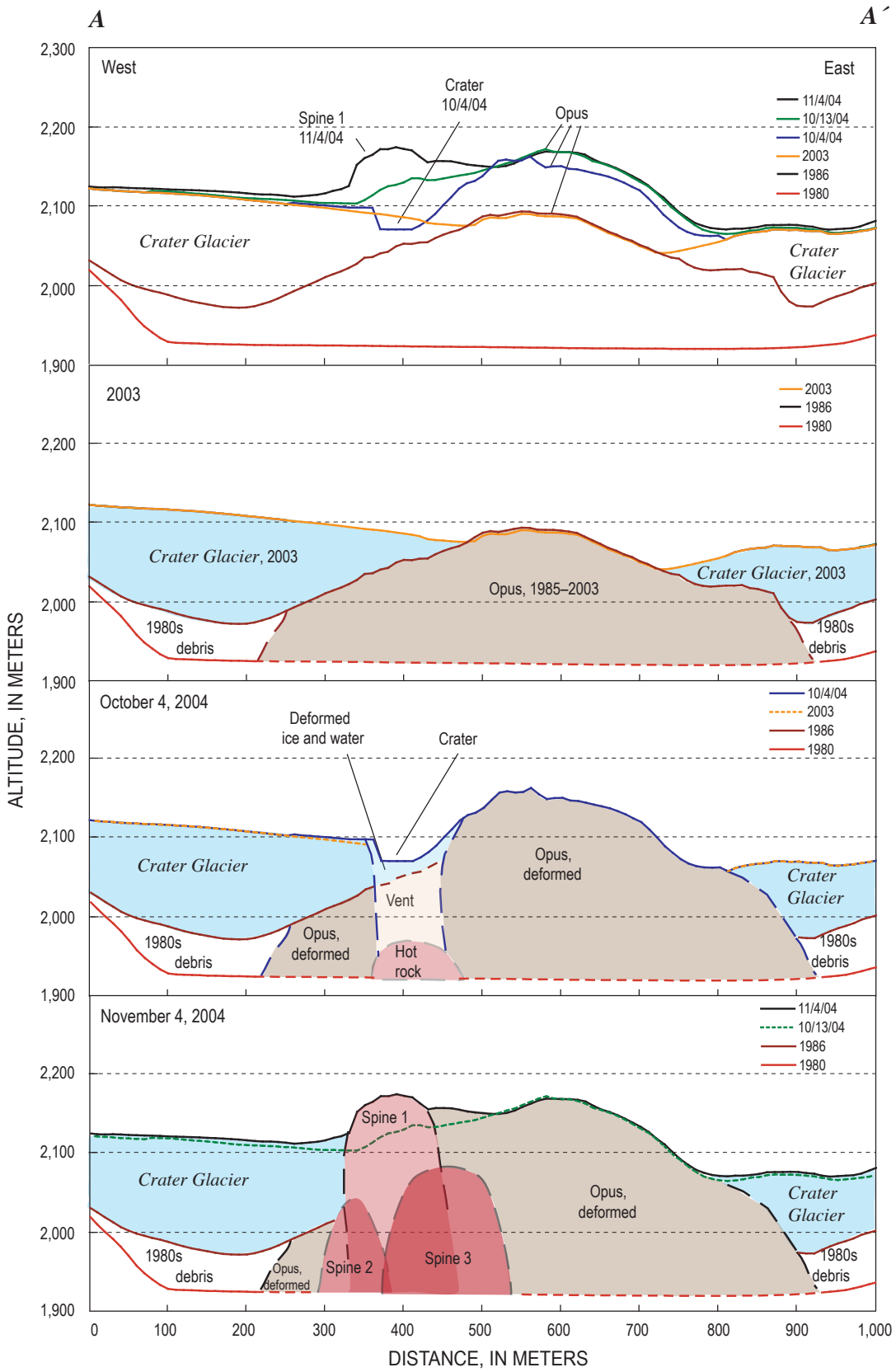

Figure 6. Cross section *A*–*A´* (location shown in figure 5) illustrating extrusion of spine 1, intrusion of spines 2 and 3, and deformation of Opus and glacial ice. Top panel shows known profiles for the dates given, and other panels illustrate geologic interpretations on given dates.

subsequently by deformation and eventual burial. Warming at the surface of the welt to as much as 50°C on October 10, 2004, presaged the appearance of juvenile rock above ground on October 11 (Schneider and others, this volume, chap. 17). Spine 1 extruded from October 11 to 15. Owing to poor weather, the timing of spine 2 emplacement is less well constrained. Observations and study of oblique photographs showed that its growth began after October 15 and finished by October 24.

Spine 1 grew at a steep angle as a solid blocky slab from a south-facing slope on the west part of Opus. By October 14, it was 85×60 m, ~60 m high, dipping 50° northwest, and had volume of ~0.6×10^6 m^3 (table 2, fig. 6). Using the outline of spine 1 on the DEM of November 4, we calculate that the total volume of spine 1 was then ~0.9×10^6 m^3. Spine 1 extruded rapidly, 15–20 m/d and 2–3 m^3/s (table 2).

Although observations between October 15 and 24 were insufficient to delineate the nature of spine 2's growth directly, it emerged just south of spine 1 and appeared at the surface from north to south as though the deformed glacier ice from which it emerged had unzipped rapidly southward. It emanated from the October 4 vent (figs. 5, 7) and moved southward along subglacial slopes to form an elongate body oriented north–south at the surface (table 2). Its growth ceased when it encountered steep opposing slopes of the 1980 crater. Assuming vertical boundaries downward from the November 4 surface to the 1986 surface allows a volume calculation of about 2×10^6 m^3. The spine's estimated volume and interval of emplacement imply a time-averaged extrusion rate of ~3 m^3/s.

Deformation Accompanying Spine Growth

Between October 14 and November 4, the locus of maximum deformation propagated south along an axis oriented ~S. 20° W. Deformation diminished with distance normal to this axis. Opus and the 1980–86 dome were essentially static during this period (fig. 7). Severely deformed ice on the welt just east of its axis moved a few meters to the north; farther south, it moved as much as 60 m to the southeast and subsided (fig. 7). On glacier surfaces to the east, distinctive features moved 5–40 m eastward and rose 5–20 m. Farther north, glacial features moved a few meters northward. The few traceable points on ice west of the actively deforming welt rose a few meters, but only one feature nearest the northwest margin of the welt moved significantly westward, by ~10 m (fig. 7, point wg1).

Phase 3, Recumbent Growth of Spines 3 and 4: October 24, 2004–April 9, 2005

Growth of Whaleback Spine 3: October 24–December 18, 2004

During mid-October, spine 3 began intrusive growth and pushed into pre-2004 rock, deforming the welt, disrupting glacier ice, and forming a cryptodome beneath the welt (fig. 8). Evidence in support of intrusion included (1) deformation along an axis S. 19° E. that coincided with the axis of spine 3 when it later emerged (fig. 5), (2) upward and southward motion of pre-2004 rock along a trend similar to that of the whaleback when it emerged (figs. 5, 7), and (3) warming of rock at the surface near the axis of deformation (Schneider and others, this volume, chap. 17).

Spine 3 breached the deformed surface of the welt and advanced rapidly to the south-southeast between late October and mid-December to form a smooth-surfaced whaleback feature 300–460 m long and 120–145 m wide (tables 1, 2). Between October 24 and 27, spine 3 emerged from an area about 50 m southeast of spine 1, through older dome and crater-floor rock along the crest of the deforming welt (fig. 9). By early November, it was 320×125 m, with a long axis oriented S. 18° E. (fig. 7). As the spine pushed southward from mid-November through December, its long axis pivoted 9° eastward (to S. 27° E.) about its origin at the vent (table 2).

The surface of the whaleback had a cool and smooth, but striated, surface except on the west, where it was broken and blocky. The striations at the surface of the whaleback were interpreted as slickensides (fig. 10). Growth of the whaleback also lifted a partial roof composed of fractured 1980–86 dome rock and crater-floor debris and transported it southward during November 4–29 (fig. 10). Cashman and others (this volume, chap. 19) show that the smooth outer carapace of the whaleback comprised powdered, partially sintered 2004 dacite plus small amounts of 1980–86 dacite; they interpret this material as fault gouge formed through comminution as the solid spine rubbed and ground against older rock during its ascent in the conduit.

The stable crust of spine 3 insulated the hot rock within so that surface temperatures were low. Thermal images commonly showed a ~200°C zone around the base of the emerging spine (fig. 11*A*), and hot cracks showed rock temperatures as high as 730°C. The temperature of smooth, uncracked parts of the surface diminished exponentially with distance from the source at the base of the spine and approached ambient within 50 m (fig. 11*B*). Because the temperature also decreased exponentially with time (each 10 m from source represented about a day), the moving surface of the spine showed a classic Fourier's Law decline in temperature (Turcotte and Schubert, 1982). Such a temperature profile resembles those observed for blocky lavas at Santiaguito, Guatemala (Harris and others, 2002, 2004), though the lava core temperatures of Mount St. Helens spines differ from those of lavas at Santiaguito in likely being 100°C or more below solidus temperature.

Subtracting the spine 1 and 2 volumes from the total volume of hot rock emplaced by spines 1, 2, and 3 (Schilling and others, this volume, chap. 8) yields values for spine 3 volume and for its extrusion rate between late October 2004 and early January 2005 (table 2). Extrusion rate (flux through the 1986 surface) was ~5 m^3/s until November 4. Extrusion rates then declined from 4.4 to 2.5 m^3/s between late November and early January (table 2).

Table 2. Dimensions, orientation, volume, and growth rate of the welt and spines of Mount St. Helens, Washington, at various dates.

[Applicable interval for linear and volumetric growth rates and direction is from date of previous DEM to date of DEM given for row, unless specifically indicated.]

Phase	Date of DEM	Spine/ Welt	Dimensions (m)	Orientation of welt or spine	Linear growth rate, direction, period of interest, and GPS station name where applicable	Volume ($\times 10^6$ m^3)	Volumetric growth rate (m^3/s)
1—Precursory vent clearing	Oct. 4, 2004	Welt	370×370	Equant	~70 m/d, South, Sept. 29–Oct. 4	5 [a]	12 Sept. 29–Oct. 4
	Oct. 14, 2004	Welt	470×380	Long axis north-south	~10 m/d, South, Oct. 4–14	11 [a]	7
2—Initial spines	Oct. 14, 2004	Spine 1	85×60	Strikes S55W; dips 50° NW	15-20 m/d, S35E, Oct. 11–14	0.6	~2 Oct. 11–14
	Nov. 4, 2004	Spine 1	150×45	Strikes S58W; dips 80° NW		0.9	~3 Oct. 14–15
		Spine 2	240×50	Long axis, Due S	~25 m/d, South, Oct. 15–24	2	3 Oct. 15–24
3—Recumbent growth of whaleback spines	Nov. 4, 2004	Spine 3	320×125	Long axis S18E; dip at vent 30°	11.4 m/d, ~ S5W, Nov. 4–7	9	4.7 Oct. 13–Nov. 4
	Nov. 20, 2004	Spine 3	420×125	Long axis S19E	11 m/d, S22E, Nov. 4–20		
	Nov. 29, 2004	Spine 3	440×145	Long axis S23E	10.3 m/d, S19E, Nov. 21–29, ELEA [b] 10.5 m/d, S21E, Nov. 20–29	18	4.4 [a] Nov. 4–29
	Dec. 11, 2004	Spine 3	460×120	Long axis S27E	7–8 m/d, ~S20E [c]	23	4.1 [a]
	Jan. 3, 2005	Spine 4	210×130	Long axis S27E	4–7 m/d, ~S20E [c]	5.5	2.5 [a]
	Feb. 1, 2005	Spine 4	340×145	Long axis S28E	8.3 m/d, S19E, Jan. 15–16, CDAN [b]	10	1.8 [a]
	Feb. 21, 2005	Spine 4	400×150	Long axis S31E	5.8 m/d, S30E, Feb. 8–14, AHAD [b] 4.5 m/d, S32E, Feb. 1–21	14	2.4 [a]
	Mar. 10, 2005	Spine 4	440×140	Long axis S35E	3.9 m/d, S39E, Feb. 21–Mar. 10	17	1.8 [a]
	Apr. 19, 2005	Spine 4	490×140	Long axis S40E	2.6 m/d, S71E, Mar. 10–Apr. 19 Spine 4 decouples from vent during this interval.	21	1.5 [a]
4—Spine thrusts over previous spines	Apr. 19, 2005	Spine 5	100×90	Long axis S25E; dip at vent 40°	3.5–4.5 m/d, S10E [c]	1	1.5 [a]
	June 15, 2005	Spine 5	340×170	Long axis S9E	3–4 m/d, S along axis [c]	8	1.4 [a]
	July 14, 2005	Spine 5	285×105	Long axis; S5E; dip at vent 54°	2–3.5 m/d, S along axis [c]	11	1.3 [a]
	Aug. 10, 2005	Spine 5				15	
5—Spines grow to west then thrust over one another	Aug. 10, 2005	Spine 6	100×90	Long axis S43W	3–4 m/d, ~West [c]	1; compound spine 6 is ~12	2.0 [a]
	Sept. 20, 2005	Spine 6	350×280	Long axis S47W	3–4 m/d, ~West [c]	6; compound spine 6 is ~17	1.6 [a]
	Oct. 24, 2005	Spine 7	110×40	Long axis S44W	3–4 m/d, ~West [c]	New lava, spines 6+7, ~9	0.9 [a]
	Dec. 15, 2005	Spine 7	260×~250	Long axis S74W	~3 m/d, ~West [c]	New lava, spines 6+7, ~12	0.7 [a]
	Feb. 9, 2006	Spine 7	310×~300	Long axis S83W; dip at vent 50°	2.2 m/d, S80W, up 50°	New lava, spines 6+7, ~15	0.6

[a] Schilling and others (this volume, chap. 8).

[b] LaHusen and others (this volume, chap. 16).

[c] Major and others (this volume, chap. 12).

Growth of Spine 3: Onset of Recumbent Growth

Although the spine in early November 2004 appeared to grow more or less vertically from the axis of the welt, it in fact originated from a source beneath spine 1 and extended southward two to three times as fast as it pushed upward. Between November 4 and 7, identifiable features on the spine's surface moved ~32 m S. 5° W. (fig. 10). Vertical movement of the spine was poorly constrained but appeared to be ~12 m up. The south end of the spine extended almost 30 m S. 19° E., an orientation matching that of its long axis. A possible explanation for the contrast in surface-vector directions and overall spine extension is that, at this early stage of its growth, the spine rotated slightly westward while pushing south-southeast along its axis.

Deformation Adjacent to Spine 3 in Early November

Between November 4 and 7, areas to the east of spine 3 moved tens of meters parallel to the spine or were pushed in easterly directions, and areas to the west and north of spine 3 moved less than 10 m or remained static. Rock debris adjacent to the eastern margin of spine 3 moved parallel to the east margin by almost 30 m (fig. 10*A*). Rock debris farther east moved smaller distances. Motion of the rock debris had no detectable vertical component. Fractured and previously uplifted glacial ice less than 200 m east of the spine moved 10–15 m along trends ranging from southeast to east (fig. 10*A*). During November 4–7, a GPS unit west of the whaleback, CLF4, moved 8 m south-southwest and subsided 2 m

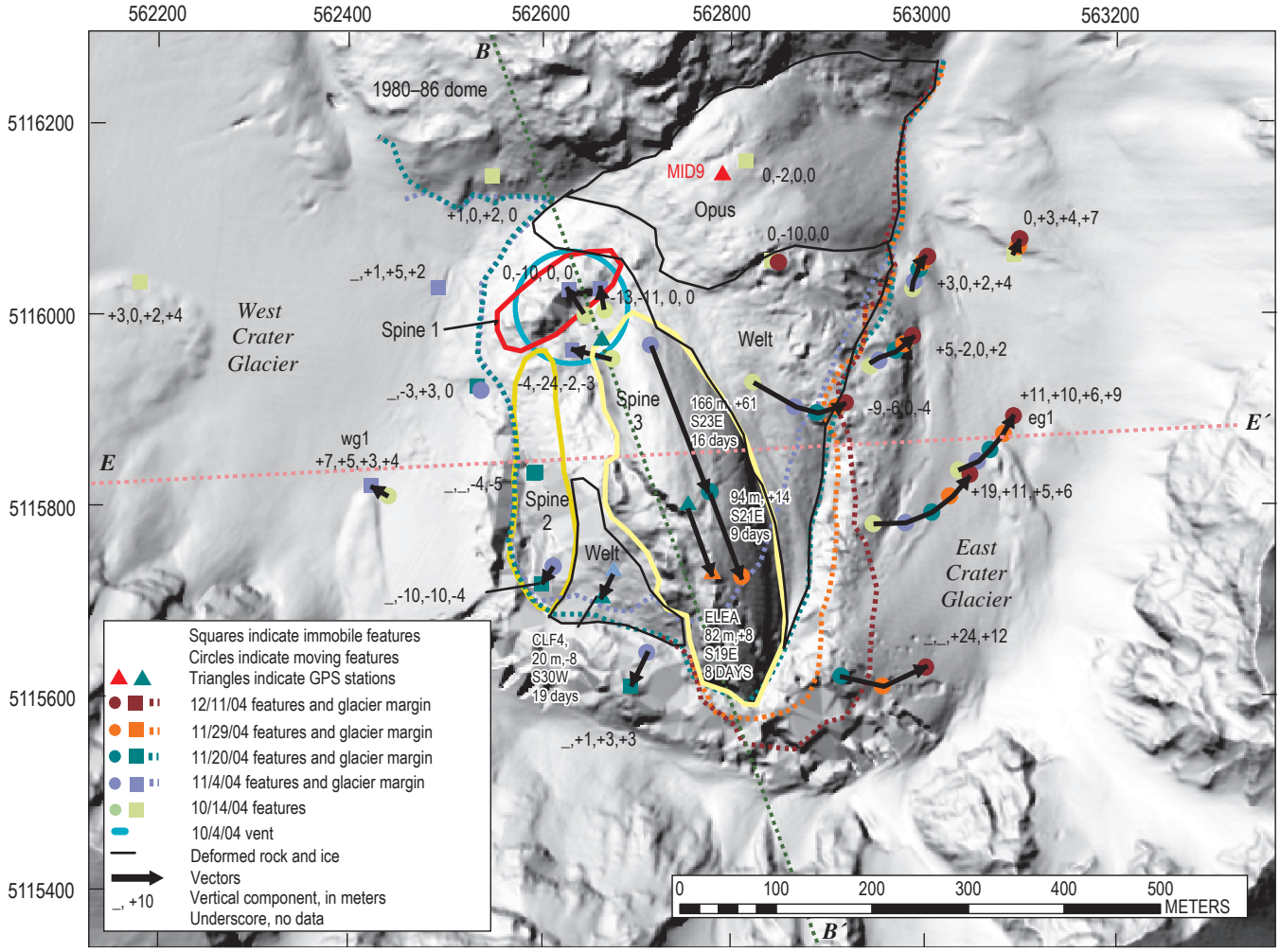

Figure 7. Deformation vectors for the period October 14–December 11, 2004, shown on DEM of November 20. Squares and dots indicate features tracked for dates identified by color in key. These colored symbols delimit deformation vectors of each of the four time intervals between relocation of features. For quantitative data (example: _, -3, +3, 0), numbers are vertical components of vectors, in meters, for each interval. Underscores indicate no data for that interval. Dotted lines indicate dome-glacier margins for dates indicated by color in key. Lines ***B–B´*** and ***E–E´*** are traces of cross sections shown in figures 8 and 14, respectively.

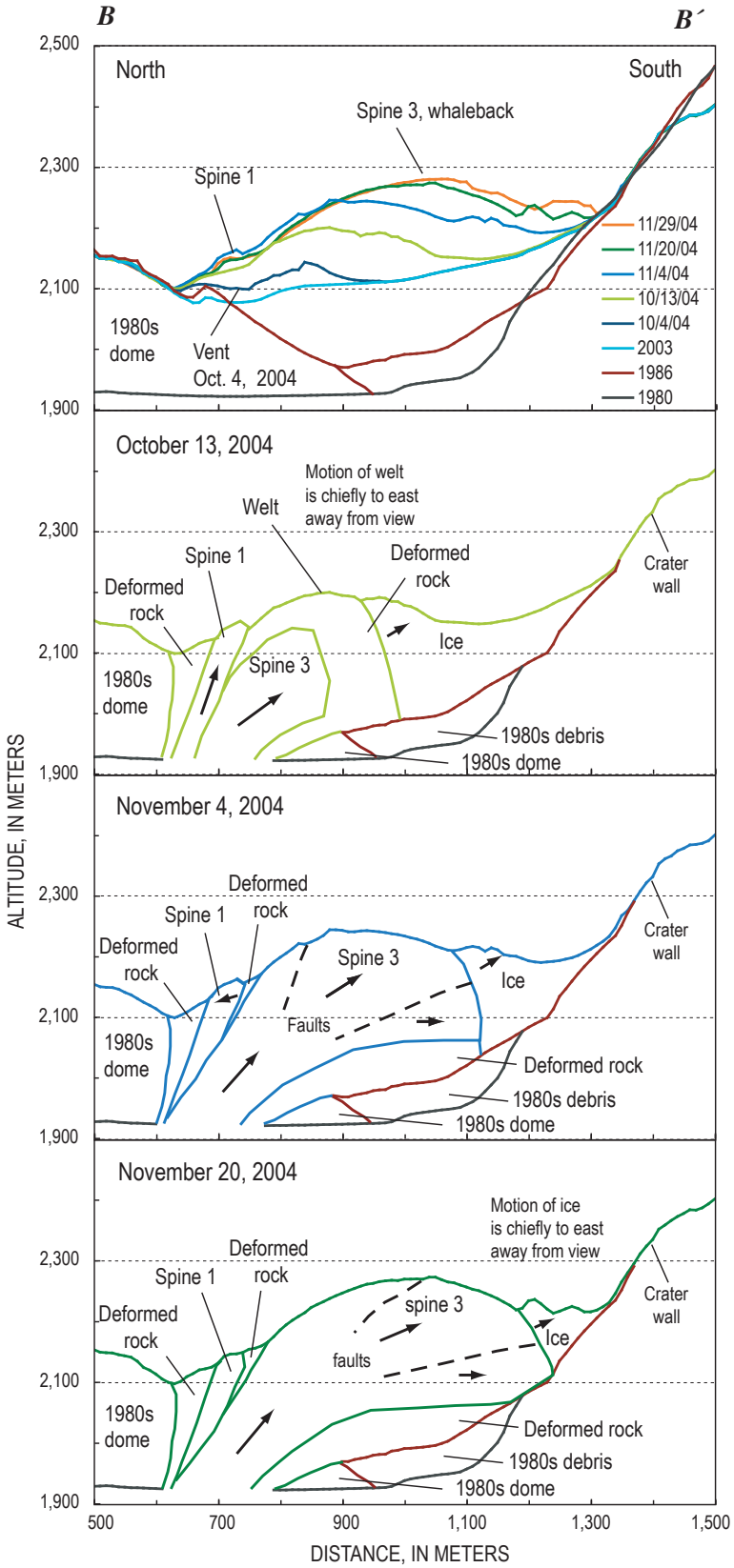

Figure 8. North-south cross section ***B–B´*** (location shown in figure 7) illustrating intrusion and recumbent growth of spine 3. Top panel shows known profiles for the dates given, and other panels illustrate geologic interpretations on given dates.

(LaHusen and others, this volume, chap. 16). Nearly static areas during this time included spines 1 and 2, Opus, and the west arm of Crater Glacier.

Striations and Relative Motion of Spine 3 in Early November

Growth of spine 3 and nearby deformation patterns explain otherwise enigmatic bidirectional striation patterns on the spine in early November 2004. On November 4, 7, and 10, striations plunging 31° N. 66° E. on the east face of spine 3 were superimposed on fainter striations plunging 20° N. 5° E. (fig. 10*B*). At the north end of the spine near the vent, only fainter N. 5° E. striations existed. A cursory analysis in early November suggested that the striations recorded a change in direction of spine growth, with the fresh striations indicating the most recent direction. However, our photogrammetric analysis indicates instead that welt debris adjacent to the whaleback was being dragged at a rate of almost 10 m/d along the base of the emerging spine along a ~S. 32° E. trend (fig. 10). This vector minus the true-growth vector yields a vector whose direction (N. 66° E.) matches the direction of the freshest east-flank striations (fig. 10*B*). Deformation patterns east of the spine thus suggest a simple explanation in which the fresh striations recorded a growth direction relative to debris being dragged southward, and the faint striations recorded the true growth direction of the spine.

Continuing Recumbent Growth of Spine 3

Through November, spine 3 continued to advance to the south-southeast (S. 19° E. to S. 23° E.) at a linear rate of 10–11 m/d (fig. 7). Judging from the slope of the northern face, initial vertical components of motion were ~30°. As features on the spine moved to the south, their vertical motions gradually diminished to zero by ~300 m from the vent, and thereafter they began to subside (LaHusen and others, this volume, chap. 16; this study). The southerly (S. 5° W.) motion of features on the spine turned to south-southeast in mid-November (fig. 7). As the spine axis and growth direction converged, its whaleback form began to take on a smooth gouge-covered appearance on the east and west flanks.

Superposition of spine 3 outlines from November to December 2004 upon the 1986 surface suggests that the growing spine encountered opposing slopes of the 1980 crater wall in mid-November (fig. 8). The surface outline of the spine first overlapped the steep north-sloping crater wall at the bed of the glacier sometime between November 4 and 20 (fig. 12*A*). Northeastward acceleration of GPS spider MID9 north of spine 3 and south of the 1980–86 dome beginning November 12 probably corresponded to the time at which spine 3 began to push against the opposing slope of the 1980 crater beneath the glacier (fig. 13).

As spine 3 continued to impinge on steep, opposing subglacial slopes of the crater wall in late November and December, the spine axis began to rotate eastward (table 2, fig. 12*A*) and the spine began to break. Axis orientation changed 8° eastward from November 20 to December 11 (table 2). Between November 20 and 29, fracturing and separation of the first piece of spine 3 was apparent (figs. 2*A*, 2*B*), consistent with northeastward acceleration of GPS station MID9 during November 23–27 ("1st breakup" in fig. 13*A*). By November 29, this small spine fragment had completely separated, and by December 11, the rotating spine had pushed it into a steaming heap along its margin with east Crater Glacier (fig. 2*C*). A second, more substantial fragment separated and decoupled in early December. Northeastward acceleration and deceleration of MID9 suggests that the period of the fracture and decoupling of the resultant spine fragment spanned December 6–12 ("2nd breakup" in fig. 13*A*).

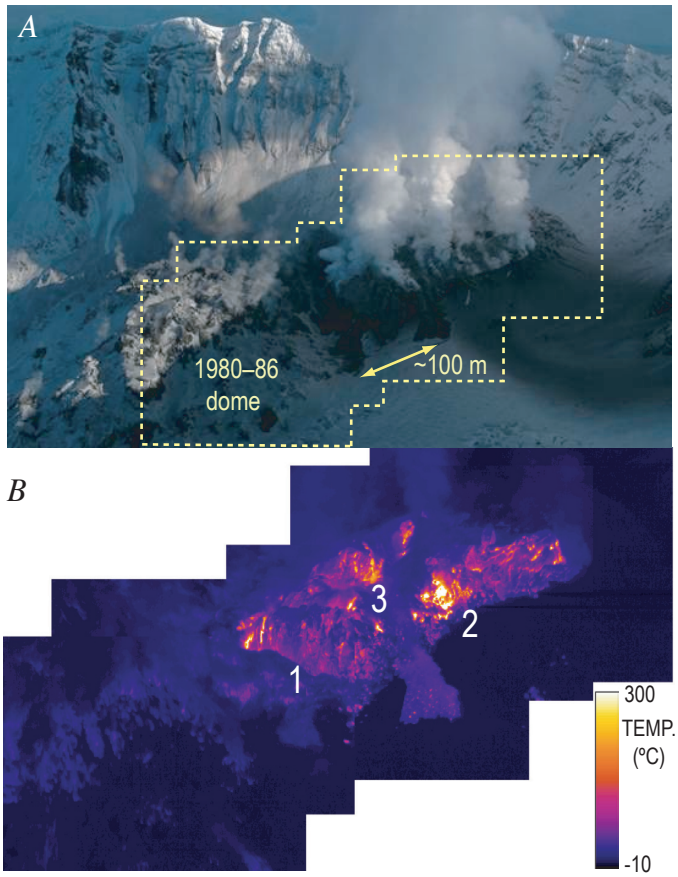

Figure 9. Mount St. Helens crater floor on October 27, 2004; view from northwest, illustrating spines 1–3. *A*, Photograph showing 1980–86 dome and ongoing extrusion, with fresh ash on Crater Glacier west of new dome. *B*, Mosaic of thermal-infrared images located in *A* from same date and time. Numbers indicate spines 1–3. Maximum temperature in field of view is 600°C (scale is set such that all temperatures greater than 300°C are white). Spine 3 has emerged since previous TIR survey on October 24. Thermal imagery shows hot debris fan and hot blocks on ice and firn near spine 1 and between spines 1 and 2. USGS photo by J.W. Vallance; thermal images by D.J. Schneider.

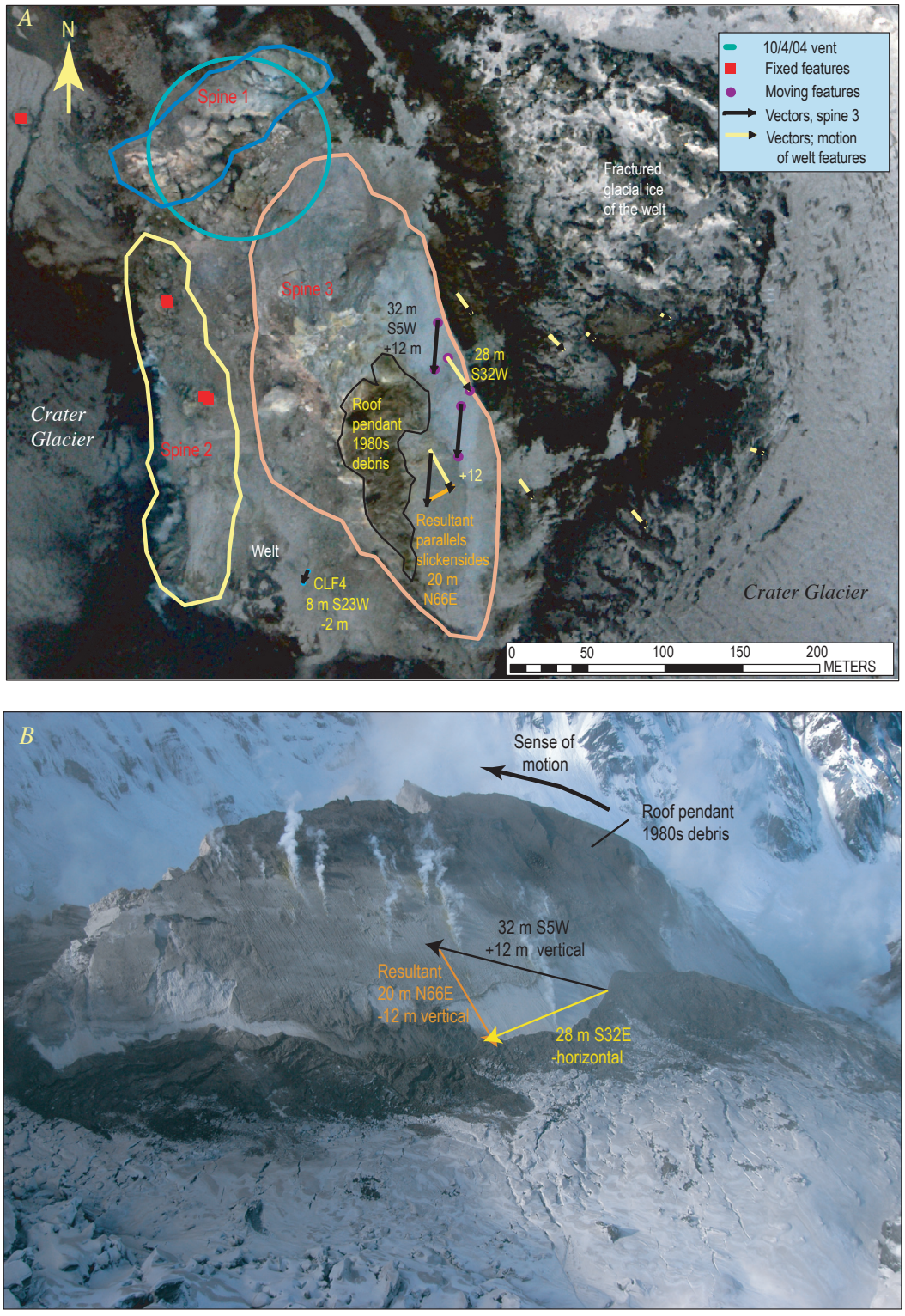

Figure 10. Mount St. Helens crater floor in early November 2004. *A*, Rectified vertical aerial photograph of dome taken November 7, 2004, with handheld camera from an airplane. The photograph was subsequently rectified using features on 1980–86 dome, Opus, and Crater Glacier for both November 4 and 7 so that its central part is tied to geographic coordinates of the November 4 DEM. The aerial photograph shows deformation vectors in plan view for November 4–7. *B*, Oblique photograph looking west at spine 3 on November 4, 2004, showing faint striations parallel to deformation vector, $\vec{V}_{black}$, and young pronounced striations parallel to vector $\vec{V}_{orange}$, where subscripts indicate vector colors in photograph. Debris adjacent to whaleback moves in the near-horizontal plane parallel to $\vec{V}_{yellow}$ such that $\vec{V}_{yellow} - \vec{V}_{black} = \vec{V}_{orange}$. USGS photos by J.S. Pallister.

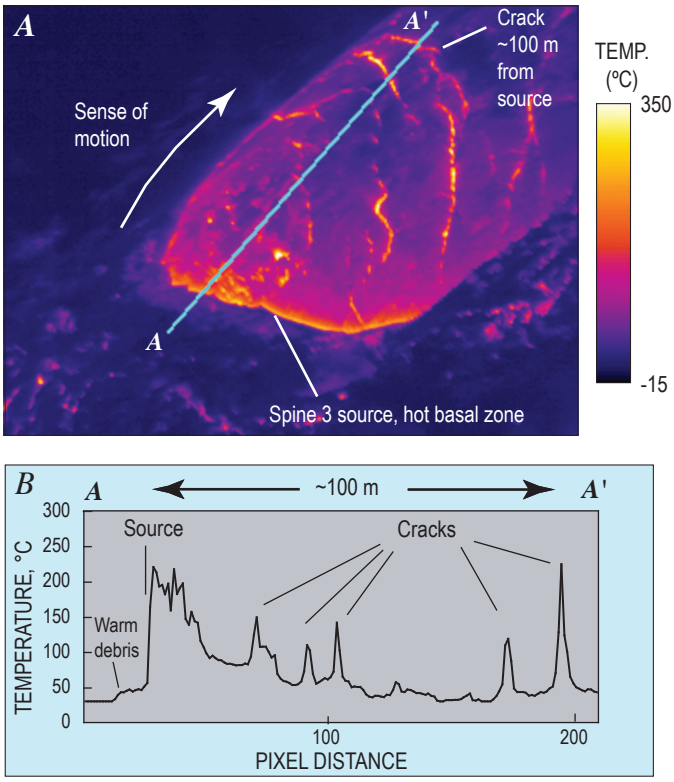

Figure 11. Thermal aspect of spine 3 surface on November 29, 2004. *A*, Thermal-infrared image from helicopter, view to southeast, by J.W. Vallance. *B*, Temperature profile from north to south.

There was no big north-south crack in a December 4 image (R.L. Helz, written commun., 2004). However, a December 8 image revealed a well-developed crack, confirming that during that interval a substantial part of the spine had begun to separate from its west flank along a longitudinal fracture oriented parallel to the spine's axis. December 11 photographs (fig. 2*C*), DEM (Schilling and others, this volume, chap. 8), and geologic map (Herriott and others, this volume, chap. 10) revealed that this fragment had largely decoupled and had begun to subside westward by that date. During November to mid-December numerous other small spine fragments separated from spine 3, mostly to the west. Generally, fragments separating to the west slowly subsided and stagnated, whereas the few separating to the east were bulldozed eastward.

Late October–Mid-December Deformation of Surrounding Areas during Spine 3 Growth

In response to recumbent dome growth from late October to mid-December, areas east of spine 3 rotated eastward about a pivot axis near Opus, showing horizontal displacements as great as 100 m. Areas west of spine 3 subsided or stagnated and moved less than 20 m (figs. 7, 14*A*). All areas east of spine 3 rotated eastward in such a fashion that displacement per unit time increased from north to south. Ice masses on the welt subsided and then migrated eastward across the boundary between stagnant ice and the Crater Glacier, whereupon they began to rise. During this interval all ice on the east Crater Glacier rose between 10 and 50 m, with largest vertical displacements occurring to the south and the smallest to the north (figs. 7, 14*A*). In effect, rotating dome and welt rock bulldozed the glacier eastward, compressing and lifting it such that its cross-sectional profile changed from concave to convex (figs. 2, 14*A*).

Spine 1 moved in response to the emerging spine 3, then stabilized as that new spine continued to grow. Spine 1 was displaced about 40 m north-northwest and tilted from a dip of 50° to 80° northwest between mid-October and early November (fig. 7). Comparison of the October 14 DEM with those of November (figs. 5, 7) shows the change in position of spine 1 with respect to the October 4 vent position. This displacement and rotation coincided with southward growth and emergence of spines 2 and 3. The displacement and rotation were to the northwest, directly away from the origin of spine 3's southward extrusion, and are likely to have been a response to spine 3 emergence rather than growth of spine 2.

Spine 2 and the area between spines 2 and 3 rotated slightly and subsided between October and December. In late October and early November, spine 2 moved as much as 20 m to the northwest at its south end but remained relatively stable to the north. In late October, the top of spine 2 was as much as 20 m higher than the adjacent glacier surface (fig. 9). As spine 3 grew, spine 2 subsided by 20–25 m (fig. 7). By late November, spine 2 had become a nondescript entity hidden below the level of west Crater Glacier, with talus and rockfall encroaching upon it from the more prominent spine 3 to the east (fig. 2*B*). The GPS spider CLF4, placed on the welt October 27, was perched between spines 2 and 3 as spine 3 emerged. The spider had moved ~44 m S. 24° W. and subsided 13 m by November 19, when it was buried by rockfall from spine 3 (LaHusen and others, this volume, chap. 16). As spine 3 advanced, it pushed parts of the dome south and west of it to the southwest, but, after its leading edge passed by and the spine began rotation in the opposite direction, subsidence of areas west of spine 3 began—possibly caused by removal of buttressing from the east.

West Crater Glacier, south and west of the spine complex, responded during a brief interval as spine 3 approached but otherwise remained relatively static from late October to mid-December (fig. 7). Dome growth after November 4 caused no detectable deflection of west Crater Glacier. A slow increase in altitude of the west glacier, caused in part by accumulation of snow, occurred as spine 3 grew. Areas of the glacier immediately south of the dome complex moved tens of meters as the whaleback approached (fig. 7), but then they stopped.

Breakup of Spine 3 and Formation of Spine 4: December 18, 2004–April 8, 2005

Spine 3 broke up and decoupled as spine 4 formed between mid-December 2004 and early January 2005. Photograph sequences showed fractures oriented diagonally across

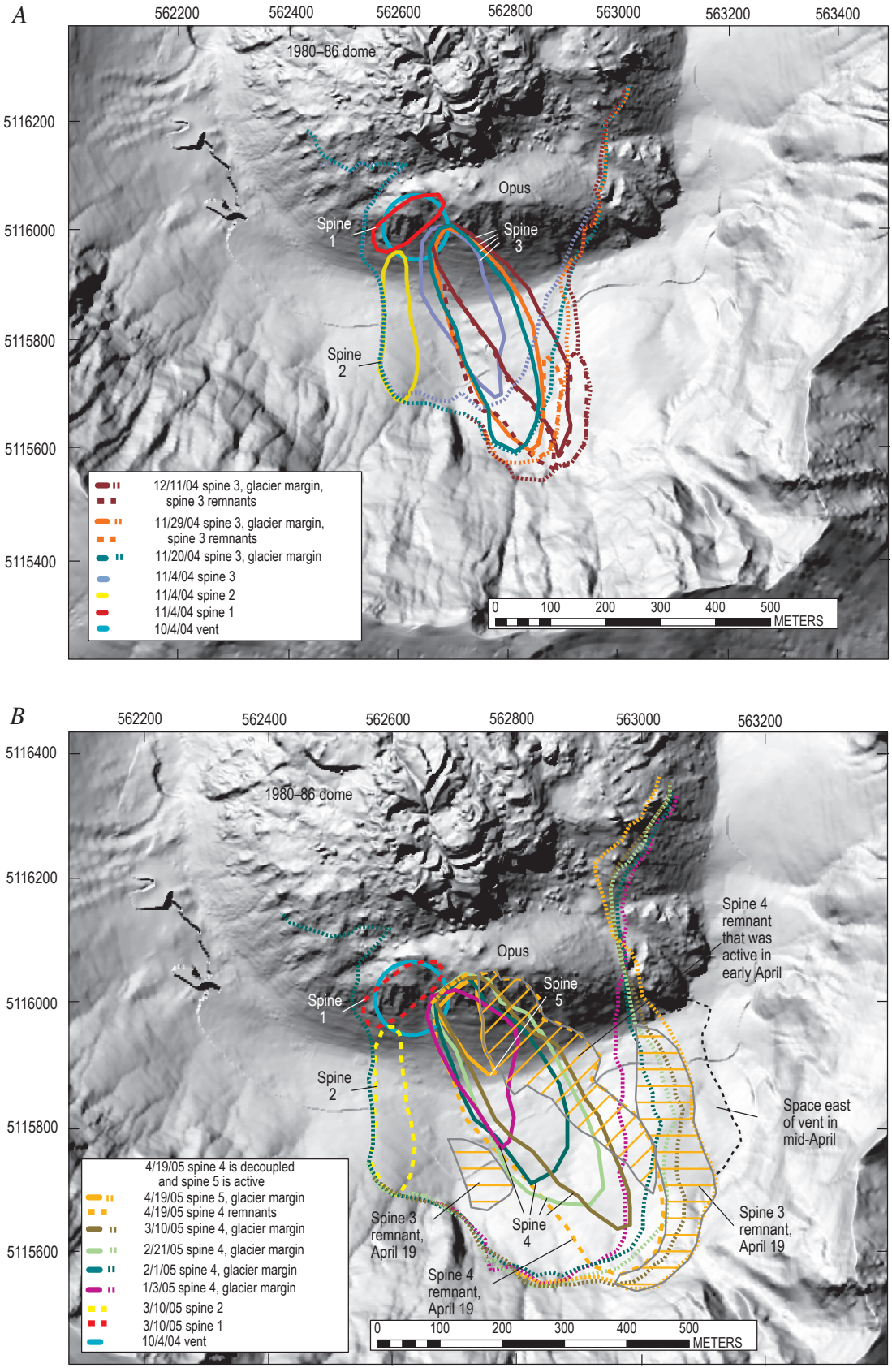

Figure 12. Outlines of active spines and dome-glacier margins at Mount St. Helens, Washington, superimposed on 1986 DEM. *A*, November 4–December 11, 2004. *B*, January 3–April 19, 2005.

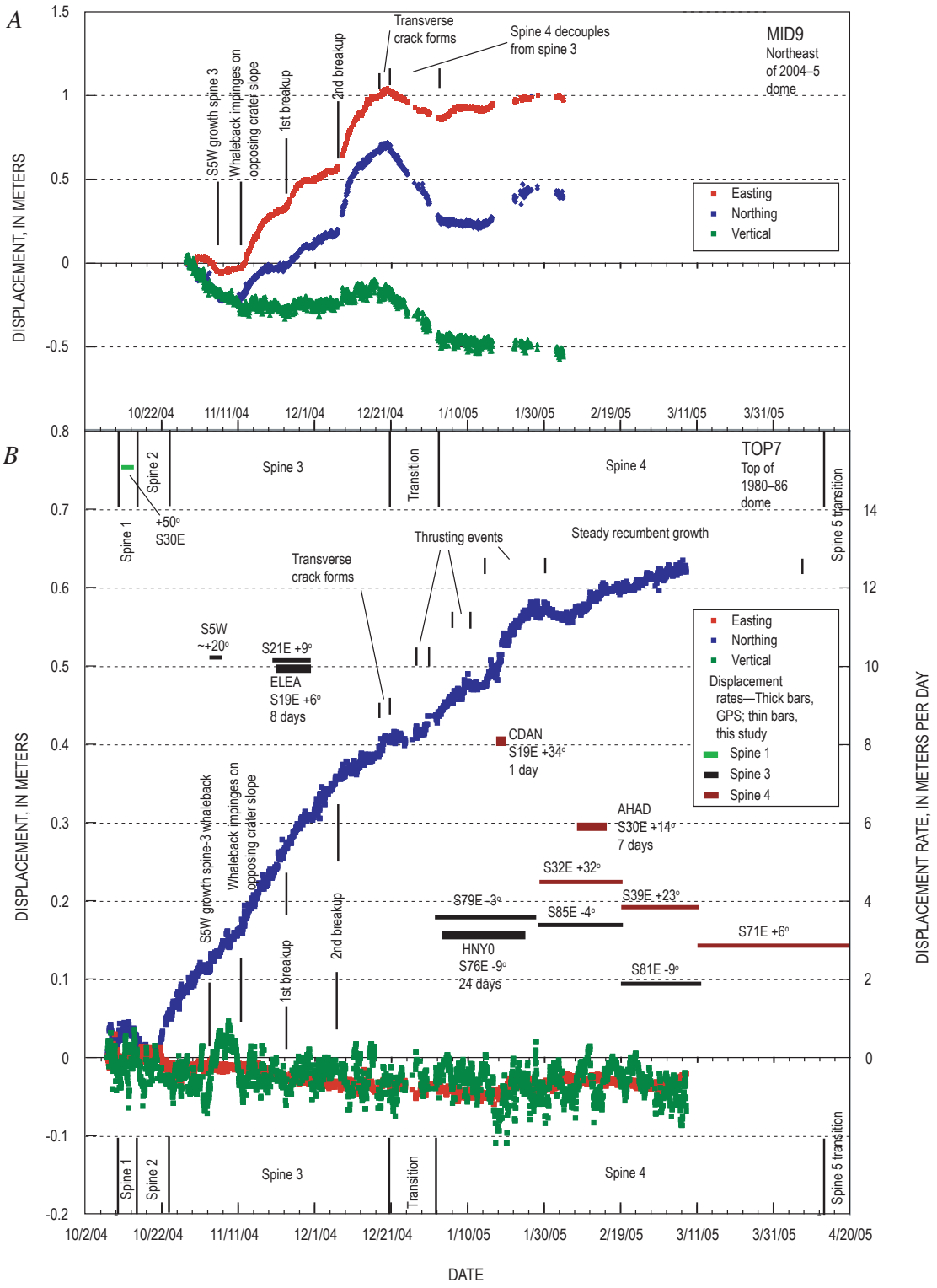

Figure 13. Plots of displacement versus time for GPS stations MID9 (*A*), located between 2004–5 and 1980–86 domes, and TOP7 (*B*), located at apex of 1980–86 dome, with intervals of spine growth and key events during spine growth, as well as linear extrusion rates of GPS receivers and features tracked in this study superimposed on GPS time series. Initial locations shown in figures 7 and 15. Because of their locations just northeast and north of spines 3 and 4, MID9 and TOP7 stations commonly accelerated opposite spine growth when spine met resistance to its growth and decelerated when that resistance was relieved. GPS data from LaHusen and others (this volume, chap. 16).

spine 3 that formed and became more prominent beginning about December 18 (Major and others, this volume, chap. 12). Station MID9 reversed its direction of motion from northeast to southwest on December 20 (LaHusen and others, this volume, chap. 16), an event correlated approximately to the formation of the transverse fractures (fig. 13). Southward thrusting of spine 4 over the slowing bulk of spine 3 had become evident by December 24–28 (figs. 2*D*, 2*E*; supplementary movie 2 in Iverson and others, 2006). A second fracture south of the first formed by January 3, 2005, and the decoupling of spine 4 from spine 3 could be considered complete by that time (fig. 2*E*). We infer that cessation of MID9's southwestward motion on January 3 corresponded to complete decoupling of spines 3 and 4.

Between January 3 and April 2005, spine 4 pushed south-southeast from a source located ~70 m east of spine 1. Spine 4 had whaleback morphology similar to that of spine 3 but underwent several cycles of thrusting over spine 3 before it established steady near-uniform growth. Photographs (figs. 2*E*, 2*F*) and time-lapse video (Iverson and others, 2006; Major and others, this volume, chap. 12, appendix 1) reveal thrusting events during January 6–12 and January 14–February 2. The TOP7 GPS spider accelerated northward during each of these events (fig. 13*B*). Time-lapse photography and GPS records for the period of February 2–April 9, 2005, suggest nearly uniform, steady southward growth and no further thrusting events.

By early January spine 4 had a crest oriented S. 27° E. and dimensions of 210×130 m (table 2, fig. 15). Spine 4 grew to ~440 m in length by early March before beginning to break up in April (fig. 16). As with spine 3 during November and December, the long axis of spine 4 began to pivot eastward about its origin at the vent. This rotation began once the spine started to impinge on slopes of the crater wall (figs. 12, 17); its long-axis orientation swung 12° eastward between mid-February and its breakup in mid-April (table 2, fig. 12*B*). This response suggests that the moving spine extended deep enough to be influenced by the slopes of the 1980 crater at depth, as modeled in cross sections (figs. 16, 17).

Linear extrusion rates of spine 4 diminished during January 3–April 10, as shown by analysis of photographs taken at hourly to daily intervals from fixed sites at the eastern crater mouth (Sugar Bowl) (Major and others, this volume, chap. 12), the motions of GPS spiders on the spine (LaHusen and others, this volume, chap. 16), and time-averaged results from this study (fig. 13, table 2). A GPS station, CDAN, moved 8 m/day along a path of S. 19° E. and 34° upward between January 15 and 16. A second station, AHAD, moved 5.9 m/d along a path of S. 30° E. and 14° upward between February 8 and 15 (fig. 13) (LaHusen and others, this volume, chap. 16). A rate and direction estimate using features on successive DEMs for the longer interval between February 1 and 21 was slower: 4.5 m/d along a path of S. 32° E.

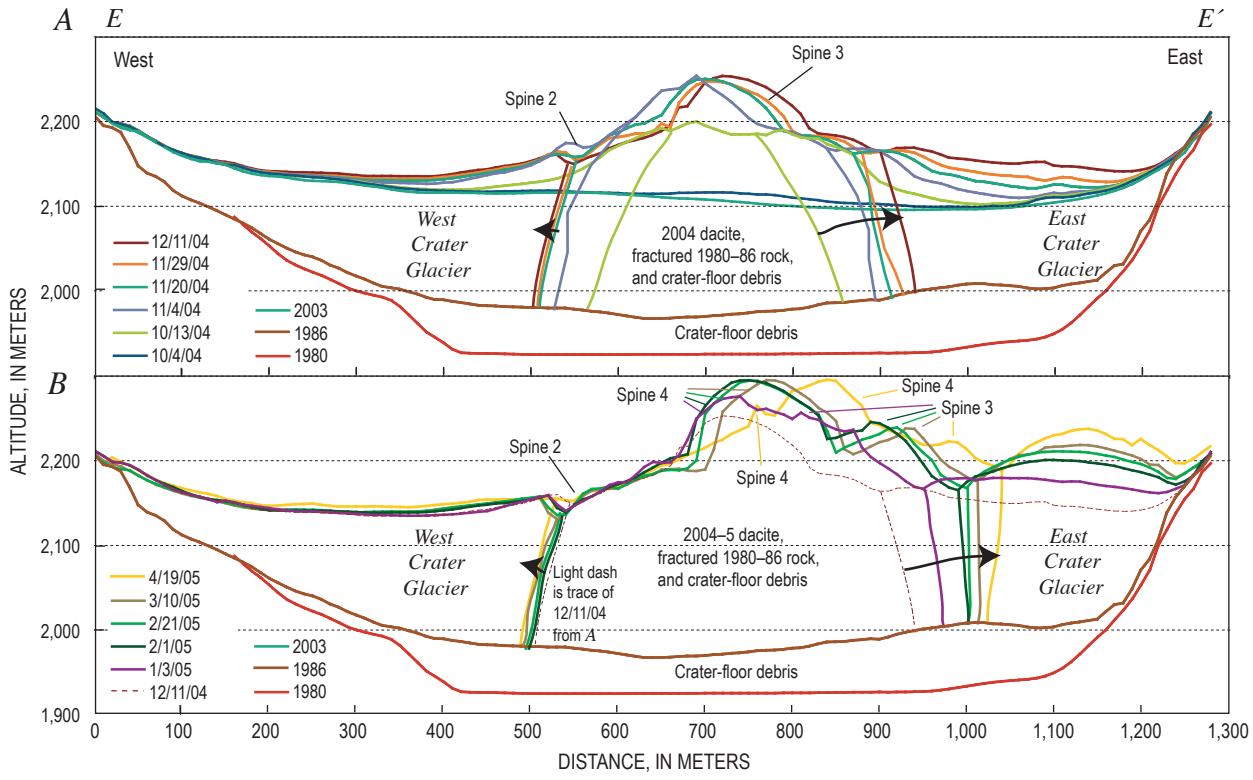

Figure 14. East-west cross section ***E–E´*** (location shown in figures 1 and 7) illustrating response of glacier to recumbent growth of spine 3. *A*, Profiles for October 13–December 11, 2004. *B*, Profiles for January 3–April 19, 2005.

and 32° upward (figs. 13, 15). This slower rate is about the same as spine 4 extrusion rates reported by Iverson and others (2006) and Major and others (this volume, chap. 12), who compared daily Sugar Bowl photographs. With time, extrusion rates diminished and directions became more easterly: 3.9 m/d along a path of S. 39° E. and 23° upward between February 21 and March 10. This decreased to 2.6 m/d along a path of S. 71° E. and 6° upward between March 10 and April 19. We estimated a time-averaged rate of advance for the period of January through mid-March by measuring advance of the leading edge of the whaleback in cross section (fig. 16). Between January 3 and March 10, the advance of ~300 m gave a rate between 4 and 5 m/d. Rates were as high as 8 m/d during some briefer intervals (table 2).

The initial volume of spine 4 on January 3, 2005, as it splintered from spine 3, was 5.5×10^6 m^3, and total volumes of hot rock reported for different times during the spine 4 extrusion (Schilling and others, this volume, chap. 8) allow calculation of spine 4 volumes and time-averaged, volumetric extrusion rates between January and April 2005 (table 2). Time-averaged extrusion rates for these intervals suggest a spurt in growth from February 1 to 21. The growth spurt occurred during the same interval in which spine 4 transitioned from intermittent thrusting to steady recumbent growth.

Deformation of Areas Surrounding Spine 4 Growth during January–April 2005

Spine 4 growth during January through April caused areas to the east to rotate eastward about a pivot near Opus. Displacements were as great as 200 m (fig. 15). In response to motion of the welt to the south of Opus, ice masses stranded

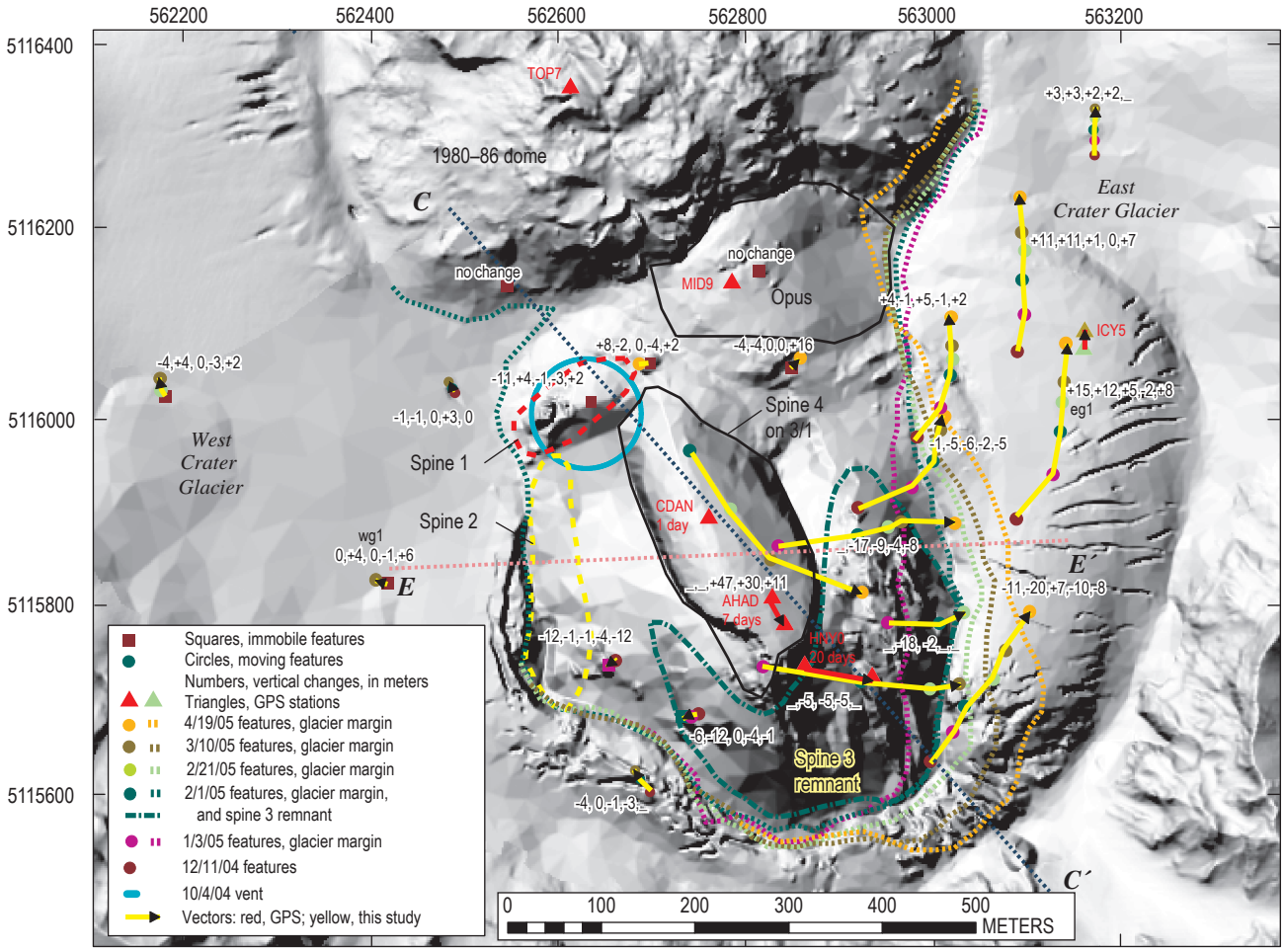

Figure 15. Deformation vectors for the period from January 3 to April 19, 2005, shown on DEM of February 1, 2005. Squares and dots indicate features tracked for dates identified by color in key. These colored symbols delimit deformation vectors of each of the five time intervals between relocation of features. Numbers are vertical components of vectors, in meters, for each interval. Underscores indicate no data for that interval. Dotted lines indicate dome-glacier margins for dates indicated by color in key. Dashed lines ***C–C´***, and ***E–E´*** are traces of cross sections shown in figures 16 and 17.

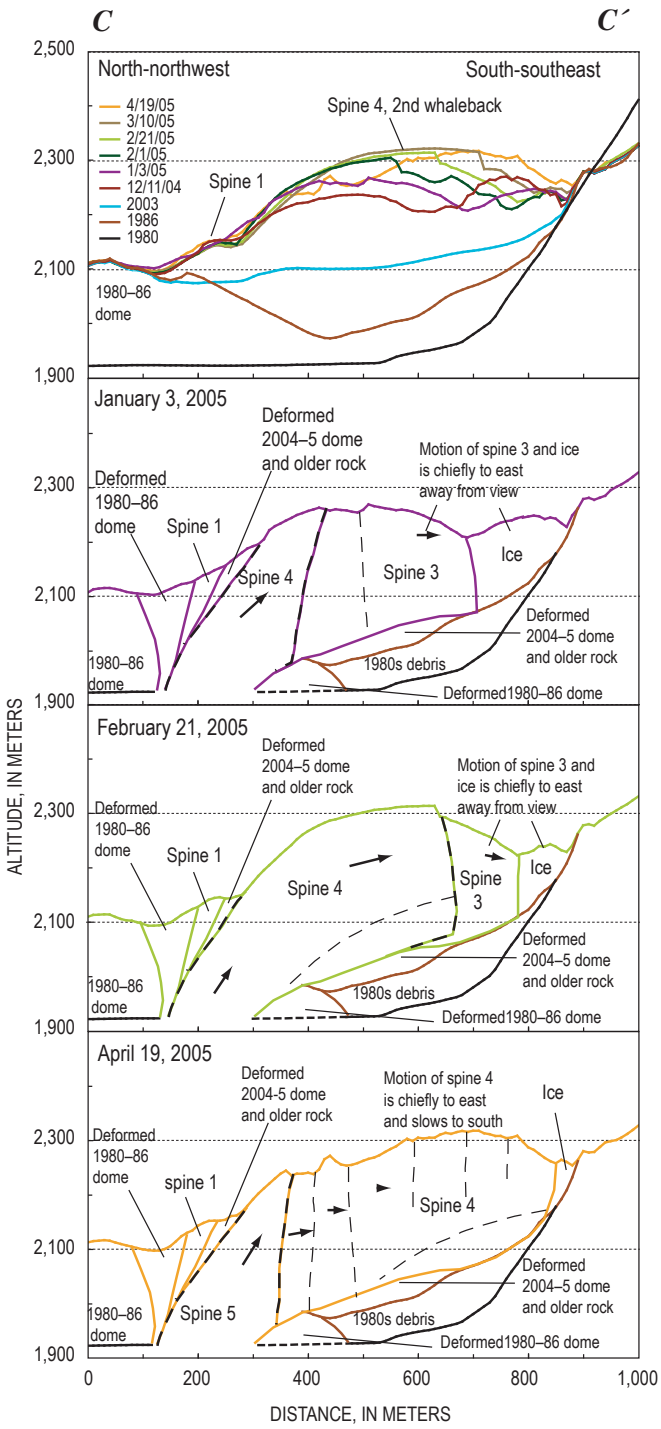

Figure 16. North-northwest to south-southeast cross section *C*–*C´* (location shown in figure 15) illustrating extrusion and recumbent growth of whaleback, spine 4. Top panel shows known profiles for dates given, and other panels illustrate geologic interpretations on given dates. Dashed lines indicate inferred faults.

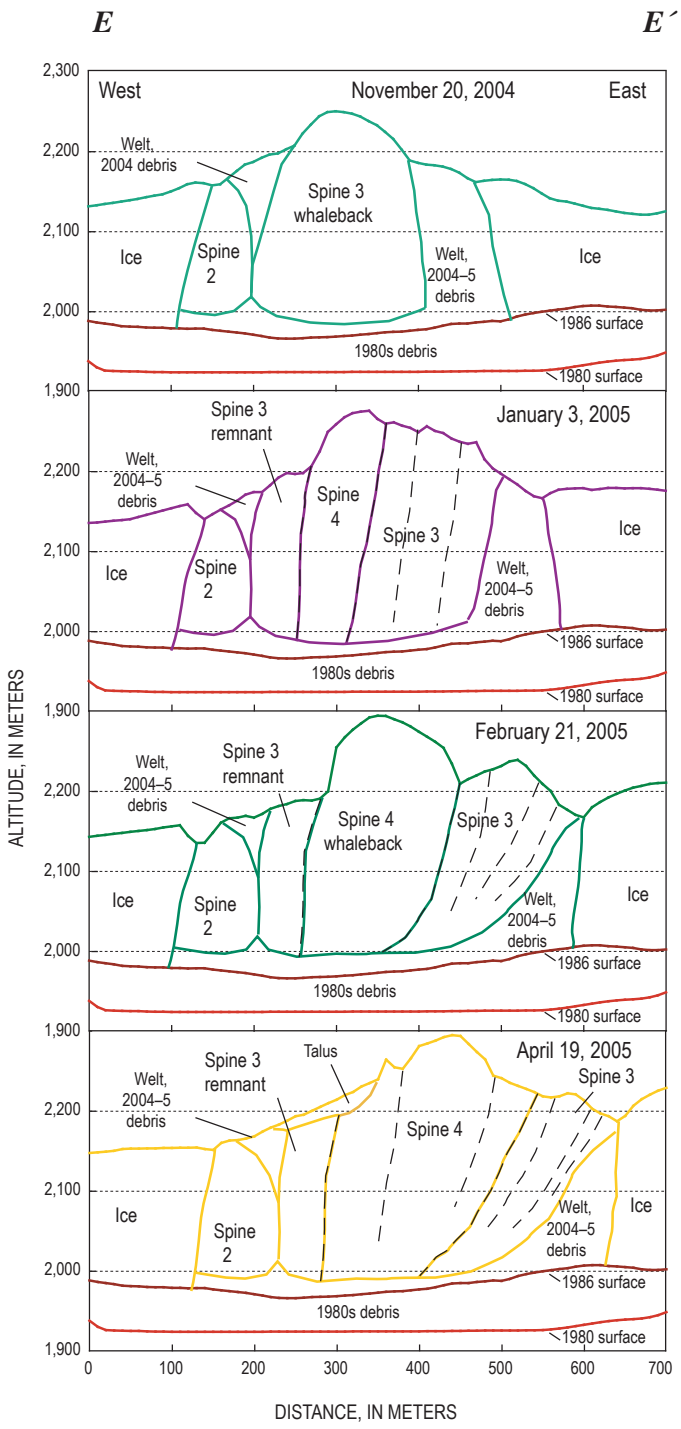

Figure 17. East-west cross section *E*–*E´* (location shown in figure 15) illustrating extrusion and recumbent growth of spines 3 and 4. Panels illustrate geologic interpretations on given dates. Dashed lines indicate inferred faults; heavy and light line weights indicate contacts between spines and within spines, respectively.

on the welt moved eastward until they crossed into the realm of the active east Crater Glacier, whereupon they flowed northward as part of the glacier. Recognizable remnants of the disintegrating spine 3 shifted eastward 100 m or more by February 1. Areas closest to spine 4 moved fastest. Between January 3 and February 1, an area on spine 3 south of spine 4 moved 107 m S. 79° E. at a rate of 3.7 m/d and subsided slightly (fig. 15). The GPS station HNY0, located ~40 m to the east, moved 3.2 m/d, S. 76° E., and also subsided (fig. 13) (LaHusen and others, this volume, chap. 16). Continuing deformation at nearby sites was S. 85° E., 3.6 m/d, and S. 81° E., 1.9 m/d, during February 1–March 10 (fig. 15).

Spine 4 bulldozed and tilted spine 3 eastward, rapidly fracturing it and causing it to disintegrate (figs. 2, 3, 17). By April 19, spine 3 had been reduced to a rubbly ridge adjacent to the east Crater Glacier, and its surface area had been reduced by a factor of five (Herriott and others, this volume, chap. 10). Overthrusting caused by eastward rotation of spine 4 as it deflected off the crater wall caused the reduction in area of spine 3 (fig. 17). Except for one small area, spine 3 remnants to the west were buried by spine 4 talus.

Areas on the 2004–5 dome west of spine 4 continued to subside but moved laterally no more than about 10 m. Spine 1 subsided in December but showed no significant motion thereafter. An area near the south end of spine 2 and another on a remnant of spine 3 west of spine 4 moved less than 10 m southwest between January and February and subsided 10–20 m. Thereafter, subsidence continued at a slower pace, and no further translation of these spine 2 and 3 fragments was detectable.

As the east Crater Glacier continued to be bulldozed eastward at rates as high as 1.5 m/d, it rose tens of meters and accelerated downstream. Between mid-December 2004 and mid-April 2005, the glacier profile bulged as much as 90 m and became markedly convex (fig. 14*B*). During this interval, individual surface features on east Crater Glacier rose as much as 50 m, with the largest vertical displacements in areas east and southeast of Opus. In contrast, farther upslope to the south, features lost tens of meters in altitude as they flowed north (fig. 15). Features with eastward components of displacement in the autumn of 2004 shifted to due north displacement during winter 2005 as the glacier accelerated away from the area of constriction between the rotating dome complex and the east crater wall. The glacier had thickened so much since the onset of the eruption (as much as 130 m) that its slope had increased dramatically, and it responded by flowing north to correct the imbalance.

The Crater Glacier west and north of the spine complex responded by moving a few meters northwest during late December to April, in places rising by a few meters. Although dome growth may have had a minor effect on west Crater Glacier (fig. 15) during the winter months of 2005, accumulation of snow and normal glacier flow downslope probably accounted for most of the observed change. Areas of the glacier immediately southwest of the 2004–5 dome complex moved about 30 m northwest in response to the approach of spine 4 (figs. 12, 15).

Phase 4, Extrusion of Spine 5 across Previous Spine Debris: April 10–July 31, 2005

Spine 4 broke up, decoupled, and changed direction in mid-April 2005. Continual pressure caused by spine 4 pushing against the opposing crater wall disrupted its steady southward propagation and caused it to break apart. Repeat photographs (Major and others, this volume, chap. 12) and time-lapse photography (Iverson and others, 2006) showed development of northeast- to southwest-striking fractures cutting spine 4 at this time. These fractures became progressively more prominent from April 10 to 19. Between April 19 and 24, as the fractures grew, spine 5 began to thrust over the top of spine 4 remnants. Like spine 4, the spine 5 source was ~50 m southeast of spine 1 (fig. 15).

Spine 5 had decoupled from spine 4 by April 19, though it continued to drag the southern parts of spine 4 southward until mid-May and to displace it to the east through June. Spine 5 displayed a smooth, gouge-covered surface near the vent. It became progressively steeper with time, the slope increasing from 40° on April 19 to 54° on July 14 (fig. 18). The spine tended to fracture and crumble as it grew higher, leading to a substantial breakup and decoupling of the southern section of the spine between mid-June and mid-July. During this interval spine growth began to resemble that of the Mont Pelée spine of 1903, with a steeply thrusting lithic core surrounded by an apron of debris at the angle of repose (Blake, 1990). The thrusting spine 5 acted as the driving force for a conveyer that transported at least half of the volume of the crumbling spine southward to form a ridge of disaggregated rock with a trend of S. 10° E. in mid-June and S. 5° E. in mid-July.

From April to August 2005, we were unable to use surface deformation vectors to make independent measurements of spine growth rate because of plumes that obscured key parts of the spine in aerial photos on two of four dates. A limiting, average, lineal growth rate of 4.3 m/d can be calculated from knowing that spine 5 was 100 m long on April 19 and 340 m long on June 15. Data from Major and others (this volume, chap. 12) suggest that extrusion rates of the smooth northern surface diminished from ~4 m/d in late June to ~2 m/d by early July. Time-averaged volume flux decreased slowly between April and July (table 2).

Deformation of Areas Surrounding Spine 5 from April to July 2005

Deformation of areas surrounding spine 5 showed that the spine was deep seated only near its source and was thrusting upward over previous parts of the dome complex to the south (fig. 19). Spine 4 remnants east of spine 5 rotated northeast or east, with the pivot point about 300 m southeast of the vent in an area of stagnant spine 4 rock (near point -7,-2,-3 in fig. 19). The areas of maximum displacement were in the north adjacent to the vent. Maximum displacement east of the vent on

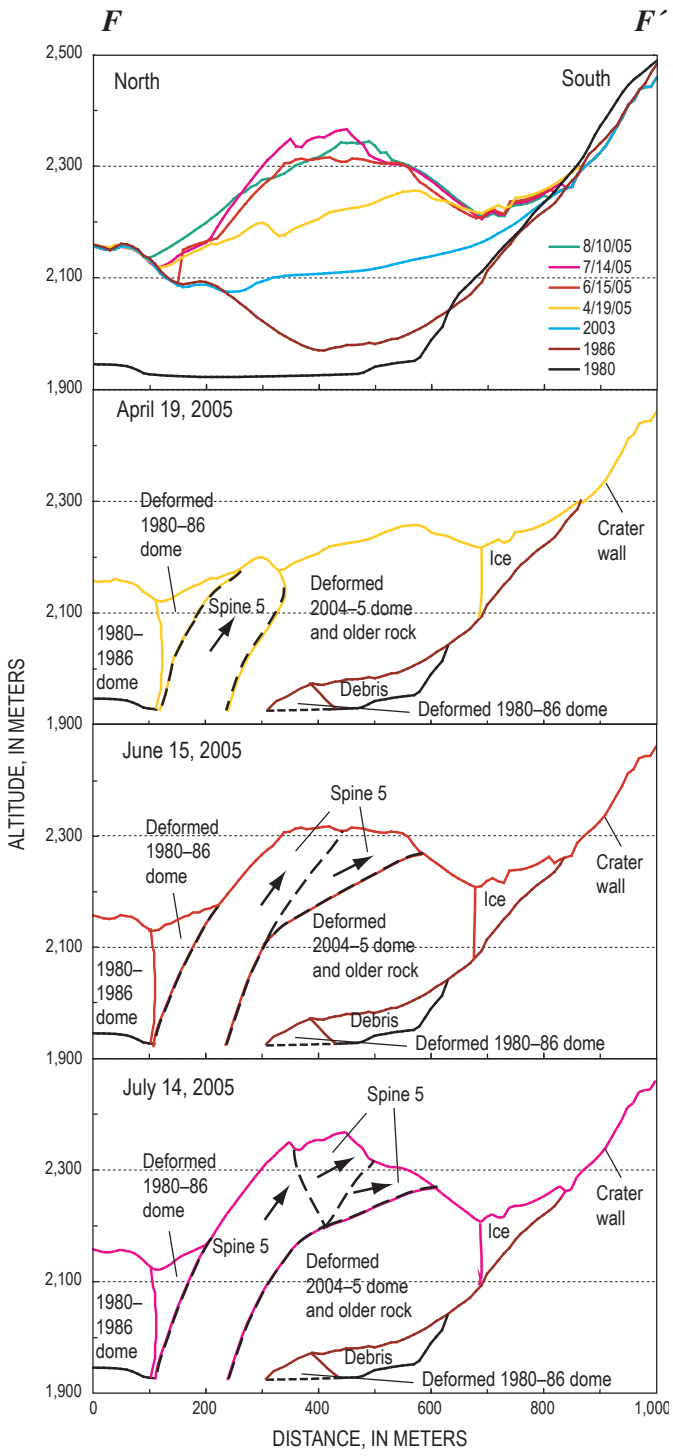

Figure 18. North-south cross section *F*–*F*´ (location shown in figure 19) illustrating extrusion and thrusting growth of spine 5. Top panel shows known profiles for dates given, and other panels illustrate geologic interpretations on given dates. Southern part of spine 5 crumbled and broke up between June 15 and July 14, 2005.

spine 4 was 40–50 m, generally to the northeast. Most of the displacement occurred in April and May; very little occurred thereafter. A feature near GPS station SEV7 moved about 40 m to the northeast and subsided 16 m (point -7, -3, -6, fig. 19). All but 2 m of translation had occurred by June 15, but subsidence continued through August. The GPS station SEV7, located ~30 m west of this feature, was deployed on May 24. By June 15 it had moved only 7 m S. 70° E., implying that about 80 percent of the translation in this area had occurred between the time of the April 19 DEM and May 24. All remnants of spine 4, including those that did not translate significantly, subsided 10–20 m during spring and early summer of 2005. Farther east, spine 3 remnants also subsided between April and June but did not translate more than ~5 m.

Areas on the dome west and north of spine 5 moved northwestward 40–60 m (fig. 19). Spine 1 was pushed ~50 m northwest (point +10, fig. 19). An isolated remnant of spine 3 to the southwest of spine 5 (point -1, fig. 19) moved about 40 m westward before it was buried. Spine 2 was buried by encroaching spine 5 talus in June and then could not be tracked, but its contact with the west Crater Glacier receded as much as 100 m westward between April 19 and August 10 (fig. 19).

Nearby parts of the west Crater Glacier began to be pushed westward and were uplifted (fig. 19). Traceable features on the west glacier moved west as much as 80 m and rose as much as 20 m near the new dome's southwest margin, but areas farther to the north and west merely flowed downslope. Station WES6, a GPS receiver located on the west glacier ~200 m west of the dome, moved 10 m N. 51° W. and rose 0.8 m between July 14 and August 10. Meanwhile, the east Crater Glacier flowed passively to the north. East Crater Glacier fractured and became greatly crevassed as it descended rapidly to the north in response to the 100 m of excess thickness it had gained between November 2004 and April 2005. No further deformation of the east glacier occurred after mid-May, and its boundary with the dome became fairly stable (fig. 19).

Phase 5, Spines 6 and 7 Extrude Westward: August 1, 2005–April 2006 (Ongoing)

Normal Faulting and Westward Growth of Spine 6: August 1–October 9, 2005

Crumbling of spine 5 presaged reorganization of the vent and growth of spine 6 in late July and early August 2005. At least seven substantial rock avalanches and two slumping events between July 18 and 31 (table 3) reduced the smooth steep (54°) slabs of spine 5 of July 14 (fig. 3) to a rubbly ridge by August 10 (fig. 3). During this period, southward motion of segments of spine 5 slowed successively from south to north in such a way that, by the end of July, only the northernmost segment remained active.

During a transitional period August 1–5 (table 1), spine motion seen in time-lapse photography (Iverson and others, 2006) became localized to the vent area, where the sense of

motion was nearly vertical, as the remainder of spine 5 began to slump slowly. A fracture system, somewhat concealed by rubble, developed along a S. 10° W. trend and divided the stagnating spine from the active extrusion as spine 6 developed and became the dominant feature, evident in images of August 10, 2005 (fig. 3).

From early to mid-August, spine 6 began moving westward, slowly at first but then more rapidly. This westward motion of the extruding mass beginning on about August 6 marked the completion of the transition from spine 5 to spine 6 (table 1). Time-lapse photography of August 6–12 (Iverson and others, 2006) showed that spine 6 disintegrated continuously as it extended to the west.

The spine 6 mass comprised buried spines 1 and 2, a substantial part of spine 5 that had slumped to the west, debris shed from spines 3, 4, and 5, and welt rock caught between spines 1, 2, and 3 (fig. 20). This mass thus included massive lava, as well as deformed and disintegrating blocks and debris. On August 10, the extruded lava volume in spine 6 was ~1×10^6 m^3, but the total volume of the deformed mass was ~12×10^6 m^3 (table 2). A spurt in lava extrusion occurred during the transition from spine 5 to spine 6 and continued into September (table 2).

No specific feature on spine 6 could be tracked in DEMs and vertical aerial photos between August 10 and September 20. However, the trace of the active spine and the shift of the west glacier-spine margin constrain the magnitude of translation during this period (fig. 21). The most active part of the spine migrated ~140 m N. 75° W. during the 41 days at an average rate of 3.4 m/d. Overall the most active part of the spine subsided a net ~40 m, but this value ignores vertical growth—active disintegration removed tens of meters from the apex of spine 6. The center of most active extrusion moved westward away from the original (October 4, 2004) vent area

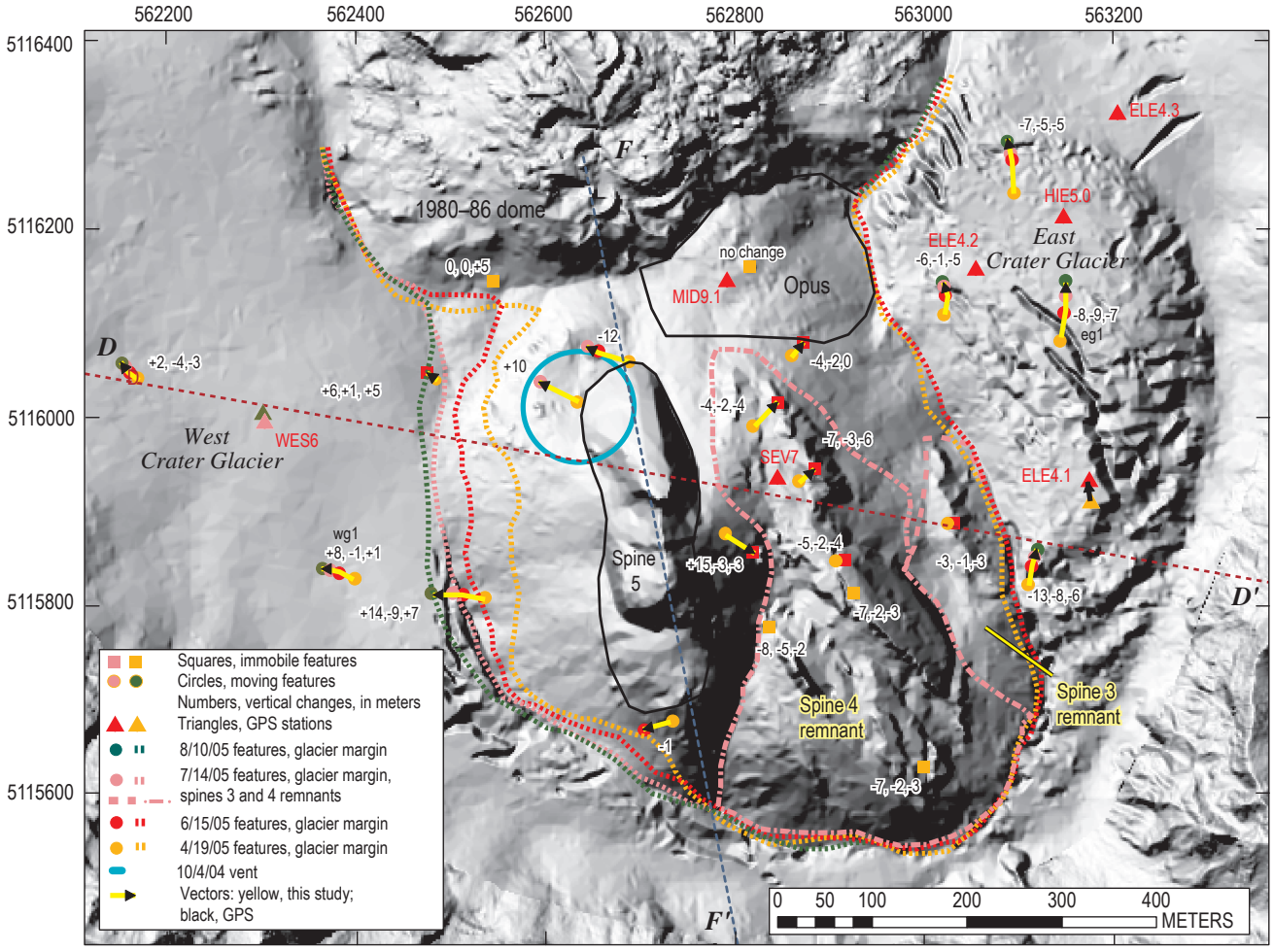

Figure 19. Deformation vectors for the period from April 19 to August 10, 2005, shown on DEM of July 14, 2005. Squares and dots indicate features tracked for dates identified by color in key. These colored symbols delimit deformation vectors of each of the three time intervals between relocation of features. Numbers are vertical components of vectors, in meters, for each interval. Underscores indicate no data for that interval. Dotted lines indicate dome-glacier margins for dates indicated by color in key. Line ***F–F´*** is trace of cross section shown in figure 18; line ***D–D´*** is trace of cross section shown in part in figure 22.

Table 3. Timing, style, and direction of mass-wasting events from spine 5 at Mount St. Helens, Washington, July 19–31, 2005.

[Timing and style of phenomena are inferred from time-lapse video (Iverson and others, 2006).]

Interval during which event occurred	Phenomenon	Direction
July 18–19	Avalanche	East
July 19–20	Avalanche	West
July 20–21	Avalanche	West from near apex of smooth slab
July 22–23	Avalanche	West
July 23–25	Slump	West
July 26–27	Avalanche	East
July 27–29	Slump	West from rubbly area of south part of spine
July 28–29	Avalanche	East
July 30–31	Avalanche	West

(fig. 21). Along an arc west to southwest of this new vent, the glacier-spine 6 contact receded 60–90 m westward at an average rate of 1.5–2.2 m/d (figs. 20–22).

Spine 5 Subsidence and Deformation of Surrounding Areas during August–September 2005

All parts of spine 5 translated westward and subsided as spine 6 moved away and removed its westward buttress (figs. 21, 22). Areas near spine 6 experienced maximum displacements of 40–60 m to the west and subsided by as much as 65 m. Areas close to the crest of spine 5 dropped by as much as 50 m while translating ~20 m westward. Such a pattern implies normal faulting along a northerly strike with westward dip as steep as 70°. The principal fault surface appears to coincide with a subsurface boundary sloping steeply to the west and demarcated by the contact between the subsurface remnants of spines 4 and 5 (fig. 22). This boundary could have formed a weak surface that was susceptible to subsequent subsidence. Features on spine 5 farther west of the fault trace translated more and subsided less than those near it, a pattern that implies rotational motion along a flattening fault (fig. 21). We infer that the fault is listric, dipping steeply westward along its near-surface trace and flattening as it extends deeper to the west (fig. 22).

The perspective provided by south-rim time-lapse photography (Poland and others, this volume, chap. 11) suggests that southwestern parts of spine 5 and southeastern parts of spine 6 subsided and migrated westward in tandem. Spine 5, near its eastern margin, subsided very little, apparently because the underlying spine 4–5 contact dipped gently compared to the steeper contact to the west. The most significant translation had occurred by September 20, but some areas continued to subside through October. Subsidence of spine 5, coupled with westward extension of spine 6, resulted in formation of a sag between spines 5 and 6 (figs. 21, 22).

To the east, Opus, spine 3, and spine 4 were relatively immobile, moving less than 4 m. In August and September, the GPS station SEV7, situated on spine 4 about 30 m to the east of spine 5, translated 2 m westward and subsided 3 m as the spine 5 buttress gave way. Motion on other parts of Opus, spine 3, and spine 4 was too small to be detectable (fig. 21).

While west Crater Glacier accelerated westward to northwestward and thickened, east Crater Glacier continued to flow passively northward (fig. 21). Between August 10 and October 24, traceable features on the west glacier moved west by 100–120 m and rose 20–35 m in response to the bulldozing caused by spine 6 advance (fig. 22). Ensuing crevasses radiated westward along the principal strain axis. Three GPS stations were located on west Crater Glacier for various time intervals (Walder and others, this volume, chap. 13). An example, WES6, originally about 150 m west of the dome, moved 50 m N. 51 W. and rose 13 m during August 10–September 14. In contrast, its motion in the 27 days before August 10 was only 10 m northwest and 1 m up. Advance of spine 6 pushed west Crater Glacier westward and heaped it as high as 30 m above its previous surface.

Westward Extrusion and Overthrusting of Spine 7: October 9, 2005–April 2006

Extrusion of spine 7 began in mid-October with subsurface spine intrusion centered east of spine 6 and near the trace of the October 4, 2004, vent. Subsurface intrusion gave way by November to spine extrusion, which continued through April 2006 (table 1, fig. 21*B*).

An increase in high-frequency earthquakes, beginning on October 9, 2005, marked the beginning of spine 7 growth (Moran and others, this volume, chap. 2). Fuming and heating of the surface area above the October 2004 vent observed in thermal images of October 11, 2005, revealed the first surface manifestation of the new intrusion (fig. 3). Time-lapse photographs from a camera on the south crater rim (Poland and others, this volume, chap. 11) showed general bulging of a rubbly area between spines 5 and 6 by October 13.

Uplift and westward motion that became increasingly evident between October 14 and 21 indicated extrusion of spine 7. From its origin in the depression between spines 5 and 6, spine 7 pushed upward and outward to the west, steepening on the east as it grew and overthrusting spine 6 to the west (fig. 20). By mid-November, a broken-up slabby spine had begun to emerge from the rubble-strewn slopes of the bulge. By mid-December, this slab of rock had become more coherent and prominent. As it continued to grow, the slab steepened eastward progressively, attaining a slope of 50° by April 2006. The extruding slab also pushed spine 6 and part of spine 7 across a sector extending from southwest

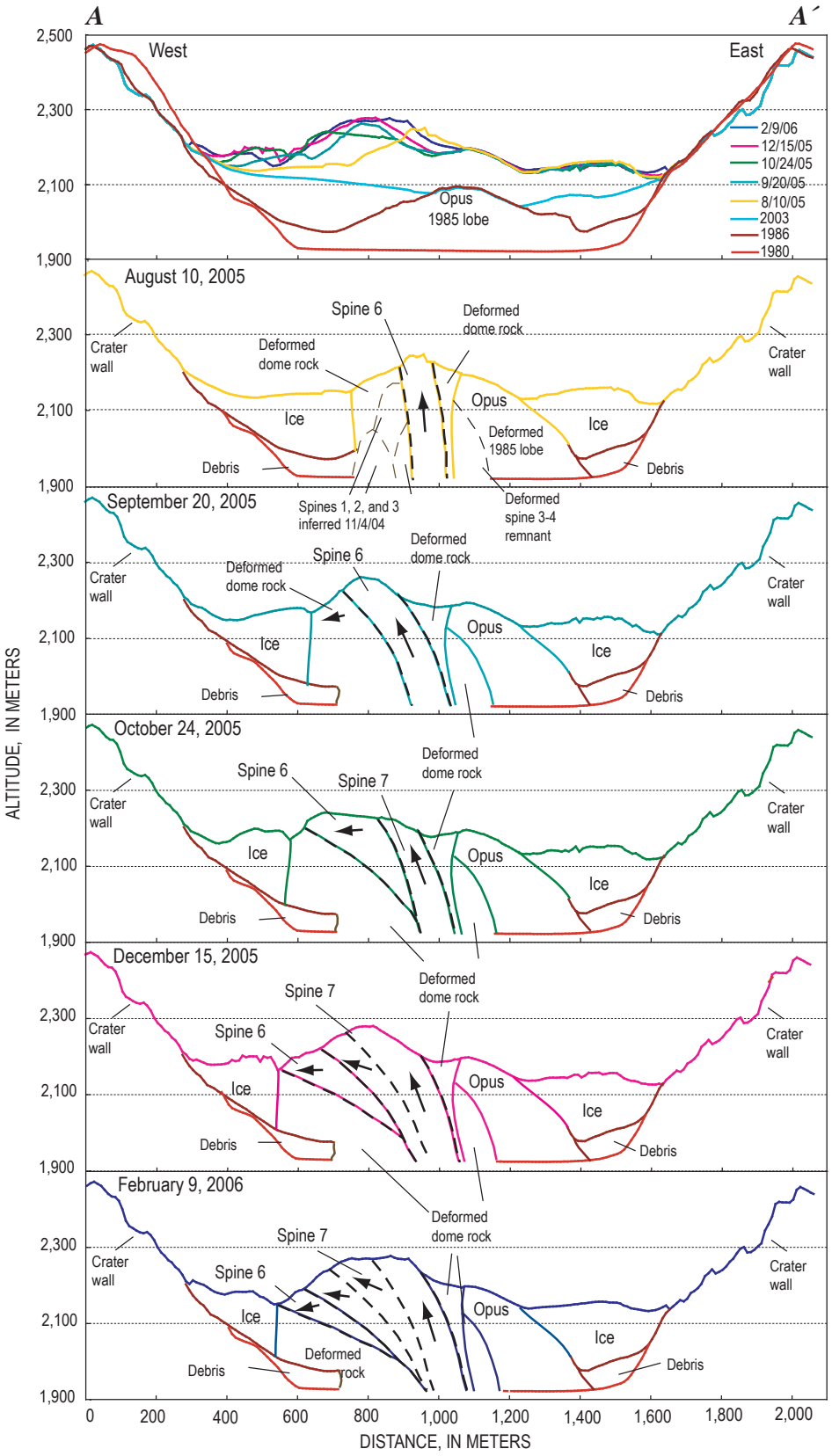

Figure 20. East-west cross section *A*–*A´* (location shown in figures 1 and 21) illustrating extrusion and thrusting of spines 6 and 7. Top panel shows known profiles for dates given, and the other panels illustrate geologic interpretations at labeled times. Dashed lines indicate thrust faults.

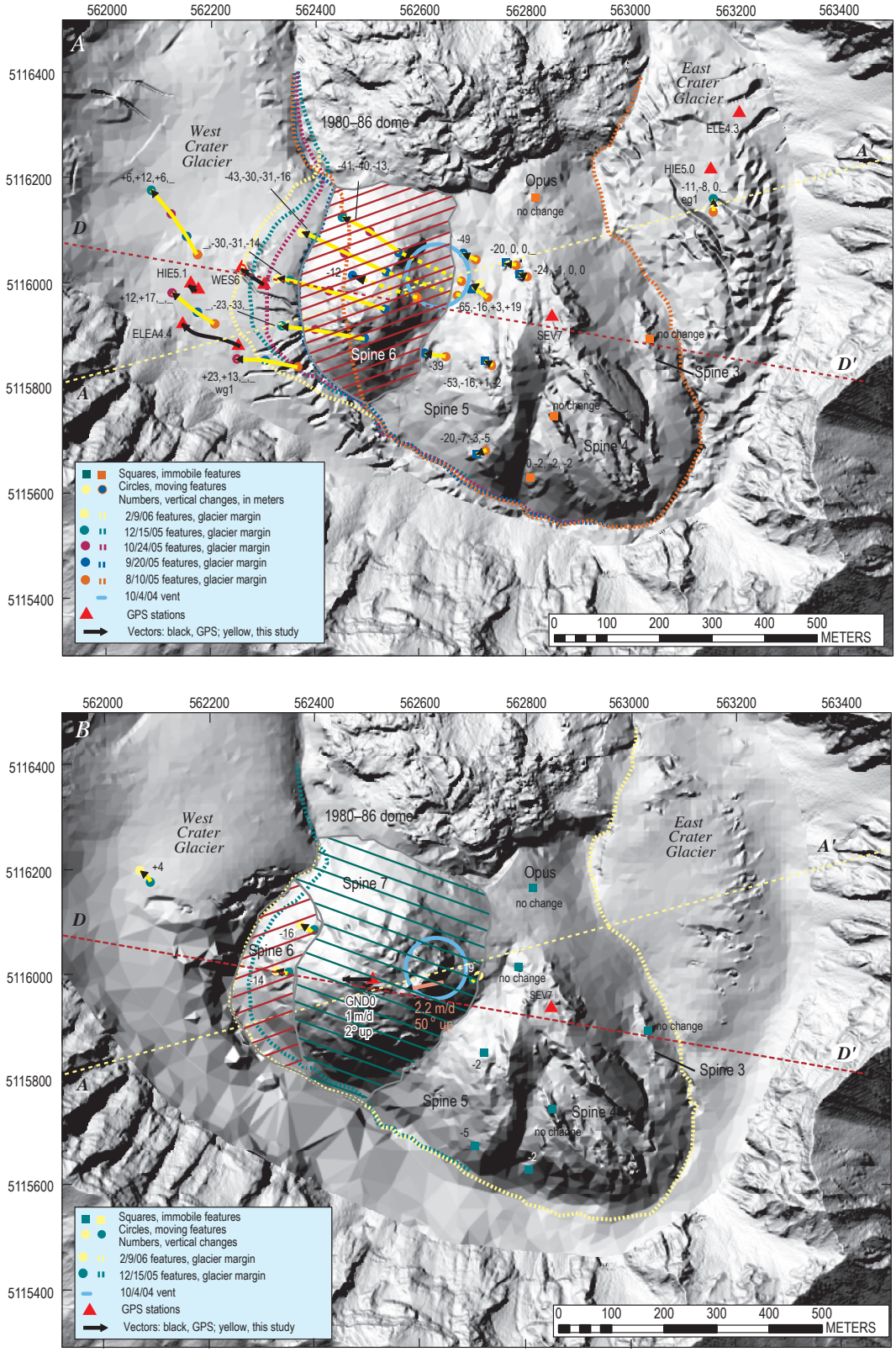

Figure 21. Deformation vectors for the period from August 10, 2005, to February 9, 2006, shown on DEMs. Squares and dots indicate features tracked for dates identified by color in key. These colored symbols delimit deformation vectors of each of the time intervals between relocation of features. Numbers are vertical components of vectors, in meters, for each interval; underscores indicate no data for interval. Red-lined pattern indicates spine 6; green-lined pattern indicates spine 7. Dotted lines indicate dome-glacier margins for dates indicated by color in key. Lines ***A–A´*** and ***D–D´*** are traces of cross sections shown in figures 20 and 22. *A*, September 20, 2005. *B*, February 9, 2006.

to northwest radially away from its source (fig. 21). Rock debris continually avalanching from the west face of spine 7 formed hot talus slopes on this side. As the spine grew through November, its rubbly western slope began to bury adjacent sections of spine 6.

Spine 7 formed a distinct entity between, and overlapping, spines 5 and spine 6. By October 24, the spine had been extruding for 10 days, and we estimate its volume as about a third of the total volume erupted since September 20, or ~1×10^6 m^3. Between October 24, 2005, and February 9, 2006, time-averaged magma flux gradually diminished (table 2).

As spine 7 moved westward and thrust over spine 6, it grew higher and steeper, and its solid eastern buttress became a progressively more prominent, finlike structure (figs. 23*A*, 23*B*). Cracks penetrated the gouge coat in distinctive patterns and moved upward and westward along with the fin (fig. 23*A*). From examination of photographs, spine 7 was ascending westward at an angle of 50° at a rate of ~2 m/d in early April (fig. 23*A*). At the same time, GPS station GND0, ~100 m west of the fin, was only moving 1 m/d horizontally westward (fig. 23*C*). This discrepancy in rate of deformation within spine 7, with steeper, faster displacement near source and slower subhorizontal displacement to the west, implies internal shearing (figs. 20, 23*D*).

Deformation during Spine 7 Extrusion: October 9, 2005–April 2006

All parts of spine 6 translated and subsided as spine 7 pushed it westward (figs. 21, 22). Features on spine 6 were subject to substantial but gradually diminishing deformation from October 9, 2005, to February 9, 2006, with maximum total displacement over this period in excess of 200 m to the west and subsidence as much as 80 m (table 4). Toward the end of this period, spine 7 moved about 1 m/d westward with no subsidence, while adjacent spine 6 moved at half that rate and subsided (table 4). Such a pattern implies shearing between spines 6 and 7 (figs. 20, 23*D*).

West Crater Glacier continued to move westward to northwestward (fig. 21). Between October and December, a single traceable feature on the west glacier moved northwest 60 m and rose 6 m in response to continuing spine impingement (fig. 21). Motion of GPS station ELE4.4, positioned farther south and closer to spine 7, slowed after October 24. It moved 1.6 m/d N. 68° W. and rose 19 m in the 34 days before October 24, whereas it moved 1.1 m/d N. 55° W. and rose 3 m in the 15 days after that date (LaHusen and others, this volume, chap. 16). Farther north, the glacier accelerated to the north in response

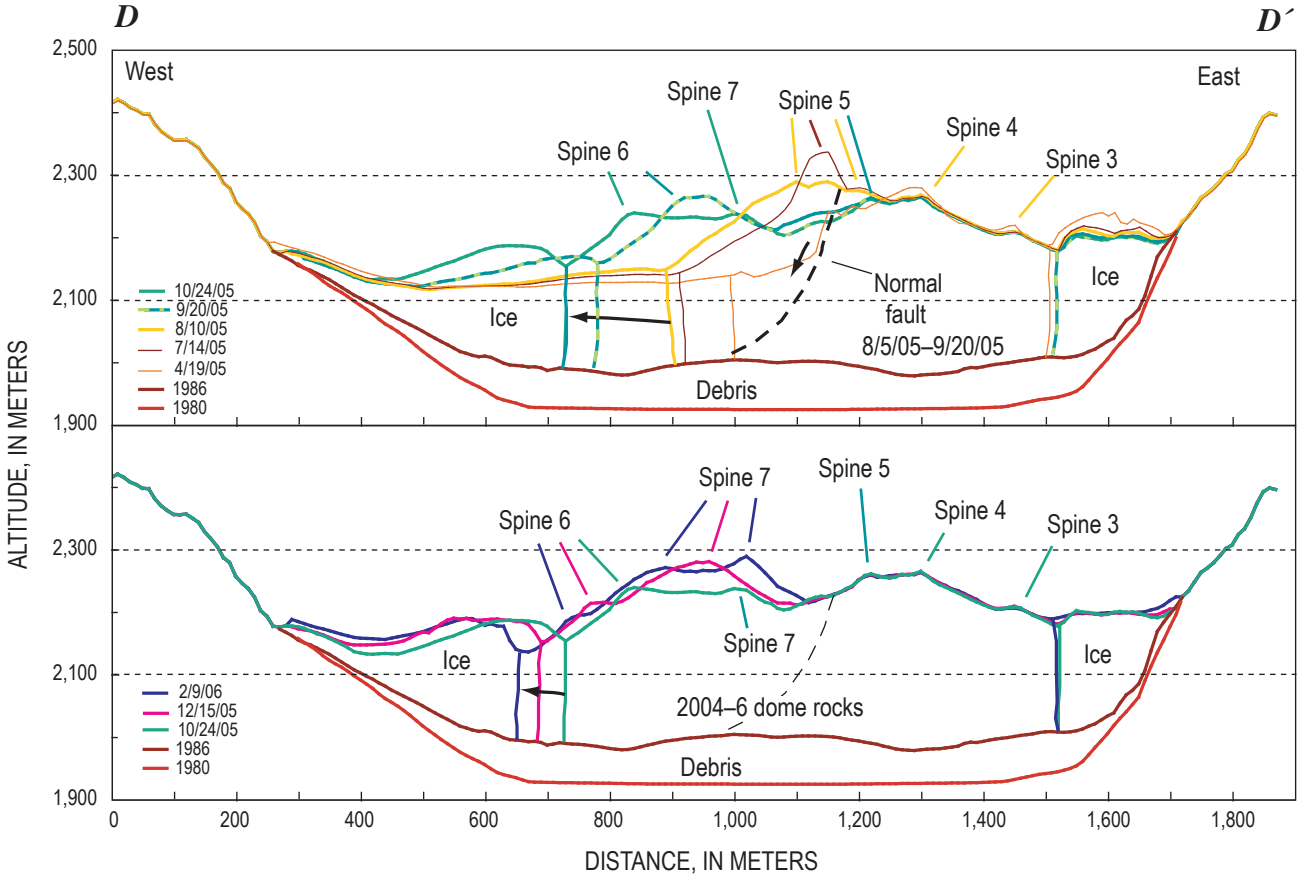

Figure 22. East-west cross section *D*–*D´* (location shown in figures 1 and 21) illustrating extrusion and thrusting of spines 6 and 7. Panels illustrate geologic interpretations at labeled times. Dashed line indicates inferred normal fault, which is located at steep west-dipping trace of spine 4 on April 19, 2005, surface.

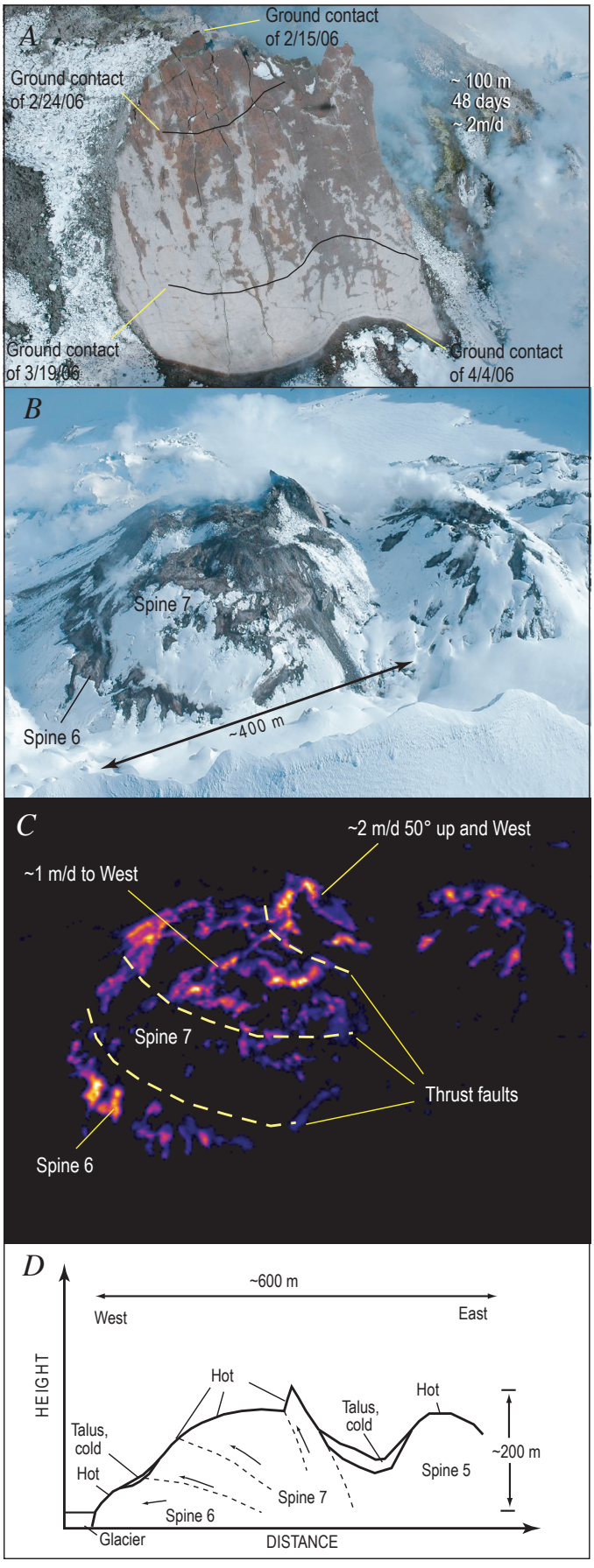

to the 30–40 m of excess elevation it had gained through uplift between August 2005 and February 2006 (fig. 21*A*).

Discussion

We consider here factors that influenced dome growth during the 2004–6 eruption. Potential near-surface controls on spine growth during the 2004–6 eruption include thick glacial ice, initial vent position and geometry, the 1986 topographic surface, and backpressure caused by spines pushing through and thrusting over debris from previous spines. We also consider the effects of dome growth on Crater Glacier. Lastly, we compare the 2004–6 Mount St. Helens dome-building eruption with well-documented historical examples at other volcanoes.

Effect of Glacier on Spine Growth

Glacier ice as thick as 150 m has apparently had little effect on the extrusion of the dome or on the growth of various spines, except to conceal substantial parts of them and to prevent shedding of disintegrating dome talus beneath the level of the glacier surface. As discussed in the introductory section, we infer that dome-glacier contacts have remained steep. Near-vertical contacts are consistent with ice-hot rock marginal boundaries observed at other locations. Examples include tuyas in British Columbia, Canada (Mathews, 1947), and ice-lava contacts at Mount Rainier (Lescinsky and Sisson, 1998). Glacial ice appeared not to impede spine growth significantly. Spines 2–4 grew recumbently to the south, pushing glacial ice aside as they progressed. Westward extension of spines 6 and 7 also pushed through thick glacial ice. The bed of the glacier was permeable enough that meltwater drained away without interacting with hot dome rock (Walder and others, this volume, chap. 13), except possibly during six brief phreatic explosions (Moran and others, this volume, chap. 6).

Vent Dimension and Location and Influence of 1980–86 Dome on Spine Growth

The depression from which the initial phreatic eruptions originated and from which the initial spine extruded was located at the west end of Opus and had an approximate

Figure 23. Photographs, thermal infrared image, and cross section of the Mount St. Helens crater on April 4, 2006. *A*, View looking west at 100-m fin showing previous ground-spine contacts. *B*, View looking northeast at spines 6 and 7. *C*, Thermal infrared image of view in *B*, looking northeast and showing thrust faults and relative motions. *D*, Schematic east-west cross section of growing spine 7, slowing spine 6, and stagnant spine 5. Orientation is roughly along line shown in *B* but extends east to spine 5. USGS photos by J.W. Vallance; thermal image by M. Logan.

Table 4. Timing, bearing, magnitude, and rate of deformation of one feature located on spine 6 at Mount St. Helens, Washington, between September 20, 2005, and February 9, 2006.

[Timing, direction, and magnitude of deformation are inferred from DEMs on given dates (Schilling and others, this volume, chap. 8).]

Interval	9/20/2005–10/24/2005	10/24/2005–12/15/2005	12/15/2005–2/9/2006
Days elapsed	34	52	56
Bearing	N80°W	N80°W	N85°W
Horizontal translation			
Displacement (m)	110	75	35
Rate (m/d)	3.2	1.4	0.6
Subsidence			
Displacement (m)	30	31	14
Rate (m/d)	0.9	0.6	0.3

diameter of 120 m (figs. 5, 12). Superimposing this vent location on the 1986 topographic surface (fig. 12) reveals that the initial vent was located on ice over the south-facing slope of the 1980–86 dome, in particular over the 1985 fault-formed ridge known as Opus. Just before the 2004 eruption, relief from the high point on Opus to the moat's floor beneath the glacier was ~130 m, and south-facing slopes were as steep as 40° under the trace of the vent (fig. 12).

The initial location of the 2004 vent, on steep south slopes of Opus, themselves buried beneath the glacier, clearly influenced the propensity of stiff spine extrusions to move southward. Several studies suggest that the magma ascending the conduit had largely solidified within a kilometer of the surface (Dzurisin and others, 2005; Iverson and others, 2006; and in this volume: Moran and others, chap. 2; Cashman and others, chap. 19; Pallister and others, chap. 30). We infer that, as the magma neared the surface in September 2004, the pre-existent solid plug of 1980–86 dome rock deflected the rising mass southward so that, near the surface, it tilted southward.

We tracked successive extrusion points at the surface by centering circles on the center of each spine origin with appropriate diameters equal to spine width (fig. 24). As the extrusion transitioned from the initial spine formation of phase 2 to well-developed whaleback-style spines of phase 3, the surface trace of the vent moved south and east. These trends continued until spine 3 began its breakup in December 2004. During the spine 3–4 transition this sense of movement reversed. However, during growth of spine 4, the southward and eastward motion recommenced. With extrusion of spine 5 during phase 4, the vent gradually moved westward back toward its original location. This motion increased with phase 5 extrusion of spine 6. With the onset of spine 7 extrusion, the surface manifestation of the vent returned to and remained within 20 m of its original position. Between vent clearing of phase 1 and initial whaleback-style intrusion of phase 3, the surface trace of the vent rapidly rose 130 m because an increasingly thick pile of lava built beneath it. Elevation of the vent trace increased slowly through extrusion of spines 4 and 5 during phases 3 and 4, then diminished with extension of spine 6 as phase 5 commenced. Extrusion of spine 7 rebuilt the lava pile beneath the vent, so that by early 2006 its trace was 200 m higher than its altitude in October 2004, though it was back to its original position in plan view.

Superimposing the position of the original vent and the seven spines on the 1986 surface suggests that the vent or conduit need not have shifted substantially at the depth of the initial erup-

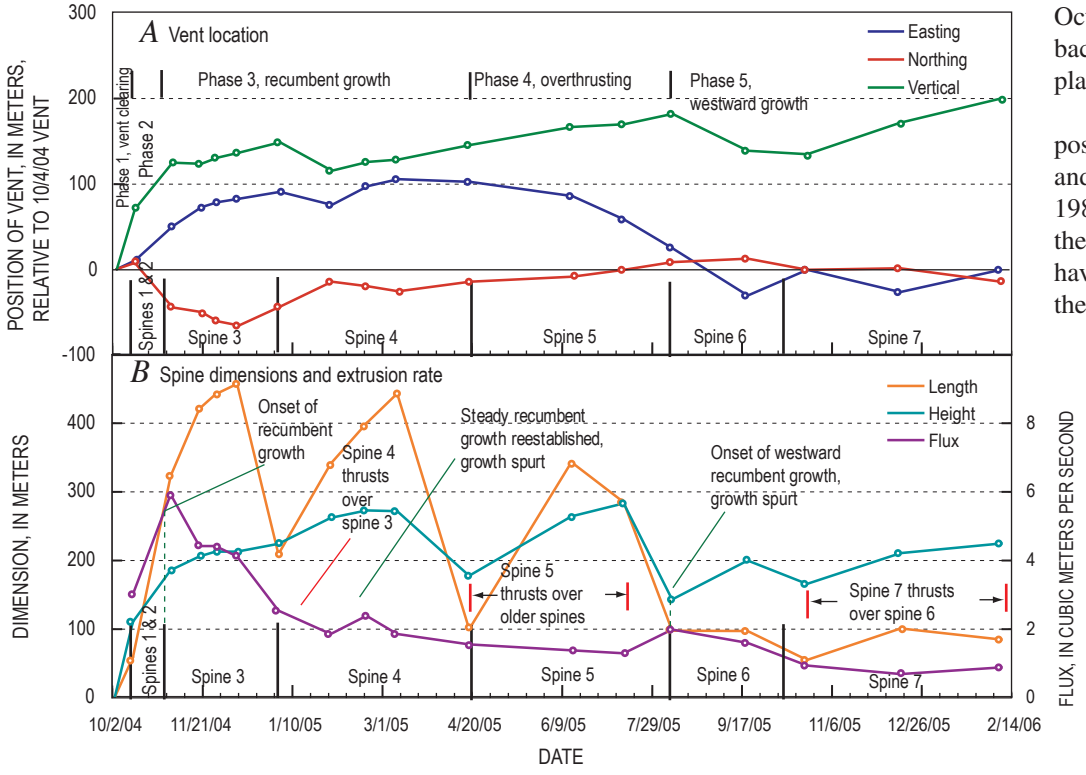

Figure 24. Plots of positions of vent, dimensions of spines, and extrusion flux versus time. *A*, Center of vent located in plan. *B*, Length of active spine, height of active spine, and lava discharge.

tion surface (figs. 12, 25). Geometry of the vent area permits origin of spines 1 through 4 from approximately the same initial vent location at the depth of the 1986 surface (fig. 12). Initially, extrusion of spines 1 and 2 covered the area directly above and to the south of the vent so that, as spine 3 began to grow upward and southward, previous spine and welt rubble diverted it eastward (fig. 12*A*). Additional dome rock and debris emplaced during spine 3 growth diverted spine 4 farther eastward. Eventually, so much dome rock had been pushed to the east that fragmented dome rock abutted the steep part of the east crater wall, and continuing spine extrusion could no longer push it aside. The subsequent spine (spine 5) therefore thrust instead over the older spines in a more southerly direction. When spine debris above the vent eventually built high enough, spine growth could extend westward across the rock debris of spines 1 and 2 (fig. 25). An inclined conduit did not simply increase in altitude; rather it shifted tens of meters southward, then south-southeastward, and finally southwestward as it evolved and grew higher (fig. 25). We suggest that vent geometry is such that spine extrusion throughout the eruption could have passed through approximately the same vent location at a depth near that of the 1986 surface and that migration of the vent's surface expression resulted from diversion by remnants of previous spines.

Influence of 1980–86 Surface on Spine Growth

Topography inherited from the 1980–86 eruption controlled growth patterns of the laterally propagating spines (figs. 12, 25). We superimposed the outlines of actively growing spines on topographic features concealed by glacier ice to assess their influence on growth patterns. Generally, we found that the 1986 topographic surface controlled recumbent

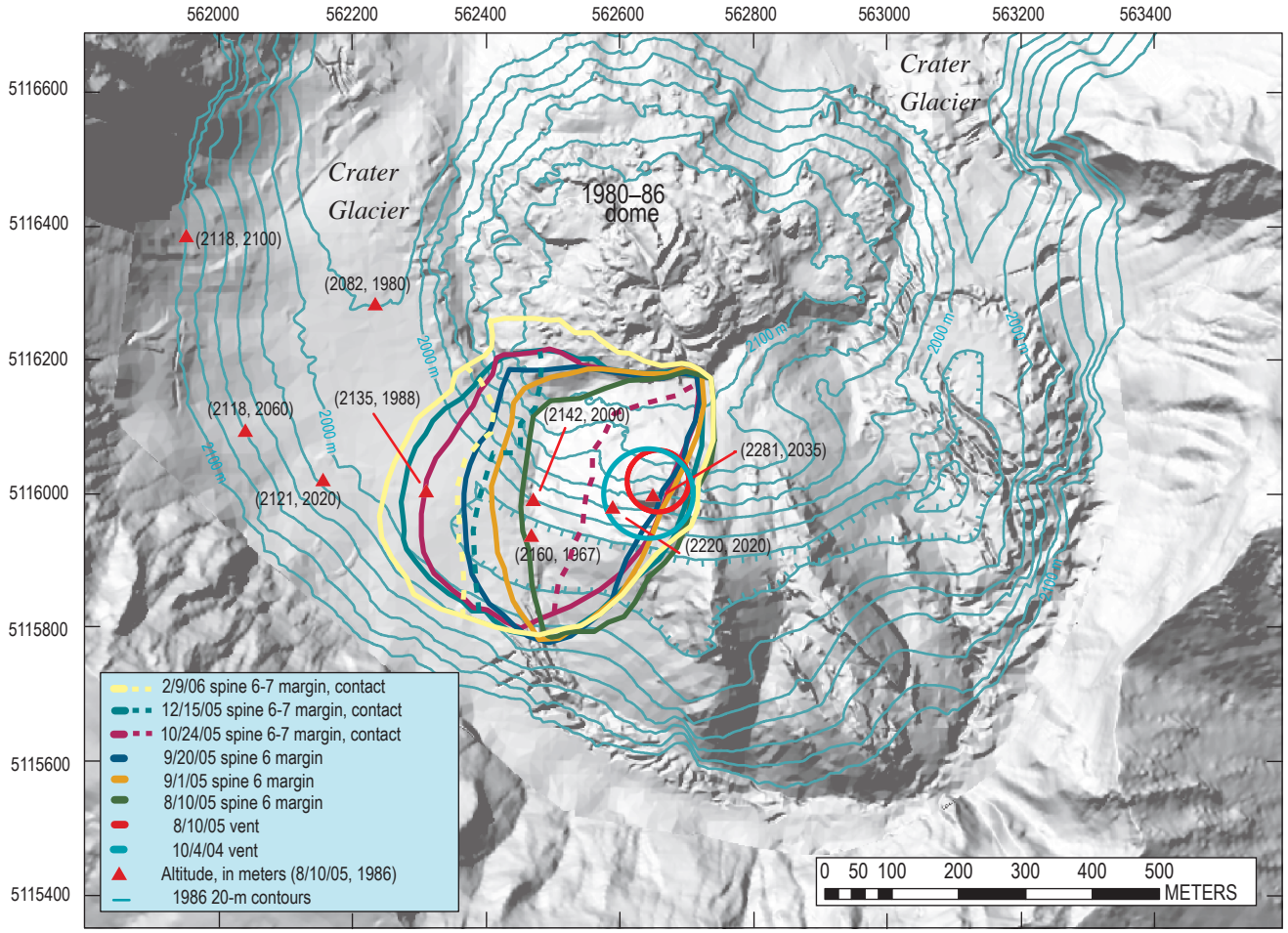

Figure 25. August 10, 2005, DEM showing outlines of spines 6 and 7 and their dome-glacier margins (solid lines) on dates indicated by colors in key. Dashed lines indicate contacts between spines 6 and 7 for appropriate dates indicated by colors in key. Select 20-m contours from 1986 DEM illustrate how composite spines 6 and 7 have migrated along a low topographic trough to west. Comparisons of altitudes on August 10, 2005, with those of 1986 are given for localities marked by red triangles.

growth directions, the rotation of spines, and how spines ultimately fragmented, but the ultimate barrier to continued lateral growth proved to be the walls of the 1980 crater modified by talus at their base and modified slightly by subsequent erosion.

After spine 1 grew, subsequent spines grew southward, in part because the crater floor sloped to the south. Spine 2 advanced due south until it encountered the steep opposing slopes of the south crater wall. Because spine 2 was then positioned directly south of the vent, the prominent whaleback of spine 3 that followed was forced slightly eastward as it advanced. Spine 3 extended across a broad basin to the south-southeast that was filled with glacial ice and welt debris. It then encountered the crater wall at an oblique angle (20°–30° from perpendicular) in mid-November 2004, and the influence of the wall deflected the snout of the spine eastward (fig. 12*A*). Once spine 4 had pushed remnants of its predecessor aside, it too progressed south-southeastward, encountered the 1980 crater wall at an oblique angle, and then rotated eastward (figs. 7, 15). A lack of such rotation before the spine arrived at buttressing slopes and fairly rapid rotation subsequently is strong evidence in support of the oblique-incidence hypothesis of rotation.

Both spines 3 and 4 began to fracture, crumble, and ultimately decouple from the source as a result of resistance to motion when they impinged on the crater wall. Spine 3 began to slow and break apart as it pushed against the crater walls in mid-November 2004. Two voluminous blocks and numerous smaller ones separated from the spine before it finally broke and fractured near its source on or about December 18, 2004. Thereafter, lava near the source slowly decoupled from remnants to the south to form spine 4. A similar sequence occurred when spine 4 itself met the wall, fractured at its root, and decoupled in April 2005 to form spine 5. In the April case, however, debris had filled the area east as far as the east crater wall, and thus spine 5 grew by southward thrusting across previous spine remnants.

Rotational motion of spines 3 and 4 in turn caused rotation of previously emplaced dome debris, welt debris, and glacier ice to the east. Southward spine propagation and oblique impingement on the crater wall apparently caused the rotation, and the less resistant expanse of glacial ice to the east permitted the rotation to proceed in that direction. By mid-April, when spine 4 and associated debris outboard of it had encountered steep slopes to the southeast as well as to the south, the counterclockwise rotation (map view) of phase 3 ceased (fig. 12*B*). Also at this time, the sense of rotation reversed from counterclockwise to clockwise, with a pivot 300 m south of the vent (fig. 19). The south end of spine 4 became fixed and the north end began to move east because the only available space east of the 2004–5 dome was located directly east of the vent (labeled "mid-April space east of vent" in fig. 12); no such space was available to the southeast.

Spine 5 thrust over remnants of spines 3 and 4 at steepening angles (fig. 18) until its perch atop those remnants became unstable. Failure along a north-south zone of weakness dipping steeply to the west allowed motion to resume along a 1986 topographic low, as spine 5 slumped together with westward growth of spine 6 (fig. 22). From April to August 2005, preexisting topography had little effect on spine growth because the active spine, 5, was shearing over previous spines rather than following old topographic surfaces. With extrusion of spine 6, westward spine migration pushed previous spine remnants and affiliated rubble westward into the topographic trough defined by the 1980–86 dome and the crater wall (fig. 25). This moat-like topography channeled growth of spine 6 such that it barely impinged on steeper slopes to the south and rode up on topographically high areas of the 1980–86 dome only near the vent, where some northward spreading and rockfall was underway. Similarly, as spine 7 thrust west into parts of spine 6, it pushed the earlier spine westward along the same topographic trough. As the volume of material to the west built, the rate of westward recession of the dome-glacier boundary slowed, and slabs of spine 7 extruded at steepening angles.

Extrinsic Control of Spine Growth Rate

An intrinsic exponential decline in overall extrusion rate (fig. 24) that probably derives from declining magma supply and pressurization is apparent during the course of the present eruption. Overprinted on this decline are several apparent increases in magma flux that may have been controlled extrinsically (spurts in fig. 24*B*). Time-averaged effusion rates commonly rise rapidly to a peak before falling slowly, resulting in an exponential decrease in eruption rate and declining growth (Harris and others, 2000). Such trends can be explained by the tapping of enclosed and pressurized magma chambers (Wadge, 1981; Harris and others, 2000). Extrinsic factors, such as changes in load, are thought to cause variation in effusion rates (Harris and others, 2003).

We hypothesized that increases or decreases in load near the surface might reduce or enhance extrusion rates, owing to increases and decreases in the mass displaced (fig. 24*B*). We plotted both relative height and length of active spines against time to test this idea. However, our results show no obvious correlation between spine length or height and extrusion rate (fig. 24*B*). A comparison between extrusion rate and style of extrusion suggests a possible correlation. Extrusion rate was greater when steady recumbent growth was established and smaller when active spines were thrusting upward at significant angles (fig. 24*B*). Steady lateral extrusion of spine 3 in late October and early November 2004 corresponded to an initial increase in discharge, and renewed steady extrusion of spine 4 in February 2005 corresponded to a slight increase in extrusion rate. A transition from thrusting to westward migration and slumping correlates to a third localized peak from late July to September 2005. Periods of resistance to movement caused by thrusting of spines at increasing angles over previous remnants also correlate with periods of diminished extrusion rate (fig. 24*B*). We suggest that such growth conditions may have acted to resist extrusion, suppressing the flux by backpressure. Slumping events and vent reorganization eased backpressure and thus enhanced flux.

Impact of Dome Growth on the Crater Glacier

Whereas the glacier had little affect on dome growth, spine growth did have a profound impact on the Crater Glacier—slicing it in two, pushing it hundreds of meters first one way then another, doubling it in thickness, but not melting it. As the response of Crater Glacier is the detailed subject of another contribution to this volume (Walder and others, chap. 13), we merely summarize the impact of spine growth on the glacier from the perspective of surface deformation vectors, which allowed us to track certain glacier features throughout nearly the entire course of the eruption. During October and November 2004, subsurface deformation owing to spine extrusion caused the glacier surface to take on first the appearance of a migrating wave of fractured ice and rock, then, with surfacing of spine 3 through that material, the appearance of bow waves of fractured snow and ice both west and east of the whaleback form. Once spine 3 divided the glacier in December 2004, it and its successor, spine 4, began slewing to the east, rotating about their tails and plowing the ice of the east glacier into a 100-m-high berm by January 2005. The berm then sluiced northward through the gap between the 1980–86 dome and the crater wall between April 2005 and February 2006 (fig. 26). Growth of spines 6 and 7, plus subsidence of dome remnants into west Crater Glacier, created a similar response between August and December 2005 whereby the glacier was first pushed up and westward (fig. 26) and then began to flow through the gap between the 1980–86 dome and crater wall. Despite its mistreatment, the glacier has lost no more than about 10 percent of its volume to contact melting as of February 2006 (Walder and others, this volume, chap. 13). Apparently, gouge-coated spines and shrouds of cold debris have effectively insulated glacier ice from hot spine interiors.

Comparison with Other Dome-Building Eruptions

Several factors set the 2004–6 dome-building eruption of Mount St. Helens apart from that of other well-documented historical domes such as those of Mount St. Helens 1980–86, Montserrat 1995–98, Santiaguito 1922–2006, and Unzen 1990–96. These include extrusion of solid spines, a propensity to form recumbent spines, interaction with glacier ice, and topographic setting. Mont Pelée in 1903 produced a spine that grew vertically but otherwise resembled whalebacks at Mount St. Helens. However, perhaps the historical dome-building eruption most similar to that of Mount St. Helens 2004–6 was the 1944–45 extrusion of the Showa-Shinzan dome at Usu volcano in Japan.

Mount St. Helens' 1980–86 dome extrusion differed from the present extrusion in extrusion rate, morphology, and process of emplacement. Excepting a one-year endogenous phase, extrusion of the 1980–86 dome occurred in discrete episodes, 16 of which were preceded by periods of accelerating endogenous growth, followed by extrusion of a viscous lobe, and terminated with periods of subsidence and lateral spreading (Swanson and Holcomb, 1990). In contrast, the present eruption has proceeded continuously with a general decline in discharge (fig. 24). Output of fresh dacite in the early phases of the present eruption occurred at a rate that is about one-half to one-third of rates measured during the 1980–86 episodes (Chadwick and others, 1988). The relentless growth during the 2004–6 eruption, however, has produced a total volume similar to that of the 1980–86 eruption in about one-fourth of the time.

Swanson and Holcomb (1990) document distinctive profiles for individual lobes emplaced during 1980–86, showing that lobes tended to adopt a characteristic slope (33°) and a characteristic height-to-diameter ratio (h/d) of about 0.32. The slope was approximately the angle of repose for coarse angular talus. In a more elaborate analysis, Iverson (1990) was able to model the characteristic slope in terms of a pressurized viscous magma enclosed by a brittle shell. Such a model is not applicable for spines of the present eruption because of the complicating influence of topographic barriers, glacial ice, and the subsolidus character of the magma, with the spines extruding in a near-solid state. Glacial ice within the crater has buttressed spines at slopes much greater than the angle of repose during the current eruption. Overall, the h/d ratio and slope for spines 3–7 ranged from 0.6 to 0.7 and from 50° to 60°, respectively. Those of initial spines were greater. Slopes higher than the angle of repose also reflect the massive and solid character of extruded spines. Such high h/d ratios are typical of upheaved domes and peléean spines (Blake, 1990).

Well-documented dome extrusion at Unzen, Japan, and Santiaguito, Guatemala, was continuous but varied in extru-

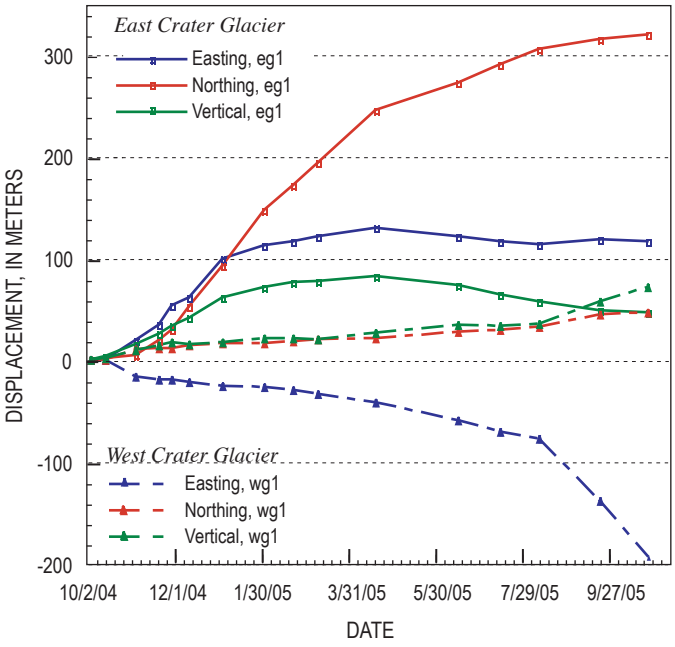

Figure 26. Displacement plots of a feature on east Crater Glacier (eg1 located at site a in fig. 2) and one on west Crater Glacier (wg1 located at site i in figs. 2*A*, 2*B*) versus time (both features are located at intervals in figs. 5, 7, 15, 19, 21).

sion rate and included both endogenous intrusion of viscous magma and extrusion of lava flows (Rose, 1980, 1987; Nakada and others, 1999; Harris and others, 2003). At Unzen, endogenous growth typified slow discharge, and exogenous growth typified more rapid discharge (Nakada and others, 1999). Over the course of the eruption, discharge slowed and endogenous growth increased proportionately (Nakada and others, 1999). Although Santiaguito has erupted continuously during 1922–2006, its growth has been episodic—waxing and waning over time scales of several years (Rose, 1987). In contrast to recent activity at Unzen, during Santiaguito's 84-year and ongoing eruption there has been a general tendency for the proportion of exogenous to endogenous growth to increase with time (Harris and others, 2003). Neither Unzen nor Santiaguito has shown the propensity to build solid-state spines at a low extrusion rate as observed during the current eruption at Mount St. Helens.

At Soufrière Hills volcano, Montserrat, Watts and others (2002) documented the morphology of lobes and spines, some of which superficially resemble those described here, and correlated them with extrusion rates. Watts and others (2002, their fig. 33) documented near-vertical spines, whaleback spines, and mega-spines that superficially resemble spines formed during the current eruption of Mount St. Helens, though similar forms here have had dimensions on a scale of hundreds of meters rather than tens of meters as observed at Soufrière Hills. With the exception of spine 1, the spines of the Mount St. Helens eruption have been larger and remained active longer than those at Soufrière Hills. Whaleback spines 3 and 4 grew during periods of months rather than days as at Montserrat, and spines 5 and 7 thrust over previous spines during periods of four months or more. The unusual, simultaneous slump and westward extrusion of spine 6 has no analogy to spine growth during any documented episode at Soufrière Hills volcano. More fluid morphologies, such as shear lobes and pancake lobes, did not occur during the Mount St. Helens 2004–6 eruption.

After its notorious eruption of 1902, Mont Pelée, Martinique, built a vertical spine that shares some characteristics with spines of the current Mount St. Helens eruption. That spine grew vertically to a height of more than 200 m in 1903 (Lacroix, 1904). Photographs (Lacroix, 1904) suggest that the spine was solid, had a gouge-coated and striated surface, and exposed a broken and massive surface on its opposite side. Like the Mount St. Helens spines, the Mont Pelée spine crumbled as it grew and eventually stagnated (Lacroix, 1904).

During its 1943–45 eruption, Showa-Shinzan dome of Mount Usu uplifted an area of as much as 1.5×1.5 km as much as 140 m (Mimatsu, 1995), generating a deformed zone reminiscent of the welt. Extrusion followed the deformation, as a jagged solid spine punched through the older roof rocks. As described by Mimatsu (1995), within nine days of initial unrest in December 1943, an area west of Mount Usu began to experience uplifting, folding, and faulting. Uplift to the west was initially strongest, after which its locus migrated in stages, eastward back toward the volcano. By June 1944, uplift ranged from 10 to 40 m. From June to November 1944, an additional 100 m of deformation accompanied 17 phreatic or phreatomagmatic explosions (Mimatsu, 1995). Finally, at the end of November 1944, the first lava spine pushed through the deformed and cratered uplifted area. Dacite spines continued to grow until August 1945. The spines commonly had a jagged appearance (Mimatsu, 1995), unlike those at Mount St. Helens. Like those at Mount St. Helens since 2004, the spines were completely solid on extrusion and showed no tendency to flow. The spines all rose more or less vertically, and none were described as having appreciable lateral components of motion (Mimatsu, 1995).

One spine at Mount Usu, Kobu-yama or Bump Mountain, did have a form more analogous to those of the present eruption of Mount St. Helens. Mimatsu (1995) describes it as having a shape like the bottom of a boat, with a coating of pulverized rock or dirt and grooves or scratches parallel to the direction of extrusion. The powdery surface is probably analogous to the gouge-coated surface of spines at Mount St. Helens. Mimatsu (1995) also described horizontal bands on Bump Mountain that were similar to the bands commonly observed on smooth surfaces of spines during 2004–6 at Mount St. Helens. The bands on Kobu-yama tended to form during periods of rain. Apparently, ash and debris that was constantly sloughing from the steep slopes of Kobu-yama stuck when the slopes were wetted. Furthermore, ash and debris accumulated at the base of the growing spine and stuck after heavy rains to form ledgelike bands that later rose as the spine extruded (Mimatsu, 1995). According to Mimatsu (1995), parts of these ledges were later shorn by falling debris.

Horizontal bands at Mount St. Helens are probably analogous, though not quite identical in origin, to those at Showa-Shinzan. Horizontal bands on spines at Mount St. Helens seem to have three forms, but all are plausibly related to moisture. The first, those most closely matching Mimatsu's (1995) description, are shelf-like accumulations of fine to coarse debris that stick to the smooth surfaces of spines at certain times, then rise with spine growth (fig. 27). At Mount St. Helens, these seem to correspond to stormy periods at the volcano. We suggest that, as at Showa-Shinzan, addition of water to mixtures of fine and coarse debris immediately adjacent to the hot base of the extruding spine creates a weak cement that subsequently dries against the hot spine. A variation on this process involves only the fine-grained ash at the base of the spine and requires relatively less moisture. These bands are much less prominent. Photographs show fine debris concentrated at the base of the spines (fig. 27). This material requires less water to form a cement and, hence less moisture is required to create horizontal bands of such fine ash. A third, most common but least prominent variety of band, appears to involve periodic darkening of the gouge-coated surface. No one has examined these closely enough to understand if there is an accumulation of material associated with them or if they are merely stains. We speculate that many of them are related to nightly dew. All of these bands are fragile and ephemeral.

Conclusions

Spine extrusion and associated near-vent deformation at Mount St. Helens during 2004–6 presented an opportunity to test and apply various methods to track, measure, and characterize the dynamics and morphologies of extrusion and nearby deformation during a dome-forming eruption. We summarize here our chief conclusions drawn from our data and the methodology that generated it.

Thermal infrared (TIR) surveys proved useful in differentiating events and structures that were cold from those that were hot. The TIR surveys showed that the explosions of October 1–5 were phreatic rather than magmatic. Imagery from TIR surveys also proved useful in identifying areas where spines were about to emerge. These were apparent as broad areas that warmed substantially in the days immediately prior to extrusion. Once spines began extruding, regular TIR surveys helped document their growth, character, and structures within them. Finally, TIR images helped monitoring crews identify places on

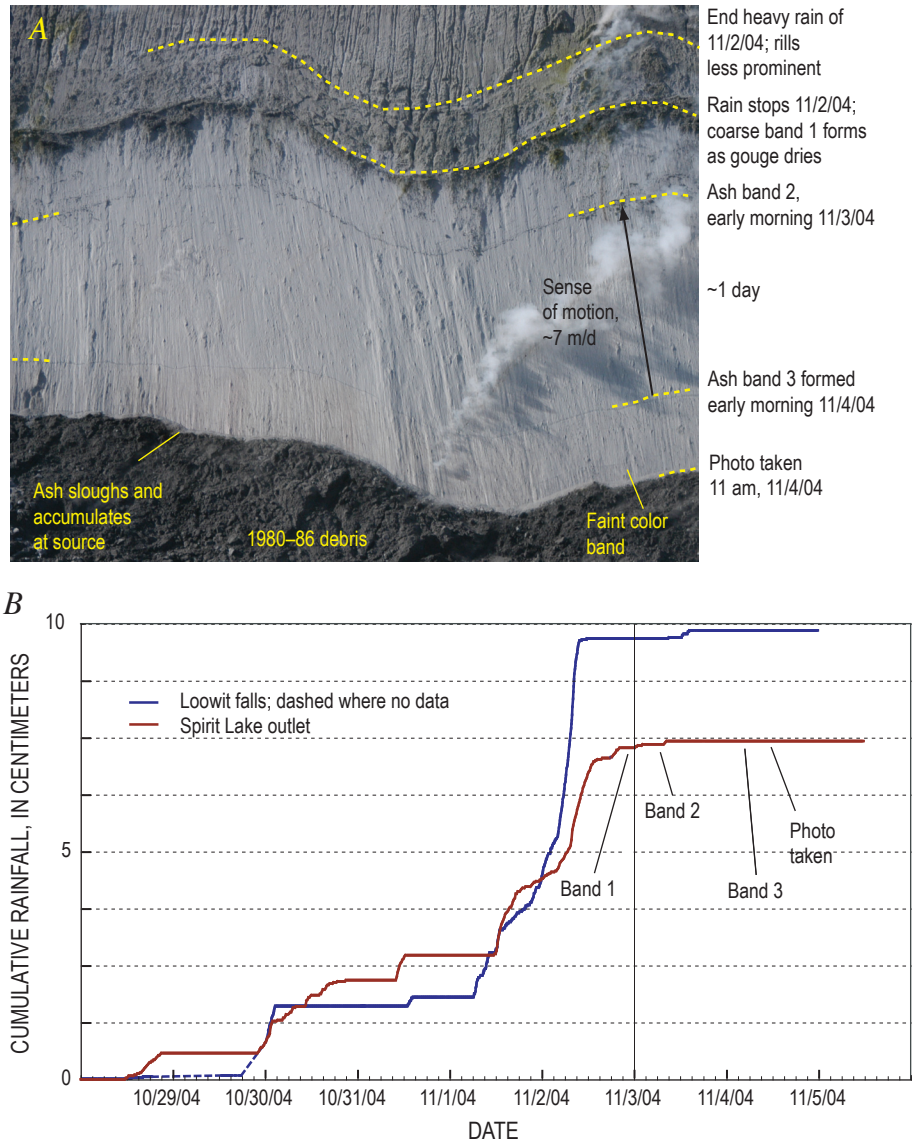

Figure 27. Photograph of emerging spine and plot of rainfall from October–November 2004. *A*, Close-up view of spine 3 east flank at 11 a.m. on November 4, 2004. Coarse band 1 consists of mixtures of ash and coarse lithic lapilli, more subtle bands 2 and 3 consist of ash, and very faint ones may be stains. Band formation is associated with increases in moisture. USGS photo by J.S. Pallister. *B*, Cumulative rainfall versus time from USGS gages at Loowit falls (crater mouth) and at Spirit Lake outlet and time of emergence of notable bands. Rainfall data courtesy of K. Spicer, USGS.

the dome cool enough to place GPS instruments and accelerometers (Schneider and others, this volume, chap. 17).

Data collected as part of this study along with others in this volume suggest solid-state extrusion throughout the current dome-building episode. TIR measurement of deep cracks and newly exposed surfaces give temperatures well below the solidus of the dacite magma being erupted. Morphology of the various spines exhibits no flowage features like lobes, coulees, or ramp structures. Indeed, yield strength has apparently been so high that the spines can stand at steep slopes until they crumble. New spines have typically formed as previous ones have undergone brittle failure and fracturing, then shearing off to form stagnant crumbling masses.

Tracking of features in successive sets of aerial photographs and DEMs has enabled the development of surface-deformation vector fields during 17 time intervals, which have varied in duration from 1 to 55 days. Each vector field gives a comprehensive spatial sense of deformation during that interval. Each also indicates the nature of advance or motion during the interval. Time-lapse photography and GPS instruments provided extra detail on much finer time scales for specific localities and localized fields of view, but the DEM tracking provided a valuable synoptic perspective.

Chief near-surface controls on spine extrusion during the 2004–6 eruption have been vent location, relict surfaces such as the 1980 crater structure and the 1980–86 dome, and spine remnants emplaced during previous phases of the present eruption—but not glacial ice. Ice as thick as 150 m has obscured eruptive processes, prevented formation of marginal angle-of-repose talus fans, and encouraged steep boundary slopes to the new dome complex through buttressing, but it has not significantly impeded spines pushing through it. Spines initially emerged at a location over the steep south-facing slope of the 1980–86 dome, which dictated their initial southward propagation. The glacier-filled space of the moat between the 1980 crater walls and the 1980–86 dome permitted southward propagation of spines 2 to 4 and funneled spines 6 and 7 westward. Spine 2 impinged on the opposing slope of the crater and stopped. In contrast, recumbent whaleback spines 3 and 4 impinged at oblique angles and rotated eastward before cracking up. Although the vent location at the 2004–6 surface shifted east and south more than 100 m before moving back to the west, its altitude increased ~200 m due to piling up of lava over the initial vent. The vent position relative to its initial trace at the 1986 surface need not have moved substantially. Once spine remnants occupied all available open space to the south, new spines thrust over previous remnants. Resistance to extrusion during intense periods of thrusting may have slowed extrusion rates because of backpressure effects during certain time intervals.

Although Crater Glacier had minimal influence on the growing spines, spine growth affected the glacier dramatically, initially dividing it into two arms and then bulldozing it hundreds of meters first east (east arm), then west (west arm), while heaping it more than 100 m higher than its original altitude.

The 2004–6 eruption has thus far differed from other well-documented historical eruptions in its solid-state character, its recumbent growth style, and its interaction with the glacier. On the basis of historical records, most domes grow endogenously; exogenously to produce thick units with a high aspect ratio and, sometimes, longer lava flows; or a combination of both (Blake, 1990). Peléean spines like those at Mont Pelée or Soufrière Hills are similar to those of the current eruption, but the 1943–45 eruption of Mount Usu provides the closest historical analogue. Perhaps the most similar of historically documented domes are those sometimes referred to as upheaved plugs (Blake, 1990). Such plugs appear to push up bodily like pistons and, when they reach the surface, have sufficient strength not to deform or spread outward but instead ascend vertically. Mimatsu (1995) beautifully documents the evolution of one such upheaval dome from 1943 to 1945 at Mount Usu in Japan. The intriguing variations in pluglike dome construction and evolution at Mount St. Helens since 2004, not previously well documented, have been recumbent growth and interaction with an unusual combination of topographic constraints and glacial ice.

Acknowledgments

We thank Andy Harris and Michelle Coombs for careful reviews of this manuscript. Andy's very detailed comments, in particular, greatly improved the paper. Cascades Volcano Observatory staff were generous with their time, their ideas, and their data.

References Cited

Ball, M., and Pinkerton, H., 2006, Factors affecting the accuracy of thermal imaging cameras in volcanology: Journal of Geophysical Research, v. 111, no. B11, B11203, doi.10.1029/2005Jb003829, 14 p.

Blake, S., 1990, Viscoplastic models of lava domes, *in* Fink, J.H., ed., Lava flows and domes, emplacement mechanisms and hazard implications: Berlin, Springer-Verlag, International Association of Volcanology and Chemistry of the Earth's Interior, Proceedings in Volcanology 2, p. 89–126.

Cashman, K.V., Thornber, C.R., and Pallister, J.S., 2008, From dome to dust; shallow crystallization and fragmentation of conduit magma during the 2004–2006 dome extrusion of Mount St. Helens, Washington, chap. 19 *of* Sherrod, D.R., Scott, W.E., and Stauffer, P.H., eds., A volcano rekindled; the renewed eruption of Mount St. Helens, 2004–2006: U.S. Geological Survey Professional Paper 1750 (this volume).

Chadwick, W.W., Archuleta, R.J., and Swanson, D.A., 1988, The mechanics of ground deformation precursory to dome-

building extrusions at Mount St. Helens 1981–1982: Journal of Geophysical Research, v. 93, no. B5, p. 4351–4366, doi:10.1029/88JB01345.

Dzurisin, D., Vallance, J.W., Gerlach, T.M., Moran, S.C., and Malone, S.D., 2005, Mount St. Helens reawakens: Eos (American Geophysical Union Transactions), v. 86, no. 3, p. 25, 29.

Dzurisin, D., Lisowski, M., Poland, M.P., Sherrod, D.R., and LaHusen, R.G., 2008, Constraints and conundrums resulting from ground-deformation measurements made during the 2004–2005 dome-building eruption of Mount St. Helens, Washington, chap. 14 *of* Sherrod, D.R., Scott, W.E., and Stauffer, P.H., eds., A volcano rekindled; the renewed eruption of Mount St. Helens, 2004–2006: U.S. Geological Survey Professional Paper 1750 (this volume).

Gerlach, T.M., McGee, K.A., and Doukas, M.P., 2008, Emission rates of CO_2, SO_2, and H_2S, scrubbing, and preeruption excess volatiles at Mount St. Helens, 2004–2005, chap. 26 *of* Sherrod, D.R., Scott, W.E., and Stauffer, P.H., eds., A volcano rekindled; the renewed eruption of Mount St. Helens, 2004–2006: U.S. Geological Survey Professional Paper 1750 (this volume).

Harris, A.J.L., Murray, J.B., Aries, S.E., Davies, M.A., Flynn, L.P., Wooster, M.J., Wright, R., and Rothery, D.A., 2000, Effusion rate trends at Etna and Krafla and their implications for eruptive mechanisms: Journal of Volcanology and Geothermal Research, v. 102, p. 237–270.

Harris, A.J.L., Flynn, L.P., Matías, O., and Rose, W.I., 2002, The thermal stealth flows of Santiaguito dome, Guatemala: Implications for the cooling and emplacement of dacitic block-lava flows: Geological Society of America Bulletin, v. 114, no. 5, p. 533–546.

Harris, A.J.L., Rose, W.I., and Flynn, L.P., 2003, Temporal trends in lava dome extrusion at Santiaguito 1922–2000: Bulletin of Volcanology, v. 65, p. 77–89.

Harris, A.J.L., Flynn, L.P., Matías, O., Rose, W.I., and Cornejo, J., 2004, The evolution of an active lava flow field: an ETM+ perspective: Journal of Volcanology and Geothermal Research, v. 135, p. 147–168.

Harris, A.J.L., Dehn, J., Patrick, M.R., Calvari, S., Ripepe, M., and Lodato, L., 2005, Lava effusion rates from hand-held thermal infrared imagery; an example from the June 2003 effusive activity at Stromboli: Bulletin of Volcanology, v. 68, no. 2, p. 107–117.

Herriott, T.M., Sherrod, D.R., Pallister, J.S., and Vallance, J.W., 2008, Photogeologic maps of the 2004–2005 Mount St. Helens eruption, chap. 10 *of* Sherrod, D.R., Scott, W.E., and Stauffer, P.H., eds., A volcano rekindled; the renewed eruption of Mount St. Helens, 2004–2006: U.S. Geological Survey Professional Paper 1750 (this volume).

Iverson, R.M., 1990, Lava domes modeled as brittle shells that enclose pressurized magma, with application to Mount St. Helens, *in* Fink, J.H., ed., Lava flows and domes, emplacement mechanisms and hazard implications: Berlin, Springer-Verlag, International Association of Volcanology and Chemistry of the Earth's Interior, Proceedings in Volcanology 2, p. 47–69.

Iverson, R.M., Dzurisin, D., Gardner, C.A., Gerlach, T.M., LaHusen, R.G., Lisowski, M., Major, J.J., Malone, S.D., Messerich, J.A., Moran, S.C., Pallister, J.S., Qamar, A.I., Schilling, S.P., and Vallance, J.W., 2006, Dynamics of seismogenic volcanic extrusion at Mount St. Helens in 2004–05: Nature, v. 444, no. 7118, p. 439–443, doi:10.1038/nature05322, supplementary movie 2 at http://www.nature.com/nature/journal/v444/n7118/suppinfo/nature05322.html.

Lacroix, A., 1904, La Montagne Pelée et ses eruptions: Paris, Maison et Cie, 662 p.

LaHusen, R.G., Swinford, K.J., Logan, M., and Lisowski, M., 2008, Instrumentation in remote and dangerous settings; examples using data from GPS "spider" deployments during the 2004–2005 eruption of Mount St. Helens, Washington, chap. 16 *of* Sherrod, D.R., Scott, W.E., and Stauffer, P.H., eds., A volcano rekindled; the renewed eruption of Mount St. Helens, 2004–2006: U.S. Geological Survey Professional Paper 1750 (this volume).

Lescinsky, D.T., and Sisson, T.W., 1998, Ridge-forming, ice-bounded lava flows at Mount Rainier, Washington: Geology, v. 26, p. 943–946.

Major, J.J., Kingsbury, C.G., Poland, M.P., and LaHusen, R.G., 2008, Extrusion rate of the Mount St. Helens lava dome estimated from terrestrial imagery, November 2004–December 2005, chap. 12 *of* Sherrod, D.R., Scott, W.E., and Stauffer, P.H., eds., A volcano rekindled; the renewed eruption of Mount St. Helens, 2004–2006: U.S. Geological Survey Professional Paper 1750 (this volume).

Mathews, W.H., 1947, "Tuyas"; flat topped volcanoes in northern British Columbia: American Journal of Science, v. 245, p. 560–570.

Mimatsu, M., 1995, Showa-Shinzan diary, expanded reprint: Sapporo, Suda Seihan Co., 179 p.

Moran, S.C., Malone, S.D., Qamar, A.I., Thelen, W.A., Wright, A.K., and Caplan-Auerbach, J., 2008a, Seismicity associated with renewed dome building at Mount St. Helens, 2004–2005, chap. 2 *of* Sherrod, D.R., Scott, W.E., and Stauffer, P.H., eds., A volcano rekindled; the renewed eruption of Mount St. Helens, 2004–2006: U.S. Geological Survey Professional Paper 1750 (this volume).

Moran, S.C., McChesney, P.J., and Lockhart, A.B., 2008b, Seismicity and infrasound associated with explosions at Mount St. Helens, 2004–2005, chap. 6 *of* Sherrod, D.R.,

Scott, W.E., and Stauffer, P.H., eds., A volcano rekindled; the renewed eruption of Mount St. Helens, 2004–2006: U.S. Geological Survey Professional Paper 1750 (this volume).

Nakada, S., Shimizu, H., and Ohta, K., 1999, Overview of the 1990–1995 eruption at Unzen Volcano: Journal of Volcanology and Geothermal Research, v. 89, nos. 1–4, p. 1–22, doi:10.1016/S0377-0273(98)00118-8.

Pallister, J.S., Thornber, C.R., Cashman, K.V., Clynne, M.A., Lowers, H.A., Mandeville, C.W., Brownfield, I.K., and Meeker, G.P., 2008, Petrology of the 2004–2006 Mount St. Helens lava dome—implications for magmatic plumbing and eruption triggering, chap. 30 *of* Sherrod, D.R., Scott, W.E., and Stauffer, P.H., eds., A volcano rekindled; the renewed eruption of Mount St. Helens, 2004–2006: U.S. Geological Survey Professional Paper 1750 (this volume).

Poland, M.P., Dzurisin, D., LaHusen, R.G., Major, J.J., Lapcewich, D., Endo, E.T., Gooding, D.J., Schilling, S.P., and Janda, C.G., 2008, Remote camera observations of lava dome growth at Mount St. Helens, Washington, October 2004 to February 2006, chap. 11 *of* Sherrod, D.R., Scott, W.E., and Stauffer, P.H., eds., A volcano rekindled; the renewed eruption of Mount St. Helens, 2004–2006: U.S. Geological Survey Professional Paper 1750 (this volume).

Queija, V.R., Stoker, J.M., and Kosovich, J.J., 2005, Recent U.S. Geological Survey applications of Lidar: Photogrammetric Engineering and Remote Sensing, v. 71, no. 1, p. 5–9.

Rose, W.I., 1980, The geology of Santiaguito volcanic dome Guatemala: Hanover, N.H., Dartmouth College, Ph.D. dissertation, 253 p.

Rose, W.I., 1987, Volcanic activity at Santiaguito volcano, 1976–1984, *in* Fink, J.H., ed., The emplacement of silicic domes and lava flows: Geological Society of America Special Paper 212, p. 17–27.

Schilling, S.P., Carrara, P.E., Thompson, R.A., and Iwatsubo, E.Y., 2004, Posteruption glacier development within the crater of Mount St. Helens, Washington, USA: Quaternary Research, v. 61, no. 3, p. 325–329.

Schilling, S.P., Thompson, R.A., Messerich, J.A., and Iwatsubo, E.Y., 2008, Use of digital aerophotogrammetry to determine rates of lava dome growth, Mount St. Helens, Washington, 2004–2005, chap. 8 *of* Sherrod, D.R., Scott, W.E., and Stauffer, P.H., eds., A volcano rekindled; the renewed eruption of Mount St. Helens, 2004–2006: U.S. Geological Survey Professional Paper 1750 (this volume).

Schneider, D.J., Vallance, J.W., Wessels, R.L., Logan, M., and Ramsey, M.S., 2008, Use of thermal infrared imaging for monitoring renewed dome growth at Mount St. Helens, 2004, chap. 17 *of* Sherrod, D.R., Scott, W.E., and Stauffer, P.H., eds., A volcano rekindled; the renewed eruption of Mount St. Helens, 2004–2006: U.S. Geological Survey Professional Paper 1750 (this volume).

Swanson, D.A., and Holcomb, R.T., 1990, Regularities in growth of the Mount St. Helens dacite dome, 1980–1986, *in* Fink, J.H., ed., Lava flows and domes, emplacement mechanisms and hazard implications: Berlin, Springer-Verlag, International Association of Volcanology and Chemistry of the Earth's Interior, Proceedings in Volcanology 2, p. 3–24.

Thelen, W.A., Crosson, R.S., and Creager, K.C., 2008, Absolute and relative locations of earthquakes at Mount St. Helens, Washington, using continuous data; implications for magmatic processes, chap. 4 *of* Sherrod, D.R., Scott, W.E., and Stauffer, P.H., eds., A volcano rekindled; the renewed eruption of Mount St. Helens, 2004–2006: U.S. Geological Survey Professional Paper 1750 (this volume).

Turcotte, D.L., and Schubert, G., 1982, Geodynamics: New York, John Wiley, 450 p.

Wadge, G., 1981, The variation of magma discharge during basaltic eruptions: Journal of Volcanology and Geothermal Research, v. 11, p. 139–168.

Walder, J.S., Schilling, S.P., Vallance, J.W., and LaHusen, R.G., 2008, Effects of lava-dome growth on the Crater Glacier of Mount St. Helens, Washington, chap. 13 *of* Sherrod, D.R., Scott, W.E., and Stauffer, P.H., eds., A volcano rekindled; the renewed eruption of Mount St. Helens, 2004–2006: U.S. Geological Survey Professional Paper 1750 (this volume).

Watts, R.B., Herd, R.A., Sparks, R.S.J., and Young, S.R., 2002, Growth patterns and emplacement of the andesitic lava dome at Soufrière Hills Volcano, Montserrat, *in* Druitt, T.H., and Kokelaar, B.P., eds., The eruption of Soufrière Hills Volcano, Montserrat from 1995 to 1999: Geological Society of London Memoir 21, p. 115–152.

A Volcano Rekindled: The Renewed Eruption of Mount St. Helens, 2004–2006
Edited by David R. Sherrod, William E. Scott, and Peter H. Stauffer
U.S. Geological Survey Professional Paper 1750, 2008

Chapter 10

Photogeologic Maps of the 2004–2005 Mount St. Helens Eruption

By Trystan M. Herriott[1], David R. Sherrod[2], John S. Pallister[2], and James W. Vallance[2]

Abstract

The 2004–5 eruption of Mount St. Helens, still ongoing as of this writing (September 2006), has comprised chiefly lava dome extrusion that produced a series of solid, fault-gouge-mantled dacite spines. Vertical aerial photographs taken every 2 to 4 weeks, visual observations, and oblique photographs taken from aircraft and nearby observation points provide the basis for two types of photogeologic maps of the dome—photo-based maps and rectified maps. Eight map pairs, covering the period from October 1, 2004, through December 15, 2005, document the development of seven spines: an initial small, fin-shaped vertical spine; a north-south elongate wall of dacite; two large and elongate recumbent spines ("whalebacks"); a tall and elongate inclined spine; a smaller bulbous spine; and an initially endogenous spine extruded between remnants of preceding spines. All spines rose from the same general vent area near the southern margin of the 1980s lava dome. Maps also depict translation and rotation of active and abandoned spines, progressive deformation affecting Crater Glacier, and distribution of ash on the crater floor from phreatic and phreatomagmatic explosions. The maps help track key geologic and geographic features in the rapidly changing crater and help date dome, gouge, and ash samples that are no longer readily correlated to their original context because of deformation in a dynamic environment where spines extrude, deform, slough, and are overrun by newly erupted material.

Introduction

During its 2004–5 eruptive activity, Mount St. Helens extruded solid dacite lava onto the May 18, 1980, glacier-covered crater floor south of the 1980s lava dome. Beginning in October 2004, a series of seven spines extruded during the first 15 months of the eruption, following seismic unrest that began September 23, 2004. Two prominent whaleback-shaped spines (3 and 4) that erupted from late October 2004 to April 2005 followed two small spines (1 and 2) extruded in October 2004. From April through July 2005, tall, inclined spine 5 overrode remnants of previous spines to reach the dome's maximum altitude as of September 2006 (Schilling and others, this volume, chap. 8); this spine subsequently subsided and partially disintegrated. Finally, beginning in early August 2005, spines 6 and 7 extruded westward, a marked change from previous spines, which were shoved south along the crater floor. Remnant spines (those no longer actively extruding) were rapidly degraded and overrun by subsequent spines. Crater Glacier, which formed after the cataclysmic 1980 eruption (Schilling and others, 2004; Walder and others, this volume, chap. 13), was nearly bisected during the initial two months of the eruption and formed distinct east and west limbs that were substantially deformed in response to emplacement of the new lava dome.

Intensive monitoring of the eruption by the U.S. Geological Survey's Cascades Volcano Observatory (CVO) has been supplemented by photographic documentation of the dome's growth (this volume: Poland and others, chap. 11; Major and others, chap. 12; Dzurisin and others, chap. 14), including a series of 9×9-in. vertical aerial photographs. We present eight photogeologic maps traced from vertical aerial photographs of the Mount St. Helens crater that encompass 15 months of the eruption from October 1, 2004, through December 15, 2005. Each map is presented as both a photo-based and an accompanying rectified map without a photo base. The maps depict (1) the growth, stagnation, and subsequent burial or degradation of seven dacite spines (fig. 1); (2) the translation and rotation of geologic and geographic features throughout the evolution of the ongoing dome eruption; and (3) the progressive deformation of Crater Glacier as the growing dome displaced ice south of the 1980–86 dome. The photo-based maps also serve as a base for plotting locali-

[1] Department of Earth Science, Webb Hall, University of California, Santa Barbara, CA 93106; now at P.O. Box 750255, Fairbanks, AK 99775

[2] U.S. Geological Survey, 1300 SE Cardinal Court, Vancouver, WA 98683

ties of, and giving geologic and geographic context to, rock, gouge, and ash samples that were collected on the growing lava dome. Photographic documentation of sample context is crucial in a constantly changing setting in which a sample's original location loses significance, as when the base of a coherent spine sampled in January 2005 becomes a pile of transported and undifferentiated rubble by May 2005.

Methods

We compiled maps of the 2004–5 dacite dome eruption at Mount St. Helens on a sequence of ~1:12,000-scale vertical aerial photographs taken by Bergman Photographic Services on contract to CVO (Schilling and others, this volume, chap. 8). Photo pairs encompassing the crater rim, new lava dome, and the 1980–86 lava dome were selected and examined with a stereoscope. The crater rim and 1980s lava dome provided a reasonably stable frame of reference in the dynamic crater environment. On the photographs we mapped units that highlighted changes in dome growth and morphology, as well as changes in the 1980s dome, rock debris, and glacial ice surrounding the dome. Uncertainties of the map units result from working without the benefit of on-the-ground field mapping, which early in the eruption was deemed too hazardous owing to possible explosions or rockfalls and rock avalanches. Our intent is to provide a heightened visual record of the locations and characteristics of major features and deposits in the crater during the ongoing eruption.

Two types of photogeologic maps were prepared—photo-based and rectified. The latter lacks a base image in its final presentation. The visual content of the aerial photographs is immense, and unit boundaries are commonly vivid; however, the aerial photographs are not rectified, and therefore the photo-based maps are subject to scale variability and distortion within an individual image. Consequently, areas of, and distances between, map units on the photo-based maps are only comparable qualitatively. The rectified geologic maps allow quantitative comparison and complement the visually rich, nonrectified photo-based maps.

Although the two map series are based on the same photo pairs for any given date, variations exist within each map pair (photo-based and rectified). Dissimilarities result primarily from compiling the two types of maps at separate times but are compounded by employing different methods for assessing the contact locations (see below). Without doubt, the greater magnification and clarity possible with the plotter used to make the rectified maps resulted in a finer degree of detail, especially in differentiating gouge-covered surface, unroofed spine, and talus. Ultimately, small differences within map couplets persist. The two map series are not intended to be rigorously comparable but rather to be viewed and used for their individual strengths as discussed above.

Photo-Based Geologic Maps

We selected photographs on the basis of observable changes since previous photo coverage, visual clarity of crater

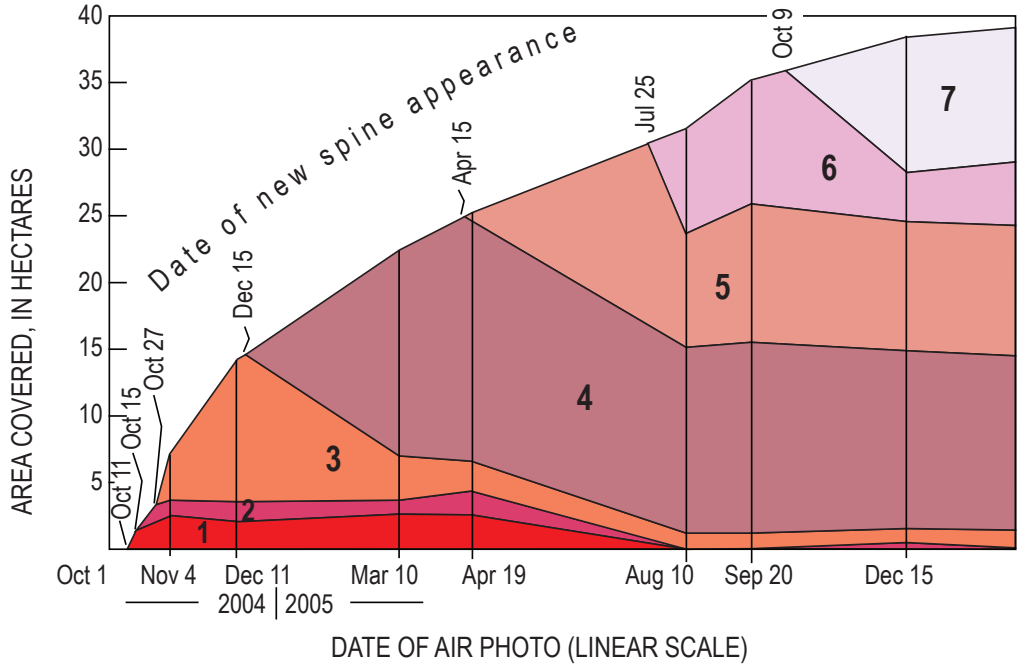

Figure 1. Area of Mount St. Helens' new dome and proportional coverage of individual spines through time. Areas measured from rectified photogeologic maps produced for dates of air photos shown. Date of new spine appearance from Vallance and others (this volume, chap. 9).

Table 1. Imagery used for photogeologic maps.

[Photo number (ex: 6-5) reported as flightline and frame number. Samples are whole-rock and gouge samples used for geochemical analyses described elsewhere in this volume. For brevity, sample numbers lack "SH" prefix (for example, complete sample No. is SH300). For stereographic pair, first listed is left-hand photo, southerly of pair; all flightlines oriented north-south. Column for georegistration points indicates number of points used in transformation to better rectify the photogrammetric geologic map.]

Date of photography	Figure No.	Photo used	Samples shown on photo map	Pair used for rectified map	Georegistration points
10/1/2004	2, 3A	6-5	No new dome	6-4, 6-5	19
11/4/2004	4, 3B	6-4	300, 301-1, 302-2, 304-1, 304-2	6-3, 6-4	15
12/11/2004	5, 3C	6-3	305	6-2, 6-3	19
3/10/2005	6, 3D	7-2	306, 307, 308, 309, 310, 311-1B, 312	7-2, 7-1	10
4/19/2005	7, 8A	6-4	313, 314, 315, 316	6-3, 6-4	19
8/10/2005	9, 8B	1-3	317, 318, 319, 320, 321, 322, 323	1-2, 1-3	22
9/20/2005	10, 8C	1-2		1-2, 1-3	15
12/15/2005	11, 8D	1-3	324	1-2, 1-3	25

features, and pertinence to appropriate geographic setting of sample localities. These selection criteria winnowed the aerial photograph series from 18 to 8 sets (table 1). Our procedure began by scanning (300 dpi) each of the chosen set of photographs. The scanned images were enlarged and framed to encompass a similar area at roughly similar scale. We then traced rock, ash, and glacier units using Adobe ® Illustrator 10 software. Although the photo-based maps are neither rectified nor georeferenced, we attempted to maintain the same field of view and azimuthal orientation (top to the north) of maps throughout the photo-based series.

We studied photo pairs stereoscopically and analyzed apparent three-dimensional surface morphology to identify photogeologic features and draw detailed map-unit contacts. Dashed lines on the maps indicate ambiguous contact locations. Thermal imagery and digital elevation models (DEMs) constructed from each set of photos (Schilling and others, this volume, chap. 8; Vallance and others, this volume, chap. 9) augmented the interpretation of geologic features and deposits viewed on the aerial photographs. We resolved additional crater details by referring to the extensive collection of oblique aerial photographs taken in the crater during field work by CVO scientists and by comparing aerial photographs with repeat images from time-lapse cameras at three fixed locations near the crater rim (this volume: Poland and others, chap. 11; Major and others, chap. 12; Dzurisin and others, chap. 14). These supplementary data elucidate areas within the crater that are obscured in the aerial photographs by condensed steam, shadows, or snow, or are difficult to interpret in plan view.

Rectified Geologic Maps

Conventional photogrammetric methods were used to rectify photogeologic maps. We mapped contacts while viewing paired vertical aerial photos stereoscopically on a Kern PG-2 optical-mechanical stereographic plotter. Our instrument at CVO lacks an electronic digitizer, so the resulting pencil-on-mylar maps were scanned and hand digitized using MapInfo ® Geographic Information System (GIS) software. Points of known geographic position, such as prominences on the crater rim and on the 1980s dome within the crater, served as pseudobenchmarks by which the maps were registered geographically. The crater-rim control points are prominent apices and craggy summits whose locations were derived from a lidar image with 2-m cells produced in November 2004. The 1980s-dome control points are rock spires recognizable on a 1988 high-resolution topographic map of the crater floor.

The PG-2 plotter produced rectified maps under most conditions; however, the photos encompass substantial altitude variation, more than 600 m, across short horizontal distances. Parallax-free models are therefore difficult to achieve, and a small amount of distortion may occur in the resulting maps. The problem is exacerbated by using the crater rim for geographic registration, whereas the area of geologic interest lies entirely on the crater floor, substantially lower in altitude. Moreover, snow cornices modify the crater rim in winter, with some forming prominent topographic apices recognizable in DEMs and aerial photos; these windblown snow and ice features can rebuild in slightly different geographic positions from photo to photo, a source of error for which we cannot system-

atically account. The crater rim itself retreats episodically by erosion, but no noticeable changes caused by this effect were observed in the 15 months that span our geologic maps.

To minimize distortion, the scanned pencil-on-mylar images were transformed by rubbersheeting methods. Specifically, the image was brought into its approximately correct position by a transformation matrix (general perspective projection transformation) and then by triangular irregular net adjustment (for fuller discussion of methodology, see Schilling and others, this volume, chap. 8). The transformations involved 15 to 25 registration points, except for the imagery of March 10, 2005, which used 10 points (table 1).

Ultimately, the resulting precision and probably the accuracy of the rectified maps is within plus or minus 12 m. This value is acceptable owing to the 1:12,000 scale of the aerial photographs and the standard convention that a geologic map should portray precision to at least 1 mm on the map. The precision was tested empirically by draping the resulting linework on existing DEMs. The crater rim was traced as part of each rectified map to provide a visual-empirical guide for comparison with the crater rim on the DEM. Rock spires on the 1980–86 dome provided intracrater tie points to further assess precision. The crater-rim test shows that all tracings lie within 5 m of each other. As a test of accuracy, the rock-spire test gives geographic coincidence generally within 1–5 m, with a few strays as far as 10 m. The resulting rectified maps are more than adequate, in both precision and accuracy, for the cataloging and archiving of geologic information.

Sample Localities

CVO staff collected (chiefly by helicopter dredge) and analyzed 26 samples of 2004–5 lava-dome dacite after the first dacite spine erupted in mid-October 2004 (Pallister and others, this volume, chap 30; Thornber and others, 2008). Sample localities (table 1) are plotted on the photo-based maps that depict relevant geologic and geographic features, providing approximate spatial and temporal context for the samples.

Description of Photogeologic Map Units

Map units described here include rock and debris from the 2004–5 dacite dome, phreatic or phreatomagmatic and rockfall-generated ash deposits, crater floor debris, 1980s lava dome, and deformed and undeformed glacial ice. Labels coupled with a plus sign (+) indicate where thin surficial deposits blanket other map units. The underlying map unit is listed first, followed by the symbol of the blanketing deposit. For example, unit label `gd+a` indicates deformed glacier overlain by a veneer of ash (see Dome Map Units, below).

We use lava dome, or simply dome, to describe the composite feature that comprises extrusive spines or lobes, endogenous growth, and talus. We mapped each spine as an individual unit of extrusive lava, typically massive, and analogous to a lobe or flow. Endogenous growth of some spines results in a rubbly surface. A whaleback is a smooth, striated spine, be it recumbent or vertical. The terms “new” and “old” dome are used informally to differentiate between the 2004–5 and 1980–86 lava domes, respectively.

The term Opus identifies an informally named part of the 1980s dome that was displaced southward during a 1985 eruption. The name originated from a benchmark used to track this movement and later was extended through casual usage to denote the entire elongate geographic ridge that resulted. Opus became important during the renewed eruption in 2004 because the conduit breached the surface near it, deforming both Opus and the adjacent Crater Glacier.

Crater Glacier deformed because of upwarping early in the eruption and then by lateral compression as extruded lava shoved the glacier aside. We demarcate deformed and undeformed glacial ice by tracing the abrupt topographic break in slope between them. This boundary was a deformation front within a compositionally coherent unit, unlike lithologic contacts, which are planar features separating discrete bodies of rocks or deposits.

2004–2005 Dacite Dome Map Units

Spines—Lava lobes, numbered 1–7 according to eruptive sequence of dacite lava extruded onto floor of Mount St. Helens crater during eruption ongoing since October 2004 (Vallance and others, this volume, chap. 9). Moderately porphyritic, with phenocrysts of plagioclase, amphibole, hypersthene, and Fe-Ti oxides. Includes three gross textural features—surface gouge; unroofed, ragged spine; and remnant spine—described below. Thus, map symbol may be a composite; for example, **s4u** indicates unroofed, ragged part of spine 4 after erosion has destroyed its smooth carapace. Spines defined as follows:

s7 Spine 7—Initially endogenous dacite spine; extruded between remnants of spines 5 and 6 beginning in October 2005. Longest-lived and latest in sequence as of September 2006

s6 Spine 6—Rubble-covered dacite spine; extruded during August and September 2005. Grew coincident with and adjacent to a graben, or sag, that developed west of spine 5

s5 Spine 5—Large south-trending dacite spine; extruded from late April through July 2005. Highest spine measured as of September 2006 (Schilling and others, this volume, chap. 8)

s4 Spine 4—Large, elongate, south-trending dacite whaleback; extruded from late December 2004 through late April 2005

s3 Spine 3—Large, elongate, south-trending dacite whaleback; extruded from late October through late December 2004. First occurrence of gouge-mantled spine with striated carapace, characteristic of all subsequent spines

s2 Spine 2—Elongate south-trending dacite spine; extruded in middle to late October 2004

s1 Spine 1—Small northeast-trending finlike dacite spine; initial effusive product; extruded in mid-October 2004

u Unroofed spine—Part of actively growing spine that no longer retains gouge-mantled carapace, which typically was shed through repeated rockfalls

r Spine remnants—Partially intact rubble of inactive spines. Moved constantly as growth of new spine wedged them away from vent

g Gouge—Cataclastic carapace 1–2 m thick that characterized surfaces of spines 3–7 where they first emerged from the vent. Commonly removed by fracturing and degradation

t Talus—2004–5 dacite dome talus resulting from rockfall from active and abandoned spines. May be darker in color than adjacent hot talus where wet or covered by damp ash

a Ash—Tephra, produced chiefly by phreatic or phreatomagmatic explosions and rockfalls. Shown separately on some maps are the following units:

a2 Ash from March 8, 2005, explosion—Primary magmatic and accidental lithic tephra generated during largest phreatomagmatic explosion of ongoing eruption. Resulted from near-vent fallout from plume of steam and ash that rose to about 11 km height

a1 Ash from October 1, 2004, explosion—Fine ash that blanketed northwest sector of Mount St. Helens crater

v Vent for October 1, 2004, explosion—Pit about 50 m in diameter that produced a short-lived steam-and-ash plume of phreatic or phreatomagmatic origin. Source of first explosive activity of ongoing eruption

b Ballistic craters—Depressions in glacier caused by bomb impacts during October 1, 2004, and March 8, 2005, explosions

Other Crater Map Units

rp Crater-floor roof pendant—Crater-floor debris that rested atop spine 3 upon its initial extrusion

gl Crater Glacier—Glacial ice and enclosed rock debris that accumulated subsequent to May 18, 1980, crater-forming eruption. Compression and thickening by crater-floor uplift and extrusion of new lava dome increased rate of flow northward around 1980s dome. Shown separately are the following:

gd Deformed Crater Glacier—Deformed, typically uplifted and crevassed glacial ice shoved aside as lava dome grew

gs Stranded glacial ice—Remnant of ice from east glacier left perched on flank of Opus by crater-floor uplift

la Lahar deposits—Remnants of small muddy debris flows and tiny pyroclastic flows generated by interaction of hot dacite dome rock and snow or glacial ice

cd Crater-floor debris and talus—Rubble uplifted by actively growing 2004–5 dacite dome

cw Crater wall—Strata forming crater walls and outer flanks of Mount St. Helens. Unit only appears on rectified maps

op Opus—Ridge created on south side of 1980s dome by a small graben that formed during October 1985 eruption

od 1980–86 lava dome—Older dome emplaced during a 6-year period following the May 18, 1980, crater-forming eruption

h Melt pit—Steeply walled pits at glacier/lava dome contact melted out by fumaroles. Unit only appears on rectified maps

* 2004–5 sample location—Sample location, showing number (for example, 300; the SH prefix is not included in the map label); most samples collected by helicopter dredging tools. Shown only on photo-based maps

Discussion of Photogeologic Maps

Our discussion of the maps focuses on salient geologic, geographic, topographic, and glacial features generated during the first 15 months of the eruption. These include spine evolution, phreatic and phreatomagmatic explosions, uplifted crater-floor rocks, deformation of Opus, deformation of the Crater Glacier, and extensive rockfall-generated ash deposits. We do not discuss all features depicted in the images, as our goal is to provide a guide for visualizing the most notable changes on the crater floor between the dates of successive maps.

October 1, 2004

The October 1 phreatic explosion left its mark on the crater scene photographed that afternoon (fig. 2). Dark-gray ash (a1) mantles the western crater floor, having emanated from a prominent vent (v) in the Crater Glacier. Numerous craters on west Crater Glacier define a more restricted field of ballistic craters (a1b).

Adjacent to the vent on the east is highly fractured and uplifted glacial ice (gd), a welt approximately 52,000 m^2 in extent that grew rapidly as magma ascended toward the surface (fig. 3*A*). The base of the topographic rise to the welt, distinctive in stereo viewing but not readily apparent in the single base image of figure 2, defines the contact separating deformed from undeformed glacier. With time, some of the deformed ice seen in figure 2 became isolated from the main mass of Crater Glacier. The Opus ridge (op) is also deformed.

November 4, 2004

The November 4 image shows spine 3 (s3) and remnants of spines 1 (s1r) and spine 2 (s2r) of the new dome (fig. 4). The east-flank carapace of spine 3 is a well-preserved striated gouge surface (s3g). A distinctly whiter band marks the freshest gouge along the eastern base. Remnants of spines 1 and 2 are north and west, respectively, of spine 3.

At least one roof pendant (rp) of old dome and crater-floor debris is atop spine 3. In the photo, the pendant is seen as the darker area near the crest of the spine (fig. 4). Dark-gray

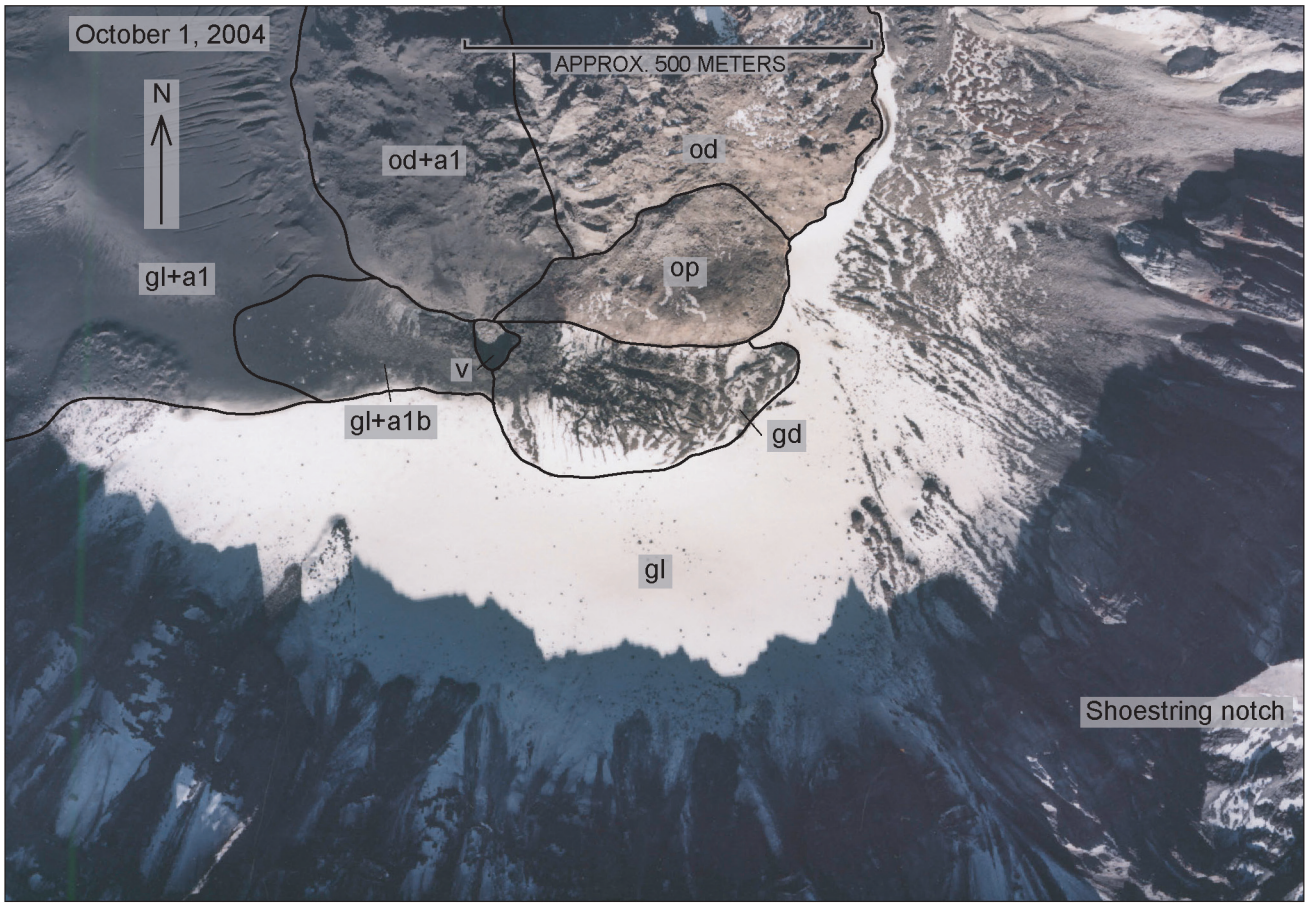

Figure 2. Photo-based geologic map of Mount St. Helens' new dome from aerial photo taken October 1, 2004. For explanation of unit symbols, see text. Shoestring notch is an informal geographic name for the topographic cleft that is the truncated head of the Shoestring Glacier, which was largely destroyed in the 1980 eruption of Mount St. Helens.

debris (cd) along the eastern periphery of spine 3 represents deformed fragments of the 1980–86 dome, first dragged southward 100–200 m on the roof of spine 3 and then eroded off (fig. 3*B*). Uplifted crater floor material lies east of the 1980s dome debris (fig. 3*B*).

East of the new dome is the highly deformed east limb of Crater Glacier (gd), crisscrossed by crevasses to form a serac field. The growing dome has nearly split the glacier, such that its east and west limbs have become geographically distinct. Nevertheless, the glacier remains contiguous around the south side of the new dome.

Deformation of Opus (op) is largely complete but is not easily discerned at the scale of this aerial image (fig. 4); stagnant and broken glacial ice mantles its south side. Increased heat flow on its western side has melted snow from an irregular area, but the exposed, darkened mass of jumbled rock is likely little different in form from the snow-covered nonthermal area of Opus.

Two or three small debris fans and more lobate, slurried deposits (la) originate from spine 1 remnants. Thinner lahar deposits extend along a narrow trace down the center of the cleft that separates the west flanks of the new and 1980s domes from the west limb of Crater Glacier (gl) (fig. 4).

December 11, 2004

Rain, melted snow, or condensed steam has left the snow-free areas very dark gray on this overcast day (fig. 5). Spine 3 has greatly lengthened, earning the name "whaleback." Its gouge-mantled surface (s3g), where wet, is dark grayish brown. The western slope of spine 3 has spalled to form talus (t), including some large house-size blocks. All the uplifted crater-floor debris seen along the west flank in previous images is now indistinguishable, likely buried by talus. Along the southeast side, steam and coarse blocks mark an elongate slab of spine 3 (s3u), detached, deformed, and wedged between spine 3 and the glacier (fig. 3*C*). Spine 1 and 2 remnants remain visible, although they are somewhat obscured by steam in this image (fig. 5).

Notable deformation continues on the east limb of Crater Glacier (gd), but only small changes occur along its west limb. The glacier remains intact along the south side of the new dome, but it has narrowed greatly to only about 60 m (fig. 3*C*). Glacial ice on parts of Opus has disappeared, causing an expansion of the area of Opus (compare figs. 3*B*, 3*C*).

March 10, 2005

Geomorphically prominent spine 4 has by this time supplanted spine 3, which underwent rapid fragmentation during early January 2005 (fig. 6). Spine 4 evolved as the northernmost part of spine 3 split along a vertical fracture and decoupled at its root from the rest of spine 3 to the south. As it grew southward, spine 4 isolated a small relic of spine 3 (s3ru) to the west as it bulldozed the remainder to the east (Vallance and others, this volume, chap. 9); these remnants emit steam where they abut glacial ice along the east margin. The stunning striated and gouge-mantled carapace of spine 4 (s4g), as well as the crevassed and thickened tongue of the deformed glacier (gd, east of spine 4; see below), take center stage in this photo. Remnants of spines 1 and 2 are increasingly ragged in appearance. Virtually no uplifted crater-floor debris remains adjacent to the new spines, as it has been buried by talus (t).

A large phreatomagmatic explosion on March 8 distributed ash (a2) across the north and east sectors of the crater, but large ballistic fragments fell chiefly north and northwest of the new dome. Opus and its shroud of snow and ice lie pinched between the new and 1980s domes. The stagnant ice on Opus (unit gs on fig. 3*D*) is now fully separated from the actively deforming glacier.

The east limb of Crater Glacier deformed dramatically through March and into April, producing the prominent, lobate deformation front visible near the southeast margin of the 1980–86 dome. The amplified glacial deformation slowed significantly in subsequent weeks.

April 19, 2005

Spine 5 (s5) at this time lies at the north end of the spine 4 whaleback remnants, with much of its gouge-covered surface (s4rg still intact (fig. 7). Extensive sloughing of spine 4 was first observed following a 2-week stormy period in late March 2005. Spine 4's southward growth and collision with the southern crater wall caused its breakup. Spine 3 (s3ru) is reduced to remnants flanking spine 4. Spine 1 and 2 remnants persist, although spine 2 (s2r) steams vigorously where shoved into the western limb of the glacier, so that little of it is visible in this photo (fig. 7).

Snowfall subsequent to the March 8 phreatomagmatic explosion buried the thin veneer of ash and ballistic fragments from that event. Distinctive ash (a) blanketing the east limb of the crater glacier on this image is a localized deposit that resulted from a large hot rockfall off the northeast face of spine 4 remnants (fig. 8*A*). Blocky rockfall material stopped abruptly at a topographic rise on the deformed east glacier; the rise is well pronounced in stereo viewing, but not readily apparent in figure 7. Ash elutriated and surged ahead for a short distance, forming the darkest of the deposit seen in the photo (gd+a, northern extent) (fig. 7). Even finer ash traveled south, presumably downwind, before being deposited (gd+a, southern extent).

August 10, 2005

Spine 6 (s6) separates from spine 5 at this time and edges westward (fig. 9), contrasting with previous spines that pushed along a south-southeastward trajectory. This new growth pattern focuses deformation of Crater Glacier in its west arm. The heretofore relentlessly moving terrain of spine 3, 4, and 5 remnants stagnates over the next few months (compare spatial relations in figs. 8*B*, 8*C*, 8*D*). Spine 3 remnants (s3ru) are vis-

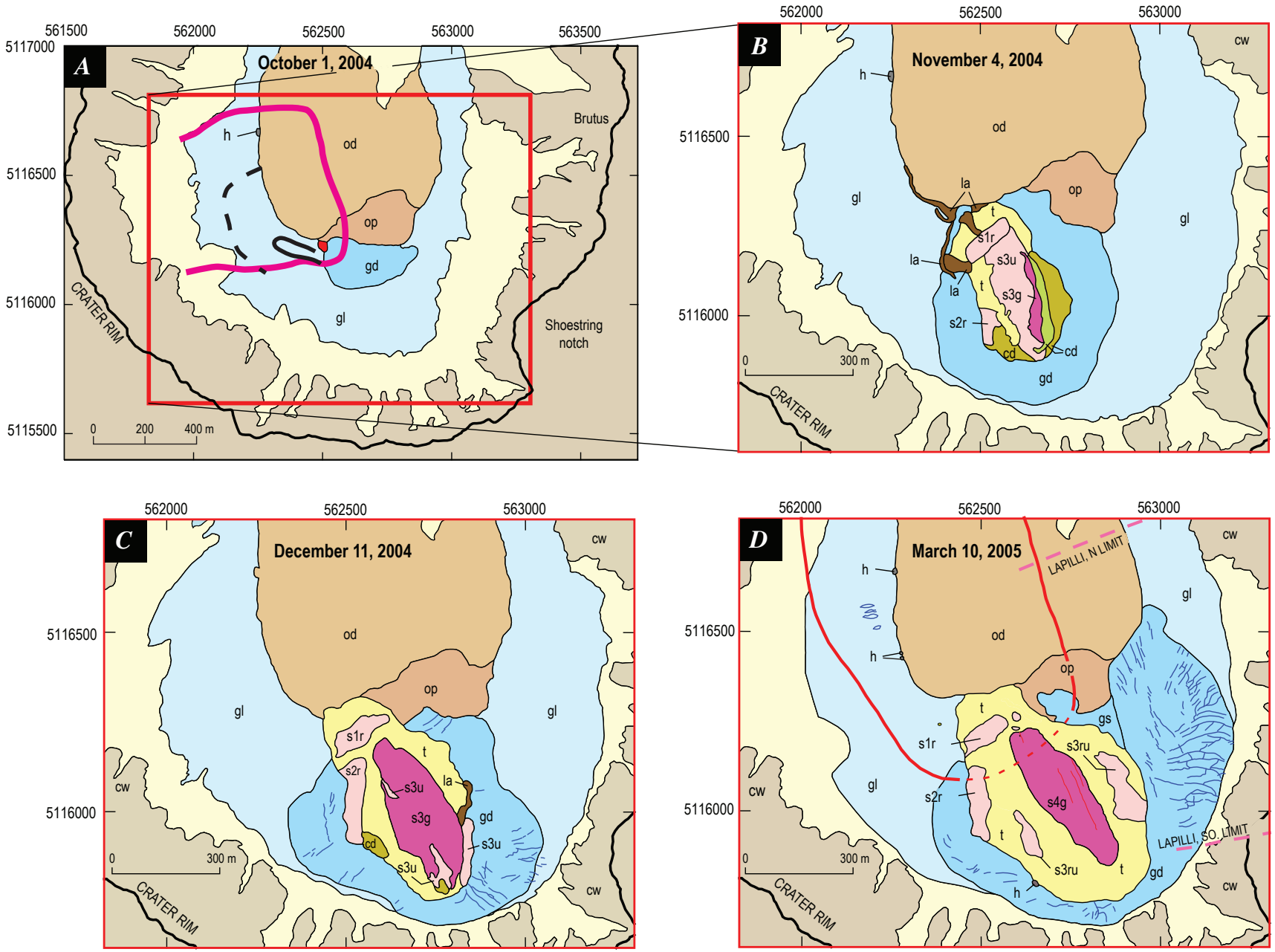

Figure 3. Rectified geologic maps of Mount St. Helens' new dome. *A,* October 1, 2004. *B*, November 4, 2004. *C*, December 11, 2004. *D*, March 10, 2005.

EXPLANATION

FEATURES ASSOCIATED WITH NEW DOME

- s3u / s3g — Spine of 2004–2005 eruption (ongoing in December 2005)—Darker area mantled by gouge
- t — Talus from flank of spine
- la — Lahar deposits from area of new dome
- cd — Crater-floor debris
- Wedge of downdropped crater-floor debris
- Vent for phreatomagmatic eruption of October 1, 2004

TEPHRA DEPOSITS ON MAP OF MARCH 10, 2005

- Distribution of coarse ballistics—Dashed where lack of snow cover makes limit of cratering indistinct
- Northern and southern limits of lapilli and ash

TEPHRA DEPOSITS ON MAP OF OCTOBER 1, 2004

- Ash distribution
- Ballistic fallout
  - Inner, dense fall
  - Outer limit of sparse fall

OTHER FEATURES IN CRATER

- h — Melt pit at glacier margin
- Talus from crater walls and 1980–86 dome
- gl / gd — Glacial ice—Darker area deformed by dome growth
- od / op — 1980–86 dome—Darker area is Opus ridge (op)
- cw — Strata of crater walls and outer flanks
- Notable crevasse on glacier—Resulting from dome emplacement. Only crevasses that developed after the previous map date are shown

Figure 3.—Continued.

Figure 4. Photo-based geologic map of Mount St. Helens' new dome from aerial photo taken November 4, 2004. Stars mark sample localities; see table 1.

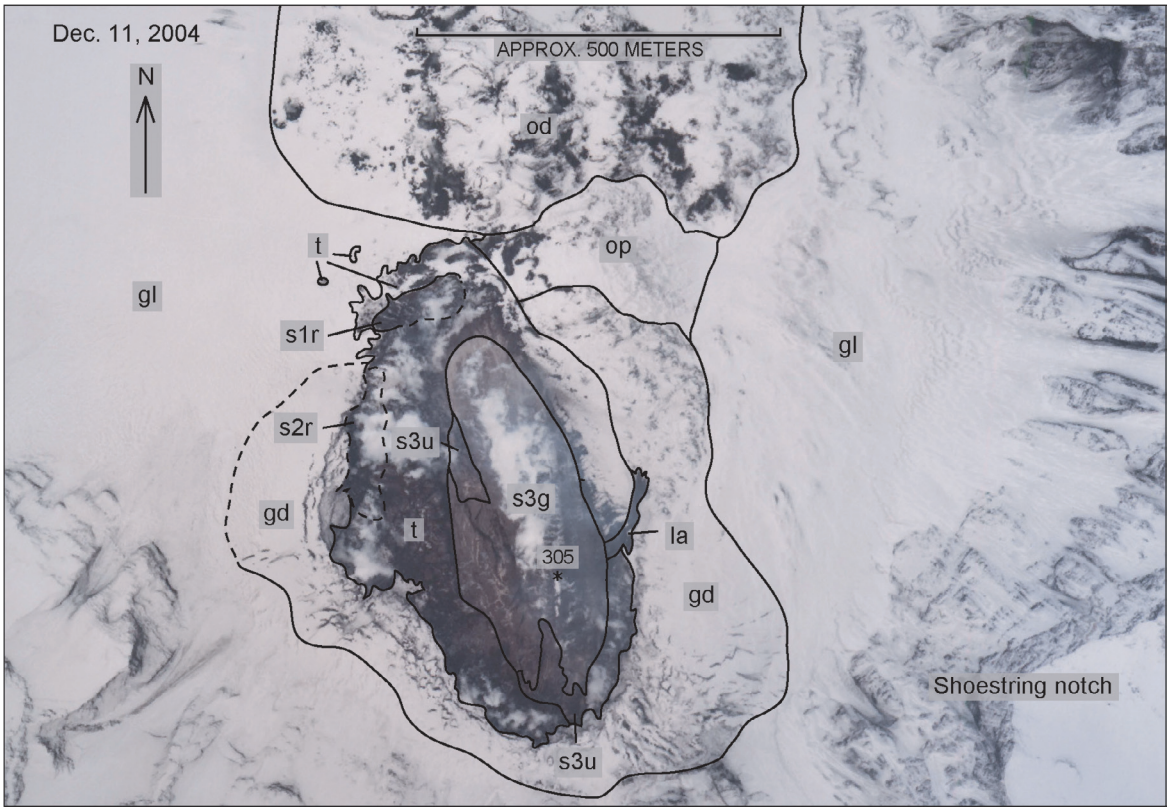

Figure 5. Photo-based geologic map of Mount St. Helens' new dome from aerial photo taken December 11, 2004. Star marks sample locality; see table 1.

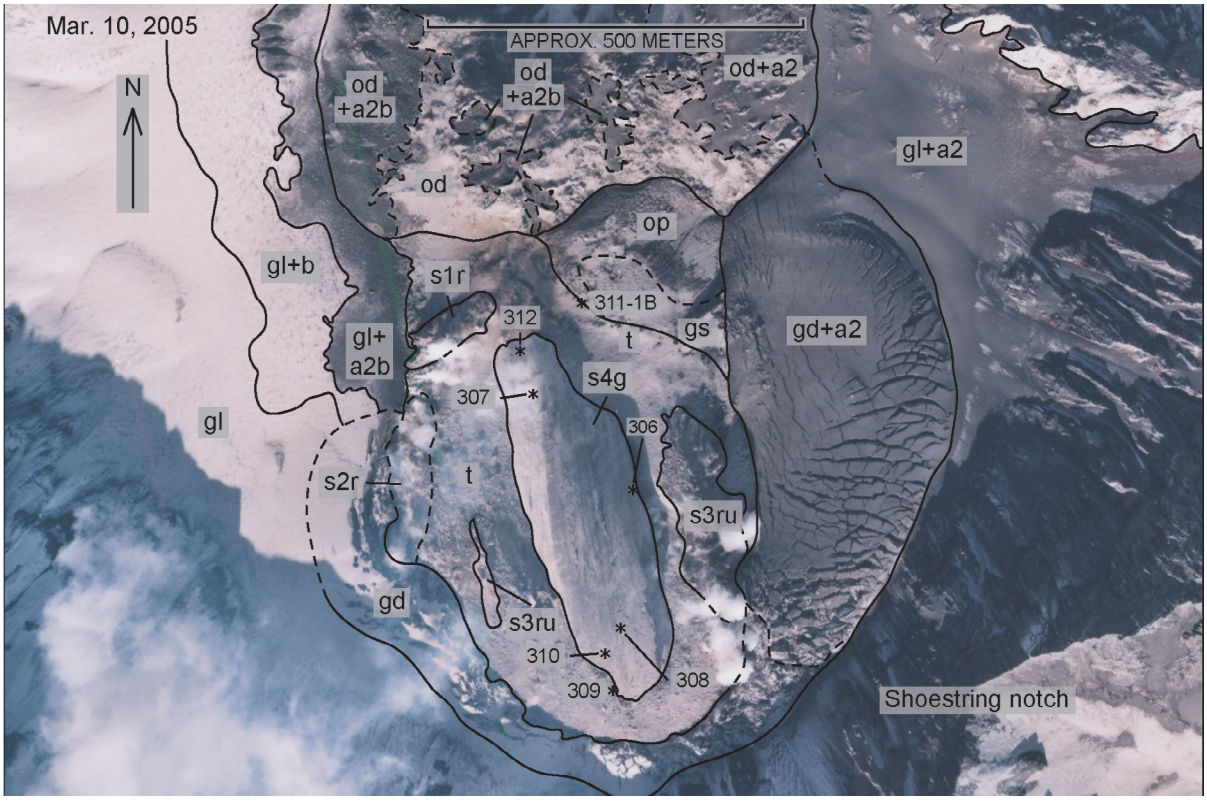

Figure 6. Photo-based geologic map of Mount St. Helens' new dome from aerial photo taken March 10, 2005. Stars mark sample localities; see table 1.

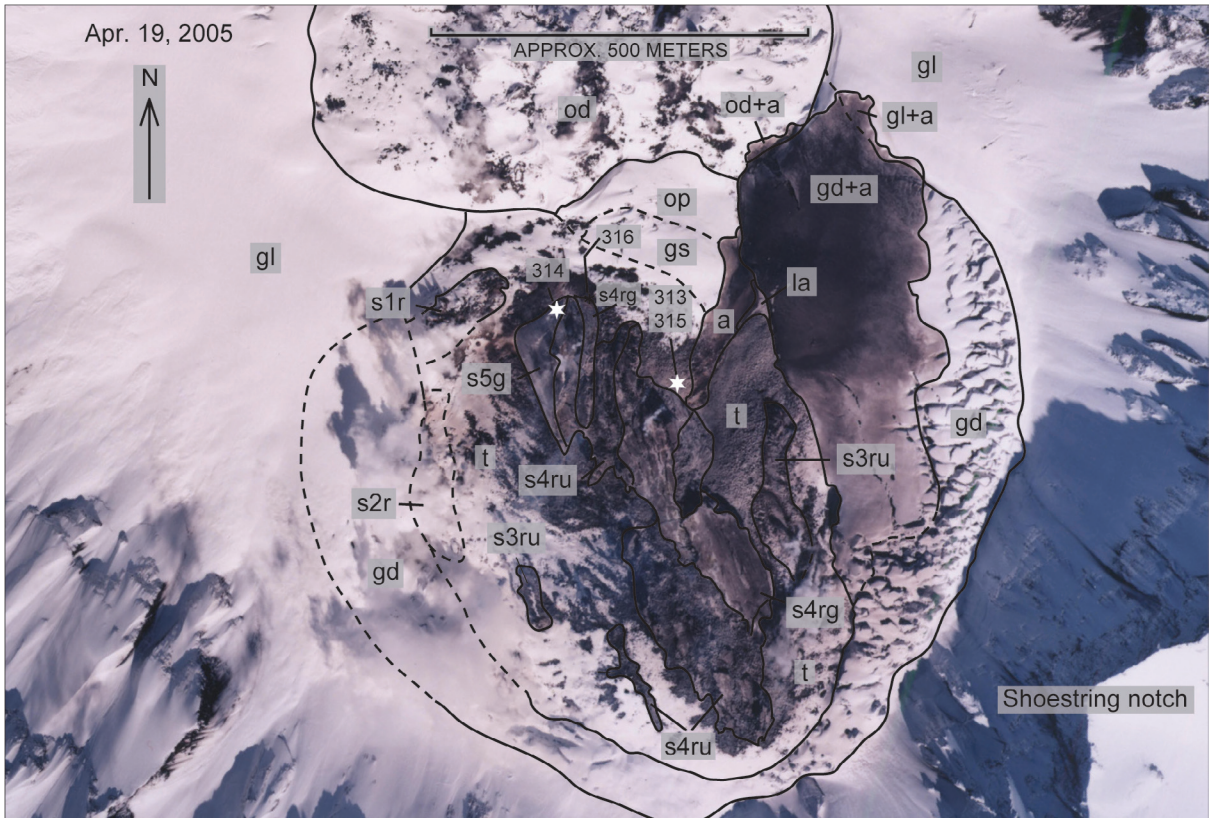

Figure 7. Photo-based geologic map of Mount St. Helens' new dome from aerial photo taken April 19, 2005. Stars mark sample localities; see table 1.

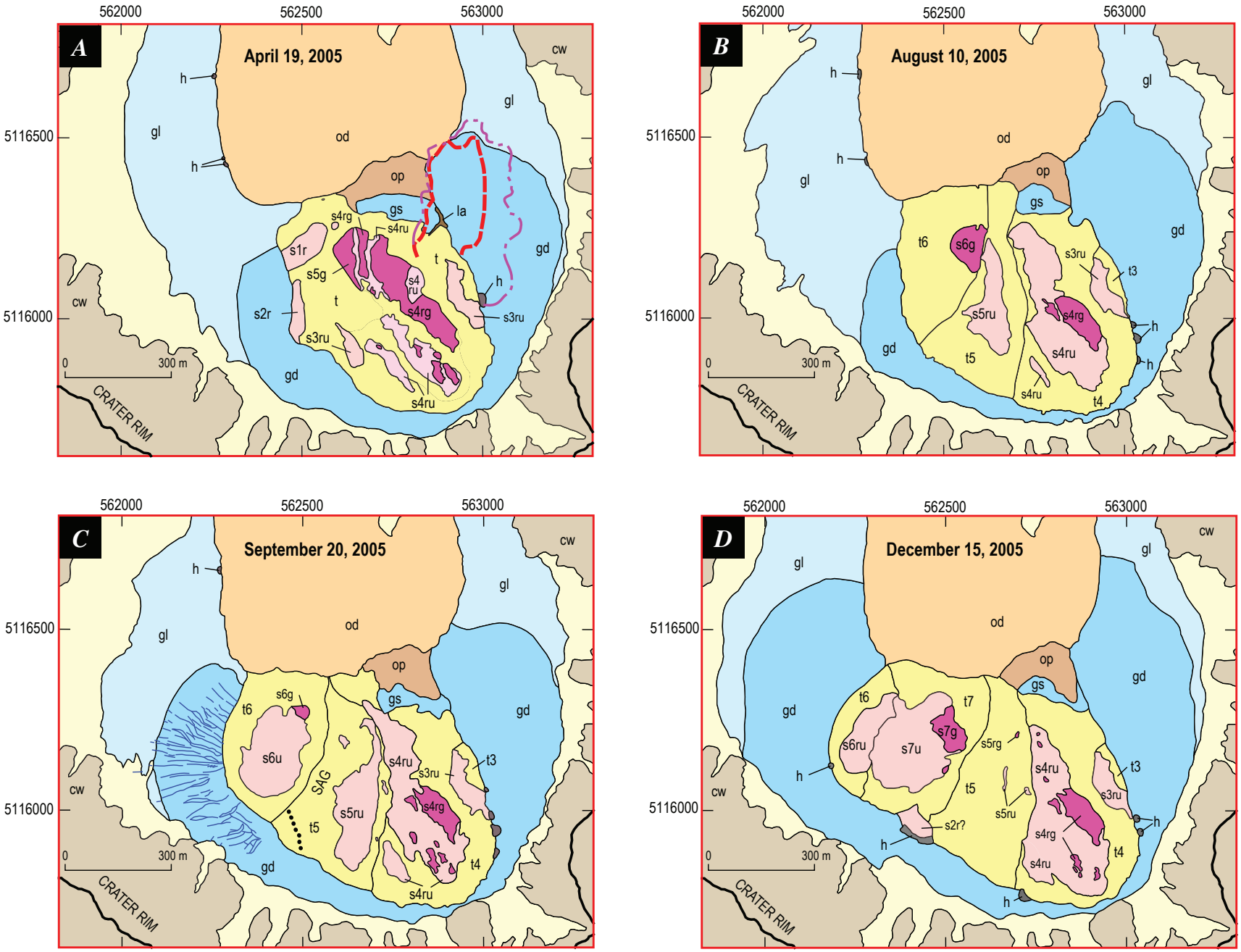

Figure 8. Rectified geologic maps of Mount St. Helens' new dome. *A*, April 19, 2005. *B*, August 10, 2005. *C*, September 20, 2005. *D*, December 15, 2005.

EXPLANATION

FEATURES ASSOCIATED WITH NEW DOME

s3u / s3g — Spine of 2004–2005 eruption (ongoing in December 2005)—Darker area mantled by gouge

t — Talus from flank of spine

Steaming lineament—On figure 8*C*. Likely marks incipient renewed exposure of spine 2 from beneath mantle of talus as seen on figure 8*D*

TEPHRA DEPOSITS ON MAP OF APRIL 19, 2005

Limit, density current of ashy sediment from rockfall

Outer limit of dilute ash from rockfall

OTHER FEATURES IN CRATER

h — Melt pit at glacier margin

Talus from crater walls and 1980–86 dome

gl / gd — Glacial ice—Darker area deformed by dome growth

od / op — 1980–86 dome—Darker area is Opus ridge (op)

cw — Strata of crater walls and outer flanks

Notable crevasse on glacier—Resulting from dome emplacement. Only crevasses that developed after the previous map date are shown

Figure 8.—Continued.

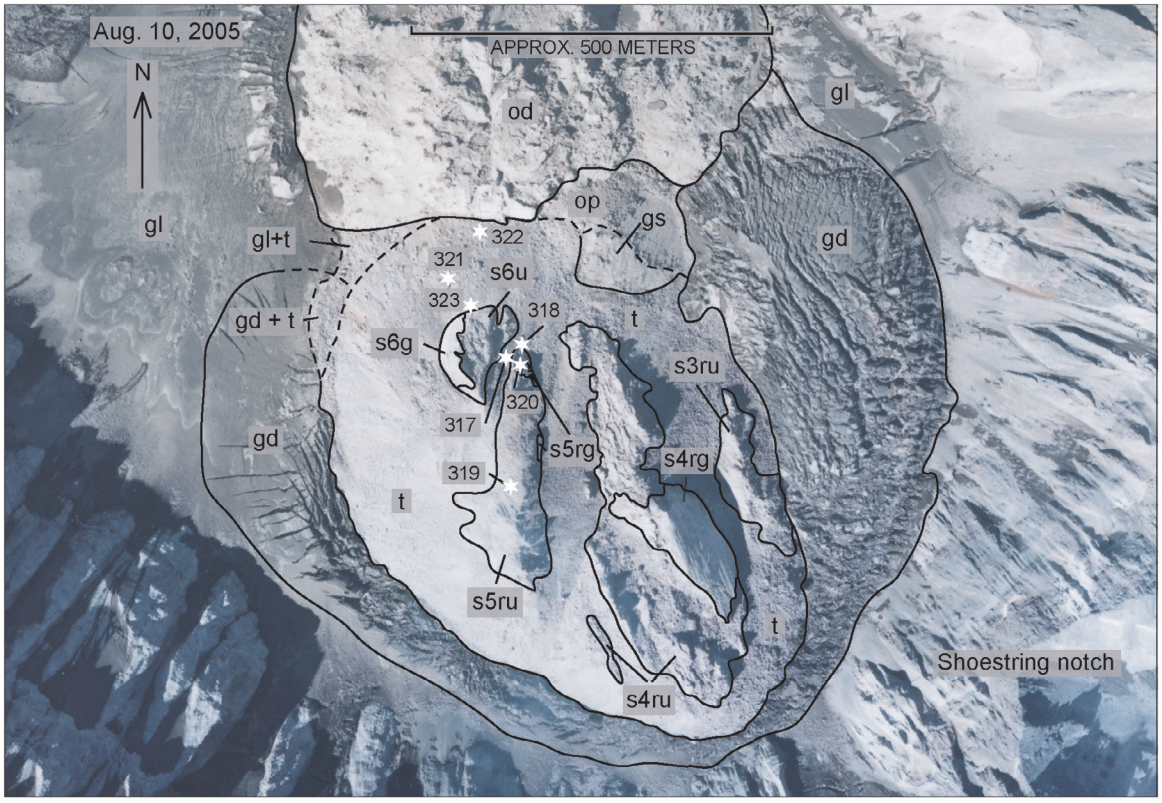

Figure 9. Photo-based geologic map of Mount St. Helens' new dome from aerial photo taken August 10, 2005. Stars mark sample localities; see table 1.

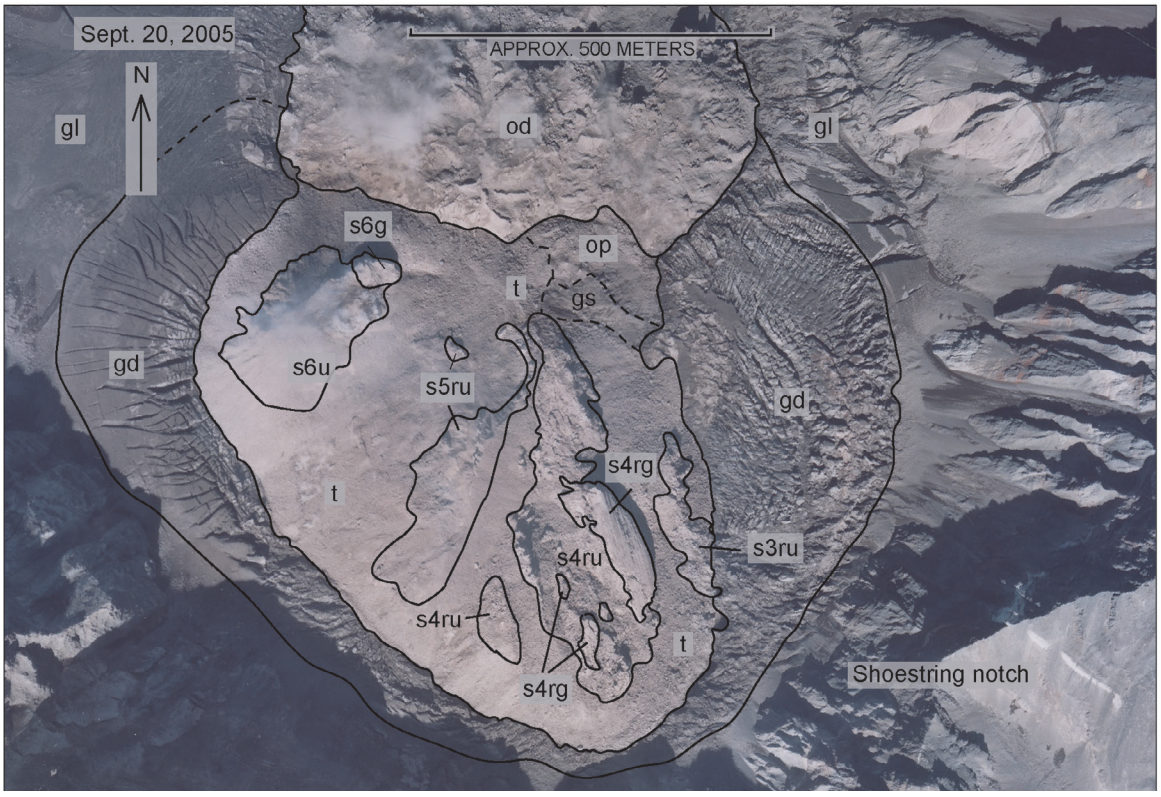

Figure 10. Photo-based geologic map of Mount St. Helens' new dome from aerial photo taken September 20, 2005.

ible only on the eastern periphery of the dome, whereas talus from spines 5 and 6 (t5, t6) now buries all remnants of spines 1, 2, and 3 to the west.

The washed-out appearance of the August 10 image (fig. 9) results from dust generated by summer rockfalls from both the new dome and the crater walls. Much of the light-dark color contrast in this photo arises from the water content of the dusted surface, which is darker where underlain by snow or ice.

September 20, 2005

Spine 6 (s6) continues to propagate westward (fig. 10). On its east side, rockfalls continue to incise the relatively small remaining parts of the gouge-mantled carapace (s6g). Abundant rockfalls from spine 5 have unroofed the core of that spine (s5ru), which now has a prominent axial crest. Spine 6's net westward motion is accompanied by subsidence between the actively growing part of the dome and the relatively stationary remnants of spines 3, 4, and 5 (fig. 8*C*).

Deformation in the west arm of Crater Glacier increases as spine 6 grows westward. Large new crevasses radiate outward from the contact with the expanding dome (fig. 8*C*). To the south, the band of glacial ice that bridges the east and west limbs of Crater Glacier has narrowed to about 6 m in width (fig. 8*C*).

December 15, 2005

In early October, spine 7 (s7) emerged from the sag that formed between spine 6 and remnants of spine 5 (fig. 11; Vallance and others, this volume, chap. 9). Spine 7 grew westward, pushing spine 6 remnants westward, overthrusting them, and burying them in talus. A small sliver of spine 6 (s6ru) still crops out along the margin of west Crater Glacier. Snow covers the largely cooled terrain of spines 3, 4, and 5, distinguishing it from the snow-free, hot, actively growing region of the dome. Spine 4 and 5 remnants are becoming more prominent as their cores are exhumed by rockfalls.

The deformation of Crater Glacier along its west arm is remarkable in this image (fig. 11). Deformation since August 2005 has created a jumbled serac field west of spine 6 remnants, and numerous crevasses underlie the snow-covered areas of the deformed west arm of the glacier.

Acknowledgments

We thank Christina Heliker and Steve Schilling for their insightful manuscript reviews, which led to greater clarity. Any remaining errors are the sole responsibility of the authors. The first author also thanks A.R. Wyss for his comments on an early version of the text.

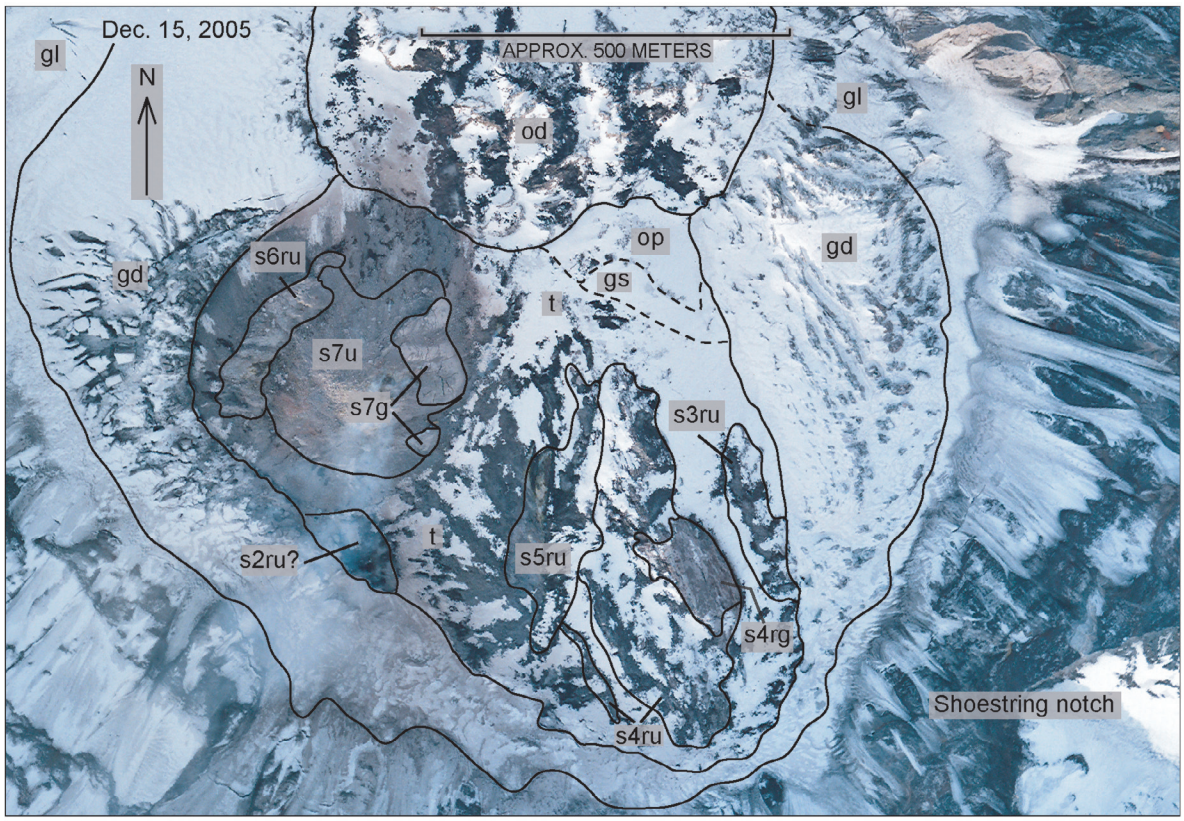

Figure 11. Photo-based geologic map of Mount St. Helens' new dome from aerial photo taken December 15, 2005.

References Cited

Dzurisin, D., Lisowski, M., Poland, M.P., Sherrod, D.R., and LaHusen, R.G., 2008, Constraints and conundrums resulting from ground-deformation measurements made during the 2004–2005 dome-building eruption of Mount St. Helens, Washington, chap. 14 *of* Sherrod, D.R., Scott, W.E., and Stauffer, P.H., eds., A volcano rekindled; the renewed eruption of Mount St. Helens, 2004–2006: U.S. Geological Survey Professional Paper 1750 (this volume).

Major, J.J., Kingsbury, C.G., Poland, M.P., and LaHusen, R.G., 2008, Extrusion rate of the Mount St. Helens lava dome estimated from terrestrial imagery, November 2004–December 2005, chap. 12 *of* Sherrod, D.R., Scott, W.E., and Stauffer, P.H., eds., A volcano rekindled; the renewed eruption of Mount St. Helens, 2004–2006: U.S. Geological Survey Professional Paper 1750 (this volume).

Pallister, J.S., Thornber, C.R., Cashman, K.V., Clynne, M.A., Lowers, H.A., Mandeville, C.W., Brownfield, I.K., and Meeker, G.P., 2008, Petrology of the 2004–2006 Mount St. Helens lava dome—implications for magmatic plumbing and eruption triggering, chap. 30 *of* Sherrod, D.R., Scott, W.E., and Stauffer, P.H., eds., A volcano rekindled; the renewed eruption of Mount St. Helens, 2004–2006: U.S. Geological Survey Professional Paper 1750 (this volume).

Poland, M.P., Dzurisin, D., LaHusen, R.G., Major, J.J., Lapcewich, D., Endo, E.T., Gooding, D.J., Schilling, S.P., and Janda, C.G., 2008, Remote camera observations of lava dome growth at Mount St. Helens, Washington, October 2004 to February 2006, chap. 11 *of* Sherrod, D.R., Scott, W.E., and Stauffer, P.H., eds., A volcano rekindled; the renewed eruption of Mount St. Helens, 2004–2006: U.S. Geological Survey Professional Paper 1750 (this volume).

Schilling, S.P., Carrara, P.E., Thompson, R.A., and Iwatsubo, E.Y., 2004, Posteruption glacier development within the crater of Mount St. Helens, Washington, USA: Quaternary Research, v. 61, no. 3, p. 325–329.

Schilling, S.P., Thompson, R.A., Messerich, J.A., and Iwatsubo, E.Y., 2008, Use of digital aerophotogrammetry to determine rates of lava dome growth, Mount St. Helens, Washington, 2004–2005, chap. 8 *of* Sherrod, D.R., Scott, W.E., and Stauffer, P.H., eds., A volcano rekindled; the renewed eruption of Mount St. Helens, 2004–2006: U.S. Geological Survey Professional Paper 1750 (this volume).

Thornber, C.R., Pallister, J.S., Rowe, M.C., McConnell, S., Herriott, T.M., Eckberg, A., Stokes, W.C., Johnson Cornelius, D., Conrey, R.M., Hannah, T., Taggart, J.E., Jr., Adams, M., Lamothe, P.J., Budahn, J.R., and Knaack, C.M., 2008, Catalog of Mount St. Helens 2004–2007 dome samples with major- and trace-element chemistry: U.S. Geological Survey Open-File Report 2008–1130, 9 p., with digital database.

Vallance, J.W., Schneider, D.J., and Schilling, S.P., 2008, Growth of the 2004–2006 lava-dome complex at Mount St. Helens, Washington, chap. 9 *of* Sherrod, D.R., Scott, W.E., and Stauffer, P.H., eds., A volcano rekindled; the renewed eruption of Mount St. Helens, 2004–2006: U.S. Geological Survey Professional Paper 1750 (this volume).

Walder, J.S., Schilling, S.P., Vallance, J.W., and LaHusen, R.G., 2008, Effects of lava-dome growth on the Crater Glacier of Mount St. Helens, Washington, chap. 13 *of* Sherrod, D.R., Scott, W.E., and Stauffer, P.H., eds., A volcano rekindled; the renewed eruption of Mount St. Helens, 2004–2006: U.S. Geological Survey Professional Paper 1750 (this volume).

A Volcano Rekindled: The Renewed Eruption of Mount St. Helens, 2004–2006
Edited by David R. Sherrod, William E. Scott, and Peter H. Stauffer
U.S. Geological Survey Professional Paper 1750, 2008

Chapter 11

Remote Camera Observations of Lava Dome Growth at Mount St. Helens, Washington, October 2004 to February 2006

By Michael P. Poland[1], Daniel Dzurisin[2], Richard G. LaHusen[2], Jon J. Major[2], Dennis Lapcewich[3], Elliot T. Endo[2], Daniel J. Gooding[2], Steve P. Schilling[2], and Christine G. Janda[2]

Abstract

Images from a Web-based camera (Webcam) located 8 km north of Mount St. Helens and a network of remote, telemetered digital cameras were used to observe eruptive activity at the volcano between October 2004 and February 2006. The cameras offered the advantages of low cost, low power, flexibility in deployment, and high spatial and temporal resolution. Images obtained from the cameras provided important insights into several aspects of dome extrusion, including rockfalls, lava extrusion rates, and explosive activity. Images from the remote, telemetered digital cameras were assembled into time-lapse animations of dome extrusion that supported monitoring, research, and outreach efforts. The wide-ranging utility of remote camera imagery should motivate additional work, especially to develop the three-dimensional quantitative capabilities of terrestrial camera networks.

Introduction

During the 20th century, advances in technology have added an array of geophysical and geochemical instrumentation to the modern volcanologist's toolkit. The study of active volcanoes has relied increasingly upon datasets derived from such technology to infer the mechanics of volcanic processes, which often occur at depth. As detailed in this volume, many geophysical and geochemical techniques have been applied to improve understanding of eruptive activity at Mount St. Helens in 2004–6. Visual surveillance in volcanology, however, remains critical for providing "ground truth" necessary to confirm inferences drawn from geophysical and geochemical data.

Visual observations can be recorded by imaging systems on the ground or in an aircraft or spacecraft. For example, photogrammetric applications of aerial photography to volcanoes include quantification of large-scale deformation before the 1980 eruption of Mount St. Helens (Moore and Albee, 1981) and calculations of erupted volumes at Stromboli, Italy, in 2002–3 (Baldi and others, 2005) and at Mount St. Helens in 2004–6 (Schilling and others, this volume, chap. 8). Ground-based visual imagery is equally important for observing volcanic activity, having the advantages of low cost, frequent image acquisition, and flexibility in deployment. Starting in September 2004, we made extensive use of terrestrial cameras to investigate activity at Mount St. Helens using a continuously operating Webcam located 8 km north of the volcano and repeat photographs from a network of remote, telemetered digital cameras. The imagery was used to evaluate broad-scale eruptive activity in near real time, correlate geophysical signals with changes in eruptive activity, investigate dome extrusion processes, track the evolution of the eruption (including deformation of glacial ice) over time, and assess weather conditions for planning fieldwork.

We describe here the remote camera deployments and the activity recorded at Mount St. Helens during the period October 2004 to February 2006. Other types of camera deployments and applications at Mount St. Helens are described elsewhere in this volume. Results from high-rate, small field-of-view photography experiments designed to measure small-scale changes in dome extrusion are described by Dzurisin and others (this volume, chap. 14). Major and others (this volume, chap. 12) discuss quantitative dome-growth measurements

[1] U.S. Geological Survey, PO Box 51, Hawaii National Park, HI 96718

[2] U.S. Geological Survey, 1300 SE Cardinal Court, Vancouver, WA 98683

[3] U.S.D.A. Forest Service, Gifford Pinchot National Forest, 10600 NE 51st Circle, Vancouver, WA 98682

using images from a single remote camera in combination with a digital elevation model.

Previous Uses of Visual Observation Systems to Monitor Active Volcanoes

Volcanology is fundamentally an observational science, and repeat observations from fixed locations have proven critical to the documentation and interpretation of many volcanic processes. During dome extrusion in 1902–5 at La Montagne Pelée, Martinique, Lacroix (1908) collected photographs from fixed vantage points to record the development of the dome over the course of the extrusive phase of the eruption. In 1944–45, Mimatsu Masao, the postmaster of the Sobetsu Post Office in Japan, lacked camera equipment but documented the growth of the Showa-Shinzan dome at the base of Mount Usu in a detailed diary and with careful sketches. His unique surveying methods included a fixed observation point behind the post office, from where he viewed the growing dome by resting his chin on a level and by using a series of horizontally stretched cords as reference lines. His drawings of the uplift and dome growth from this vantage point were presented at the 1948 International Association of Volcanology conference in Oslo, Norway, and what came to be known as "Mimatsu diagrams" were praised as "the only existing records of the entire birth of a volcano" (Mimatsu, 1995).

One of the best known volcano photographic sequences was taken by Gary Rosenquist at Mount St. Helens during the landslide and lateral blast of May 18, 1980. The Rosenquist photos, and similar sequences taken from other locations around the volcano at the start of the eruption, were critical to understanding the development of the landslide and lateral blast (Voight, 1981; Voight and others, 1981; Moore and Rice, 1984), lahar initiation (Pierson, 1985), pyroclastic stratigraphy (Criswell, 1987), and the question of whether or not the blast was a product of one or two explosions (Hoblitt, 2000). Fixed-vantage-point cameras from more than 100 repeat terrestrial photography and time-lapse film stations were also a key tool for studying dome building at Mount St. Helens during 1980–86 (Topinka, 1992).

The development of digital cameras has facilitated the use of visual observation systems at volcanoes. At Kīlauea Volcano, Hawai'i, time-lapse digital cameras powered by solar panels and encased in weatherproof boxes now record details of volcanic events, including ground deformation, vent collapses, and surface breakouts of lava (Orr and Hoblitt, 2006). Repeat views from remote digital cameras have also been employed at Soufrière Hills volcano[4], Montserrat, where they provided important visual documentation of dome growth (Watts and others, 2002) and of the 2003 catastrophic dome collapse (Herd and others, 2005).

Remote Camera Systems Used at Mount St. Helens

During October 2004 to February 2006, two types of remote camera systems were used for visually monitoring eruptive activity at Mount St. Helens—a Webcam and a network of remote, telemetered digital cameras. These systems are described below.

Webcam

A Webcam, herein referred to as the "VolcanoCam," was installed in 1996 at the U.S. Department of Agriculture–Forest Service's Johnston Ridge Observatory (JRO; fig. 1), 8 km north of Mount St. Helens (fig. 2*A*). At that time, the installation of the camera was more of an Internet novelty for the Gifford Pinchot National Forest (GPNF) and the Mount St. Helens National Volcanic Monument. The GPNF had just established one of the first Web sites within the Forest Service, and the addition of the VolcanoCam, they hoped, would provide a boost to forest recreation use by stimulating general interest in the area.

The VolcanoCam operated with minimal problems for 7 years until it suffered a mechanical failure in June 2003. Funding problems delayed replacement of the camera for more than a year. New equipment was finally procured and installed on September 23, 2004—coincidentally the day that seismic unrest began at Mount St. Helens. The new VolcanoCam was a color charge-coupled camera that provided a signal of 525 TV lines at 30 frames per second (terminology from the National Television System Committee standards). Still images were uploaded every five minutes to the Forest Service's national Web server. The clock on the camera was not synchronized to Internet time and was probably only accurate to within about 1 minute.

Access to the camera was initially limited to Forest Service and USGS staff, but the VolcanoCam was opened for public access on September 27, 2004, and immediately became a major attraction (http://www.fs.fed.us/gpnf/volcanocams/msh/, last accessed January 28, 2008). The number of hits on the VolcanoCam Web site became so large that the main Forest Service Web server crashed several times, and excessive bandwidth use threatened the main U.S. Department of Agriculture Web servers. A Web caching system alleviated the most serious bandwidth concerns. Fourth-quarter 2004 statistics for all Federal government Web sites later revealed that the Forest Service enjoyed the largest quarterly increase in customer satisfaction ever recorded for a Federal government Web site, due mainly to the worldwide popularity of the VolcanoCam.

[4] Capitalization of "Volcano" indicates adoption of the word as part of the formal geographic name by the host country, as listed in the Geographic Names Information System, a database maintained by the U.S. Board on Geographic Names. Noncapitalized "volcano" is applied informally—eds.

Despite its relative simplicity, the VolcanoCam was a remarkably useful educational resource and volcano-monitoring tool. Many of the thousands of emails received by the Forest Service in late 2004 regarding the VolcanoCam were from teachers across the United States, offering their thanks for the opportunity to view volcanic activity in their classrooms. In addition, the VolcanoCam proved to be a valuable tool for volcanologists, enabling rapid assessment of volcanic activity and weather conditions from any location having Internet access. The camera also demonstrated limited infrared capabilities. Nighttime observations were important for detecting magma extrusion and rockfall events, and they garnered substantial interest from the general public. An independent Web site managed by Mr. Darryl Luscombe even made available daily movies from sequential "glow" images collected during the previous night (http://www.luscombe-carter.com/index.html, last accessed January 28, 2008).

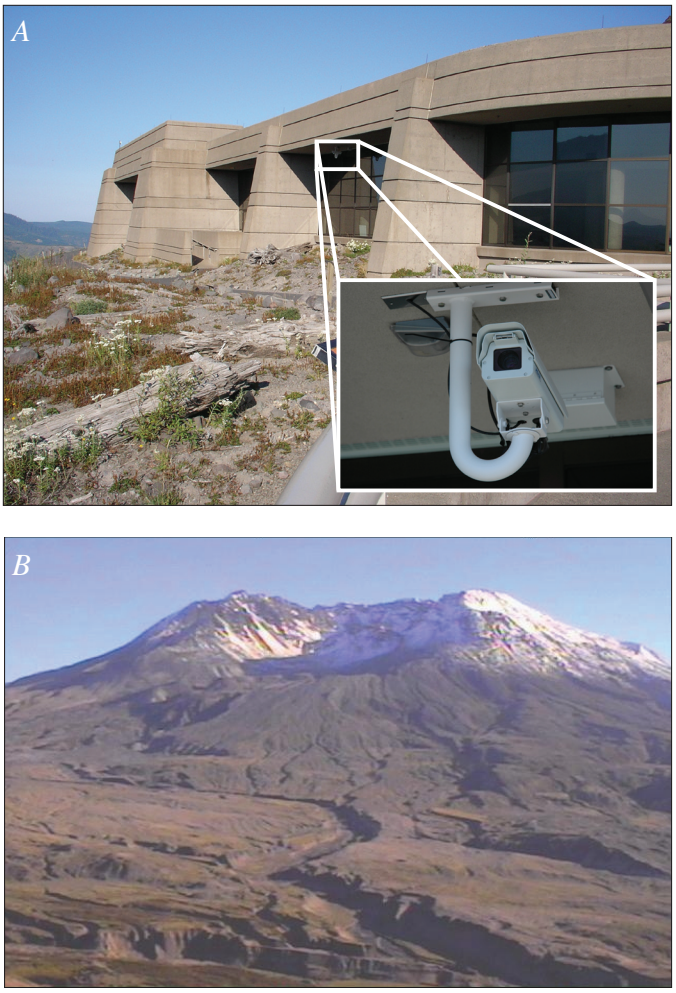

Figure 1. Field setting for U.S. Department of Agriculture Forest Service VolcanoCam at Mount St. Helens, Washington. *A*, Camera position beneath eave of Johnston Ridge Observatory. USGS photo by J.P. Griswold, August 25, 2006. Inset shows camera. USGS photo by S.P. Schilling. *B*, Example of VolcanoCam view of the volcano acquired on September 24, 2004.

Remote, Telemetered Digital Cameras

In early October 2004, the value of having a visual monitoring station close to the volcano became obvious because the VolcanoCam's view of the locus of renewed activity was blocked by the 1980–86 lava dome. To meet this need, staff at the USGS Hawaiian Volcano Observatory constructed a remote, telemetered digital camera, based on models used at Soufrière Hills volcano, Montserrat (Herd and others, 2005), and sent it to the Cascades Volcano Observatory (CVO) for deployment at Mount St. Helens. The system included an Olympus C–3030 3.3-megapixel camera with a × 3 optical zoom lens. The camera was connected through a serial port to a 900-MHz radio mounted in a weatherproof box (fig. 3). The

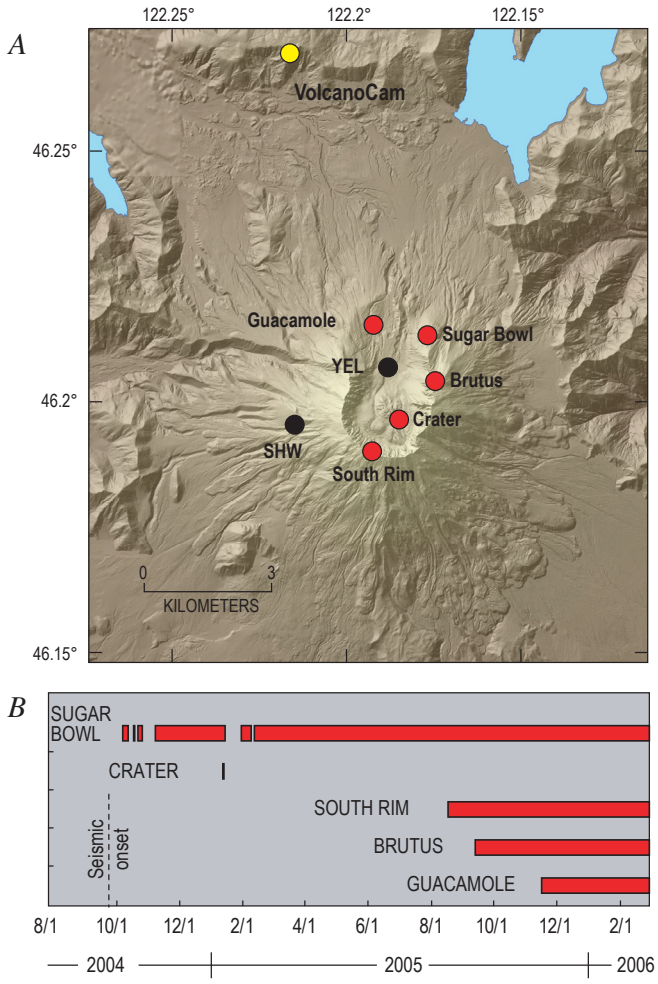

Figure 2. Remote, telemetered digital cameras used during monitoring of Mount St. Helens, Washington, 2004–6. *A*, Map showing locations of U.S. Geological Survey remote cameras (red dots) and U.S. Department of Agriculture Forest Service VolcanoCam (yellow dot). Black dots show locations of seismic stations that are referred to in figures 10 and 11. Hillshade-relief base map is from digital elevation model (DEM) of October 2005. *B*, Timeline with dates of operation (red bars) for remote, telemetered digital cameras through February 2006. Usable images were lacking on about half of all operating days, owing to inclement weather.

box was fastened to a tripod and pointed towards the deforming area in the southeast part of the crater (fig. 4). Power was supplied by a solar panel and batteries with enough capacity to ensure that the camera and radio would operate even during long periods of cloudy weather. Image resolution, zoom, and timing of acquisition were controlled from a computer located at the Forest Service's Coldwater Ridge Visitor Center, about 13 km northwest of the crater, using PhotoPC public domain software (http://www.lightner.net/lightner/bruce/photopc/ppc_use.html, last accessed January 28, 2008). Images were time stamped according to the camera time. The controlling computer could be reached via ftp from CVO through a satellite link, thereby providing access to imagery in near real time.

The remote camera was installed on October 10, 2004, on Sugar Bowl dome, immediately northeast of the breach in the 1980 crater wall and 2.3 km from the intensely deforming area, or welt (Dzurisin and others, this volume, chap. 14), in the southeast part of Mount St. Helens crater (fig. 2). The goals for the Sugar Bowl camera deployment were to (1) establish a visual record of volcanic activity, which could be used to test inferences drawn from geophysical, geological, and geochemical measurements, (2) monitor volcanic activity in near real time, and (3) provide a means of assessing general conditions in the volcano's crater to support field operations. Sugar Bowl offered a good view of the welt and subsequent dome growth (fig. 4*B*) from a point relatively safe from the mild explosive activity that characterized the early stages of the eruption.

A few problems resulted in a loss of imagery from the digital camera. Although high winds minimized snow accumulation, rime ice built up when temperatures were below freezing, obscuring the camera's view (fig. 5). The ice was removed manually during site visits, but it often persisted for weeks at a time when no field work was conducted. The system functioned well during the period October 2004 to February 2006,

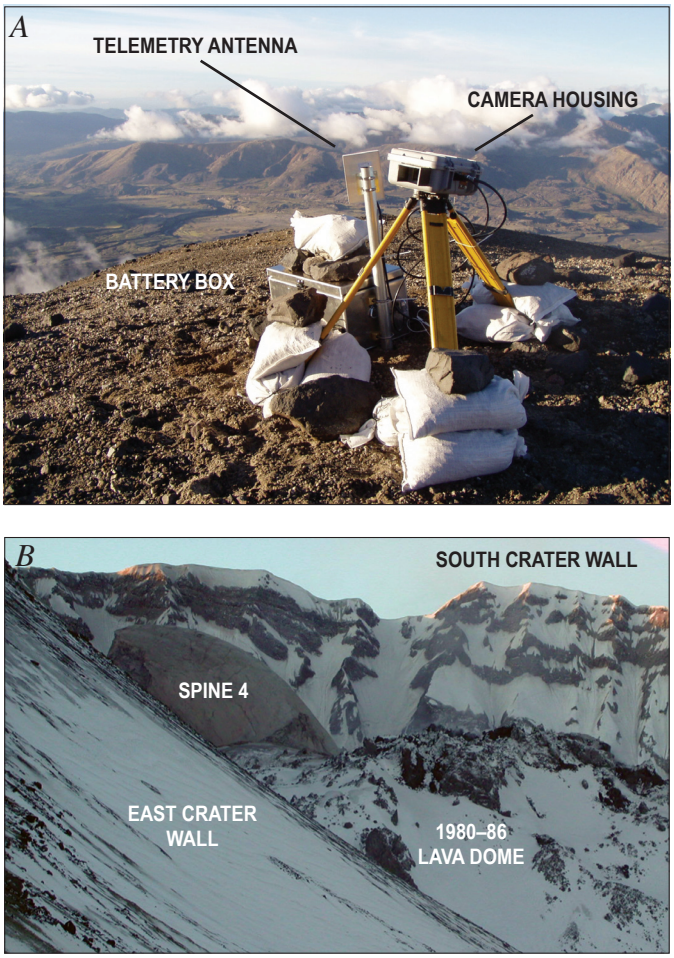

Figure 4. Setting and view for Sugar Bowl remote telemetered camera at Mount St. Helens, Washington. *A*, Field site atop Sugar Bowl dome, 2 km from active vent. Solar panel is out of view to the right. USGS photo by M.P. Poland, October 10, 2004. *B*, Example of camera view, acquired on February 10, 2005, showing spine 4.

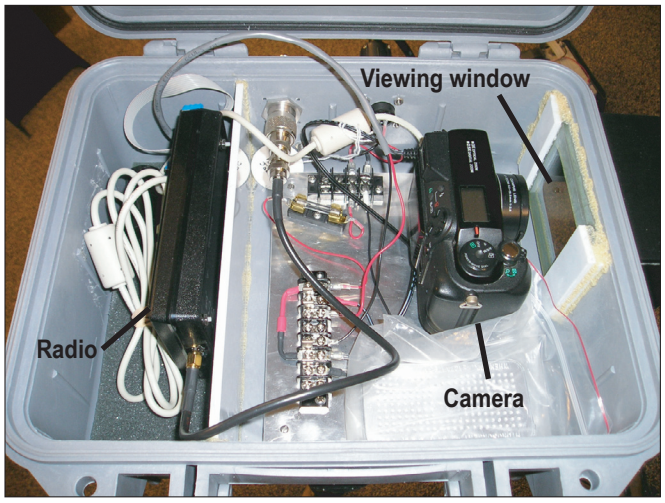

Figure 3. Interior of weatherproof box that contains camera and radio telemetry for Sugar Bowl remote, telemetered digital camera system. USGS photo by M.P. Poland, October 10, 2004.

with only a few lapses in image acquisition (fig. 2*B*) caused by mechanical breakdowns and abrasion of the viewing window by blowing volcanic ash. When the camera was operating, cloudy or icy weather resulted in no usable imagery for approximately half of the total deployment time.

The Sugar Bowl camera became an important tool in monitoring, research, and public outreach efforts, and it motivated the deployment of four additional instruments (Crater, Brutus, South Rim, and Guacamole; fig. 2) by the end of 2005. These new systems used similar equipment and software as the Sugar Bowl camera (fig. 6*A*). The Crater camera was installed by a helicopter sling operation within a few hundred meters of the growing dome on January 14, 2005. A location close to the dome was selected to provide close-up images that might be used to test dome-growth models (fig 6*B*). This camera suffered a mechanical failure several hours after it was put into

place and was subsequently destroyed by a small explosion during the early morning of January 16, 2005. During the summer and fall of 2005, additional cameras were installed on the crater rim: Brutus (fig. 6*C*), 1.1 km east-northeast of the vent, and South Rim (fig. *6A, D*), 0.7 km southwest of the vent. As dome building focused in the southwestern part of the crater during late 2005, a camera was established on the floor of the breach in the 1980 crater: Guacamole (fig. 6*E*), 2.6 km north of the vent. Taken together, these camera systems provided a variety of different views of the growing lava dome.

Insights from Remote Camera Imagery

The remote cameras provided important, and sometimes unexpected, insights into volcanic activity at Mount St. Helens during 2004–2006. For example, the VolcanoCam confirmed that the extrusion of lava had begun in October 2004. Visual and infrared observations from a helicopter on October 11, 2004, noted a craggy, hot (maximum temperature of 580°C), rocky "fin," indicating that lava had reached the surface (Scott and others, this volume, chap. 1; Vallance and others, this volume, chap. 9). During the night of October 11 and the morning of October 12, the VolcanoCam showed signs of glow reflected off steam in the vicinity of the new spine, providing a valuable supplement to the earlier visual and infrared data and accessible to anyone with Internet access.

Both the VolcanoCam and the Sugar Bowl remote camera also had excellent views of explosive activity at Mount St. Helens. VolcanoCam photos posted to the Internet every five minutes provided useful, though approximate, constraints on the duration, magnitude, and timing of the early October 2004 explosions. Following that period, only two additional significant explosions occurred, on January 16 and March 8, 2005 (Scott and others, this volume, chap. 1; Moran and others, this volume, chap. 6). The January 16 explosion occurred shortly after 0300 Pacific standard time (PST, Greenwich mean time minus 8 hours) during a period of poor weather in the middle of the night and was not visible to either the VolcanoCam or Sugar Bowl systems. In contrast, the March 8 event took place at approximately 1725 PST during a time of clear weather (Scott and others, this volume, chap. 1; Moran and others, this volume, chap. 6). Analysis of Sugar Bowl imagery proved useful for the interpretation of seismic and acoustic data recorded during the event (Moran and others, this volume, chap. 6).

Figure 5. Rime-ice accumulation on Sugar Bowl telemetered digital camera at Mount St. Helens, Washington. Ice buildup was a common problem on camera systems during fall and winter months. USGS photo by S.P. Schilling, October 24, 2004.

Visual imagery from remote cameras was useful in the recognition and analysis of rockfall from the lava spines. Although background glow from the growing dome had been observed in VolcanoCam imagery starting on the night of October 11, 2004, brief, brighter flashes were noticed by Internet observers beginning on January 13, 2005 (such flashes probably occurred earlier than this date but were not observed because of either their low intensity or poor weather). These images prompted seismologists to review the overnight seismic records and led to the recognition that the flashes were associated with rockfall signals. A major VolcanoCam flash occurred at about 0303 PST on February 22, 2005, and was accompanied by a large seismic signal (fig. 7). Visual inspection by field crews on the following day recognized a new scar on the growing lava dome, confirming the occurrence of a large rockfall during the previous night.

Significant rockfall events during daylight hours were accompanied by bursts of ash that often drifted above the crater rim (Moran and others, this volume, chaps. 2 and 6). Combining imagery from the remote, telemetered digital cameras, which was available within minutes of acquisition, with real-time seismic data allowed for rapid recognition of the rockfall source. An example occurred on April 26, 2005, at approximately 1126 Pacific daylight time (PDT, Greenwich mean time minus 7 hours), when a part of spine 4 disintegrated, sending a small ash plume above the crater rim (fig. 8).

The volume of extruded lava at Mount St. Helens during 2004–2006 was calculated every 1–2 months by differencing digital elevation models (DEMs) derived from aerial photography or lidar data (Schilling and others, this volume, chap. 8). More frequent, but necessarily qualitative, estimates of the relative rate of lava extrusion could be made by examining time-lapse sequences acquired by the remote, telemetered digital cameras. For example, in December 2004, a marked decline in the release of seismic energy (Moran and others, this volume, chap. 2) suggested that the eruption was slowing. When a sequence of daily images from the Sugar Bowl remote camera was reviewed, however, it became clear that the overall rate of lava extrusion had not changed significantly across the lull in seismicity. The measurement of extrusion rates can be quantified by combining a DEM with the remote camera imagery, as demonstrated using data from the Sugar Bowl camera by Major and others (this volume, chap.

12). In an attempt to assess whether dome extrusion occurred smoothly or by a series of irregular surges correlative with seismicity, high-rate photography of a small field of view of patches on the growing lava dome was performed, but several factors limited the success of this experiment (Dzurisin and others, this volume, chap. 14).

Evolution of the Dome Complex Shown by Animations of Camera Imagery

Perhaps the most useful aspect of remote camera observations during 2004–6 at Mount St. Helens was the

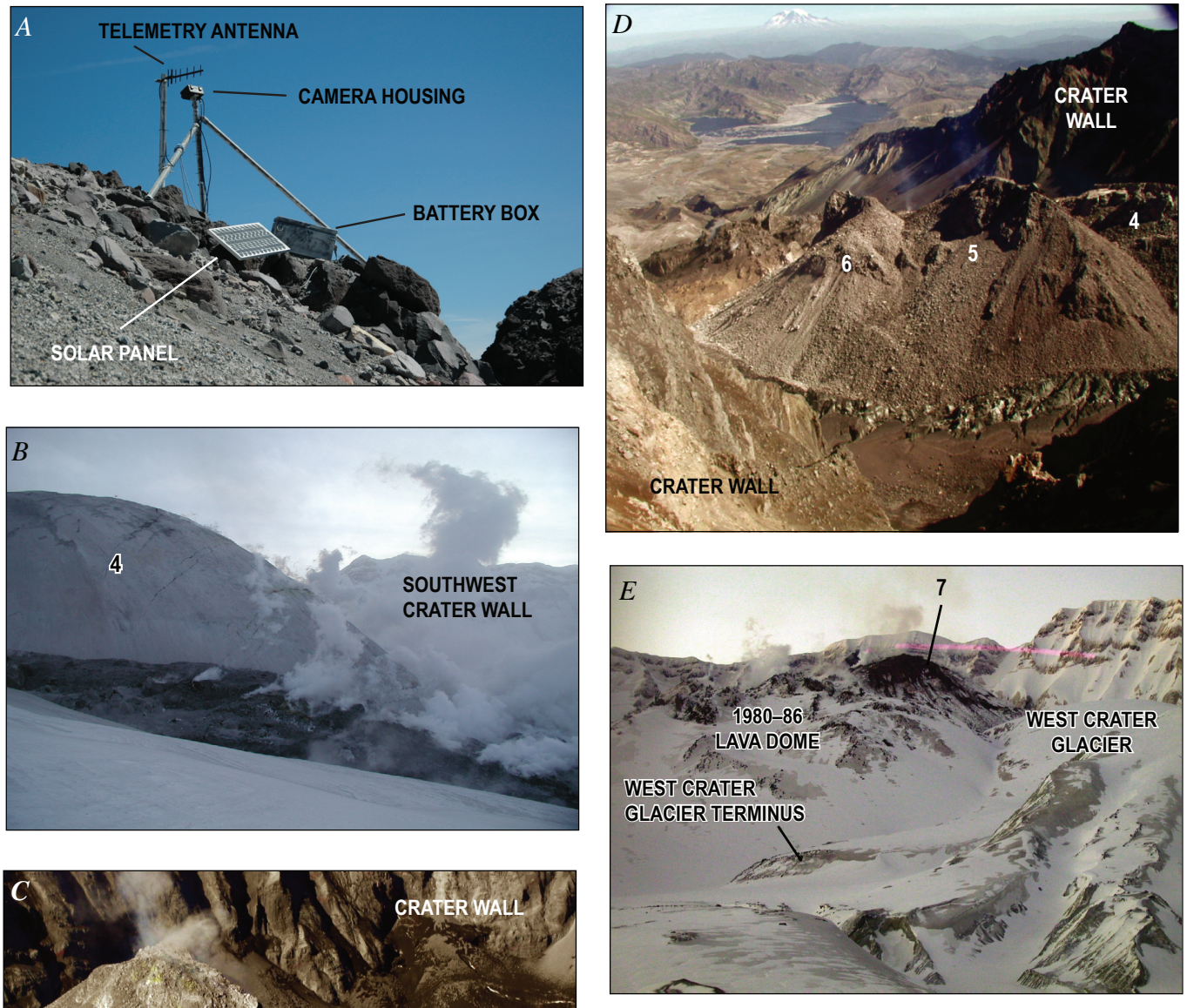

Figure 6. Other remote-camera setups and views at Mount St. Helens, Washington. Numbers on photos refer to spines as defined by Vallance and others (this volume, chap. 9). *A*, South Rim site, which also exemplifies equipment and installation style of Crater, Brutus, and Guacamole cameras. USGS photo by S.P. Schilling, August 19, 2005. *B*, Example of view from Crater camera, acquired January 15, 2005. *C*, Example of view from Brutus camera, acquired September 20, 2005. *D*, Example of view from South Rim camera, acquired August 19, 2005. *E*, Example of view from Guacamole camera, acquired February 24, 2006. Pink streak in middle of image is caused by sun damage to camera.

documentation of the lava dome complex's morphological evolution over time. During clear weather and rime ice-free conditions, and regardless of the presence of field personnel, the remote, telemetered cameras provided high-quality views of the volcano from common vantage points. Imagery was therefore directly comparable over time, and visualizing the changing morphology of the lava dome complex by animating images into time-lapse movies proved to be an important tool for monitoring and interpreting volcanic activity.

Time-lapse animations of images from the Sugar Bowl, Brutus, South Rim, and Guacamole remote camera are provided as supplementary digital data to this report (Major and others, this volume, chap. 12, appendix 1, found on the DVD accompanying the volume and on the Web version of the work). Below, we describe and interpret the time-lapse animations of dome growth at Mount St. Helens obtained from the remote, telemetered digital cameras during the period October 2004 to February 2006. This account relies heavily on the Sugar Bowl camera for observations during the first year of the eruption, when that was the only remote camera that had been deployed. The observations that follow are drawn solely from remote camera imagery and do not rely on other data. The account is not meant to supplant but rather to complement descriptions of dome growth derived from other types of observations and data that are contained elsewhere in this volume. The chronology of 2004–6 activity is reported in this volume by Scott and others (chap. 1), Schilling and others (chap. 8), Vallance and others (chap. 9), and Herriott and others (chap. 10). In addition, geophysical and geochemical time series from the eruption are summarized by Moran and others (chaps. 2 and 6), Lisowski and others, (chap. 15), LaHusen and others (chap. 16), Gerlach and others (chap. 26), and Pallister and others (chap. 30).

Between October 2004 and February 2006, dome growth at Mount St. Helens occurred through the extrusion of seven distinct spines (Scott and others, this volume, chap. 1; Vallance and others, this volume, chap. 9). Spines 1 and 2, formed in mid-October 2004, were the smallest of the extrusions, and they were active for the shortest periods of time. Owing to their location along the south margin of the 1980–86 lava dome, they were not visible to the Sugar Bowl camera or the VolcanoCam and were documented only by observations (including thermal imagery) from helicopter overflights. The growth of spines 3–7, however, was visible

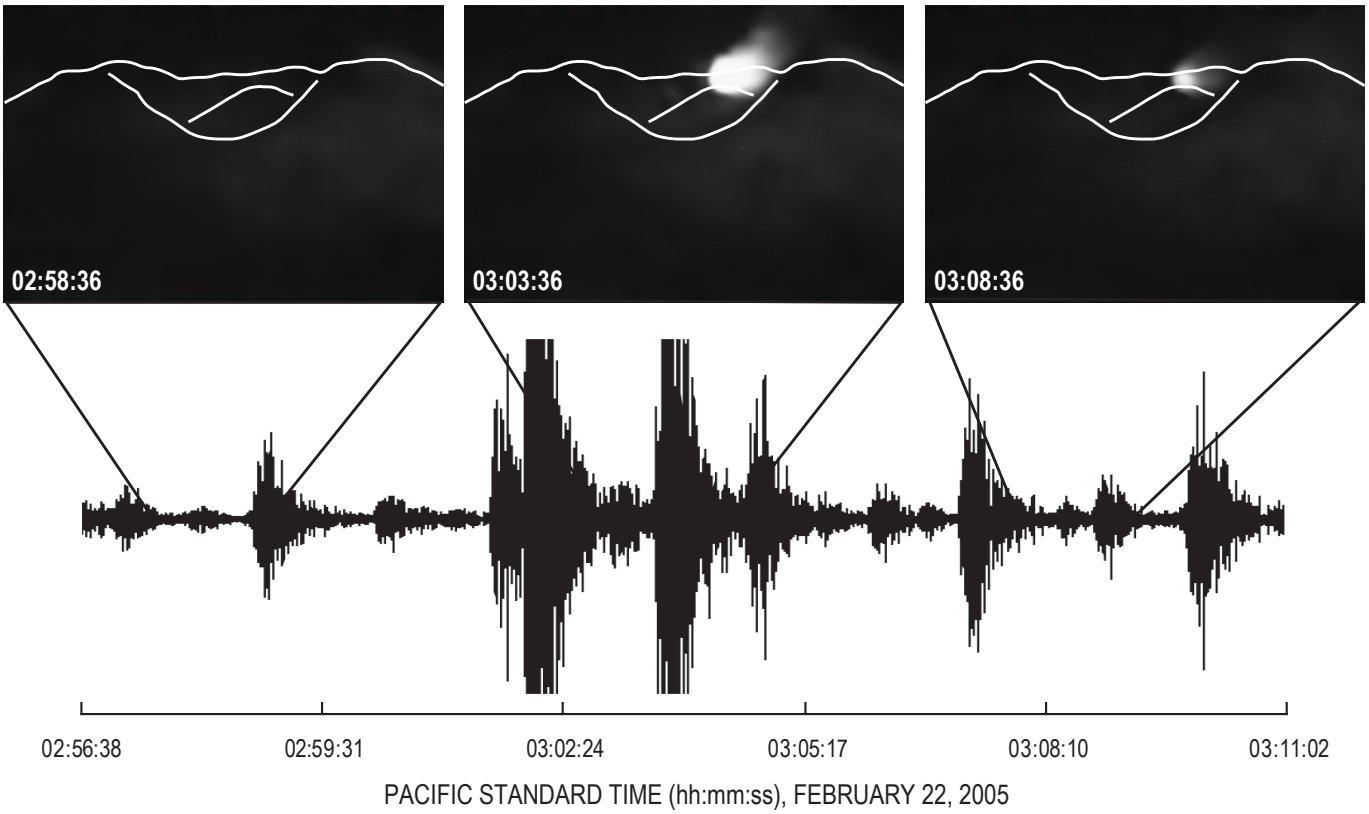

Figure 7. Use of nighttime images from the U.S. Department of Agriculture Forest Service VolcanoCam to track rockfalls at Mount St. Helens, Washington. Top, consecutive images from February 22, 2005 (PST), showing one of the largest rockfalls of that year. Bright patch is a reflection in steam clouds of incandescence created by the sudden exposure of hot material. Outline of Mount St. Helens and 1980–86 lava dome provided for context. VolcanoCam clock was not synchronized to Internet time, so it is probably only accurate to plus or minus 1 minute. Bottom, seismic record from station SHW (see fig. 2*A* for station location).

from the Sugar Bowl camera except for a brief interval during the growth of spine 6.

The Sugar Bowl camera was deployed after the welt had largely formed in the southeastern part of the crater. During the first week of image acquisition, the camera recorded growth of a small knob that protruded from the welt along the southeast margin of the 1980–86 lava dome. The knob disappeared during October 20–27, 2004, a period of inclement weather when no visual observations (either by remote camera or field personnel) were possible. Judging from oblique aerial photos, the bulge appeared to be crater-floor debris and ice that was pushed up and later collapsed during the initial stages of dome extrusion (J. Major, written commun., 2006).

Spine 3 first became apparent in Sugar Bowl camera imagery on October 29, 2004, when uplift of the welt accelerated rapidly. The spine continued to grow steadily towards the southeast until mid-December, when imagery from December 17 showed that cracks had formed along the north side of the extrusion. These cracks continued to develop throughout the remainder of the month, eventually leading to the formation of an independent spine of lava (spine 4). The breakup of spine 3 may have been caused when it impinged upon the

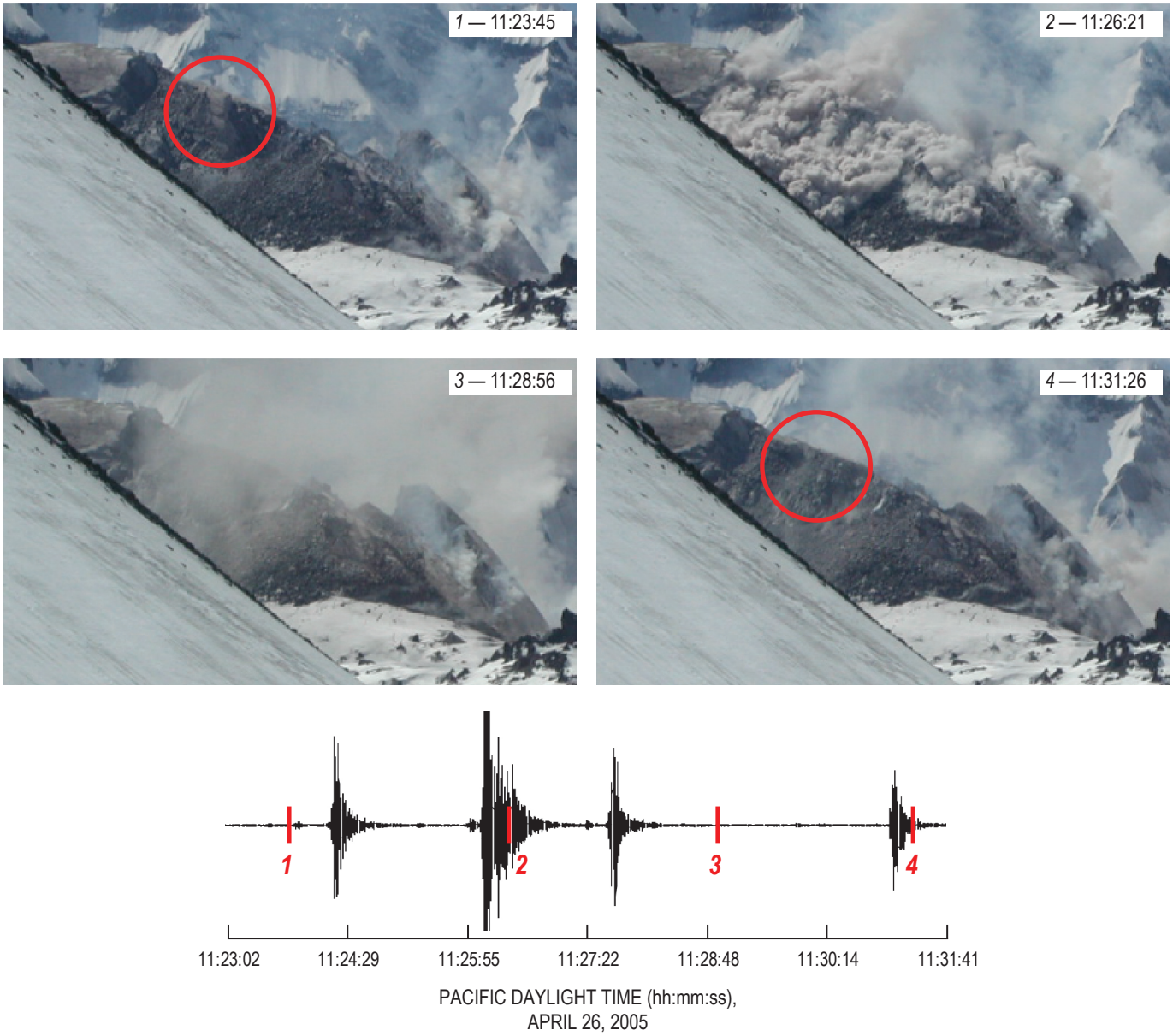

Figure 8. Seismic record from station YEL (bottom) and consecutive images from Sugar Bowl remote camera (top) for April 26, 2005 (PDT), showing major rockfall (source identified by red circle). See figure 2*A* for location of YEL.

southeastern crater wall (Vallance and others, this volume, chap. 9). The apparent extrusion velocity at the vent did not seem to change over this time period, judging from the photographic sequence from the Sugar Bowl camera and calculations of lineal extrusion rates (Major and others, this volume, chap. 12). If extrusion was constant, spine 3 was undergoing horizontal compression as lava continued to extrude from the vent, which probably caused it to fracture (Moran and others, this volume, chap. 2).

Spine 4, which was also characterized by dominantly southeastward motion, first rose to a higher altitude than spine 3, then began to override the latter in early January 2005. Sugar Bowl imagery suggests that the smooth surface of spine 4 began to fracture and disintegrate sometime between March 15 and April 13, 2005. A more definitive date is difficult to assign, because the view from Sugar Bowl was obscured by ice and clouds between those two dates, but field observations show that disintegration began about April 10 (Vallance and others, this volume, chap. 9). The increasingly fractured, but still coherent, spine continued to move to the southeast until April 24, 2005, by which time significant motion (that is, motion on the order of meters per day) had ceased and extrusive activity shifted from spine 4 to spine 5. Major and others (this volume, chap. 12) document this transition using quantitative lineal extrusion rates based on Sugar Bowl imagery.

The Sugar Bowl camera observed the initial formation of spine 5 between April 14 and 18, 2005, when upward motion and lineal extrusion rate (Major and others, this volume, chap. 12) of that spine became independent of spine 4. Spine 5 extruded at a steep angle (about 60°–70° from horizontal) from the vent and was subject to two cycles of construction and destruction during its life. Construction dominated until May 13, 2005, when a large part of the spine collapsed. Spine disintegration competed with extrusion to keep the spine at a relatively constant height from that time through June 4, 2005, when a second period dominated by construction began. By July 1, 2005, spine 5 had reached its highest altitude, although a period of more frequent collapses began around June 30, 2005. A few tens of meters of dome elevation were lost between July 1 and 3, 2005. Upward motion of spine 5 continued, but the highest altitude of the extrusion remained nearly constant between July 3 and 14, 2005, as collapses from the upper part of the spine compensated for the addition of new lava at its base. By July 15, 2005, destructive processes began to outpace spine construction, and the height of the spine decreased daily. Sugar Bowl imagery suggests that the second cycle of growth and destructive phases of spine 5 had mostly ceased by August 2, 2005.

The distinction between spines 5 and 6 is difficult to constrain, but Sugar Bowl images indicate that spine 6 was moving independently of spine 5 by August 1, 2005. Growth of spine 6 was mostly vertical until August 10, 2005, when it began to move to the west without increasing in height. Sugar Bowl imagery and lineal extrusion rates (Major and others, this volume, chap. 12) suggest an apparent acceleration in westward motion starting on about August 16, 2005, and the spine height began to decrease as large collapses destroyed its upper reaches. A consequence of the motion of spine 6 towards the west was the development of a depression between spine 6 and the mostly inactive spine 5. Continued extrusion to the west occurred throughout the remainder of August and September, with the spine's motion becoming almost completely horizontal. During this time period, the westernmost part of spine 5 gradually slumped into the growing depression, probably because it was left unsupported as spine 6 moved to the west (Vallance and others, this volume, chap. 9). Interestingly, unlike other spines, spine 6 apparently did not experience an extended period of collapse and destruction towards the end of its activity. This may have been a result of its relatively low height, compared to spines 3, 4, and 5.

Growth of spines 6 and 7 was well documented by the Brutus, South Rim, and Guacamole remote cameras, which were installed during late summer 2005. Sometime between September 28 and October 17, 2005 (a period of poor weather when few observations were possible), spine 6 gave way to spine 7, which grew out of the western side of the depression between spines 5 and 6. The direction of spine 7's motion was also toward the west but included a significant component of upward motion. As a result, spine 7 pushed and overrode spine 6, obscuring the distinction between the two extrusions. Although poor weather characterized much of late 2005 and early 2006, limited imagery indicates that spine 7 continued to grow into February 2006 with two cycles of alternating height increase (when the spine was gravitationally stable) and decrease (when the spine disintegrated gradually).

Time-lapse animation sequences from the remote, telemetered cameras reveal that spines 3 to 7 each experienced cycles of growth and destruction that lasted several months. The growth stages generally involved the extrusion of smooth-sided spines (with the exception of spine 6, which was mostly covered by rubble) with little accompanying large disintegration events. During destructive phases, spine extrusion continued, but abundant rockfall destroyed the smooth carapaces and resulted in highly fractured and blocky formations surrounded by talus. The onset of the destructive phase preceded the transition to a new spine in the cases of spines 3, 4, and 5. Spines 5 and 7 both experienced multiple constructive and destructive phases, perhaps related to their steeper extrusion angles. The "great spine" at La Montagne Pelée, Martinique, which was similar in appearance to the Mount St. Helens spines, also experienced multiple construction and destruction cycles during 1902–3, although the cycles appear to have been related to an unsteady, pulsing eruption rate (Jaupart and Allègre, 1991; Tanguy, 2004). At Mount St. Helens, lineal extrusion rates derived from Sugar Bowl imagery suggest that the eruption rate during the extrusion of spine 5 was nearly constant (Major and others, this volume, chap. 12); thus, alternating cycles of spine-height increase and erosion must have been controlled by other fac-

tors, for example, the strength of the dome carapace, thermal cooling, propagation of fractures, or gravitational stresses. Vallance and others (this volume, chap. 9) discuss the history and driving mechanisms of spine construction and destruction and the transitions between spines.

In addition to lava-dome processes and morphology, deformation of the Crater Glacier—which surrounded the 1980–86 lava dome on the east, west, and south before the onset of eruptive activity in 2004 (Schilling and others, 2004)—was recorded by several of the remote cameras. The Brutus camera's field of view included the contact between the western part of the dome complex and the west arm of the glacier. By the time the camera was installed in mid-September 2005, the west arm of Crater Glacier had already been extensively compressed, thickened, and fractured. The Brutus sequence of images showed continued thickening and cracking of glacial ice as spines 6 and 7 grew toward the west. A complementary perspective was provided by the Guacamole camera, which had a view of much of the glacier's west arm (including its terminus) and recorded glacier deformation from the time of its installation in mid-November 2005. Motion of the glacier's terminus occurred at an accelerated rate between January 23 and February 16, 2006, perhaps because of a downstream-moving bulge caused by compression of the glacier by spines 6 and 7 (Walder and others, this volume, chap. 13).

Strategies for Future Deployments of Remote Camera Systems

The bulk of the contributions from visual observation systems to monitoring efforts at Mount St. Helens in 2004–2006 are necessarily qualitative because of limitations in camera views and weather conditions. Images were generally used to support inferences drawn from geophysical and geological observations or to characterize transient events and long-term processes. As demonstrated by Major and others (this volume, chap. 12), however, quantitative measurements of surface change from single camera deployments are possible.

Future camera deployments at active volcanoes should take advantage of photogrammetric principles, which will allow for more detailed analyses of surface change. For example, oblique aerial photographs that include ground control points with known positions can be used to construct DEMs of the ground surface. The technique has been demonstrated in laboratory conditions (Cecchi and others, 2003), at small scales on active lava flows at Mount Etna (James and others, 2006), and at larger scales on an entire lava dome at Soufrière Hills volcano, Montserrat (Herd and others, 2005). Expanding the use of photogrammetry to terrestrial cameras can be accomplished by deploying a pair (or more) of remote, telemetered digital cameras with views that are separated by 30°–60° in azimuth from the target area and include several ground control points. A DEM of the areas viewed in common by a pair of cameras can then be constructed, and displacements, perhaps on the order of centimeters, may be calculated by differencing DEMs from different time periods. Although the principles involved in deriving such DEMs are not new, they have yet to be applied extensively using ground-based cameras. Terrestrial systems, although limited by weather conditions, offer the benefits of low cost, low power, flexibility, and high temporal and spatial measurement density. Dome-building eruptions characterized by steady topographic change over time, like the 2004–6 activity at Mount St. Helens, offer an excellent opportunity for developing terrestrial photogrammetric systems.

Conclusions

Remote camera systems have provided important information regarding volcanic activity at Mount St. Helens during 2004–6. A Webcam and a network of remote, telemetered digital cameras observed rockfalls, explosive activity, and the steady extrusion of lava on a nearly continuous basis, interrupted only by periods of inclement weather and infrequent mechanical failures. Time-lapse animations from the remote, telemetered digital cameras are outstanding records of lava dome emplacement that can be used to aid interpretations of volcanic activity and support education and outreach efforts.

Acknowledgments

The authors would like to thank the staff of the Hawaiian Volcano Observatory, particularly Rick Hoblitt (now at the USGS Cascades Volcano Observatory), Tim Orr, Richard Herd (now at the University of East Anglia in the United Kingdom), and Kevan Kamibayashi, for constructing and testing the first of the Mount St. Helens remote, telemetered cameras and sending the instrument to CVO for deployment at Sugar Bowl dome. Remote camera deployment was conducted with the assistance of Gene Iwatsubo, Stephanie Konfal, and Kirstie Simpson; Jon Major maintained the camera after it was installed and analyzed the imagery. Seismic data used in figures 7 and 8 were provided through the Incorporated Research Institutions for Seismology by the Pacific Northwest Seismic Network. Noise-filtered images from the VolcanoCam used to produce figure 7 were provided by Darryl Luscombe; David Ramsey generated the DEM that formed the backdrop for figure 2*A*. Jane Takahashi, Richard Herd, and Seth Moran provided valuable reviews.

References Cited

Baldi, P., Fabris, M., Marsella, M., and Monticelli, R., 2005, Monitoring the morphological evolution of the Sciara del Fuoco during the 2002–2003 Stromboli eruption using multi-temporal photogrammetry: ISPRS Journal of Photogrammetry and Remote Sensing, v. 59, no. 4, p. 199–211.

Cecchi, E., van Wyk de Vries, B., Lavest, J.M., Harris, A., and Davies, M., 2003, N-view reconstruction; a new method for morphological modeling and deformation measurement in volcanology: Journal of Volcanology and Geothermal Research, v. 123, nos. 1–2, p. 181–201.

Criswell, C.W., 1987, Chronology and pyroclastic stratigraphy of the May 18, 1980, eruption of Mount St. Helens, Washington: Journal of Geophysical Research, v. 92, no. B10, p. 10237–10266.

Dzurisin, D., Lisowski, M., Poland, M.P., Sherrod, D.R., and LaHusen, R.G., 2008, Constraints and conundrums resulting from ground-deformation measurements made during the 2004–2005 dome-building eruption of Mount St. Helens, Washington, chap. 14 *of* Sherrod, D.R., Scott, W.E., and Stauffer, P.H., eds., A volcano rekindled; the renewed eruption of Mount St. Helens, 2004–2006: U.S. Geological Survey Professional Paper 1750 (this volume).

Gerlach, T.M., McGee, K.A., and Doukas, M.P., 2008, Emission rates of CO_2, SO_2, and H_2S, scrubbing, and preeruption excess volatiles at Mount St. Helens, 2004–2005, chap. 26 *of* Sherrod, D.R., Scott, W.E., and Stauffer, P.H., eds., A volcano rekindled; the renewed eruption of Mount St. Helens, 2004–2006: U.S. Geological Survey Professional Paper 1750 (this volume).

Herd, R.A., Edmonds, M., and Bass, V.A., 2005, Catastrophic lava dome failure at Soufrière Hills Volcano, Montserrat, 12–13 July 2003: Journal of Volcanology and Geothermal Research, v. 148, nos. 3–4, p. 234–252, doi:10.1016/j.jvolgeores.2005.05.003.

Herriott, T.M., Sherrod, D.R., Pallister, J.S., and Vallance, J.W., 2008, Photogeologic maps of the 2004–2005 Mount St. Helens eruption, chap. 10 *of* Sherrod, D.R., Scott, W.E., and Stauffer, P.H., eds., A volcano rekindled; the renewed eruption of Mount St. Helens, 2004–2006: U.S. Geological Survey Professional Paper 1750 (this volume).

Hoblitt, R.P., 2000, Was the 18 May 1980 lateral blast at Mt. St. Helens the product of two explosions?: Philosophical Transactions of the Royal Society of London, Series A, v. 358, no. 1770, p. 1639–1661.

James, M.R., Robson, S., Pinkerton, H., and Ball, M., 2006, Oblique photogrammetry with visible and thermal images of active lava flows: Bulletin of Volcanology, v. 69, no. 1, p. 105–108.

Jaupart, C., and Allègre, C.J., 1991, Gas content, eruption rate, and instabilities of eruption regime in silicic volcanoes: Earth and Planetary Science Letters, v. 102, nos. 3–4, p. 413–429.

Lacroix, A., 1908, La Montagne Pelée apres ses eruptions: Paris, Académie des Sciences, 136 p.

LaHusen, R.G., Swinford, K.J., Logan, M., and Lisowski, M., 2008, Instrumentation in remote and dangerous settings; examples using data from GPS "spider" deployments during the 2004–2005 eruption of Mount St. Helens, Washington, chap. 16 *of* Sherrod, D.R., Scott, W.E., and Stauffer, P.H., eds., A volcano rekindled; the renewed eruption of Mount St. Helens, 2004–2006: U.S. Geological Survey Professional Paper 1750 (this volume).

Lisowski, M., Dzurisin, D., Denlinger, R.P., and Iwatsubo, E.Y., 2008, Analysis of GPS-measured deformation associated with the 2004–2006 dome-building eruption of Mount St. Helens, Washington, chap. 15 *of* Sherrod, D.R., Scott, W.E., and Stauffer, P.H., eds., A volcano rekindled; the renewed eruption of Mount St. Helens, 2004–2006: U.S. Geological Survey Professional Paper 1750 (this volume).

Major, J.J., Kingsbury, C.G., Poland, M.P., and LaHusen, R.G., 2008, Extrusion rate of the Mount St. Helens lava dome estimated from terrestrial imagery, November 2004–December 2005, chap. 12 *of* Sherrod, D.R., Scott, W.E., and Stauffer, P.H., eds., A volcano rekindled; the renewed eruption of Mount St. Helens, 2004–2006: U.S. Geological Survey Professional Paper 1750 (this volume).

Mimatsu, M., 1995, Showa-Shinzan diary; complete records of observation of the process of the birth of Showa-Shinzan, expanded reprint [Oshima, M., translator]: Sapporo, Suda Seihan Co., 179 p.

Moore, J.G., and Albee, W.C., 1981, Topographic and structural changes, March–July 1980—photogrammetric data, *in* Lipman, P.W., and Mullineaux, D.R., eds., The 1980 eruptions of Mount St. Helens, Washington: U.S. Geological Survey Professional Paper 1250, p. 123–141.

Moore, J.G., and Rice, C.R., 1984, Chronology and character of the May 18, 1980, explosive eruptions of Mount St. Helens, *in* Explosive volcanism; inception, evolution, and hazards: Washington D.C., National Academies Press, p. 133–142.

Moran, S.C., Malone, S.D., Qamar, A.I., Thelen, W.A., Wright, A.K., and Caplan-Auerbach, J., 2008a, Seismicity associated with renewed dome building at Mount St. Helens, 2004–2005, chap. 2 *of* Sherrod, D.R., Scott, W.E., and Stauffer, P.H., eds., A volcano rekindled; the renewed eruption of Mount St. Helens, 2004–2006: U.S. Geological Survey Professional Paper 1750 (this volume).

Moran, S.C., McChesney, P.J., and Lockhart, A.B., 2008b, Seismicity and infrasound associated with explosions at Mount St. Helens, 2004–2005, chap. 6 *of* Sherrod, D.R., Scott, W.E., and Stauffer, P.H., eds., A volcano rekindled; the renewed eruption of Mount St. Helens, 2004–2006: U.S. Geological Survey Professional Paper 1750 (this volume).

Orr, T., and Hoblitt, R.P., 2006, Monitoring Kilauea Volcano using non-telemetered time-lapse camera systems [abs.]: Eos (American Geophysical Union Transactions), v. 87, no. 52, Fall Meeting Supplement, Abstract G53A-0875.

Pallister, J.S., Thornber, C.R., Cashman, K.V., Clynne, M.A., Lowers, H.A., Mandeville, C.W., Brownfield, I.K., and Meeker, G.P., 2008, Petrology of the 2004–2006 Mount St. Helens lava dome—implications for magmatic plumbing and eruption triggering, chap. 30 *of* Sherrod, D.R., Scott, W.E., and Stauffer, P.H., eds., A volcano rekindled; the renewed eruption of Mount St. Helens, 2004–2006: U.S. Geological Survey Professional Paper 1750 (this volume).

Pierson, T.C., 1985, Initiation and flow behavior of the 1980 Pine Creek and Muddy River lahars, Mount St. Helens, Washington: Geological Society of America Bulletin, v. 96, no. 8, p. 1056–1069.

Schilling, S.P., Carrara, P.E., Thompson, R.A., and Iwatsubo, E.Y., 2004, Posteruption glacier development within the crater of Mount St. Helens, Washington, USA: Quaternary Research, v. 61, no. 3, p. 325–329.

Schilling, S.P., Thompson, R.A., Messerich, J.A., and Iwatsubo, E.Y., 2008, Use of digital aerophotogrammetry to determine rates of lava dome growth, Mount St. Helens, Washington, 2004–2005, chap. 8 *of* Sherrod, D.R., Scott, W.E., and Stauffer, P.H., eds., A volcano rekindled; the renewed eruption of Mount St. Helens, 2004–2006: U.S. Geological Survey Professional Paper 1750 (this volume).

Scott, W.E., Sherrod, D.R., and Gardner, C.A., 2008, Overview of the 2004 to 2006, and continuing, eruption of Mount St. Helens, Washington, chap. 1 *of* Sherrod, D.R., Scott, W.E., and Stauffer, P.H., eds., A volcano rekindled; the renewed eruption of Mount St. Helens, 2004–2006: U.S. Geological Survey Professional Paper 1750 (this volume).

Tanguy, J.-C., 2004, Rapid dome growth at Montagne Pelée during the early stages of the 1902–1905 eruption; a reconstruction from Lacroix's data: Bulletin of Volcanology, v. 66, no. 7, p. 615–621, doi:10.1007/s00445-004-0344-z.

Topinka, L., 1992, Basic photography at Mount St. Helens and other Cascade volcanoes, *in* Ewert, J. and Swanson, D., eds., Monitoring volcanoes; techniques and strategies used by the staff of the Cascades Volcano Observatory, 1980–90: U.S. Geological Survey Bulletin 1966, p. 195–217.

Vallance, J.W., Schneider, D.J., and Schilling, S.P., 2008, Growth of the 2004–2006 lava-dome complex at Mount St. Helens, Washington, chap. 9 *of* Sherrod, D.R., Scott, W.E., and Stauffer, P.H., eds., A volcano rekindled; the renewed eruption of Mount St. Helens, 2004–2006: U.S. Geological Survey Professional Paper 1750 (this volume).

Voight, B., 1981, Time scale for the first moments of the May 18 eruption, *in* Lipman, P.W., and Mullineaux, D.R., eds., The 1980 eruptions of Mount St. Helens, Washington: U.S. Geological Survey Professional Paper 1250, p. 69–86.

Voight, B., Glicken, H., Janda, R.J., and Douglass, P.M., 1981, Catastrophic rockslide avalanche of May 18, *in* Lipman, P.W., and Mullineaux, D.R., eds., The 1980 eruptions of Mount St. Helens, Washington: U.S. Geological Survey Professional Paper 1250, p. 347–377.

Walder, J.S., Schilling, S.P., Vallance, J.W., and LaHusen, R.G., 2008, Effects of lava-dome growth on the Crater Glacier of Mount St. Helens, Washington, chap. 13 *of* Sherrod, D.R., Scott, W.E., and Stauffer, P.H., eds., A volcano rekindled; the renewed eruption of Mount St. Helens, 2004–2006: U.S. Geological Survey Professional Paper 1750 (this volume).

Watts, R.B., Herd, R.A., Sparks, R.S.J., and Young, S.R., 2002, Growth patterns and emplacement of the andesitic lava dome at Soufrière Hills Volcano, Montserrat, *in* Druitt, T.H., and Kokelaar, B.P., eds., The eruption of Soufrière Hills Volcano, Montserrat, from 1995–1999: Geological Society of London Memoir 21, p. 115–152.

A Volcano Rekindled: The Renewed Eruption of Mount St. Helens, 2004–2006
Edited by David R. Sherrod, William E. Scott, and Peter H. Stauffer
U.S. Geological Survey Professional Paper 1750, 2008

Chapter 12

Extrusion Rate of the Mount St. Helens Lava Dome Estimated from Terrestrial Imagery, November 2004–December 2005

By Jon J. Major[1], Cole G. Kingsbury[1], Michael P. Poland[2], and Richard G. LaHusen[1]

Abstract

Oblique, terrestrial imagery from a single, fixed-position camera was used to estimate linear extrusion rates during sustained exogenous growth of the Mount St. Helens lava dome from November 2004 through December 2005. During that 14-month period, extrusion rates declined logarithmically from about 8–10 m/d to about 2 m/d. The overall ebbing of effusive output was punctuated, however, by episodes of fluctuating extrusion rates that varied on scales of days to weeks. The overall decline of effusive output and finer scale rate fluctuations correlated approximately with trends in seismicity and deformation. Those correlations portray an extrusion that underwent episodic, broad-scale stick-slip behavior superposed on the finer scale, smaller magnitude stick-slip behavior that has been hypothesized by other researchers to correlate with repetitive, nearly periodic shallow earthquakes.

Introduction

Aerial and terrestrial photography are effective ways of monitoring morphological changes that occur during volcanic eruptions (see, for example, Zlotnicki and others, 1990; Yamashina and others, 1999; Baldi and others, 2000, 2005; Honda and Nagai, 2002; Herd and others, 2005; Thompson and Schilling, 2007; Poland and others, this volume, chap. 11; Schilling and others, this volume, chap. 8). Some camera deployments and photography campaigns are aimed chiefly at monitoring volcanic activity qualitatively, whereas others endeavor to gather photographs sufficient to make quantitative (photogrammetric) measurements of static features or dynamic processes. For example, aerial photography has been used to estimate volumes of volcanic deposits and lava domes, to measure magnitudes of edifice deformation, to estimate volumetric loss during dome collapse, and to model development of volcano glaciers (for example, Moore and Albee, 1981; Jordan and Kieffer, 1981; Zlotnicki and others, 1990; Sparks and others, 1998; Schilling and others, 2004; Herd and others, 2005; Schilling and others, this volume, chap. 8). Similarly, ground-based photographs have been used to provide dynamic data of active processes, such as velocity estimates of large debris avalanches and lateral blasts (Voight, 1981), short-term (days) growth rates of lava domes (Yamashina and others, 1999), and motion of lava flows (James and others, 2006), and for geometric reconstructions of volcanic stratigraphy (Dungan and others, 2001). Commonly, stereoscopic imagery is used in such analyses, but apparent parallax caused by movement of an object in repeat photographs from a fixed position has also been exploited.

During the 2004–5 eruption of Mount St. Helens, oblique terrestrial imagery from remotely stationed cameras was one of the chief methods for monitoring the nature and pace of the eruption (Poland and others, this volume, chap. 11). Cameras were deployed principally to monitor the eruption visually without exposing scientists to unnecessary risk and to provide ancillary information on conditions in the crater (such as weather, the amount of steaming, or blowing ash) for purposes of planning field work. They were not deployed specifically for photogrammetric purposes.

Quantitative analysis of oblique terrestrial imagery commonly requires stereoscopic imagery or well-controlled nonstereoscopic imagery from multiple camera positions (Wolf and Dewitt, 2000). From October 2004 through December 2005 and beyond (Poland and others, this volume, chap. 11), however, we obtained repeat, ground-based imagery of the Mount St. Helens eruption from a single, fixed-position

[1] U.S. Geological Survey, 1300 SE Cardinal Court, Vancouver, WA 98683

[2] U.S. Geological Survey, PO Box 51, Hawaii National Park, HI 96718

camera located near the mouth of the volcano's crater. After August 2005, other ground-based cameras were located elsewhere around the volcano (Poland and others, this volume, chap. 11), but none of those provided stereoscopic imagery. In this paper, we employ a methodology for quantifying the linear extrusion rate of a growing silicic lava dome from the imagery obtained by the camera deployed near the crater mouth, summarize the results of spatial and temporal variations of dome growth and extrusion rates from November 2004 through December 2005, and compare our results with corresponding time series of seismic-energy release and local deformation measured by continuous Global Position System (GPS) receivers (Moran and others, this volume, chap. 2; LaHusen and others, this volume, chap. 16). Previously, average extrusion rates of silicic lava domes have been determined for discrete, short-lived eruptions or eruptive episodes (for example, Huppert and others, 1982; Swanson and others, 1987; Nakada and others, 1995; Sparks and others, 1998), although extrusion rates of a continuous, decadal-scale eruption have been measured by Rose (1987) and by Harris and others (2003). Demonstration of fine-scale temporal and spatial rate variation during a long-term, continuous extrusion is rare, however (for example, Sparks and others, 1998). Our data provide further insights on fine-scale behavior of sustained silicic dome growth, and they provide constraints for mathematical models that elucidate the physics of dome growth (for example, Barmin and others, 2002; Melnik and Sparks, 2005; Iverson and others, 2006; Iverson, this volume, chap. 21; Mastin and others, this volume, chap. 22).

The Sugar Bowl Camera

To photographically monitor dome growth at Mount St. Helens, we deployed a camera at the northeast end of the volcano's crater, on the Sugar Bowl lava dome, about 2.3 km from the locus of eruptive activity (fig. 1*A*). We used an Olympus 3030Z camera having a serial port (fig. 1*B*).

The camera utilizes a 1/1.8 inch solid-state sensor and has a nominal 6.5–19.5 mm focal length lens, equivalent to a 32–96 mm lens on a 35-mm camera. The camera was programmed to expose images at its maximum focal length and to record them at 1,280×960 pixels (~1.2-megapixel images). The relatively low-resolution setting was intended to permit rapid capture and transmission of images of explosions or other dynamic phenomena. Communications with the camera and transmission of images were enabled via radio through the serial port. Images were transmitted to a base-station computer located at the Mount St. Helens National Volcanic Monument's Coldwater Ridge Visitor Center, ~13 km downvalley (northwest) from the volcano. Once an image was transmitted, the camera acquired another image. The rate at which an image could be transmitted through the radio link governed the frequency of image acquisition, but in general images were acquired about every 3 minutes during daylight hours. Approximately once per hour the base-station computer transmitted an image to the Cascades Volcano Observatory. As needed, the computer could be queried to retrieve images more frequently. Periodically, all images were retrieved from the Coldwater Ridge Visitor Center.

The camera, deployed in a weatherproof housing (fig. 1*B*), began operating on October 10, 2004 (Poland and others, this volume, chap. 11). It was replaced by another camera and remounted on a fixed pipe in February 2006 and replaced again in May 2006. Owing to episodic cloud cover, ice rime, pitting of the window glass, and unit failures, usable imagery is discontinuous over the period of deployment. In this paper we focus on imagery obtained from November 2004 through December 2005, roughly the first year of the eruption that began in October 2004.

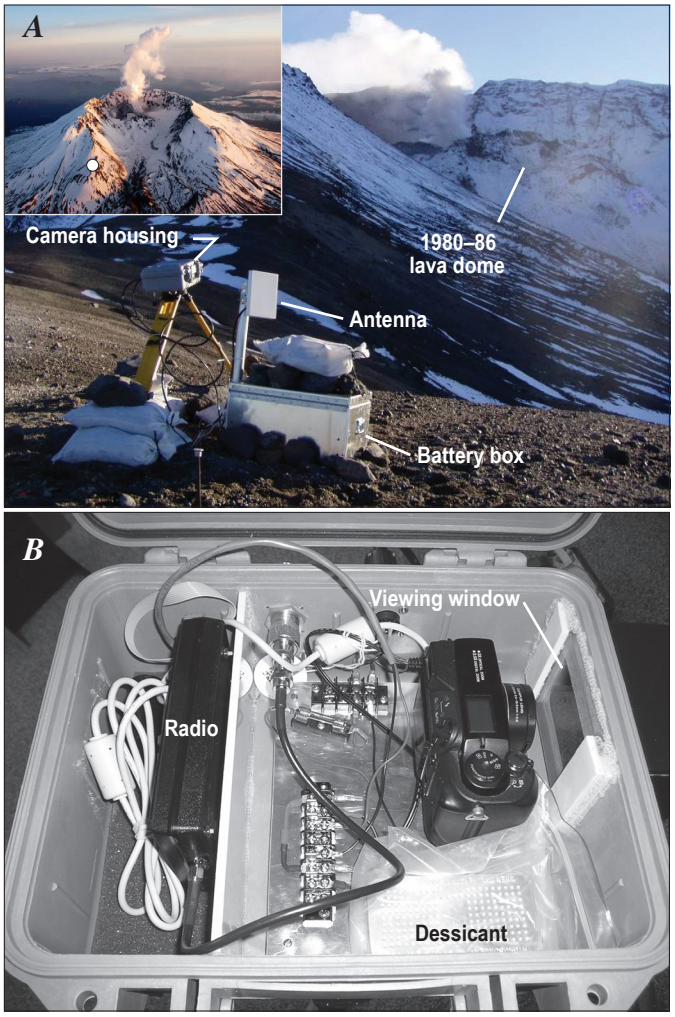

Figure 1. Photographs showing the camera system at Sugar Bowl lava dome. *A*, Deployed system at crater mouth. View is to southwest. Inset shows site location (white dot) on Sugar Bowl dome. Locus of eruptive activity is marked by emission of steam immediately to left rear of the partly snowclad 1980s lava dome. *B*, Camera and radio inside weatherproof housing.

Methodology

Theory of Terrestrial Image Analysis

The style of terrestrial imagery is defined on the basis of the orientation of the camera axis at the time of exposure. A horizontal terrestrial image is obtained when the camera axis is oriented horizontally at the time of exposure. If the camera is properly leveled before exposure, the x and z photographic axes are, respectively, oriented horizontally and vertically. Armed with precise information about camera and lens characteristics and an ability to pinpoint the optical center, or principal point, of a photograph, one can employ simple trigonometry to determine the horizontal and vertical angles between the camera axis and the rays to points in an object space (Wolf and Dewitt, 2000; fig. 2). If the camera is inclined from the horizontal, the resulting photograph is considered an oblique terrestrial image. In that case, computations of the angular differences between the camera axis, the rays to objects of interest, and a horizontal plane must account for the angle of inclination of the camera (Wolf and Dewitt, 2000).

The geometric relations among a camera's position, L, its focal length, f, the principal point of the photograph, o, the inclination angle of the camera axis, θ, and the horizontal and vertical angles to an image point are shown in figure 3. The horizontal angle, α_a, between the vertical plane containing image point a and the vertical plane containing the camera axis, Lo, is given by (Wolf and Dewitt, 2000):

$$\alpha_a = \tan^{-1}(x_a / f\sec\theta - z_a \sin\theta). \quad (1)$$

To conform to sign conventions, negative inclination angles refer to depression below, and positive inclination angles to elevation above, the horizontal (Wolf and Dewitt, 2000). In equation 1, correct algebraic signs must be applied to x_a, z_a, and θ. The vertical angle,β_a, to image point a is given by

$$\beta_a = \tan^{-1}(z_a \cos\theta / (f\sec\theta - z_a \sin\theta)\sec\alpha_a). \quad (2)$$

In equation 2, the algebraic sign of β is automatically obtained from the sign of the z_a coordinate (Wolf and Dewitt, 2000).

Although equations 1 and 2 allow determination of the horizontal and vertical angles to any image point relative to the camera axis, they represent an underdetermined system of equations with respect to quantifying horizontal or vertical distances unless some geodetic control can be established between the camera and an object of interest. Typically, control is provided by interior and exterior referenced orientations. Interior orientation includes camera

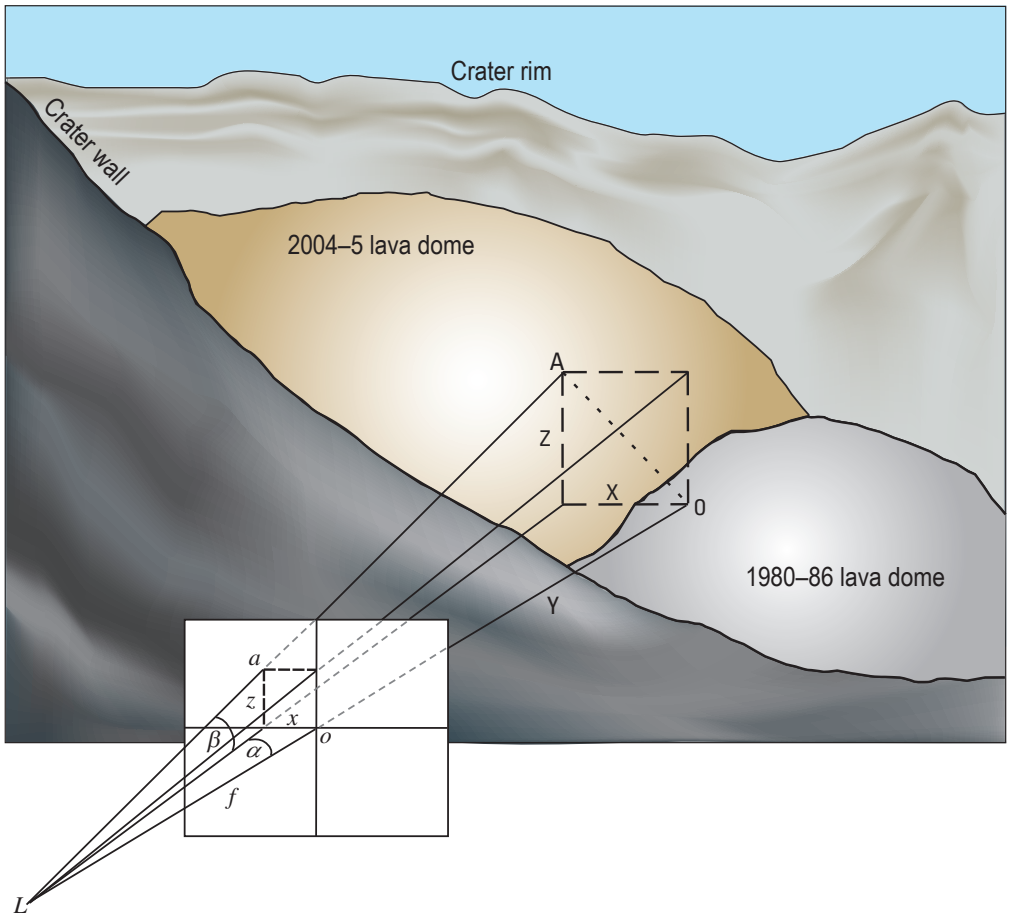

Figure 2. Diagram showing relations among optical rays from photographed objects and images projected in the focal plane for a horizontal terrestrial image. For clarity, positions of the focal plane and lens nodal point have been reversed. Focal length of the lens, f, and principal point of the image, o, are shown relative to L, the lens nodal point or position of the camera. Projections of object point, A, and the horizontal (X) and vertical (Z) distances of the object point relative to the camera axis are shown on the projected image as a, x, and z, respectively. Object distance, Y, horizontal angle, α, between the vertical plane containing the object point and the vertical plane containing the camera axis, and vertical angle, β, from a horizon line to the object point are also shown.

calibration parameters such as lens focal length, location of the image principal point, and corrections for lens distortion. Exterior orientation refers to the position and orientation of the camera with respect to a ground-based reference frame or with respect to the photographed object (Wolf and Dewitt, 2000; Molander, 2001). Orientation with respect to a ground-based reference frame is commonly accomplished by combining camera control (position and orientation) with object-space control (through established control points within the field of view).

In the absence of sound calibration parameters, one can approximate interior orientation of a digital camera from metadata contained in an image's exchangeable image format (EXIF) file and by assuming that the principal point is at the center of the image. At maximum focal length, zoom lenses commonly have minimal distortion, even on consumer-grade cameras. Such assumptions, of course, can introduce large errors to a photogrammetric analysis.

In the absence of independently established control points, one way to establish exterior orientation of a fixed camera is by measuring the orientation and position of the camera with respect to a photographed object. For the Sugar Bowl camera, we lack rigid calibration parameters. We do, however, have empirical calibration parameters from four similar cameras. In the absence of a solid camera calibration, we used averaged parameters obtained from the calibrations of those other cameras (table 1). We imposed exterior control on the imagery by measuring the camera orientation (direction of the camera axis and angle of inclination) and its location (using GPS), and we established its position relative to the proximal part of the actively growing dome by measuring coordinates and distances between the camera and the dome on sequential digital elevation models (DEMs) (Schilling and others, this volume, chap. 8; fig. 4). By fixing the distance between the camera and the near-vent area of the dome between sequential DEMs, knowing the camera orientation, and employing averaged lens characteristics, we solved all necessary trigonometric equations and roughly quantified magnitudes and rates of dome growth.

Resolving horizontal and vertical displacement rates within the focal plane of the image provided only apparent rates of extrusion, however. Quantifying more accurate linear

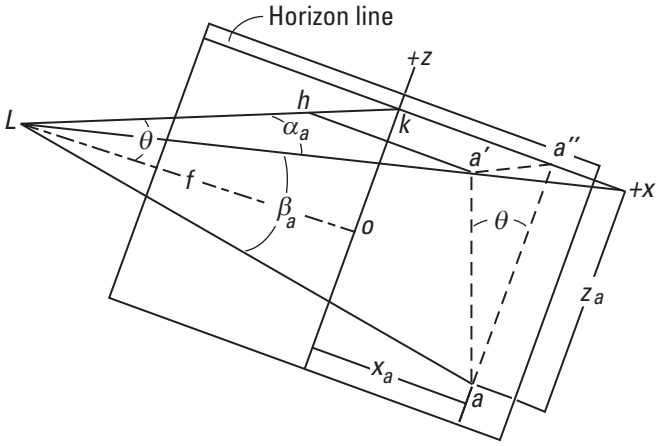

Figure 3. Diagram showing relations among optical rays from photographed objects and images projected in the focal plane of the camera for an oblique terrestrial image (slightly modified from Wolf and Dewitt, 2000; diagram copyright The McGraw-Hill Companies, Inc.). For clarity, the positions of the focal plane and lens nodal point have been reversed (see fig. 2). Focal length of the lens, *f*, principal point of the image, o, and angle of inclination of the camera axis, θ, are shown relative to *L*, the lens nodal point or position of the camera, and a horizontal line (*+x*). The projection of object point A (not shown) and its position relative to the photograph coordinate system (*+x*, *+z*) are shown on the projected image as *a*, x_a, and z_a, respectively. Line *Lk* is a horizontal line that intersects the photograph at point *k*. Line *aa´* is a vertical line, with *a´* located in a horizontal plane. Points *h* and *a*'' represent geometric projections used in the derivation of equations 1 and 2. Angles α_a and β_a are the horizontal and vertical angles of the image point, *a*, relative to horizontal and vertical axes. See Wolf and Dewitt (2000) for detailed discussions of geometric relations and derivations of equations 1 and 2.

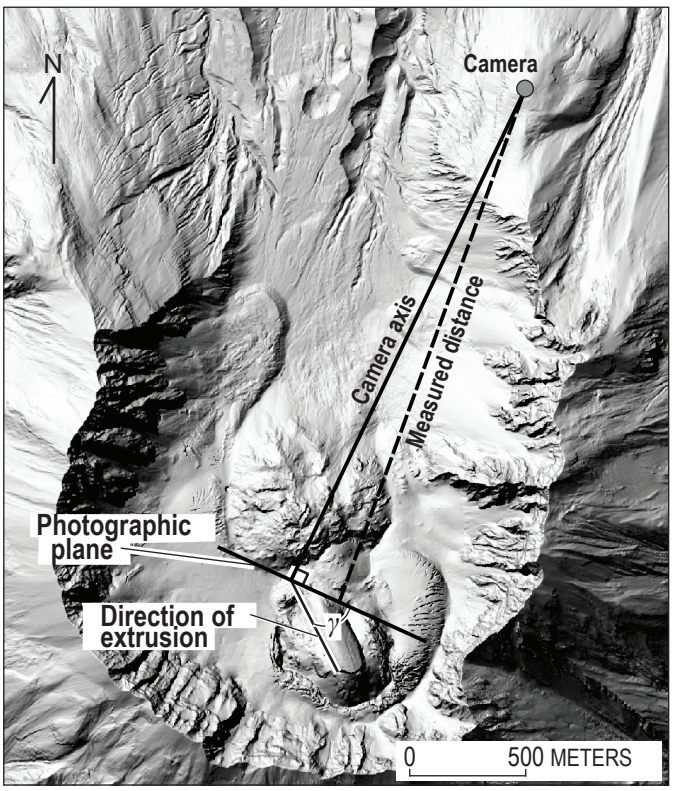

Figure 4. Digital elevation model of Mount St. Helens for February 21, 2005, showing positions of Sugar Bowl camera and 2004–5 lava dome, and relation between camera axis and obliquity of extrusion, γ. Measured distance is from camera to an identifiable feature on the dome. Trigonometric manipulation of this distance and the angular difference between that axis and the camera axis allowed computation of the distance along the camera axis.

Table 1. Camera characteristics and orientation parameters for the Sugar Bowl imagery, Mount St. Helens, Washington.

Parameter	Value
Camera characteristics	
Maximum sensor width [1]	7.76 mm
Maximum pixels at 1.2 megapixel setting	1,280 (1,280 × 960)
Field of view (at maximum focal length)	21°±1°
Resolvable pixel footprint at nominal distance to dome	~ 0.65 m
Lens characteristics	
Lens focal length (maximum) [1]	20.8 mm±1.2 mm
Lens distortion (radial) [1]	$\leq 10^{-4}$ mm
Camera orientation	
Inclination angle	7°±0.5°
Axis azimuth	207°±0.5°
Spatial measurements	
Camera location (UTM coordinates, zone 10, datum is WGS84)	5118137N, 563633E, ±10 m
Distance from camera to plane tangent to proximal dome	2,315 m ± 30 m
Obliquity of extrusion relative to focal plane	27°–53°±2°

[1] Values of these parameters represent averages obtained from empirical calibrations (using Photomodeler Pro 5) of four other Olympus C3030Z cameras.

extrusion rates of the dome required resolving trigonometric differences between the apparent direction of motion in the focal plane and the actual direction of motion. Again, by using sequential DEMs of the dome, we measured the angle of obliquity, γ, between the focal plane and the principal direction of dome growth (fig. 4). Analysis of a three-dimensional pyramid formed by the principal motion vectors (fig. 5) revealed that the angle, δ, between the vector of apparent motion in the focal plane (vector **c** in fig. 5) and the vector of actual motion (vector **V** in fig. 5) is related to the obliquity angle, γ, measured on the DEMs by

$$\delta = \tan^{-1}(R \tan \gamma), \qquad (3)$$

where R is the ratio of the horizontal motion vector (vector **b** in fig. 5) to the resolved motion vector, **c**, in the focal plane (fig. 5). From that relation, simple trigonometric relations can be solved to estimate the extrusion rate in the direction of dome growth. Our methods and analysis are, of course, subject to many possible errors (discussed below) and are limited to extrusion rates that exceed about 1 to 1.5 m/d (displacements of about 2 to 3 pixels per day; table 1). Nevertheless, they represent useful procedures for extracting quantitative information from relatively low-resolution images from a fixed position obtained from an uncalibrated (and now damaged) camera.

Tracking Distinctive Features

To estimate extrusion rates, we followed movements of distinctive features on the lava dome between selected images. These features consisted of sharp edges, intersecting fractures, fracture tips, spots, or other stable, distinctive markers that could be readily identified and that persisted through multiple images, typically from a few days to about two weeks. To begin, an initial image (November 10, 2004) was imported into graphical design software and its apparent principal point (the center of the image) identified. Coordinates of features of interest on the dome were then computed relative to that apparent principal point (fig. 6). Subsequent images (separated by roughly 24 hours when possible) were then imported and manually coregistered with the preceding image, and the positions of displaced features of interest were updated. Coordinates of distinctive features on the dome in proximity to the vent area were entered into a spreadsheet, and equations 1 and 2 solved for the employed camera parameters (table 1) and measured distances between the camera and the dome (the distance was updated with each new DEM). The solutions, along with elapsed times between photographs, provided a time series of apparent horizontal and vertical displacement rates for selected proximal points on the actively growing dome. Typical rates of apparent horizontal and vertical displacement, and standard deviations of those rates, were estimated by averaging apparent displacement rates of 3 to 10 points per image. Apparent linear extrusion rates in the focal plane were determined by resolving the averaged horizontal and vertical displacement rates, and the standard deviation errors on those averaged rates were propagated to the resolved solution using standard methods (for example, Bevington and Robinson, 1992). An average extrusion rate in the direction of dome growth was determined by resolving the average appar-

ent extrusion rate in the focal plane with respect to the angle of obliquity of extrusion.

Sources of Error

Several sources of error are inherent in a quantitative analysis of oblique imagery from the Sugar Bowl camera. A fixed source of error involves the quantification of lens characteristics, camera orientation, and spatial measurements (table 1) that affect the interior and exterior control imposed on the imagery. More random is the operator error incurred during image analysis.

Lens characteristics used in this analysis represent average values obtained from calibrations of four similar cameras. Variations of 1.2 mm about the assumed focal length (table 1) cause ±7 percent variation of the averaged apparent extrusion rates we report. Calibrated radial distortion in imagery was essentially negligible (table 1) and was thus ignored in our analyses. Repeated measurements of the inclination and azimuth of the camera housing during field visits minimized orientation error (table 1), although frequent misalignments among sequential photographs show that wind and transient snow and ice loads caused minor variations in orientation.

Spatial measurement errors revolve around accuracy of the camera location, inherent errors in the DEMs, measurement of the distance from the camera to the active extrusion, and measurement of the obliquity of the extrusion with respect to the camera axis. Replicable GPS measurements of the camera location and coordinate determinations in a GIS of selected locations on the active extrusion limit the error of the distance between the camera and the active extrusion to about ±30 m, or about 1-percent error on the measured distance (table 1). Inherent errors in the DEMs (Schilling and others, this volume, chap. 8) are small compared to other measurement errors and are thus ignored. For much of the period from November 2004 to August 2005, the dome grew along azimuths ranging from 150° to 170° (Schilling and others, this

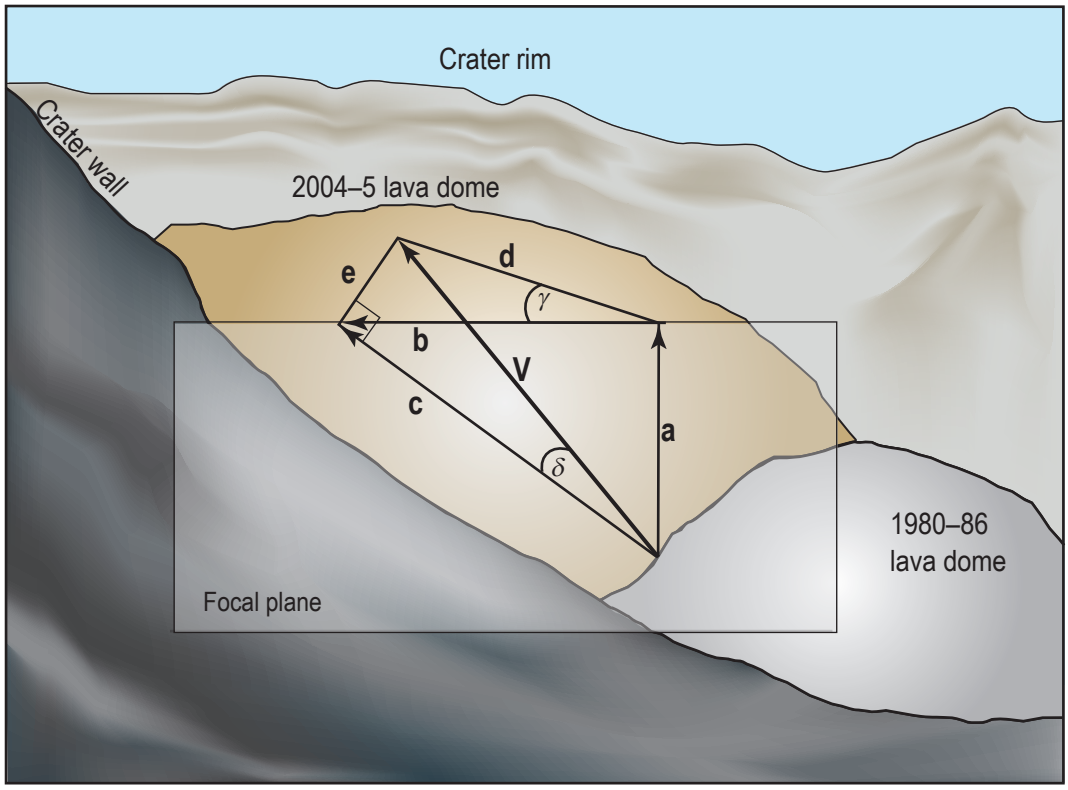

Figure 5. Diagram of a three-dimensional pyramid showing relations among the apparent vector of the average rate of motion, **c**, within a vertical plane perpendicular to the camera axis, the actual vector of extrusion, **V**, and the angle of obliquity of extrusion, γ. Triangle **abc** is oriented vertically and perpendicular to the camera axis, and triangle **ebd** is oriented orthogonally to triangle **abc** (that is, in the plane of the topographic digital elevation model). As a result, triangle **ecV** is a right triangle. Note that leg **e** is common to triangles **ecV** and **ebd**. Therefore, $\mathbf{e} = \mathbf{b} \tan \gamma = \mathbf{c} \tan \delta$. Solving this equality leads to $\tan \delta = (\mathbf{b}/\mathbf{c}) \tan \gamma$, or $\delta = \tan^{-1}(R \tan \gamma)$, where $R = \mathbf{b}/\mathbf{c}$. Thus, by measuring the angle of obliquity of extrusion, γ, on a DEM, one can employ simple trigonometry to resolve the apparent average rate of motion in the focal plane to the estimated rate of extrusion in the direction of dome growth.

volume, chap. 8; Vallance and others, this volume, chap. 9), about 30°–50° oblique to the focal plane of the camera (which had an azimuth of 117°; table 1). From about mid-August through December 2005, motion was chiefly westward (~270° azimuth), about 25°–30° oblique to the focal plane of the camera. Repeated measurements of these obliquity angles within a GIS constrained these values to within a few degrees (table 1). Errors of ±2° about the measured obliquity angles cause ±2 percent variation in the reported averaged extrusion rates.

Aside from assumptions about lens characteristics and estimates of the distance from the camera to the dome, our most critical sources of error revolve around selection of the photographic principal point, the accuracy to which sequential photographs were coregistered, and the accuracy with which moving points were identified and tracked. For purposes of the analysis reported here, the principal point to which all measurements are referenced was selected simply as the center of the first base image, and all subsequent images were coregistered to that principal point. Owing to minor variations in fields of view resulting principally from winds and snow and ice loads on the housing, the principal point of the base image was not always the principal point of subsequent images. The distinctive dome features we followed were identified at the pixel level where possible, but the relatively low resolution of the images and the sometimes challenging lighting made pixel-level identification frequently difficult. Manual identification of displaced point positions could thus be in error by a few pixels. Overall, the greatest errors in the analysis were introduced through assumptions about lens focal length and through manual image registration and feature tracking.

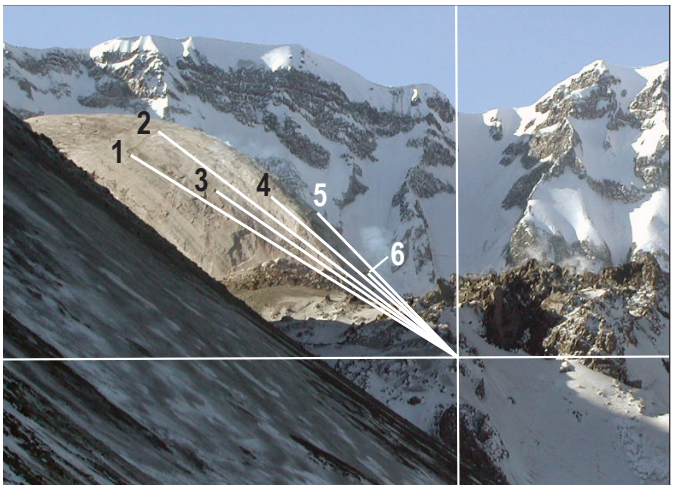

Figure 6. Example of photograph taken by the Sugar Bowl camera of the 2004–5 dome in the crater of Mount St. Helens, illustrating a distribution of points used to track motion. Because the image has been cropped, the principal point of the original photograph, which serves as the origin to which point coordinates (for example, 1 to 6) are referenced, is offset. In this image, the 2004–5 dome is about 130 m tall. Photograph taken on March 6, 2005, at 17:08:38 UTC.

Given the several sources of error that potentially affect our analysis, quantifying the cumulative error on our estimates of extrusion is a daunting task. Instead, we computed standard deviations of mean vertical and horizontal displacement rates in the focal plane from a collection of points on the proximal part of the active extrusion. Using standard practices (for example, Bevington and Robinson, 1992), we propagated the standard deviations of those mean values to the resolved extrusion rates in the focal plane and carried the propagated errors over to the resolved extrusion rates in the direction of dome growth to approximate a magnitude of error associated with our estimates of extrusion rate.

Results

Episodic growth and disintegration of several solidified lava spines characterized emplacement of the 2004–5 dome (Schilling and others, this volume, chap. 8; Vallance and others, this volume, chap. 9). Two minor spines, not visible from Sugar Bowl, breached the surface in October 2004. From late October 2004 until mid-April 2005, dome growth proceeded chiefly through emplacement and disintegration of two recumbent spines (spines 3 and 4) dubbed ‘whalebacks’ (Schilling and others, this volume, chap. 8; Vallance and others, this volume, chap. 9; fig. 7; supplemental movie in appendix 1). The character of growth changed following disintegration of spine 4 in mid-April 2005. More vertical, rather than recumbent, growth characterized spine 5 from mid-April until late July 2005 (fig. 7; supplemental movie). Following disintegration of spine 5 in late July 2005, vertical growth diminished and horizontal motion intensified as a new spine (spine 6) emerged and migrated rapidly westward. This phase of development persisted into October 2005, as a graben opened along the central part of the dome complex (see fig. 7 and supplemental movie) and growth of spine 6 became more endogenous. From mid-October through December 2005, the rapid westward migration of spine 6 slowed and vertical growth of another spine (spine 7) became notable (fig. 7; supplemental movie).

Rates of extrusion and associated motion of assorted segments of the 2004–5 lava dome varied in time and space, but for extended periods extrusion occurred at nearly steady rates. The average rate of vertical displacement varied between about 1 and 4 m/d, with a central tendency toward 2–3 m/d from November 2004 through June 2005 during growth of spines 3, 4, and 5 (fig. 8*A*). From about late June to mid-July 2005, the rate of vertical displacement of spine 5 slowed substantially, then increased from mid- to late July during a period of reinvigorated growth. Following a series of rockfalls in late July, vertical motion of spine 5 diminished, but another, though less vigorous, growth spurt occurred in early to mid-August as spine 6 emerged. In December 2005 the average vertical motion of spine 7 hovered around 1 m/d (fig. 8*A*). In contrast, the average rate of horizontal displacement (in the focal plane) during emplacement of recumbent spines 3 and

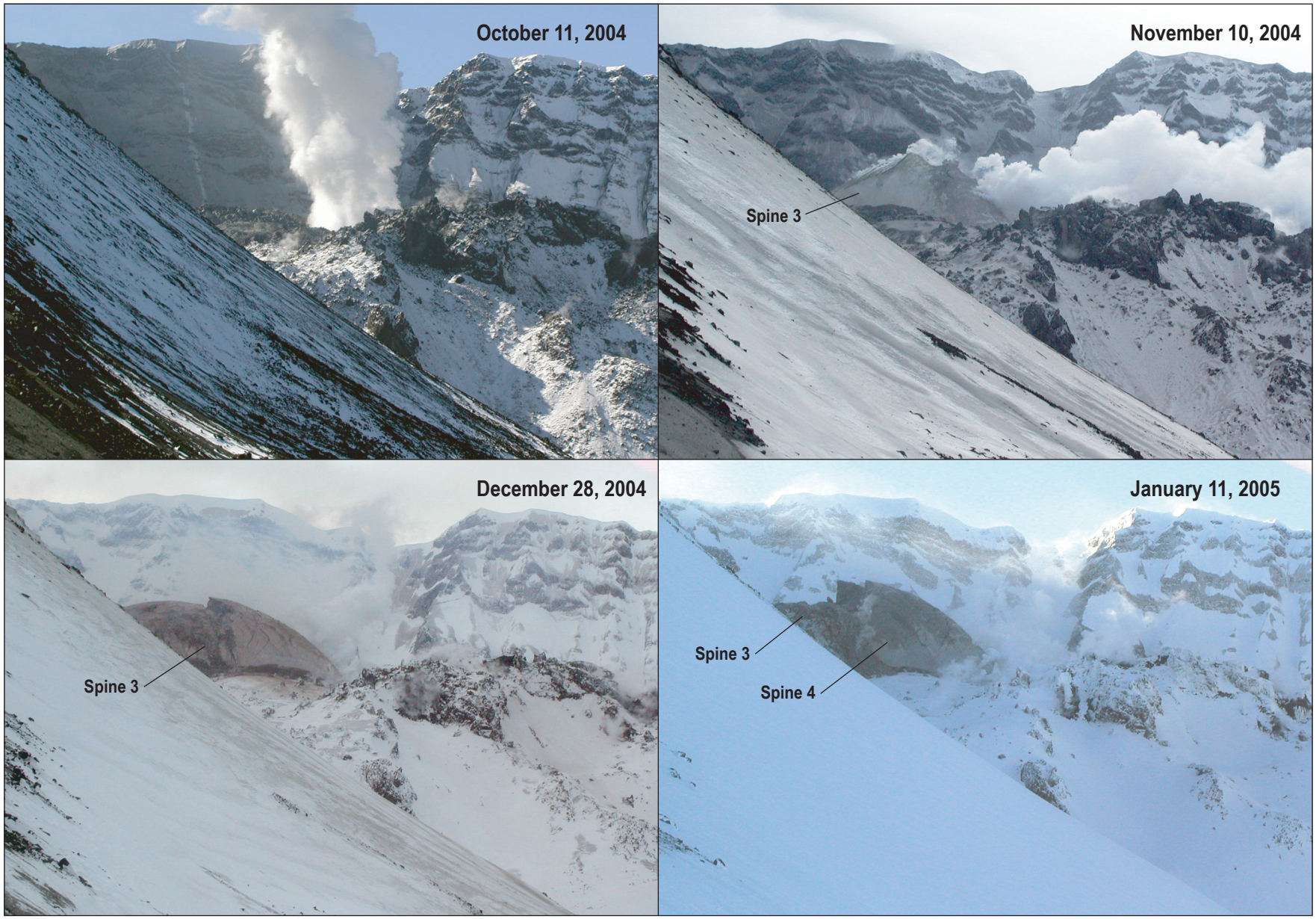

Figure 7. Time series of images from the Sugar Bowl camera illustrating growth, disintegration, and morphologic change of the new lava dome at Mount St. Helens between October 2004 and January 2006.

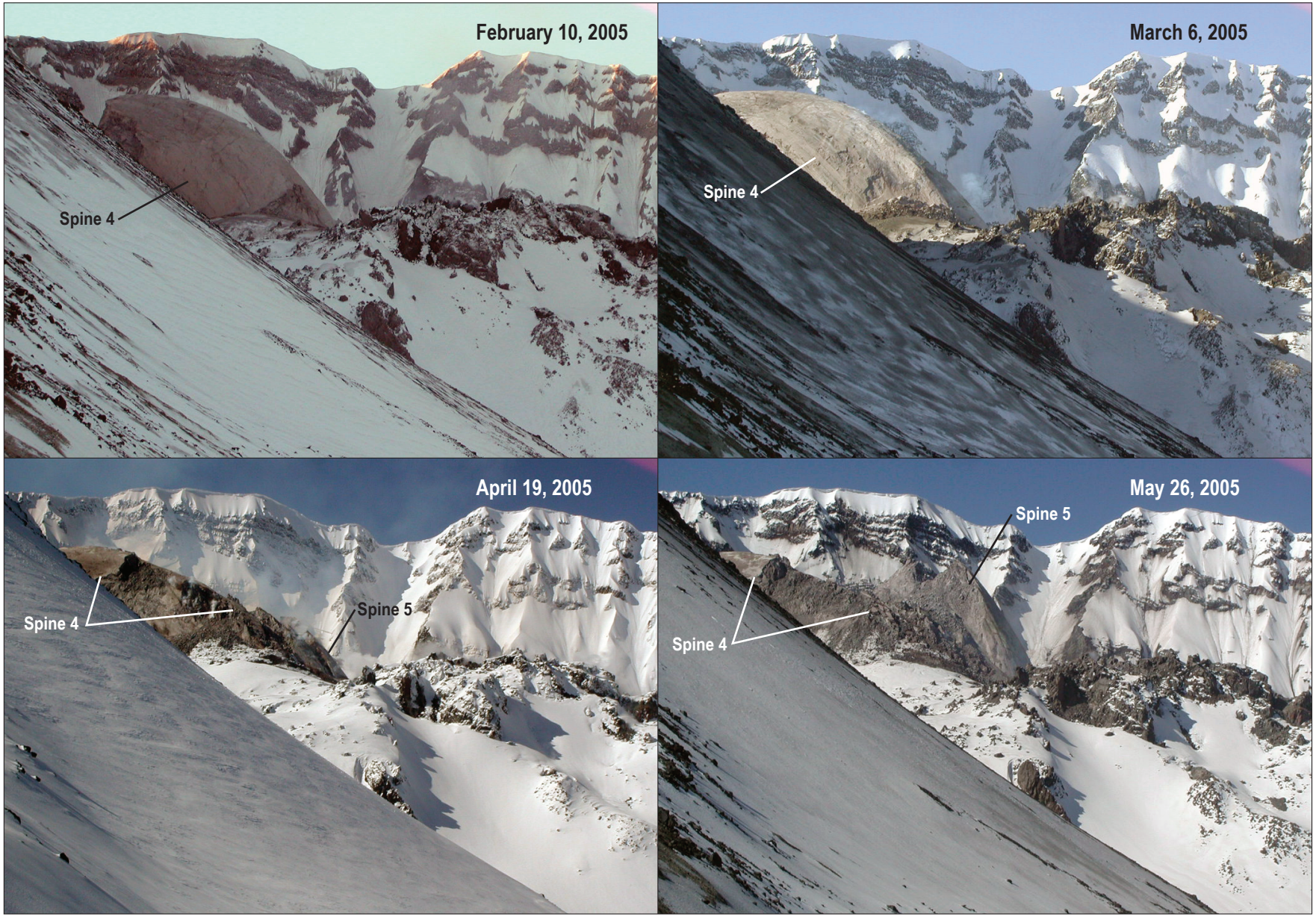

Figure 7.—Continued.

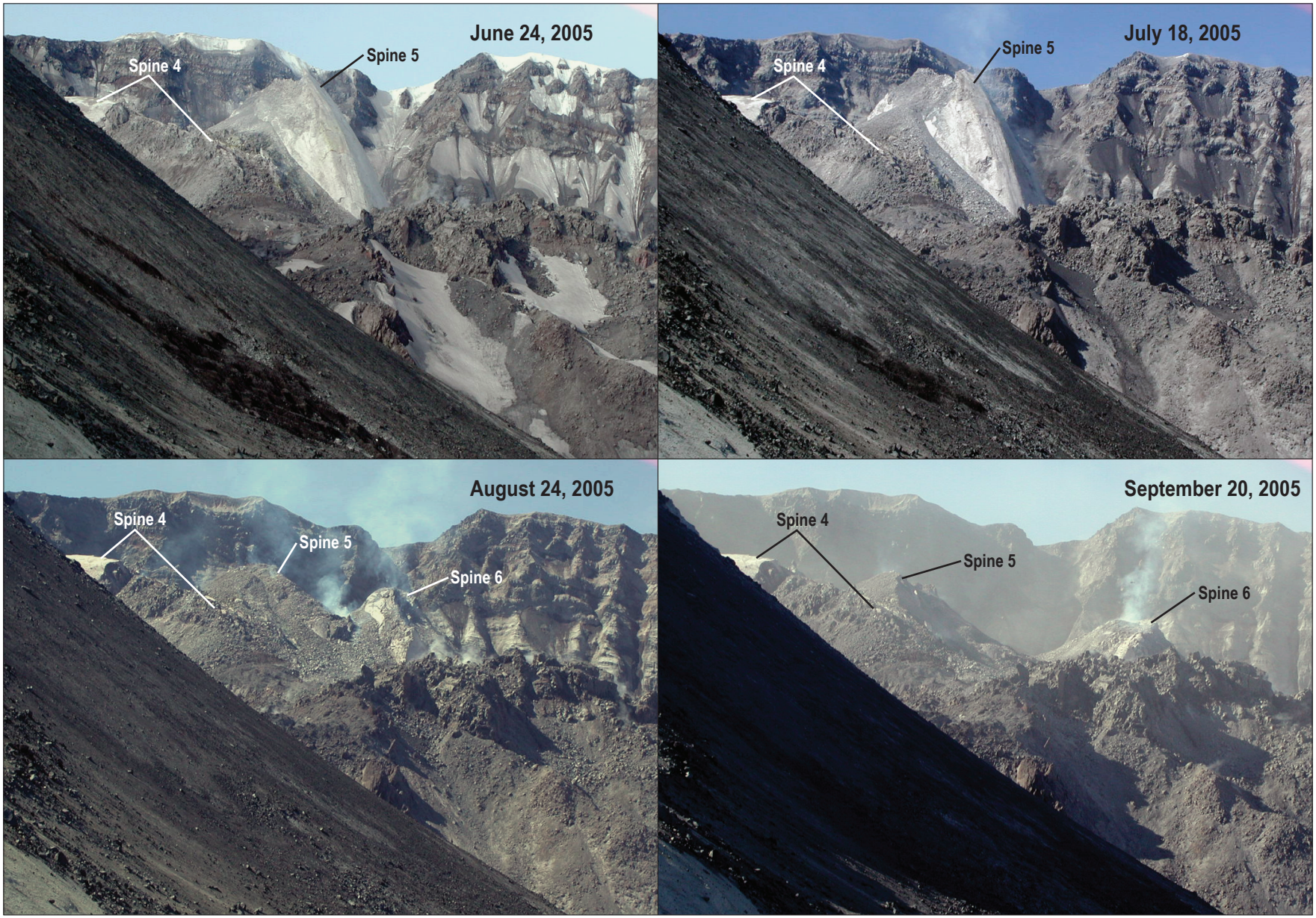

Figure 7.—Continued.

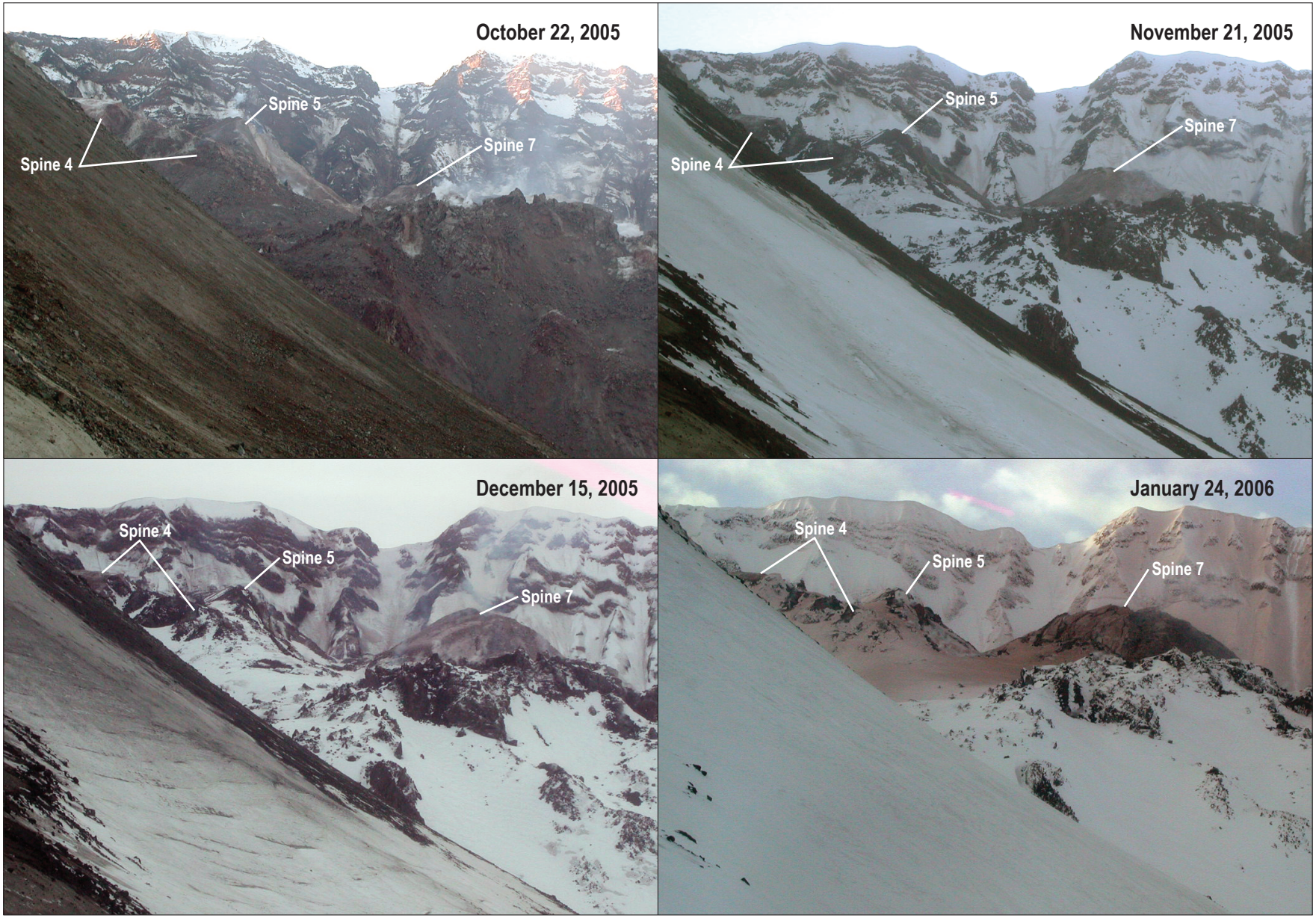

Figure 7.—Continued.

4 decreased progressively from about 5–7 m/d in November 2004 to about 3 m/d by mid-March 2005, then to fractions of a meter per day by late July 2005 after vertical growth of spine 5 became predominant (fig. 8*B*). Horizontal motion increased substantially in August (to >2 m/d) when growth of spine 6 migrated sharply westward; in December 2005, apparent horizontal motion of spine 7 hovered around 2 m/d.

Resolving the average horizontal and vertical displacement rates of the various spines into average rates of motion in the focal plane and then correcting those measurements for the angle of obliquity of extrusion shows that estimated extrusion rates declined logarithmically from November 2004 through December 2005 (fig. 8*C*). This decline is comparable to changes in magma discharge documented through analyses of DEMs (Schilling and others, this volume, chap. 8). However, several spurts of accelerated extrusion are superposed on the overall diminishing extrusion rate, and for several months lava extruded at a nearly steady rate (fig. 8*C*).

The estimated average linear extrusion rate was as great as 8–10 m/d in early November 2004 during emplacement of spine 3, hovered between 4 and 5 m/d from late December 2004 through mid-March 2005 during growth of spine 4, dropped to less than 2 m/d by mid-July 2005 during the waning stages of growth of spine 5, and then increased to about 4 m/d before spine 5 disintegrated in late July 2005. Following disintegration of spine 5, the extrusion rate again dropped to as low as 2 m/d before accelerating to about 4 m/d in August, when spine 6 emerged and migrated sharply westward. In December 2005, during growth of spine 7, the extrusion rate had again declined to about 2 m/d. GPS receivers deployed on spines 3 and 4 tracked extrusion rates in real time for limited periods (LaHusen and others, this volume, chap. 16). During the periods when usable imagery and GPS deployment coincided, estimates of extrusion rate compiled from imagery analyses are about 20–30 percent lower than the measured rates (fig. 8*C*). Given the assumptions in our analyses, our estimates of linear extrusion rate compare relatively favorably with measured rates.

Motion of the extruded lava varied spatially as well as temporally. Movement of the distal ends of recumbent spines 3 and 4 slowed as those spines enlarged, plowed over fragments of earlier spines, and impinged upon the crater wall. Differential rates of motion between distal and near-vent segments of those spines prompted development of thrust faults, large-scale fractures, and partial to complete disintegration in December 2004, January 2005, and April 2005 (fig. 7; supplemental movie; Schilling and others, this volume, chap. 8; Vallance and others, this volume, chap. 9). Such disintegration generated hot rockfalls and minor pyroclastic surges but did not trigger substantive pyroclastic flows similar to those produced by dome collapses elsewhere (for example, Ui and others, 1999; Herd and others, 2005). Following the disintegration of spine 4 (the largest of the recumbent spines) in mid-April 2005, the growth of spine 5 became focused along the western margin of the dome complex. During this phase of growth, active extrusion was effectively decoupled from the remnants of the earlier spines. From mid-April on, several remnants of spines 3 and 4 remained stable as spine 5 emerged (for example, note the stability of the intact block of spine 4 on the east margin of the dome complex between April and December 2005; fig. 7; supplemental movie). Local displacement of ground near the vent, however, showed that, on occasion, extruding solidified lava was well coupled to the immediately surrounding terrain (see supplemental movie).

Following the disintegration of spine 5 in July 2005, the dome became further segmented. As spine 6 emerged and migrated westward, the eastern segment of the dome complex remained stable, but the central segment slumped as its westward buttress was removed (fig. 7; supplemental movie). Such spatially differential motion and migration of the extruding solidified lava led to the segmented morphology of the 2004–5 dome (fig. 9), in contrast to the composite, but uniform morphology of the 1980s lava dome (see, for example, Swanson and others, 1987).

Extrusion rates estimated from the Sugar Bowl imagery are broadly correlated with overall trends in seismicity and deformation (fig. 10). From November 2004 until January 2005, the rapidly decreasing extrusion rate was synchronous with a general decline in seismic-energy release as indicated by real-time seismic amplitude measurements (RSAM) (Endo and Murray, 1991; Murray and Endo, 1992; Moran and others, this volume, chap. 2) (figs. 10*A*, *C*). The RSAM values are commonly invoked as a proxy highlighting overall seismic-energy release at volcanoes (for example, Power and others, 1994, 1995; Harlow and others, 1996; Mori and others, 1996; Voight and others, 1998). During phases of more or less steady extrusion from January to June 2005, minor increases in extrusion rate generally correlated with slight increases in RSAM. The extrusion-rate nadir and subsequent significant growth spurt in mid- to late July 2005 correspond with an equivalent nadir and subsequent minor increase in RSAM.

Correlations between trends in extrusion rate and geodetic measurements of deformation of a part of the 1980s lava dome are evident, but they are more subtle than are those with trends in seismicity (figs. 10*B*, *C*). We compare trends in extrusion rate with trends in the motion of station DOM1 located on the west side of the 1980s lava dome north-northwest of the vent of the 2004–5 eruption (Dzurisin and others, this volume, chap. 14; LaHusen and others, this volume, chap. 16). The overall logarithmic decay of the rate of lava extrusion is approximately mimicked by a corresponding logarithmic change in the northing component of motion of DOM1. Finer scale fluctuations in lava extrusion rate and motion of DOM1 are, however, typically out of phase, particularly after about the first 5 months of the eruption. For example, an increase in extrusion rate between late April and mid-June 2005 corresponds with southward movement of DOM1 (that is, a relaxation of the 1980s dome toward the 2004–5 vent). From late June through mid-July 2005, an ensuing period of declining extrusion rate corresponds with a period of increased northward movement of DOM1 (that is, movement of the 1980s dome away from the vent). An ensuing increase of extrusion

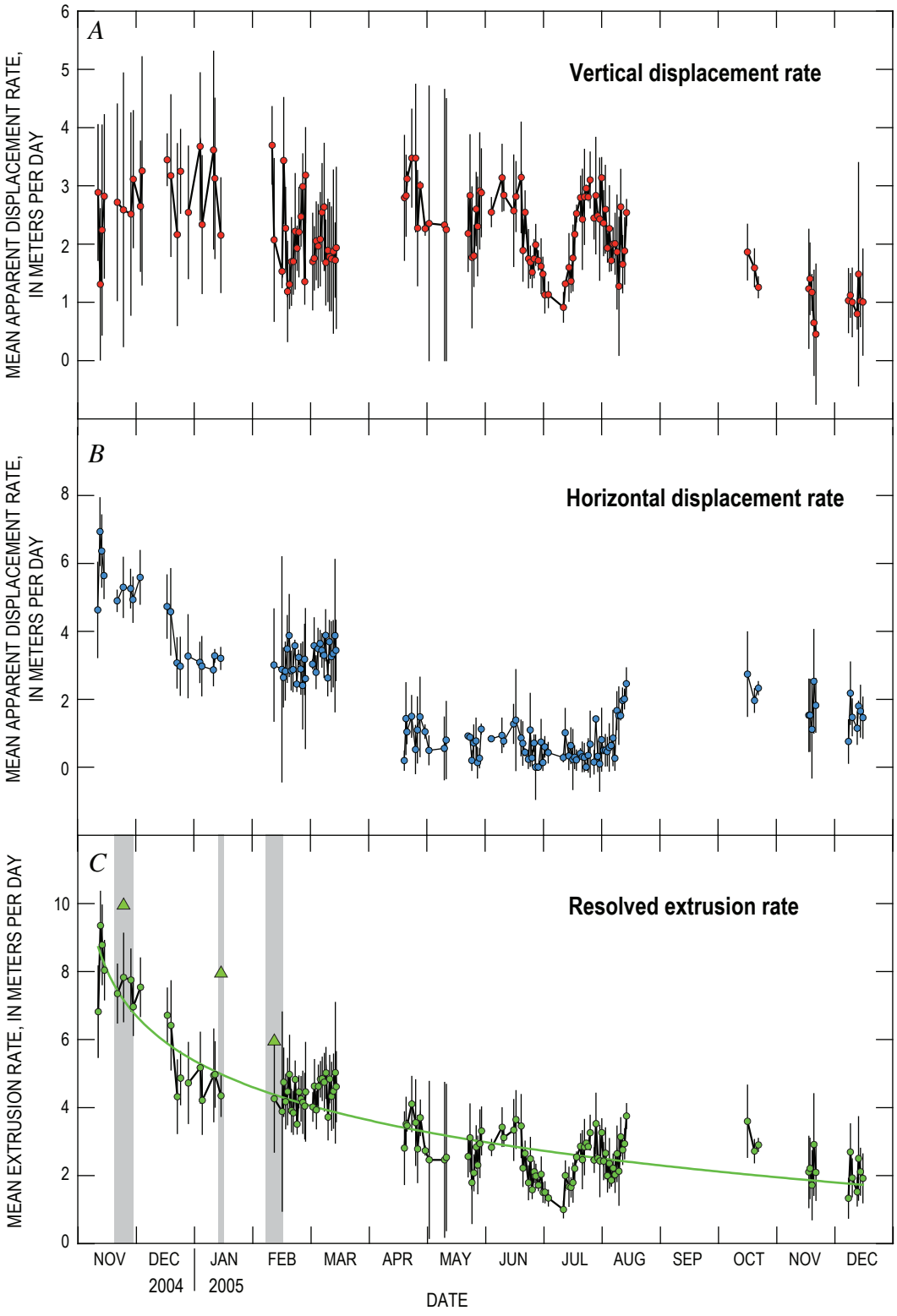

Figure 8. Time-series plot of displacement rates and extrusion rates of the 2004–5 lava dome at Mount St. Helens. Error bars represent ±1 standard deviation about the mean. *A*, Average rate of vertical displacement within the camera focal plane. *B*, Average rate of horizontal displacement within the camera focal plane. *C*, Estimated average extrusion rate of the 2004–5 lava dome in the direction of growth. The gray bands illustrate periods when GPS receivers were deployed on the lava dome, and the triangles represent the average rates of motion measured by GPS (LaHusen and others, this volume, chap. 16). A logarithmic decay curve is superposed on the data.

rate in late July again corresponds with southward movement of DOM1 (toward the vent), whereas the decrease of extrusion rate in early August corresponds with increased northward motion of DOM1 (again, away from the vent). The increase of extrusion rate documented in mid-August 2005 is not as well out of phase with the motion of DOM1 as are other periods of changing rates of extrusion, but it does correspond to a gradual change from northward motion (away from the vent) to southward motion (toward the vent). Only the northing component of motion of DOM1 appears to broadly correspond with variations in extrusion rate; there is little if any substantive correlation between extrusion rate and the easting or vertical components of motion of DOM1 (figs. 10*B*, *C*).

Discussion

Within the constraints of the interior and exterior control we imposed, the available oblique, terrestrial imagery from the Sugar Bowl camera provided a valuable means of estimating long-term linear extrusion rates over periods of weeks to months during the 2004–5 eruption of Mount St. Helens. The greatest sources of error revolved around our assumptions regarding the camera focal length and our ability to accurately coregister sequential images and follow features of interest through time. Pitting of the glass on the camera box, shadows, steam and clouds, weather-related loss of usable images, and physical changes to the dome during its growth and partial disintegration all contributed to the challenge of using the imagery. Although the locus of extrusion varied slightly during the period of analysis, errors in the imposed external control and measurements of the distance between the camera and the dome were relatively small compared to other sources of error. Indeed, the errors associated with the assumed focal length alone make the greatest difference in our comparisons of extracted versus measured extrusion rates.

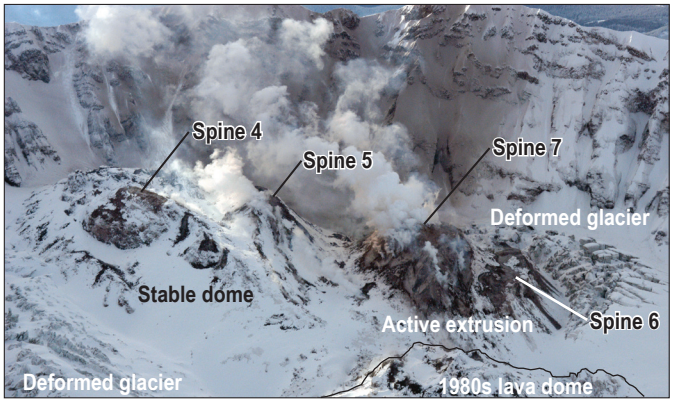

Figure 9. Oblique aerial photograph looking southwest into the crater of Mount St. Helens. Photograph illustrates the segmented morphology of the 2004–5 lava dome complex. Remnants of spines 4 and 5 are visible as discrete snowclad humps on the left and left-center of the image, and the locus of active growth, spine 7, is visible on the right side of the image. Fractured and deformed glacier ice is visible on the far left and far right sides of the image, and part of the snow-covered 1980s lava dome is visible in the bottom center of the image. USGS photograph by J.S. Pallister, December 6, 2005.

Our methodology for extracting quantitative information from the fixed-position imagery hinged upon an ability to impose external control. In the absence of a time series of DEMs, or even a single DEM, we would not have been able to solve the underdetermined system of equations posed by having imagery from only a single viewpoint. Traditional surveying could have provided the necessary measures of distance from the camera site to the dome, but the dangerous environment in the crater during the early phases of the eruption, the distance between the camera and the lava dome, the difficulty of precisely placing prisms even remotely, and the rapidly changing physical character of the dome inhibited such a strategy.

The ability to quantify the rate of extrusion, even crudely, greatly enhanced the value of the imagery. Rather than simply serving as a method to monitor the status of the eruption or the conditions in the crater, the imagery supplemented other geophysical monitoring equipment. For the most part, it provided the sole means of extracting long-term, semicontinuous quantitative information. Differencing of sequential DEMs provided long-term estimates of magma discharge (Schilling and others, this volume, chap. 8), but those DEMs were based on stereoscopic aerial photographs only acquired about once per month. Hence, DEM differencing could not provide information on the fine-scale fluctuations of extrusion rate apparent in the camera imagery. Thus, quantification of linear extrusion rate of the lava from the Sugar Bowl imagery provided information about the eruption that was unattainable by other means.

Deployment of remote cameras at Mount St. Helens clearly enhanced documentation and analysis of the eruption (Poland and others, this volume, chap. 11). The semicontinuous imagery obtained from the Sugar Bowl camera was particularly useful for analyzing long-term, relatively fine-scale (days to months) variations of the linear extrusion rate. It proved less useful for examining extrusion rate over periods of hours, given the low average rates of movement, the challenges of accurately following features of interest, and the resolution of the pixel footprint at the distances involved. Hence, the scale of the imagery had a direct bearing on the quality and utility of the information that could be extracted. Finer resolution at shorter time scales requires more narrowly focused, larger scale imagery, but obtaining such imagery can be extremely challenging (Dzurisin and others, this volume, chap. 14). Of course, measurements of linear extrusion rate do not necessarily correlate directly with measurements of volumetric extrusion rate (that is, magma discharge). Nevertheless, long-term estimates and documentation of fluctuations of this one-dimensional parameter are useful and shed insights

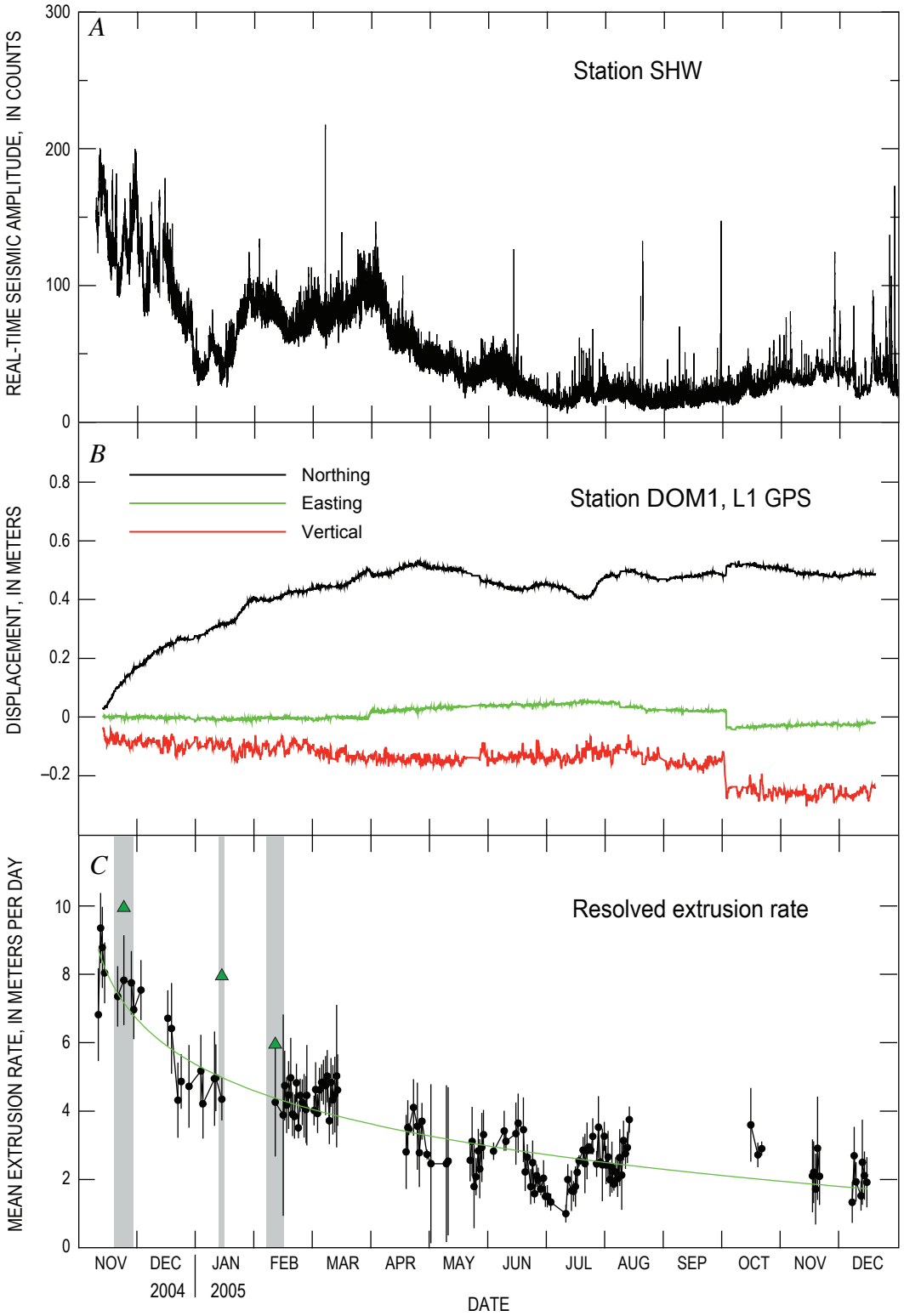

Figure 10. Time-series plots of RSAM, geodetic measurements, and extrusion rate at Mount St. Helens. *A*, Real-time seismic-amplitude measurements (RSAM) from station SHW located on the west flank of the volcano. Plot has been smoothed using a five-point moving average. *B*, GPS geodetic measurements at station DOM1 located on the western side of the 1980s lava dome. The data, obtained using the L1-band frequency, are referenced relative to a station located in the upper South Fork Toutle River valley (LaHusen and others, this volume, chap. 16). Plot has been smoothed using an 11-point moving median. *C*, Estimated average extrusion rate of the 2004–5 lava dome. See figure caption 8*C* for details.

into overall eruptive behavior, especially when trends in linear extrusion rate can be correlated with trends in other geophysical measurements.

The pulsating behavior of lava extrusion documented on time scales of days to weeks in our analysis has been observed on time scales of hours to years during emplacement of other silicic lava domes. At Soufrière Hills volcano, Montserrat, West Indies, Sparks and others (1998) noted that magma discharge pulsated on time scales of hours to months during a time when the overall discharge rate was increasing. In contrast, the pulsating behavior documented here occurred during an overall trend of declining magma discharge (Schilling and others, this volume, chap. 8). Fluctuating extrusion rates during an overall decline of magma discharge were also observed at Unzen volcano, Japan, from 1991 to 1995 (Nakada and others, 1999). Lava at Santiaguito dome, Guatemala, has extruded continuously since 1922, with 3–5-yr spurts of rapid discharge interspersed with 10–15-yr periods of slower discharge (Rose, 1987; Anderson and others, 1995; Harris and others, 2003). The Mount St. Helens 1980–86 lava dome grew through a series of 20 eruptive episodes between October 1980 and October 1986. However, each discrete extrusive episode was separated by pauses in eruptive activity that ranged from about one month to one year (Swanson and others, 1987), in contrast to the sustained, but fluctuating, extrusion that characterized the 2004–5 eruption. Sparks and others (1998) attribute pulsating extrusive behavior to a combination of deep and shallow volcanic processes. They speculate that discharge fluctuations on time scales of months to years are influenced chiefly by deep processes that control magmatic influx from the mantle and magma-chamber processes that affect magma ascent. In contrast, fluctuations on time scales of hours to weeks are attributed chiefly to pressure fluctuations caused by shallow-level processes, such as gas loss, crystallization kinetics, and mineral precipitation, which affect changes in magma properties and pressurization.

Correlations among seismicity, deformation, and extrusion rate during the 2004–5 Mount St. Helens eruption portray an extrusion that likely consisted of episodes of broad-scale stick-slip behavior. Relatively fine-scale correlations among periods of declining extrusion rate, relatively low seismicity, and northward movement of the 1980s lava dome (away from the eruptive vent) suggest episodes when the extruding solidified plug of lava was relatively well coupled to, and having difficulty evacuating, the conduit. Such a period of "stick" would be expected to result in lower seismicity, a low rate of extrusion, and increased deformation (that is, swelling) of the local terrain. In contrast, broad correlation among accelerated extrusion rate, slightly elevated seismicity, and southward movement of the 1980s lava dome (toward the eruptive vent) suggest episodes when the extruding solidified lava was relatively poorly coupled to, and slipping through, the conduit. Such periods of "slip" generated more or larger earthquakes as the lava dome lurched along (Moran and others, this volume, chap. 2) and allowed the local terrain deformed during the preceding period of stick to relax. Such episodes of broad-scale stick-slip movement complement a dynamic model of repetitive, fine-scale, stick-slip movement during sustained extrusion as proposed by Iverson and others (2006) and Iverson (this volume, chap. 21).

Long-term (months) and short-term (days) correlations between seismic intensity, deformation, and dome growth, such as documented here, have also been noted at other volcanoes. Broad correlations between seismic intensity and dome growth have been documented at Usu (Wano and Okada, 1980), Augustine (Power, 1988), Redoubt (Power and others, 1994), Unzen (Nakada and others, 1999), and Montserrat (Rowe and others, 2004), and short-term synchronicity and cyclicity between seismicity and deformation also have been observed (Voight and others, 1998). However, long-term, fine-scale correlations among fluctuations in extrusion rate, seismicity, and deformation generally have not been reported. Such correlations, as noted above, are clearly related to eruption mechanics. Indeed, Denlinger and Hoblitt (1999) have modeled short-term synchronicity and cyclicity in RSAM and deformation at Montserrat as a function of the interaction of volatile overpressure in magma and the overburden of an extruding lava dome, and Iverson (this volume, chap. 21) has hypothesized that the small, repetitive earthquakes that have occurred during the 2004–5 Mount St. Helens eruption, dubbed drumbeat earthquakes (Moran and others, this volume, chap. 2), reflect repetitive, small-magnitude (a few millimeters) stick-slip behavior of the extruding lava. Extraction of semicontinuous extrusion rates from long-term camera imagery, in conjunction with time-series of other geophysical data, clearly plays an important role in constraining dynamic eruption models and enabling forecasts of hazardous activity.

Conclusions

Imposition of interior and exterior controls on a semicontinuous series of oblique, terrestrial imagery from a fixed vantage point on the Sugar Bowl lava dome allowed quantification of fine-scale temporal behavior of the linear rate of lava extrusion during the 2004–5 eruption of Mount St. Helens. Analysis of the imagery showed that over a period of 14 months (November 2004–December 2005), the linear extrusion rate varied in both space and time. Overall, the extrusion rate declined approximately logarithmically from about 8–10 m/d in November 2004 to about 2 m/d by December 2005. However, the overall decline in the rate of extrusion was punctuated by fine-scale (days to weeks) fluctuations. The overall logarithmic decline of extrusion rate and the finer scale fluctuations correlated, approximately, with trends in seismicity and geodetic deformation. Those correlations portray an extrusion that underwent episodes of broad-scale stick-slip movement in addition to finer scale, smaller magnitude stick-slip episodes that others hypothesize to correlate with small, so-called drumbeat earthquakes. The ability to extract linear

extrusion rates from the imagery from this fixed-position camera provided a significant, and sometimes the sole, means of semicontinuously quantifying eruption dynamics during much of the first year of eruption, and those data provide an important constraint for dynamic eruption models.

Acknowledgments

As noted in this chapter, the Sugar Bowl camera was not specifically deployed with the intention of extracting quantitative information. However, when viewing the images, especially after they have been compiled into a time-lapse movie, one cannot help but realize that they contain a plethora of information about the growth, and the rate of growth, of the new lava dome. The trick is to extract that information. We thank our colleagues at the Hawaiian Volcano Observatory for providing us with the original camera and communications software; Gene Iwatsubo, Kirstie Simpson, and Stephanie Konfal for helping install the camera; Seth Moran for providing us with RSAM data; Steve Schilling for stimulating discussions as we muddled along through our analyses; Matt Logan and Dan Gooding for compiling the imagery into the movie included in the supplemental movie of appendix 1; our many colleagues at CVO who asked pointed questions at staff meetings when we unveiled our analyses; and Ren Thompson and Ricky Herd for insightful, critical reviews that kept us from wandering beyond the limits of what we could reasonably do in our efforts to extract information from these photographs.

References Cited

Anderson, S.W., Fink, J.H., and Rose, W.I., 1995, Mount St. Helens and Santiaguito lava domes; the effect of short-term eruption rate on surface texture and degassing processes: Journal of Volcanology and Geothermal Research, v. 69, p. 105–116.

Baldi, P., Bonvalot, S., Briole, P., and Marsella, M., 2000, Digital photogrammetry and kinematic GPS applied to the monitoring of Vulcano Island, Aeolian arc, Italy: Geophysics Journal International, v. 142, no. 3, p. 801–811.

Baldi, P., Fabris, M., Marsella, M., and Monticelli, R., 2005, Monitoring the morphological evolution of the Sciara del Fuoco during the 2002–2003 Stromboli eruption using multi-temporal photogrammetry: ISPRS Journal of Photogrammetry and Remote Sensing, v. 59, no. 4, p. 199–211.

Barmin, A., Melnik, O., and Sparks, R.S.J., 2002, Periodic behavior in lava dome eruptions: Earth and Planetary Science Letters, v. 199, p. 173–184.

Bevington, P.R., and Robinson, D.K., 1992, Data reduction and error analysis for the physical sciences (2d ed.): Boston, McGraw-Hill, 328 p.

Denlinger, R.P., and Hoblitt, R.P., 1999, Cyclic eruptive behavior of silicic volcanoes: Geology, v. 27, p. 459–462.

Dungan, M.A., Wulff, A., and Thompson, R.A., 2001, Eruptive stratigraphy of the Tatara-San Pedro complex, 36°S, Southern Volcanic Zone, Chilean Andes; reconstruction method and implications for magma evolution at long-lived arc volcanic centers: Journal of Petrology, v. 42, p. 555–626.

Dzurisin, D., Lisowski, M., Poland, M.P., Sherrod, D.R., and LaHusen, R.G., 2008, Constraints and conundrums resulting from ground-deformation measurements made during the 2004–2005 dome-building eruption of Mount St. Helens, Washington, chap. 14 *of* Sherrod, D.R., Scott, W.E., and Stauffer, P.H., eds., A volcano rekindled; the renewed eruption of Mount St. Helens, 2004–2006: U.S. Geological Survey Professional Paper 1750 (this volume).

Endo, E.T., and Murray, T., 1991, Real-time seismic amplitude measurement (RSAM); a volcano monitoring and prediction tool: Bulletin of Volcanology, v. 53, no. 7, p. 533–545.

Harlow, D.H., Power, J.A., Laguerta, E.P., Ambubuyog, G., White, R.A., and Hoblitt, R.P., 1996, Precursory seismicity and forecasting of the June 15, 1991 eruption of Mount Pinatubo, *in* Newhall, C.G., and Punongbayan, R.S., eds., Fire and mud; eruptions and lahars of Mount Pinatubo, Philippines: Seattle, University of Washington Press, p. 285–305.

Harris, A.J.L., Rose, W.I., and Flynn, L.P., 2003, Temporal trends in lava dome extrusion at Santiaguito 1992–2000: Bulletin of Volcanology, v. 65, p. 77–89.

Herd, R.A., Edmonds, M., and Bass, V.A., 2005, Catastrophic lava dome failure at Soufriere Hills Volcano, Montserrat, 12–13 July 2003: Journal of Volcanology and Geothermal Research, v. 148, nos. 3–4, p. 234–252, doi:10.1016/j.jvolgeores.2005.05.003.

Honda, K., and Nagai, M., 2002, Real-time volcano activity mapping using ground-based digital imagery: ISPRS Journal of Photogrammetry and Remote Sensing, v. 57, p. 159–168.

Huppert, H.E., Shepherd, J.B., Sigurdsson, H., and Sparks, R.S.J., 1982, On lava dome growth, with application to the 1979 lava extrusion of the Soufrière of St. Vincent: Journal of Volcanology and Geothermal Research, v. 14, p. 199–222.

Iverson, R.M., 2008, Dynamics of seismogenic volcanic extrusion resisted by a solid surface plug, Mount St. Helens, 2004–2005, chap. 21 *of* Sherrod, D.R., Scott, W.E., and Stauffer, P.H., eds., A volcano rekindled; the renewed eruption of Mount St. Helens, 2004–2006: U.S. Geological Survey Professional Paper 1750 (this volume).

Iverson, R.M., Dzurisin, D., Gardner, C.A., Gerlach, T.M., LaHusen, R.G., Lisowski, M., Major, J.J., Malone, S.D., Messerich, J.A., Moran, S.C., Pallister, J.S., Qamar, A.I., Schilling, S.P., and Vallance, J.W., 2006, Dynamics of seismogenic volcanic extrusion at Mount St. Helens in 2004–05: Nature, v. 444, no. 7118, p. 439–443, doi:10.1038/nature05322.

James, M.R., Robson, S., Pinkerton, H., and Ball, M., 2006, Oblique photogrammetry with visible and thermal images of active lava flows: Bulletin of Volcanology, v. 69, no. 1, p. 105–108.

Jordan, R., and Kieffer, H.H., 1981, Topographic changes at Mount St. Helens—large-scale photogrammetry and digital terrain models, *in* Lipman, P.W., and Mullineaux, D.R., eds., The 1980 eruptions of Mount St. Helens, Washington: U.S. Geological Survey Professional Paper 1250, p. 135–141.

LaHusen, R.G., Swinford, K.J., Logan, M., and Lisowski, M., 2008, Instrumentation in remote and dangerous settings; examples using data from GPS "spider" deployments during the 2004–2005 eruption of Mount St. Helens, Washington, chap. 16 *of* Sherrod, D.R., Scott, W.E., and Stauffer, P.H., eds., A volcano rekindled; the renewed eruption of Mount St. Helens, 2004–2006: U.S. Geological Survey Professional Paper 1750 (this volume).

Mastin, L.G., Roeloffs, E., Beeler, N.M., and Quick, J.E., 2008, Constraints on the size, overpressure, and volatile content of the Mount St. Helens magma system from geodetic and dome-growth measurements during the 2004–2006+ eruption, chap. 22 *of* Sherrod, D.R., Scott, W.E., and Stauffer, P.H., eds., A volcano rekindled; the renewed eruption of Mount St. Helens, 2004–2006: U.S. Geological Survey Professional Paper 1750 (this volume).

Melnik, O., and Sparks, R.S.J., 2005, Controls on conduit magma flow dynamics during lava dome building eruptions: Journal of Geophysical Research, v. 110, no. B2, B02209, 21 p., doi:10.1029/2004JB003183.

Molander, C.W., 2001, Photogrammetry, *in* Maune, D.F., ed., Digital elevation model technologies and applications; the DEM users manual: The American Society for Photogrammetry and Remote Sensing, Bethesda, Maryland, p. 121–142.

Moore, J.G., and Albee, W.C., 1981, Topographic and structural changes, March–July 1980—photogrammetric data, *in* Lipman, P.W., and Mullineaux, D.R., eds., The 1980 eruptions of Mount St. Helens, Washington: U.S. Geological Survey Professional Paper 1250, p. 123–134.

Moran, S.C., Malone, S.D., Qamar, A.I., Thelen, W.A., Wright, A.K., and Caplan-Auerbach, J., 2008, Seismicity associated with renewed dome building at Mount St. Helens, 2004–2005, chap. 2 *of* Sherrod, D.R., Scott, W.E., and Stauffer, P.H., eds., A volcano rekindled; the renewed eruption of Mount St. Helens, 2004–2006: U.S. Geological Survey Professional Paper 1750 (this volume).

Mori, J., White, R.A., Harlow, D.H., Okubo, P., Power, J.A., Hoblitt, R.P., Laguerta, E.P., Lanuza, A., and Bautista, B.C., 1996, Volcanic earthquakes following the 1991 climactic eruption of Mount Pinatubo; strong seismicity during a waning eruption, *in* Newhall, C.G., and Punongbayan, R.S., eds., Fire and mud; eruptions and lahars of Mount Pinatubo, Philippines: Seattle, University of Washington Press, p. 339–350.

Murray, T., and Endo, E.T., 1992, A real-time seismic-amplitude measurement system (RSAM), *in* Ewert, J.A., and Swanson, D.A., eds., Monitoring volcanoes; techniques and strategies used by the staff of the Cascades Volcano Observatory, 1980–1990: U.S Geological Survey Bulletin 1966, p. 5–10.

Nakada, S., Miyake, Y., Sato, H., Oshima, O., and Fujinawa, A., 1995, Endogenous growth of dacite dome at Unzen volcano (Japan), 1993–1994: Geology, v. 23, no. 2, p. 157–160.

Nakada, S., Shimizu, H., and Ohta, K., 1999, Overview of the 1990–1995 eruption at Unzen Volcano: Journal of Volcanology and Geothermal Research, v. 89, p. 1–22.

Poland, M.P., Dzurisin, D., LaHusen, R.G., Major, J.J., Lapcewich, D., Endo, E.T., Gooding, D.J., Schilling, S.P., and Janda, C.G., 2008, Remote camera observations of lava dome growth at Mount St. Helens, Washington, October 2004 to February 2006, chap. 11 *of* Sherrod, D.R., Scott, W.E., and Stauffer, P.H., eds., A volcano rekindled; the renewed eruption of Mount St. Helens, 2004–2006: U.S. Geological Survey Professional Paper 1750 (this volume).

Power, J.A., 1988, Seismicity associated with the 1986 eruption of Augustine Volcano, Alaska: Fairbanks, University of Alaska, M.S. thesis, 142 p.

Power, J.A., Lahr, J.C., Page, R.A., Chouet, B.A., Stephens, C.D., Harlow, D.H., Murray, T.L., and Davies, J.N., 1994, Seismic evolution of the 1989–1990 eruption sequence of Redoubt Volcano, Alaska: Journal of Volcanology and Geothermal Research, v. 62, p. 69–94.

Power, J.A., Jolly, A.D., Page, R.A., and McNutt, S.R., 1995, Seismicity and forecasting of the 1992 eruptions of Crater Peak vent, Mount Spurr Volcano, Alaska; an overview, *in* Keith, T.C., ed., The 1992 eruptions of Crater Peak Vent, Mount Spurr Volcano, Alaska: U.S. Geological Survey Bulletin 2139, p. 149–159.

Rose, W.I., 1987, Volcanic activity at Santiaguito volcano, 1976–1984, *in* Fink, J.H., ed., The emplacement of silicic domes and lava flows: Geological Society of America Special Paper 212, p. 17–27.

Rowe, C.A., Thurber, C.H., and White, R.A., 2004, Dome growth behavior at Soufriere Hills Volcano, Montserrat, revealed by relocation of volcanic event swarms, 1995–1996: Journal of Volcanology and Geothermal Research, v. 134, no. 3, p. 199–221.

Schilling, S.P., Carrara, P.E., Thompson, R.A., and Iwatsubo, E.Y., 2004, Posteruption glacier development within the crater of Mount St. Helens, Washington, USA: Quaternary Research, v. 61, no. 3, p. 325–329.

Schilling, S.P., Thompson, R.A., Messerich, J.A., and Iwatsubo, E.Y., 2008, Use of digital aerophotogrammetry to determine rates of lava dome growth, Mount St. Helens, Washington, 2004–2005, chap. 8 *of* Sherrod, D.R., Scott, W.E., and Stauffer, P.H., eds., A volcano rekindled; the renewed eruption of Mount St. Helens, 2004–2006: U.S. Geological Survey Professional Paper 1750 (this volume).

Sparks, R.S.J., and 19 others, 1998, Magma production and growth of the lava dome of the Soufriere Hills Volcano, Montserrat, West Indies—November 1995 to December 1997: Geophysical Research Letters, v. 25, no. 18, p. 3421–3424.

Swanson, D.A., Dzurisin, D., Holcomb, R.T., Iwatsubo, E.Y., Chadwick, W.W., Jr., Casadevall, T.J., Ewert, J.W., and Heliker, C.C., 1987, Growth of the lava dome at Mount St. Helens, Washington (USA), 1981–1983, *in* Fink, J.H., ed., The emplacement of silicic domes and lava flows: Geological Society of America Special Paper 212, p. 1–16.

Thompson, R.A., and Schilling, S.P., 2007, Photogrammetry, *in* Dzurisin, D., ed., Volcano deformation—geodetic monitoring techniques: Berlin, Springer, Springer-Praxis Books in Geophysical Sciences, p. 195–221.

Ui, T., Matsuwo, N., Sumita, M., and Fujinawa, A., 1999, Generation of block and ash flows during the 1990–1995 eruption of Unzen volcano, Japan: Journal of Volcanology and Geothermal Research, v. 89, p. 123–137.

Vallance, J.W., Schneider, D.J., and Schilling, S.P., 2008, Growth of the 2004–2006 lava-dome complex at Mount St. Helens, Washington, chap. 9 *of* Sherrod, D.R., Scott, W.E., and Stauffer, P.H., eds., A volcano rekindled; the renewed eruption of Mount St. Helens, 2004–2006: U.S. Geological Survey Professional Paper 1750 (this volume).

Voight, B., 1981, Time scale for the first moments of the May 18 eruption, *in* Lipman, P.W., and Mullineaux, D.R., eds., The 1980 eruptions of Mount St. Helens, Washington: U.S. Geological Survey Professional Paper 1250, p. 69–86.

Voight, B., Hoblitt, R.P., Clarke, A.B., Lockhart, A.B., Miller, A.D., Lynch, L.L., and McMahon, J., 1998, Remarkable cyclic ground deformation monitored in real time on Montserrat, and its use in eruption forecasting: Geophysical Research Letters, v. 25, p. 3405–3408.

Wano, K., and Okada, H., 1980, Peculiar occurrence of Usu earthquake swarms associated with recent doming activity: Jishin, v. 33, p. 215–226.

Wolf, P.R., and Dewitt, B.A., 2000, Elements of photogrammetry with applications in GIS (3d ed.): Boston, McGraw-Hill, 608 p.

Yamashina, K., Matsushima, T., and Ohmi, S., 1999, Volcanic deformation at Unzen, Japan, visualized by a time-differential stereoscopy: Journal of Volcanology and Geothermal Research, v. 89, p. 73–80.

Zlotnicki, J., Ruegg, J.C., Bachelery, P., and Blum, P.A., 1990, Eruptive mechanism on Piton de la Fournaise volcano associated with the December 4, 1983, and January 18, 1984 eruptions from ground deformation monitoring and photogrammetric surveys: Journal of Volcanology and Geothermal Research, v. 40, no. 3, p. 197–217, doi:10.1016/0377-0273(90)90121-U.

Appendix 1. Time-Lapse Photography of Mount St. Helens, 2004–2006—Movie

[This appendix appears only in the digital versions of this work in the DVD-ROM that accompanies the printed volume and as a separate file accompanying this chapter on the Web at: http://pubs.usgs.gov/pp/1750.]

The appendix is a time-lapse movie showing dome growth at Mount St. Helens from November 10, 2004, to May 10, 2006. The movie, in mpeg-1 file format and titled “Sugarbowl to May10 2006_5000.mpg,” is composed of 188 photographs taken by the Sugar Bowl remote camera. It was assembled by choosing the best image per day for times when weather was suitable for viewing the dome. File size is 23 Mb. Compiled by Matt Logan and Dan Gooding (USGS).

This page intentionally left blank

A Volcano Rekindled: The Renewed Eruption of Mount St. Helens, 2004–2006
Edited by David R. Sherrod, William E. Scott, and Peter H. Stauffer
U.S. Geological Survey Professional Paper 1750, 2008

Chapter 13

Effects of Lava-Dome Growth on the Crater Glacier of Mount St. Helens, Washington

By Joseph S. Walder[1], Steve P. Schilling[1], James W. Vallance[1], and Richard G. LaHusen[1]

Abstract

The process of lava-dome emplacement through a glacier was observed for the first time as the 2004–6 eruption of Mount St. Helens proceeded. The glacier that had grown in the crater since the cataclysmic 1980 eruption was split in two by the new lava dome. The two parts of the glacier were successively squeezed against the crater wall. Photography, photogrammetry, and geodetic measurements document glacier deformation of an extreme variety, with strain rates of extraordinary magnitude as compared to normal temperate alpine glaciers. Unlike such glaciers, the Mount St. Helens crater glacier shows no evidence of either speed-up at the beginning of the ablation season or diurnal speed fluctuations during the ablation season. Thus there is evidently no slip of the glacier over its bed. The most reasonable explanation for this anomaly is that meltwater penetrating the glacier is captured by a thick layer of coarse rubble at the bed and then enters the volcano's groundwater system rather than flowing through a drainage network along the bed. Mechanical consideration of the glacier-squeeze process also leads to an estimate for the driving pressure applied by the growing lava dome.

Introduction

Since October 2004, a silicic lava dome has been emplaced first through, and then alongside, glacier ice in the crater of Mount St. Helens. The dome has been emplaced in a near-solid state, not as liquid magma solidifying at the Earth's surface (Vallance and others, this volume, chap. 9). Heretofore, dome emplacement through a glacier was known only from a single published photograph (Simons and Mathewson, 1955, plate 6) showing a lava dome that had been emplaced through the caldera glacier of Great Sitkin Volcano, Alaska, sometime in 1945. Evidence bearing on lava-dome emplacement into ice has been presented by, for example, Gilbert and others (1996), who used geophysical methods to identify lava domes emplaced beneath the caldera glacier of Volcán Sollipulli, Chile, and by Tuffen and others (2001), who described a domelike rhyolite body that was evidently emplaced subglacially in Iceland and since exhumed. The 2004–6 eruption of Mount St. Helens has afforded the first-ever opportunity to actually document the process of lava-dome emplacement through a glacier.

The common picture of volcano-glacier interactions is one of rapid meltwater generation either as magma contacts the glacier bed—examples from Iceland have been especially well characterized, for example, the 1996 Gjálp eruption (Guðmundsson and others, 1997)—or as lava or pyroclasts are erupted onto the glacier surface (many examples are mentioned by Major and Newhall, 1989). At Mount St. Helens, however, glacier melt associated with dome emplacement has been minor, even as the glaciological consequences have been dramatic—Crater Glacier has been cut in half, and the resulting ice bodies have in succession been squeezed between the growing lava dome and the crater wall. In this paper we focus our attention on the glaciological consequences of the eruption. Condensed discussions of this material have been presented elsewhere by Walder and others (2005, 2007).

Field Setting: Crater Glacier Before October 2004

After the cataclysmic eruption of May 18, 1980, which beheaded, and in some cases completely destroyed, the glaciers that existed on the flanks of Mount St. Helens (Brugman and Meier, 1981), material from rock and snow avalanches began accumulating in the north-facing, amphitheaterlike crater (fig. 1). Mills (1992) used digitized topographic maps to

[1] U.S. Geological Survey, 1300 SE Cardinal Court, Vancouver, WA 98683

calculate the volumes of material eroded from the crater walls and accumulated on the crater floor. His results show that as of mid-1988, the thickness of accumulated material was 60 to 80 m across much of the crater floor south of the 1980–86 lava dome. The accumulated material as of mid-1988 was about 60 percent rock debris by volume and contained interstitial snow, but it was not flowing. The first reasonably clear evidence that a crater glacier had come into existence—the appearance of crevasses, which reflect flow—comes from photographs taken in September 1996 (Schilling and others, 2004). The glacier (now called Crater Glacier) at that time had a surface area of about 0.1 km^2; by September 2000, this area had increased to about 1 km^2. Proceeding similarly to Mills (1992) but using digital elevation models (DEMs), Schilling and others (2004) calculated that the material that had accumulated in the crater between May 18, 1980, and September 2000 had a thickness locally as great as 200 m and a volume of 1.2×10^8 m^3, of which about one-third comprised rock debris. If we interpret these figures in the context of Mills' discussion of what had accumulated on the crater floor as of 1988, it seems clear that the deepest part of the crater-floor fill consists primarily of rock-avalanche debris—a point to which we shall return—and would not be considered glacier ice by usual glaciological standards. The uppermost part of Crater Glacier, however, probably contains no more than 5 percent rock debris by volume, with such debris forming discrete, discontinuous layers that originate as rock-avalanche lobes (fig. 2), and glaciologists would call this material "dirty" firn and glacier ice.

To what extent is the material accumulated on the crater floor since 1980 a glacier? In framing an answer, we have to make explicit our reason for asking the question in the first place. Our focus here is not on morphology, but rather on the ice flow and deformation processes familiar to glaciologists, and how such processes affect the mechanical response of the crater-fill material to lava-dome emplacement. From this perspective, what one is tempted to call a glacier in a morphological sense is not the same as what is rheologically and mechanically glacier ice. Deformation of a material containing 60 percent rock debris by volume—Mills' (1992) estimate for the composition of the pre-1988 crater-floor fill—is surely dominated by rock-to-rock friction, not creep of any interstitial ice.

We choose to exclude from our mechanically defined glacier, as best we can, the deepest, rock-rich crater-floor fill. We do this by picking the glacier bed as the crater-floor surface

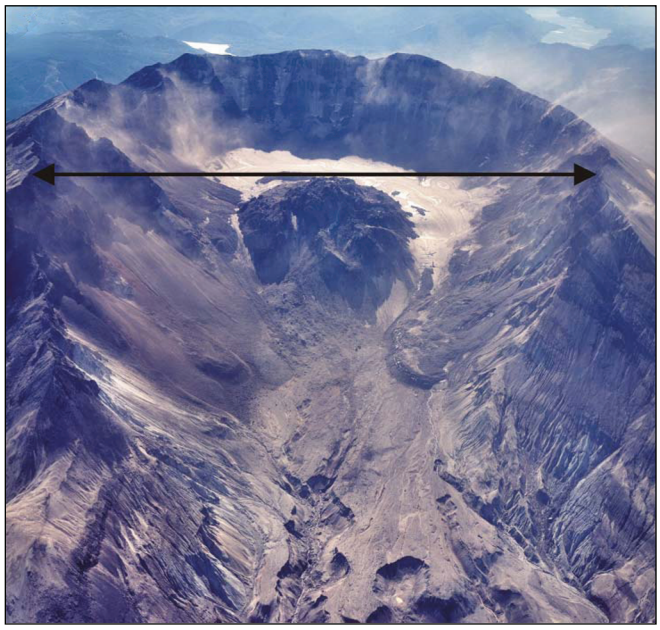

Figure 1. Oblique view of Mount St. Helens crater on October 5, 2000, looking south. Crater Glacier wraps around 1980–86 lava dome. East (left) arm of glacier is obscured by rock-avalanche debris; west (right) arm merges to the north of the lava dome with a rock-covered icy mass shed off the west crater wall. Crater width, as indicated by double-headed arrow, is about 2 km. USGS photograph by Bergman Photographic Services, Portland, Oreg.

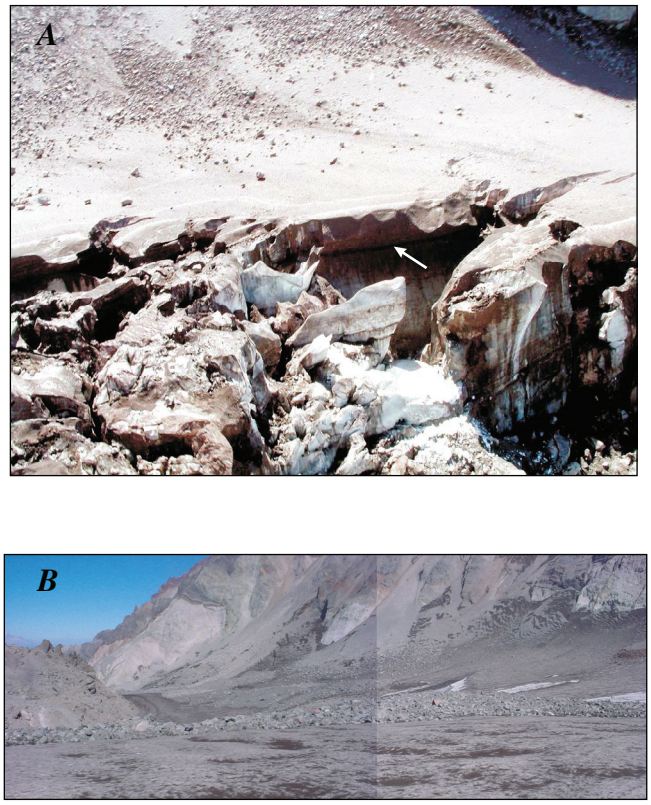

Figure 2. Glacier features in crater of Mount St. Helens. *A*, Rock layers within uppermost part of Crater Glacier, as exposed on west side of new lava dome. Distance from glacier surface to prominent debris layer (arrow) is about 3 to 5 m. View to east. USGS photograph taken August 4, 2005, by W.P. Johnson. *B*, Surface of Crater Glacier on August 20, 2003, looking north along east side of 1980–86 lava dome. Rock-avalanche lobe in center of view extended from the crater wall nearly to the south side of the lava dome and had maximum thickness of about 1 m. USGS photograph by J.S. Walder.

defined by DEMs for October 12, 1986, and November 12, 1986. This is an approximate but defensible choice for several reasons: (1) The rate of accumulation of rock debris in the crater decreased markedly after 1986 (fig. 3). (2) 1986 marks the end of the previous dome-growth episode, so accumulation after 1986 occurred within a basin with reasonably stable boundaries. (3) As we argue in appendix 1, interstitial ice within the lowest, rock-rich crater-fill material has probably melted and not been replaced by ice intruding from above. With the 1986 surface thus defined as the glacier bed, we then differenced 2003 and 1986 DEMs to calculate the glacier thickness shortly before the start of the 2004 eruption (fig. 4). Using the Mills (1992) and Schilling and others (2004) figures for rock-debris accumulation, we estimate that Crater Glacier, so defined, has an average rock content of 15 percent by volume.

A note about names. The U.S. Board on Geographic Names on June 6, 2006, approved the name "Crater Glacier" for the feature that existed before the recent eruption. However, as is documented below, Crater Glacier has been split in two by dome growth, and it is both sensible and convenient to use the informal names "west Crater Glacier" and "east Crater Glacier" for the ice masses that exist in the crater as of the time of writing.

Changes in Crater Glacier Since October 2004

Methods

Hazards posed by Mount St. Helens' eruptions severely restricted field work in the crater, so we documented eruptive effects on Crater Glacier primarily by photography and photogrammetry. We managed to collect some glacier-motion data using single-frequency global positioning system (GPS) stations slung by helicopter onto the glacier surface in 2005 and 2006. The GPS stations (LaHusen and others, this volume, chap. 16) were available for glacier monitoring only intermittently, and on several occasions had to be moved, or else they would have toppled into crevasses. Station positions were determined from short-baseline differential fixed static solutions sampled at 10-second intervals over a 25-minute period every hour. Accuracy of individual solutions was approximately 20 mm in the horizontal and 50 mm in the vertical. A running-median filter was applied to solutions to remove spikes.

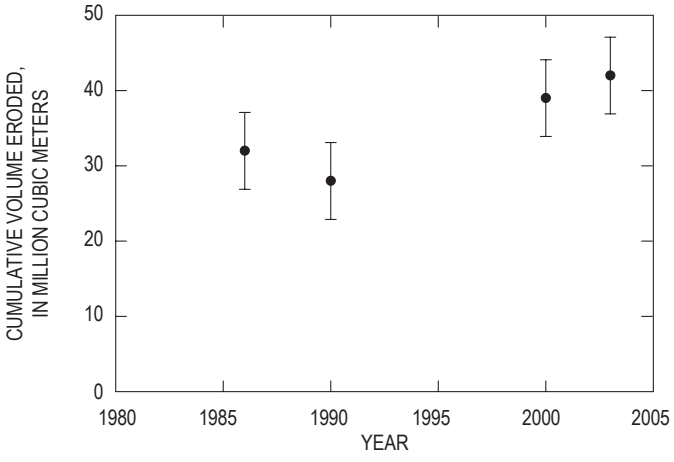

Figure 3. Cumulative volume eroded from walls of Mount St. Helens crater since the 1980 eruption, as determined by differencing digital elevation models for 1990, 2000, and 2003 with a DEM for 1980. Error bars (±1σ) are shown. Despite uncertainties in the data, it is clear that erosion rate has fallen sharply since the mid-1980s.

Morphological Changes

One of the first indirect signs of dome growth was the formation of a bulge in the south part of Crater Glacier during the last few days of September 2004 (fig. 5). An explosion on October 1, 2004, excavated a hole in the glacier (fig. 6). As the eruption proceeded, the southern part of Crater Glacier was eventually punctured by a rock spine surrounded by rubble (fig. 7), the latter perhaps comprising unconsolidated mate-

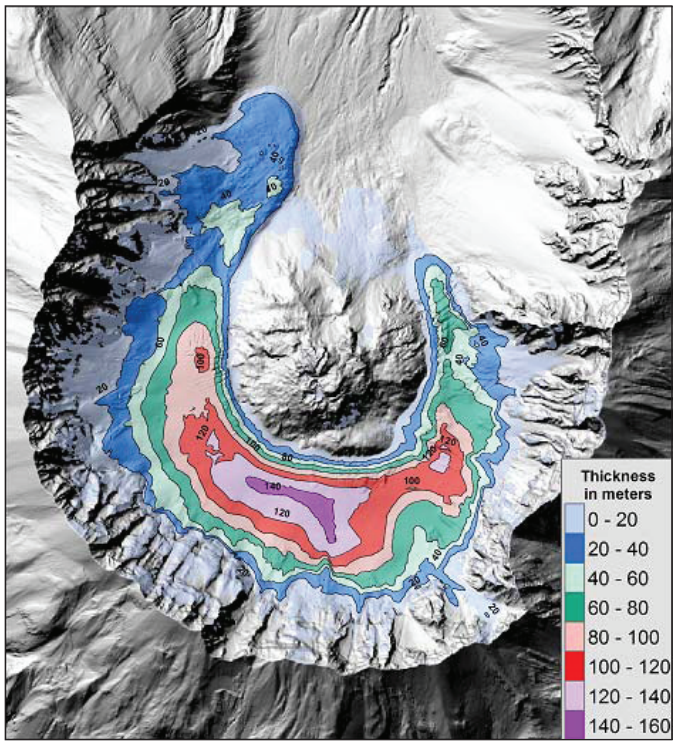

Figure 4. Map showing thickness of material accumulated on the crater floor of Mount St. Helens between October–November 1986 and September 2003. Background is a hillshade-relief map constructed from September 2003 digital elevation model. The 1980–86 lava dome is in center. As explained in text, the October–November 1986 surface is approximately the glacier bed, and the isopachs represent approximate glacier thickness.

rial that underlay the glacier. The lava dome as it exists as of October 4, 2006, is a complex of seven such spines extruded sequentially in the solid state from the same general vent area (fig. 8; Vallance and others, this volume, chap. 9). Spine 3, which began to be extruded in late October 2004, grew preferentially southward, developing a whaleback form and pushing aside firn and ice in a way reminiscent of the bow wave that precedes a ship through water (fig. 9). After spine 3 ran into the south crater wall in mid-November 2004, Crater Glacier was for all practical purposes split into two parts.

East Crater Glacier

Spine 3 spread to the east until late December 2004, then spalled greatly and was shouldered aside by spine 4—another "whaleback"—which grew until mid-April 2005. The east Crater Glacier (ECG) was effectively caught in a vise formed by the whaleback spines and the east crater wall. Owing to drought conditions that prevailed throughout most of the winter of 2004–5, there was practically no snow accumulation, and thus glacier-surface features showed very clearly. As eastward dome growth proceeded, the upwarped glacier apron on the east side of the dome (compare fig. 9) impinged against the east crater wall. However, the northernmost part of this ice apron was rotated until it formed a steplike feature trending nearly east to west (fig. 10). The ECG surface buckled, with east-west-trending crevasses forming parallel to the direction of dome spreading (fig. 11). Comparison of DEMs reveals that between mid-November 2004 and mid-April 2005, the dome/ECG contact migrated laterally by as much as 200 to 250 m and the glacier locally doubled in thickness (figs. 12, 13, 14). Expressed in terms of rates, the dome-ECG contact moved on average about 1 m/d and the glacier thickened at an astounding 0.6 m/d. By way of comparison, the average thickening rate for the "reservoir area" of a surging glacier, during the interval between surges, is perhaps 0.02 to 0.04 m/d (Raymond, 1987, p. 9123, fig. 1).

Since spine 4 quit growing in mid-April 2005, east Crater Glacier has thinned in its upper reach and thickened in its lower reach as normal flow processes redistribute ice mass downslope. Longitudinal crevasses became obvious by late April 2005; these crevasses probably reflect transverse spreading as the bowed-up surface—so evident during the squeezing episode—relaxed. As a result, the glacier surface became a field of seracs (fig. 15). The ECG terminus became steep (fig. 16) and advanced by about 150 m between April 19, 2005, and August 18, 2006.

Figure 5. Bulge in Crater Glacier next to south side of 1980–86 lava dome on September 30, 2004. Dark material on surface of fractured area is talus. Width of bulge is about 50 m. View to west. USGS photograph by D. Dzurisin.

Figure 6. Beginning of Mount St. Helens eruption through Crater Glacier on October 1, 2004. View to west. USGS photograph by J.S. Pallister.

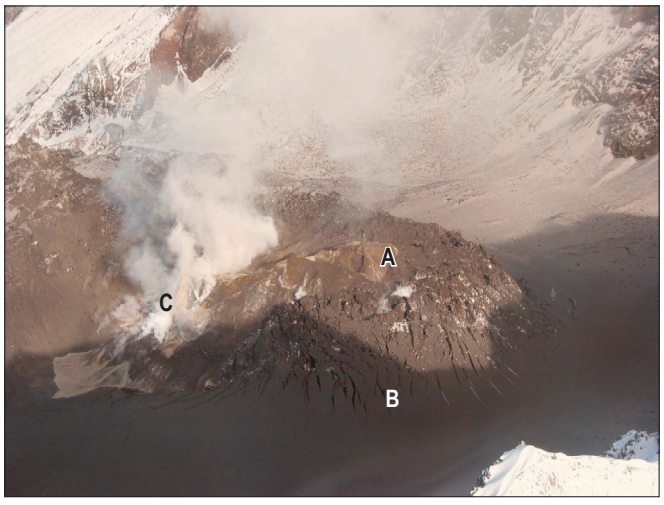

Figure 7. Upwarped, tephra-covered firn and ice around margins of new lava dome on October 11, 2004. View to northeast. A, Deformed rock at ambient temperature. B, Deformed firn and ice. C, Spine 1 (hot rock). USGS photograph by C.A. Neal.

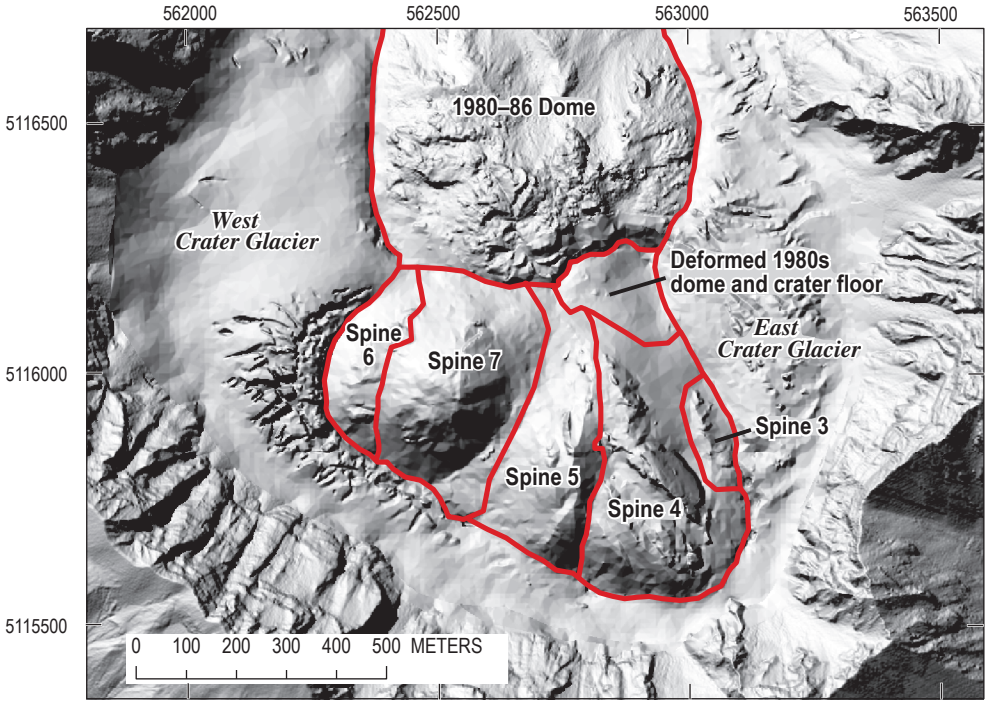

Figure 8. Map of the lava-dome spine complex in Mount St. Helens crater drawn on a hillshade-relief map from the October 24, 2005, DEM. Spines are numbered according to sequence of extrusion events, as discussed by Vallance and others (this volume, chap. 9). Coordinates referable to UTM zone 10, North American datum 1983.

Figure 9. Upwarped firn and ice around margin of new whaleback lava spine, November 20, 2004. View to east. USGS photograph by S.P. Schilling.

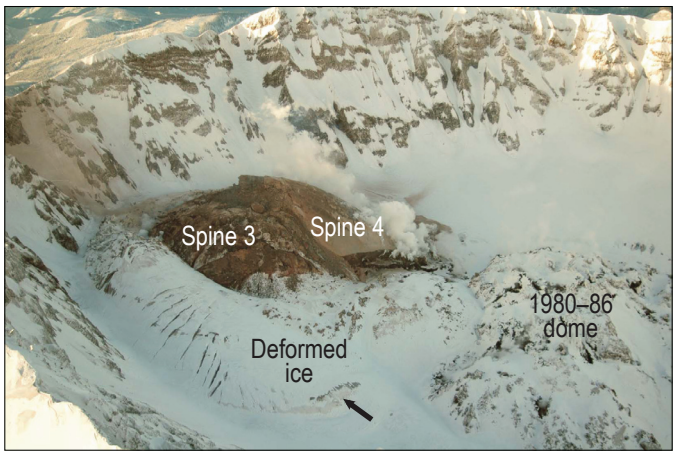

Figure 10. The new lava dome of Mount St. Helens (dominated by spines 3 and 4) and the by-then morphologically distinct east Crater Glacier (in foreground) on January 14, 2005. The bulge indicated by the arrow is not a kinematic wave but was instead formed when upwarped ice around the spine margins (see figs. 7, 8) was rotated as dome growth proceeded to east. View to southwest. USGS photograph by J.W. Vallance.

Figure 11. Upwarped surface of east Crater Glacier on February 16, 2005. View to north. Crevasses are oriented roughly east-west, paralleling direction of squeeze by new lava dome (at left). 1980s dome in left-center distance. USGS photograph by J.S. Walder.

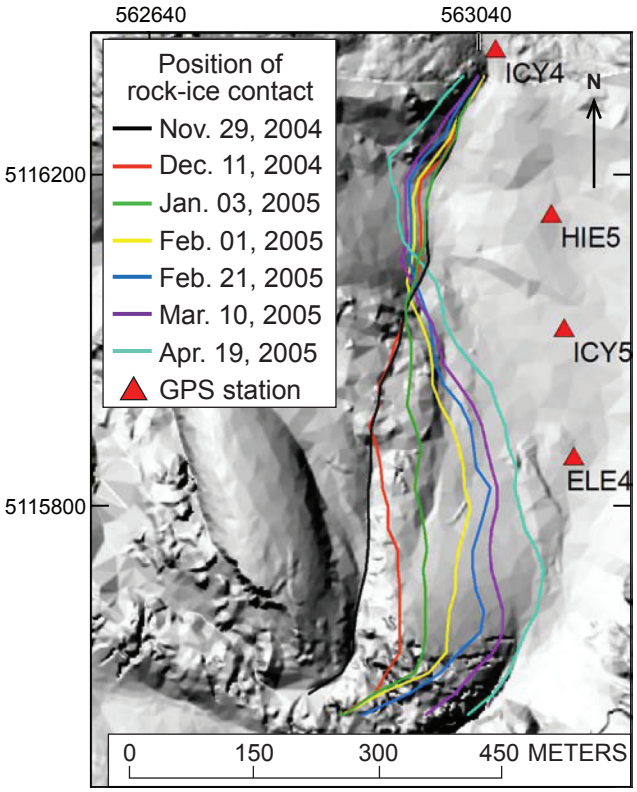

Figure 12. Migration of the contact between rock of the new lava dome and ice of east Crater Glacier during the period from November 29, 2004, to April 19, 2005. Contact position was determined from DEMs, with a probable error of about 5 m. Background image is hillshade-relief map for November 29, 2004. Coordinates are UTM zone 10 easting and northing, North American datum 1983. Eastward migration of rock-glacier contact for northing between about 5115500 and 5116000 reflects growth of new lava dome, which caused the glacier to thicken locally. The resulting enhanced ice flow to the north caused ice to encroach upon the margin of the old (1980–86) lava dome north of about northing 5116050. Also indicated are positions of four GPS stations deployed on the glacier at various times.

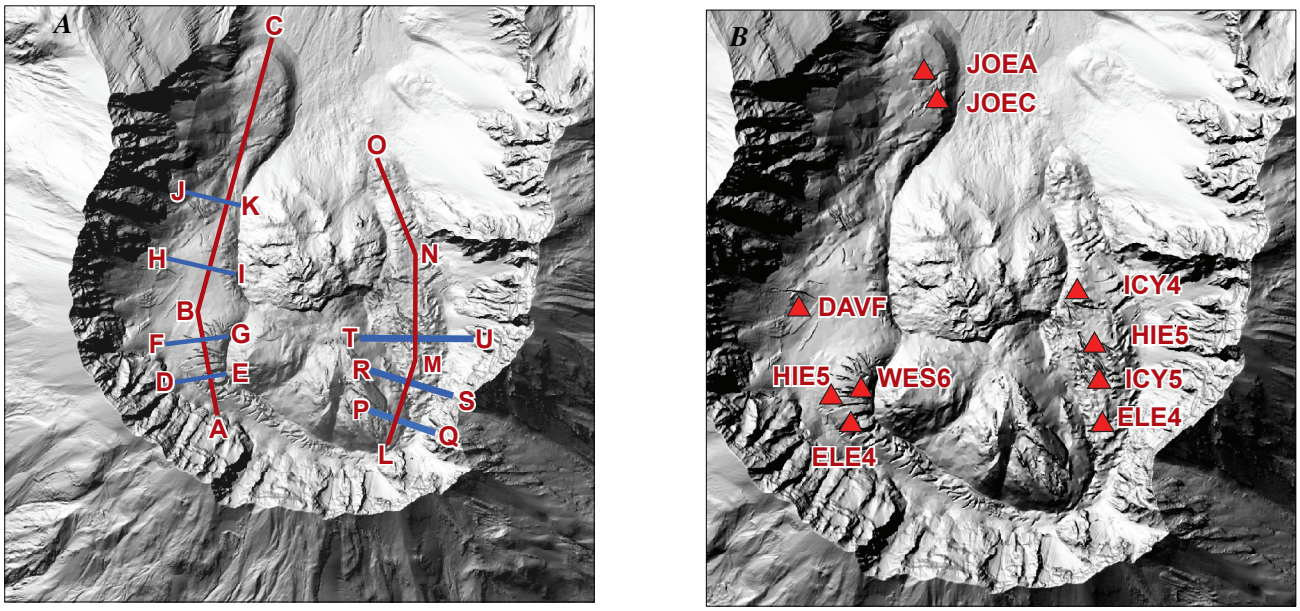

Figure 13. Hillshade-relief maps of Mount St. Helens crater constructed from photogrammetric analysis of aerial photographs dated October 24, 2005. *A*, Lines of section for which we calculated changes in glacier-surface altitude. *B*, Positions of GPS stations. Note that any individual station may not have been on the glacier on the date of the photographs. ELE4 appears twice because it was shifted from east Crater Glacier to west Crater Glacier during the course of the eruption.

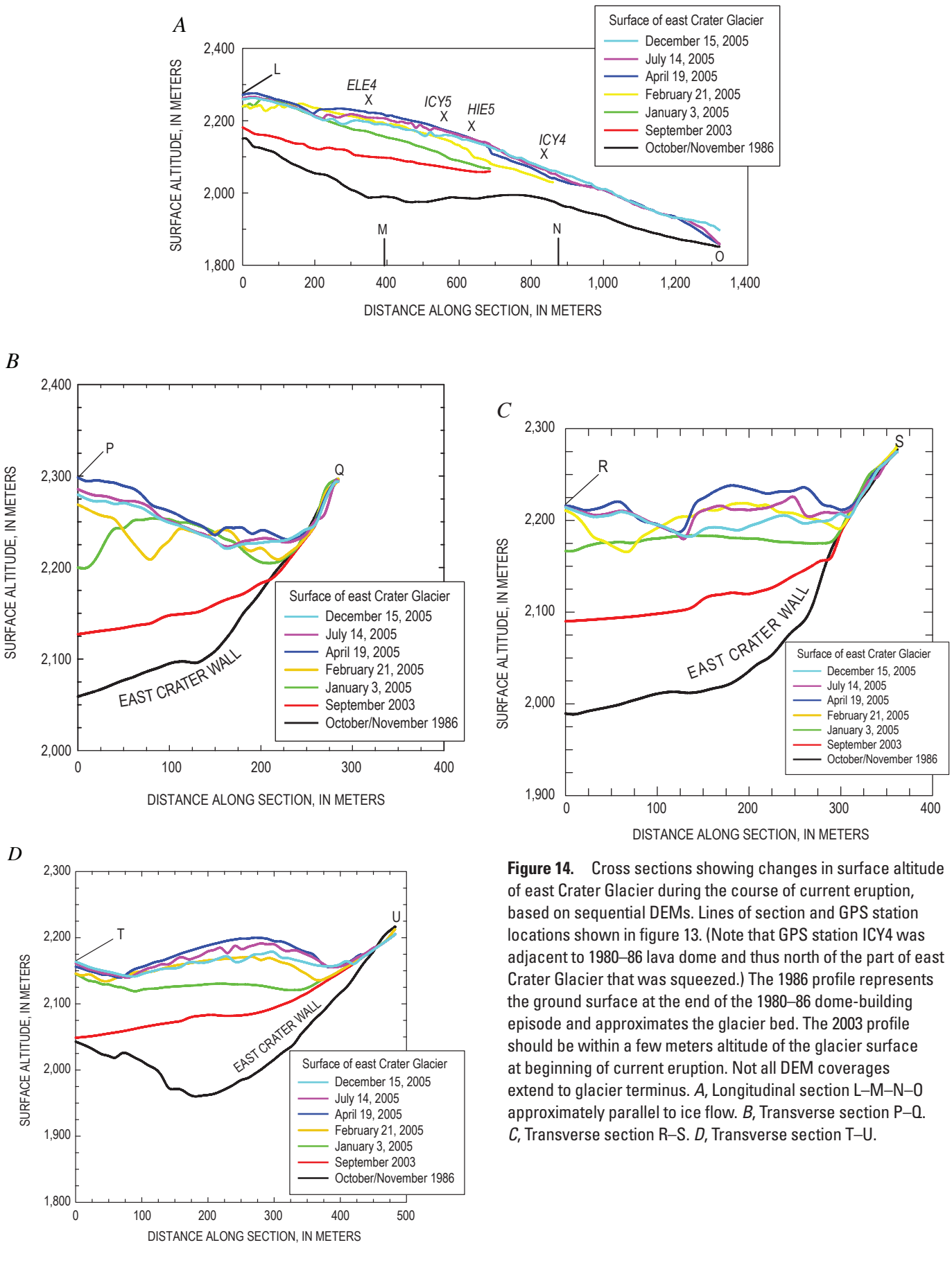

Figure 14. Cross sections showing changes in surface altitude of east Crater Glacier during the course of current eruption, based on sequential DEMs. Lines of section and GPS station locations shown in figure 13. (Note that GPS station ICY4 was adjacent to 1980–86 lava dome and thus north of the part of east Crater Glacier that was squeezed.) The 1986 profile represents the ground surface at the end of the 1980–86 dome-building episode and approximates the glacier bed. The 2003 profile should be within a few meters altitude of the glacier surface at beginning of current eruption. Not all DEM coverages extend to glacier terminus. *A*, Longitudinal section L–M–N–O approximately parallel to ice flow. *B*, Transverse section P–Q. *C*, Transverse section R–S. *D*, Transverse section T–U.

West Crater Glacier

Growth of spine 6 (Vallance and others, this volume, chap. 9) adjacent to west Crater Glacier (WCG) became noticeable in early August 2005. Surface bulging and crevassing of the glacier proceeded in much the same way as with ECG (fig. 17). Spine 6 quit growing, and spine 7 began growing and overriding spine 6, in early to mid-October 2005, but WCG continued to be squeezed owing to the push exerted by spine 7 on spine 6. Events unfolded much as with ECG: The dome-WCG contact migrated locally by >200 m (fig. 18), and the glacier locally doubled in thickness (fig. 19). A distinct bulge in the WCG surface began propagating downglacier (fig. 19*A*) and impinged upon the rather flat, mostly rock-covered terminus region, which arguably originated as a separate mass shed from the west crater wall (compare fig. 1). In summer 2006, it became clear that advance of the bulge was being accommodated by development of a shear zone within the flat terminus region (fig. 20).

Figure 15. Crevasses formed by lava-dome growth at Mount St. Helens. *A*, Longitudinal crevasses on east Crater Glacier cutting across transverse crevasses that had formed during eastward lava-dome growth (compare fig. 9), as seen on May 12, 2005. View to southwest. USGS photograph by M. Logan. *B*, Part of east Crater Glacier on July 26, 2005. View to south. Longitudinal crevasse growth by this date had effectively chopped the glacier surface into a field of seracs. USGS photograph by S.P. Schilling.

Change in Ice Volume During the Eruption

The change in glacier volume during the course of the eruption can be determined by comparing DEMs prepared for different dates. The method is discussed in appendix 2, and results are summarized in figure 21. The estimated volume decrease from the start of the eruption (October 2004) until October 2005—meaning (approximately) from the end of one ablation season to the end of the next ablation season—was $6.7\pm3.7\times10^6$ m^3, corresponding to an average rate of loss of 0.21 ± 0.12 m^3/s. The eruption has clearly not been marked by a process commonly associated with volcano-glacier interactions, namely, rapid meltwater generation (Major and Newhall, 1989). In retrospect, this is unsurprising—the eruption has been predominantly quiescent, not explosive, so scouring of the glacier surface by hot fragmental flows has been negligible; moreover, the spines have been extruded in a solid state, with surface temperature well below the solidus, and the glacier is well insulated from them by rubble (Schneider and others, this volume, chap. 17).

Ice Dynamics

Given the radical morphological changes to Crater Glacier during the eruption, described above, we should not be surprised if the glacier's dynamics were also significantly affected. Unfortunately, our complete lack of data on glacier-surface speed before the 2004 eruption complicates an assessment of how the eruption affected glacier dynamics. To try to infer a rough baseline for preeruption dynamics, we use mass-balance considerations to estimate the so-called balance velocity U_b, which is the cross-sectionally averaged speed that a glacier would have if it were in steady state (Paterson, 1994, p. 250):

$$U_b(x) = \frac{1}{W(x)\bar{H}(x)} \int_0^x \dot{b}(\xi) W(\xi)\, d\xi \quad , \qquad (1)$$

where $W(x)$ is glacier width at distance x from the "headwall" or upstream end (in this case, the south crater wall), $\bar{H}(x)$ is average depth at a cross section, and $\dot{b}(x)$ is the local mass

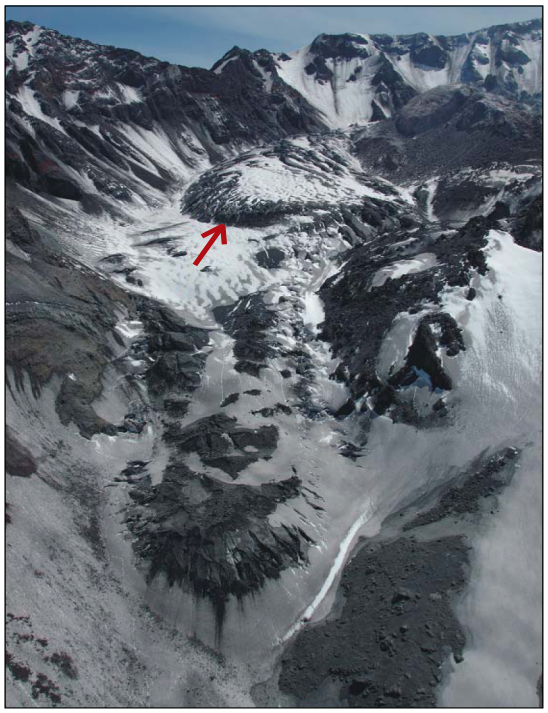

Figure 16. Terminus (lower center) of east Crater Glacier on June 15, 2005. View to south. Compare to indistinct terminus as seen about 5 years earlier (fig. 1). Arrow indicates bulge similarly indicated in figure 10. The glacier is only about 100 to 150 m wide where it passes between crater wall and old lava dome (right center) USGS photograph by S.P. Schilling.

balance expressed as a thickness per unit time. Equation 1 is simply a mathematical statement of the steady-state assumption, namely, that the glacier is neither thickening nor thinning. We apply equation 1 to what would become (during the eruption) east Crater Glacier and estimate U_b near the terminus (at a position we denote by $x = L$) by taking $L \approx 1.2$ km, $\bar{H} \approx 60$ m (fig. 14*A*), and an average value $\dot{b} \approx 4$ m/yr (from a total ice accumulation of about 80×10^6 m^3 over an area of about 1 km^2

Figure 17. West Crater Glacier adjacent to westward-growing lava dome as seen on September 2, 2005. View to southeast. The crevasse pattern in the glacier is complicated and reflects shifting directions of dome growth, but those crevasses normal to the dome-glacier margin are the youngest.
USGS photograph by M. Logan.

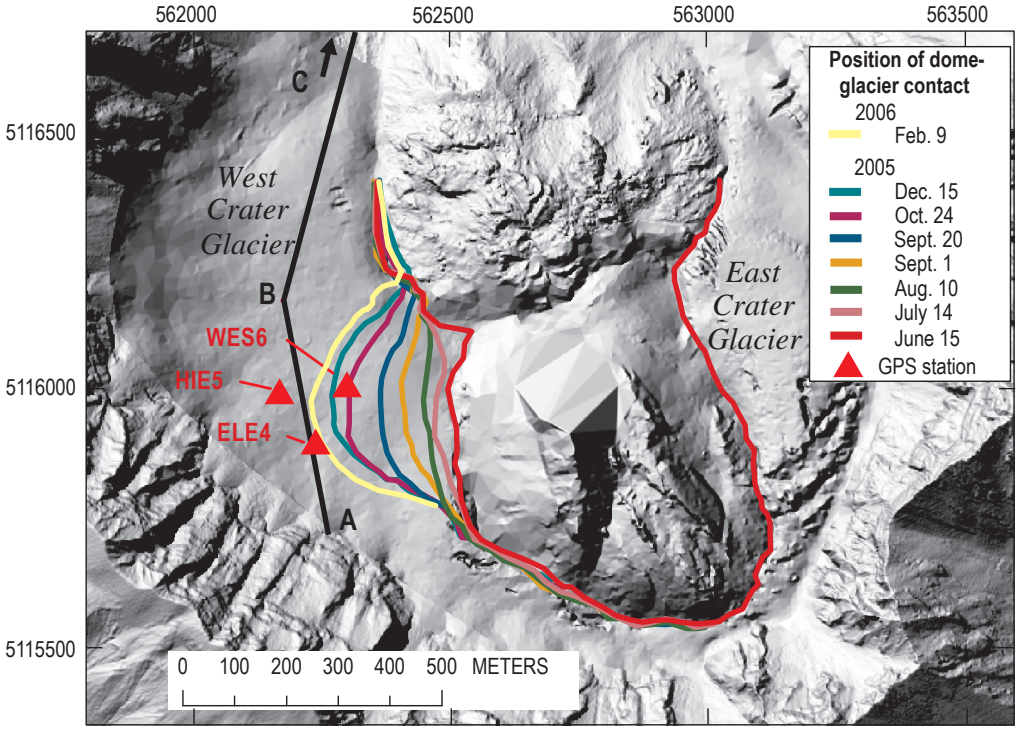

Figure 18. Migration of contact between the new lava dome and west Crater Glacier during the period June 15, 2005, to February 9, 2006. Contact position was determined from DEMs, with a probable error of about 5 m. Background image is hillshade-relief map for June 15, 2005. Coordinates are UTM zone 10 easting and northing, North American datum 1983. As the new dome grew, the glacier encroached upon margin of the old (1980–86) lava dome. Also shown are positions of three GPS stations that were deployed on the glacier at various times in 2005.

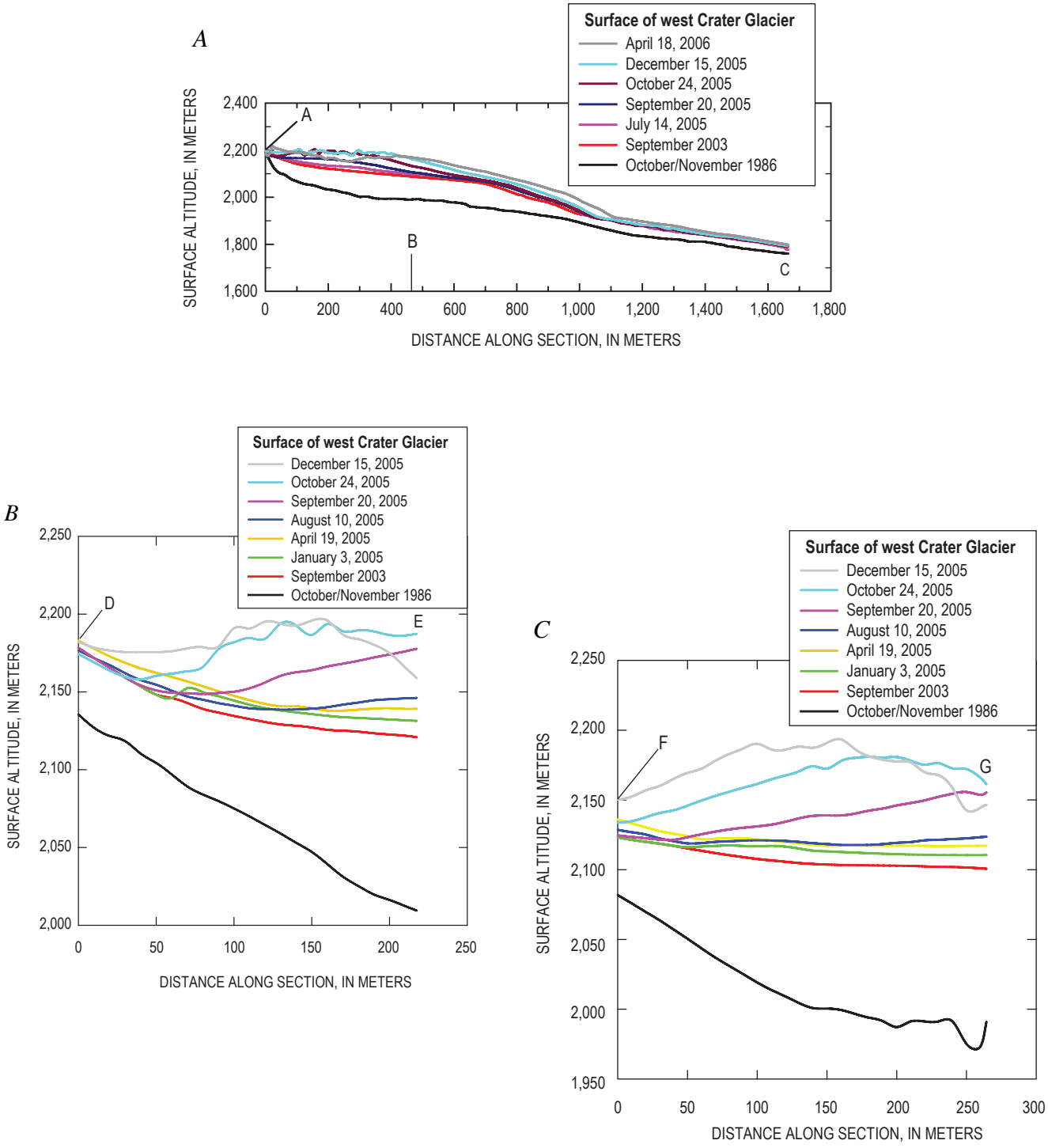

Figure 19. Change in surface altitude of west Crater Glacier during course of ongoing eruption, based on sequential DEMs. Lines of sections shown in figure 13. The 1986 profile represents the ground surface at end of the 1980–86 dome-building episode and is approximately the glacier bed. The 2003 profile should be within a few meters altitude of glacier surface at beginning of current eruption. *A*, Longitudinal section A–B–C, approximately following the thickest ice. The points labeled A, B, and C match those in figure 13*A*. *B*, Transverse section D–E. *C*, Transverse section F–G. *D*, Transverse section H–I. *E*, Transverse section J–K.

in 20 years), and by treating W as a constant. We find $U_b \approx 0.24$ m/d, which corresponds to a surface speed of about 0.29 m/d for ice with the flow-law exponent $n = 3$ (van der Veen, 1999, p. 103–106). We emphasize that this is at best a rough baseline for thinking about the preeruption surface speed, because the glacier was manifestly not in a steady state but rather growing.

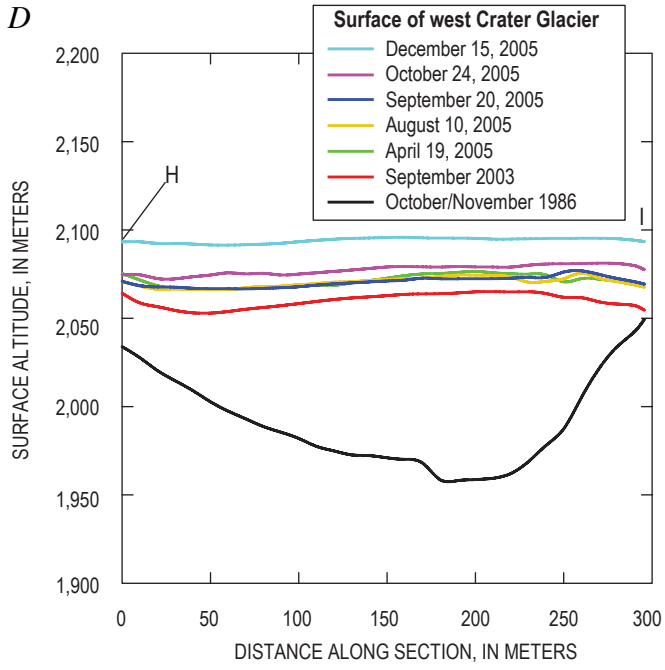

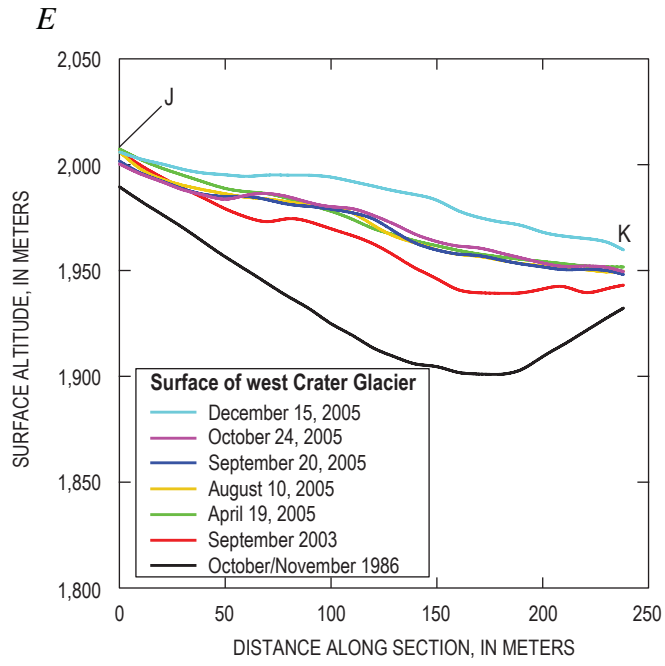

Figure 19—Continued.

East Crater Glacier

The GPS station positions during 2005 are shown in figure 13*B*; measured displacement rates are shown in figure 22. Interestingly, the balance velocity estimated above is comparable to the speed of station ICY4, which was downglacier of the

Figure 20. The glacier in Mount St. Helens crater as seen on September 12, 2006. View to south. As bulge on west Crater Glacier advanced and impinged on relatively flat terminus area, a shear zone delineated by echelon fractures developed (solid red curve). The shear zone at its northern end took on the character of a zone of compression, with crevasses parallel to direction of maximum compression (dotted red lines). Positions of GPS stations JOEA and JOEC are indicated. USGS photograph by W.E. Scott.

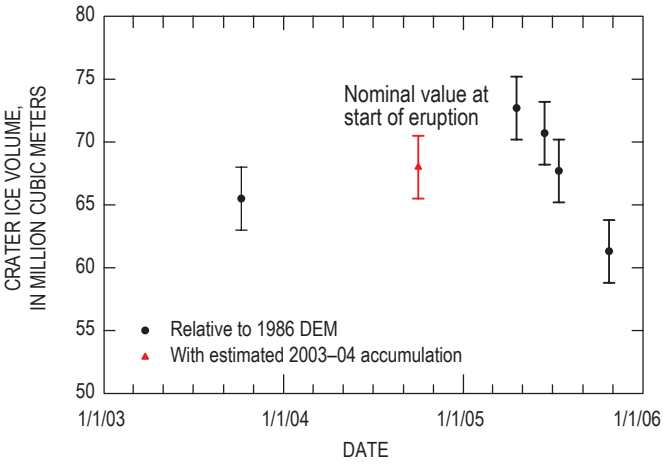

Figure 21. Total volume of glacier in Mount St. Helens crater as a function of time, with error bars (±1σ).

domain squeezed by the lava dome, on ice about 70 m thick and not far from the ECG terminus (fig. 10). In comparison, ICY5, about 300 m upglacier of ICY4, within the glacier reach being squeezed by dome growth (fig. 12) and on ice about 150 m thick, moved about 1.3 m/d, or about four times as fast as ICY4. This comparison presents a conundrum if deformation is only by simple shear and reflects a balance between gravitational driving stress and drag on the glacier bed and sides, in which case the difference in surface velocity between ICY4 and ICY5 should have been a factor of about $(150/70)^{n+1} \approx 21$ for a flow-law exponent $n = 3$ (van der Veen, 1999, p. 103–104). Moreover, owing to the nonlinear rheology of glacier ice (van der Veen, 1999, p. 13–15), the squeeze exerted on east Crater Glacier by the growing lava dome should have reduced the effective viscosity of the ice near ICY5 and made the difference in speed from ICY4 to ICY5 even greater. Resolution of the conundrum involves recognizing that gravitational driving stress is in fact resisted not only by drag but also by gradients in stress along the flow (van der Veen, 1999). A useful mechanical analogy is to think of east Crater Glacier, during the squeezing episode, as a tube of toothpaste with the cap removed. If the entire tube were squeezed uniformly, toothpaste would squirt out rapidly, but if squeezing is applied only to the part of the tube farthest from the opening, the toothpaste nearer the opening acts as a dam. Computational modeling by Price and Walder (2007) has confirmed the existence of a very strong longitudinal stress gradient.

Strain rates associated with ECG deformation can be estimated, in part, by considering the rate of eastward migration of the dome-glacier contact and the rate of glacier-surface uplift. Dividing the rate of eastward migration of the dome-glacier contact near ELE4 (fig. 12) by the glacier width (about 300 m), the average rate of contact migration for the period December 1, 2004, to January 3, 2005, corresponds to a squeeze strain rate of about –0.006/d; for the period January 3, 2005, to April 16, 2005, the squeeze strain rate was about –0.0036/d. Elongational strain rate in the downglacier direction cannot be estimated directly owing to the fact that there were never simultaneously two GPS units on the reach being squeezed. The strain rate associated with glacier thickening for the period January 3, 2005, to April 16, 2005, can be roughly estimated (see fig. 14*A*) at about (0.6 m/d)/(100 m) ≈ 0.006/d near the centerline of east Crater Glacier.

To put the ECG strain-rate values in perspective, consider ice moving through a valley constriction at a rate of 100 m/y, with the valley narrowing by 25 percent over a length of 1 km—arguably a rather severe constriction. The lateral strain rate in this case would be –0.0001/d, or about 1–3 percent of the lateral strain rate associated with squeezing of the ECG. Thickening strain rate as large as that measured at ECG is known only from surge fronts (Kamb and others, 1985; Raymond and others, 1987), although in such cases the maximum compression is oriented along the normal ice-flow direction, whereas with ECG, maximum compression was transverse to the normal ice-flow direction.

West Crater Glacier

The GPS stations on west Crater Glacier during the summers of 2005 and 2006 (fig. 13*B*) recorded the response of the glacier to westward dome growth. We discuss results for 2005 and 2006 separately.

In 2005 (fig. 23), the peak in speed of ELE4 at about day 273 (September 30) occurred a few days before the appearance of spine 7 just east of spine 6 (fig. 8; Vallance and others, this volume, chap. 9). This peak in speed probably reflects a change in the stresses applied to WCG by the dome. During the 23-day period when the GPS records overlapped, all three stations on WCG accelerated rather smoothly (fig. 23*B*); differences in azimuth of motion reflect the local direction of dome growth. The displacement records for the overlap

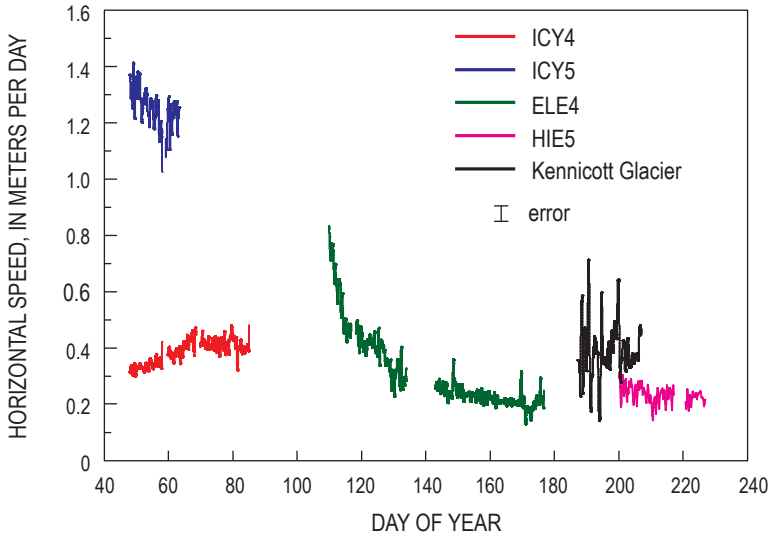

Figure 22 Horizontal speed of east Crater Glacier GPS stations. Locations of the stations shown in figure 12. Raw position data were filtered to remove spurious spikes and interpolated to 0.2-d intervals. Estimated error is 0.05 m/d. ICY4 and ICY5 were on glacier in mid- to late winter 2005 while the new lava dome was expanding eastward. ELE4 was fortuitously placed on glacier about the time that dome growth to east stopped, and it stayed on the glacier until early summer 2005. HIE5 was on the glacier in mid-summer 2005. Azimuth of motion for all stations was within 18° of north. Shown for comparison are surface-speed data (adapted from Anderson and others, 2005) for a target on Kennicott Glacier, a temperate valley glacier in Alaska, during the year 2000. The record for Kennicott Glacier shows large-amplitude, commonly diurnal fluctuations not seen at east Crater Glacier.

period were analyzed to determine direction and magnitude of the principal strain rates within the (approximately horizontal) plane determined by the three stations. Unsurprisingly, the direction of principal compression lined up closely with the trend of crevasses that formed during westward dome growth (fig. 17). Magnitudes of principal horizontal strain rates increased slowly over time, with their sum consistently negative at about –0.002/d. Making the plausible interpretation that surface uplift represents thickening of the glacier, vertical strain rate can be estimated as the average uplift rate divided by the glacier thickness, or about (0.25 m/d)/(120 m) = 0.002/d. The sum of the three principal strain rates was thus locally near zero, consistent with bulk incompressibility.

In 2006, we had motion data for three GPS stations located on WCG downglacier of the region being squeezed by the lava dome: DAVF, which operated for several months (during which time the station was relocated three times to prevent it from toppling into a crevasse), and JOEA and JOEC, which operated for about six weeks during summer (fig. 24). Station DAVF was slightly upglacier of the cross section H–I (fig. 13*A*), on ice that thickened steadily as west Crater Glacier was squeezed (fig. 19*D*). Although the motion record for DAVF (fig. 24*A*) is complicated by the effect of crevasse growth and the need to move the instrument, there is again an absence of the diurnal speed variation we would expect if glacier sliding were occurring. The motion records for JOEA and JOEC (fig. 24*B*), located only about 150 m apart, nicely document deformation associated with the shear zone shown in figure 20. Station JOEA (east of the shear zone), on ice being shoved as the bulge in the WCG surface propagates downglacier and impinges upon the terminus region, moved nearly three times as fast as JOEC (west of the shear zone). The difference in azimuth of motion between JOEA and JOEC almost certainly reflects the opening of roughly north-south-striking crevasses (fig. 20).

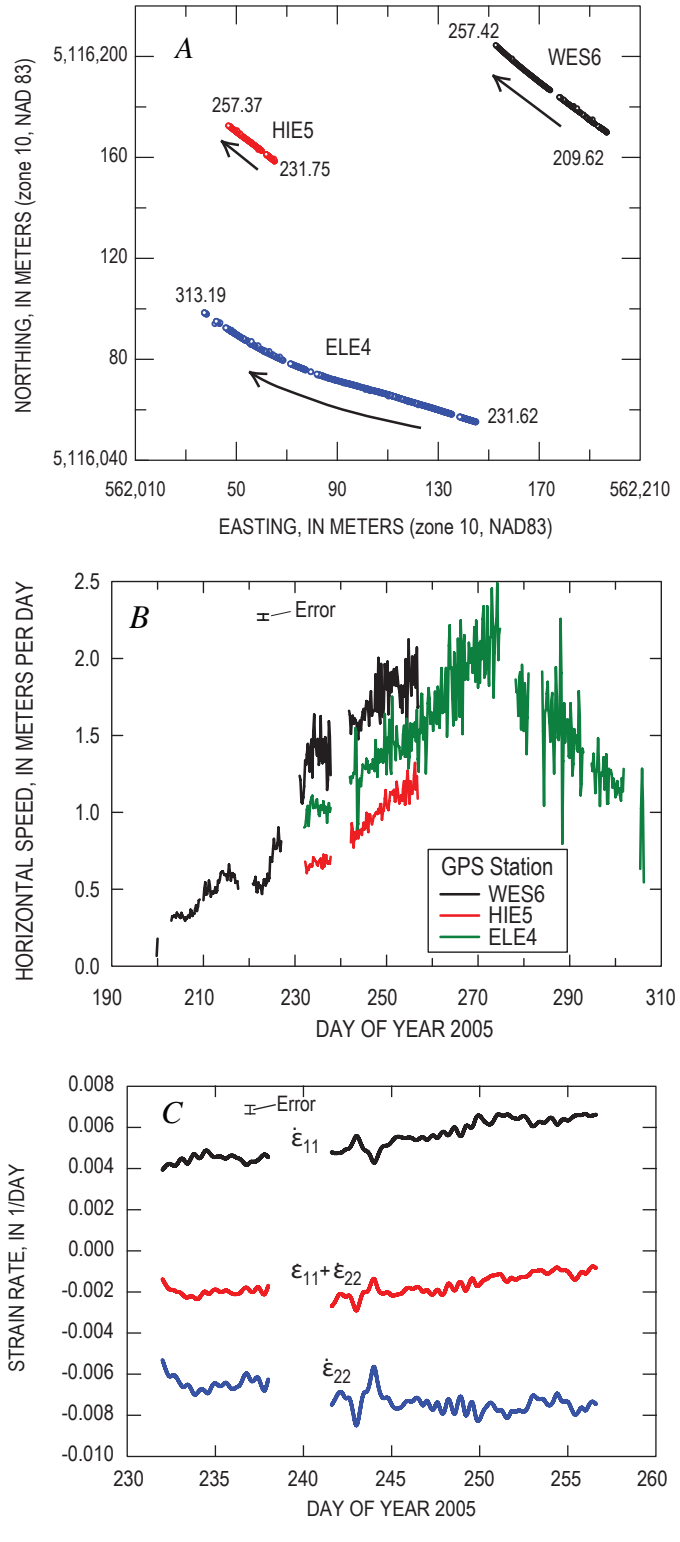

Inferences About Glacier and Volcano Hydrology

Temperate glaciers (those with ice at the melting point) move by a combination of internal creep and sliding of the ice over the bed (van der Veen, 1999). The creep component reflects the internal stress state of the glacier rather than conditions at the bed, whereas the sliding component reflects the boundary condition at the bed—in particular, how much friction there is against the bed. Measurements at many

Figure 23. GPS-derived motion data for west Crater Glacier in 2005. *A*, Displacement trajectories projected into horizontal plane, with day of year at beginning and end indicated. *B*, Horizontal speeds, calculated by filtering raw position data to remove spurious spikes, interpolating to 0.2-d intervals, and applying centered difference. Estimated error, shown by error bar, is 0.05 m/d. As with the east Crater Glacier record (fig. 22), diurnal speed fluctuations are not seen at west Crater Glacier. *C*, Principal strain rates in horizontal plane. Orientation of maximum extension ($\dot{\varepsilon}_{11}$) is N. 10° E.–S. 10° W.; orientation of maximum compression ($\dot{\varepsilon}_{22}$) is N. 80° W.–S. 80° E. For strictly incompressible ice, the sum $\dot{\varepsilon}_{11}+\dot{\varepsilon}_{22}$ would be zero.

glaciers have shown systematic differences between surface speed during the ablation (melt) season and during winter. For example, pulses of increased surface speed are commonly observed as the melt season begins (Anderson and others, 2004). More generally, surface speed in summer is higher than in winter, and large diurnal variations in surface speed are common (Fountain and Walder, 1998). As the creep component of glacier motion should be reasonably constant, variations in surface speed reflect variations in sliding speed, which is modulated by meltwater at the bed (see, for example, Harper and others, 2002). Our 2005 data for east Crater Glacier (fig. 22), however, show neither acceleration with the onset of the melt season nor a clear diurnal signal; data for west Crater Glacier from the summers of 2005 and 2006 (figs. 23, 24) similarly lack any diurnal signal. We propose as an explanation that there simply is no pressurized drainage system conveying water along the bed. Crater Glacier grew atop several tens of meters of rubble (mainly rock-avalanche debris) that had accumulated on the crater floor following the eruption of May 18, 1980 (Mills, 1992). As argued in appendix 1, much of this rubble is likely to be ice free because geothermal heat flow will have melted interstitial ice, and flow of the overlying ice downward into the rubble will have been slow. The volcanic edifice beneath this rubble is geologically complex, consisting of multiple lava flows, pyroclastic and lahar deposits, and other fragmental deposits (Crandell, 1987). Thus, water that reaches the glacier bed probably flows out of the crater through the rubble layer or downward into the volcano's groundwater system, rather than moving along the glacier bed. In support of this hypothesis, we note that there are no outlet streams at the glacier termini, although there are springs and seeps farther downslope. Discharge in Loowit Creek, which heads several hundred meters downstream of the WCG and ECG termini and drains the crater, is not measured regularly, owing to the impossibility of maintaining a permanent gaging station in the very unstable stream channel. However, such occasional discharge measurements as have been made (fig. 25) show no evidence for systematically elevated streamflow during the eruption.

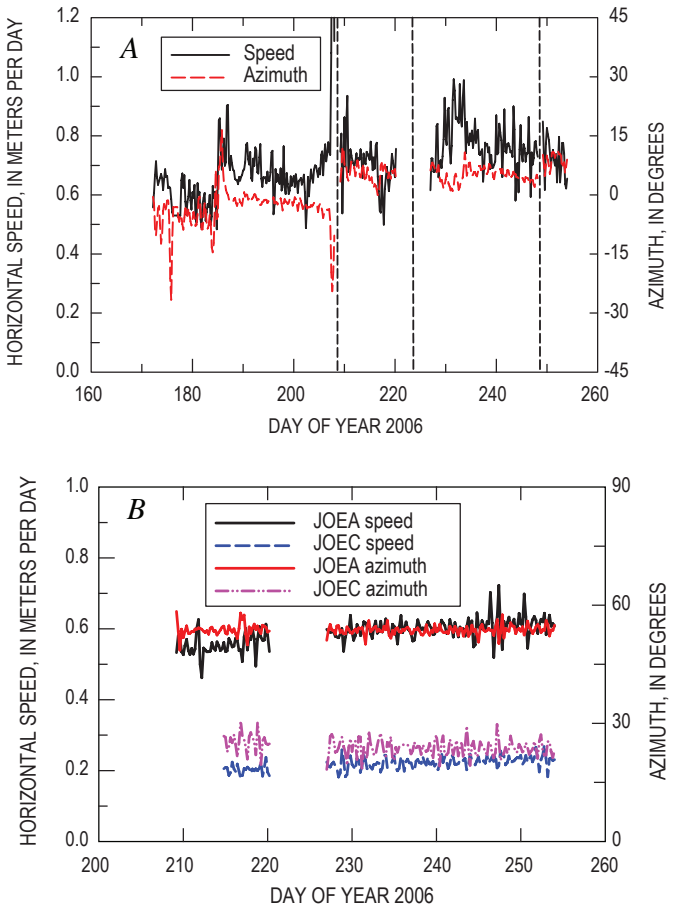

Figure 24. Motion data for GPS stations on the surface of west Crater Glacier in 2006. Estimated errors about 0.05 m/d for speed and 2 degrees for azimuth. See figure 13*B* for locations of the GPS stations. *A*, Horizontal speed and azimuth of GPS station DAVF. Dashed lines indicate breaks in data when instrument was moved to keep it from toppling into crevasses that formed during its stay. *B*, Horizontal speed and azimuth of GPS stations JOEA and JOEC.

Inferences from Glacier Dynamics Bearing on Lava-Dome Mechanics

We envisage outward push on Crater Glacier by the expanding Mount St. Helens dome as involving not glacier sliding, as usually considered by glaciologists, but low-angle thrust faulting. In our view, the glacier is being pushed over the underlying unconsolidated rock debris, with the décollement probably near the glacier bed (glacier bed being a rather ill-defined concept in the present case, as discussed earlier). Our conception of the process is sketched in figure 26. Glacier deformation

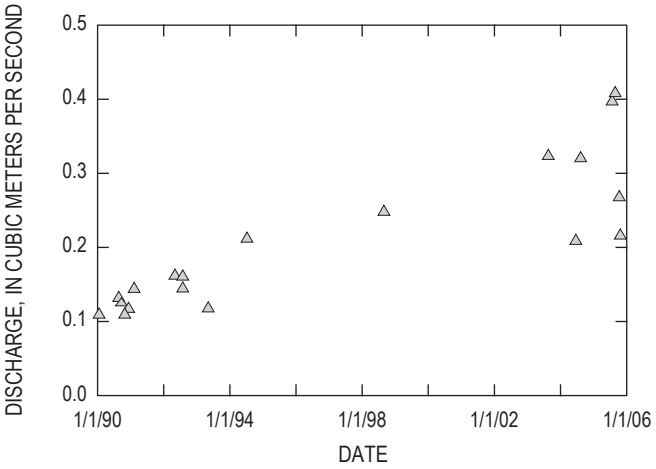

Figure 25. Discharge in Loowit Creek measured above Loowit Falls, from unpublished streamflow data collected by hydrologic surveillance staff at Cascades Volcano Observatory. Probable error in measurements is about 10 percent.

is for all intents and purposes quasistatic—accelerations can be ignored—so conservation of momentum reduces to a force balance. The force exerted by the lava dome will be balanced by the sum of resisting forces within the ice and at the glacier bed,

$$p \approx \left|\tau_{nn}\right| + (W/H)\tau_b, \qquad (2)$$

where p is the pressure (force per unit area) exerted by the lava dome, τ_{nn} is the deviatoric stress within the ice normal to the dome-glacier contact, W is the width of the glacier (that is, the distance from the dome to the crater wall), H is a typical value of ice thickness, and τ_b is the magnitude of the shear stress opposing displacement of the glacier in a direction normal to the dome-ice margin (fig. 26). If motion on the décollement involves essentially Coulomb friction (that is, frictional resistance proportional to the normal load), then $\tau_b \approx \mu\rho_i gH$, where μ is the coefficient of friction, ρ_i is the density of ice, and g is acceleration due to gravity, and our estimate for p becomes

$$p \approx \left|\tau_{nn}\right| + \mu\rho_i gW. \qquad (3)$$

We have taken the normal stress on the décollement to be equal to the ice-overburden pressure. Thus we are supposing that water pressure on the décollement is negligible, as is reasonable, because, as noted above, water at the glacier bed apparently flows downward into the volcano rather than in a pressurized drainage system along the bed.

We now estimate the magnitude of the two terms on the right-hand side of equation 3. The deviatoric stress within the ice normal to the dome-glacier contact, τ_{nn}, can be estimated if we take into account the rheological behavior of glacier ice as (see appendix 3):

$$\tau_{nn} = B\left|\dot{\varepsilon}_e\right|^{-2/3}\dot{\varepsilon}_{nn}, \qquad (4)$$

where $\dot{\varepsilon}_{nn}$ is the strain rate normal to the dome-glacier contact and the so-called effective strain rate $\dot{\varepsilon}_e$ (equal to one-half the second invariant of the strain-rate tensor) is in this case given by

$$2\dot{\varepsilon}_e^{\,2} = \dot{\varepsilon}_{nn}^2 + \dot{\varepsilon}_{tt}^2 + \dot{\varepsilon}_{zz}^2, \qquad (5)$$

where $\dot{\varepsilon}_{tt}$ is the strain rate tangential to the dome-glacier contact and $\dot{\varepsilon}_{zz}$ is the vertical strain rate. In writing equation 5, we assume that the directions normal and tangential to the dome-glacier contact are the directions of principal strain rates, an assumption that is supported by the available data. Using $B = 5.3\times10^7$ Pa·s$^{1/3}$ (Paterson, 1994; van der Veen, 1999) and the strain-rate calculations given above, we estimate $\left|\tau_{nn}\right| \approx$ 0.16–0.21 MPa. Taking $\mu \approx 0.5$ (consistent with there being considerable debris within the ice and thus much rock-to-rock friction at the décollement), $\rho_i = 900\,\mathrm{kg/m^3}$ (corresponding to glacier ice, not snow or firn), $g = 9.8$ m/s^2, and $W \approx 250$ m, the frictional term on the right-hand side of equation 3 has a magnitude of about 1.1 MPa. Frictional resistance on the décollement therefore dominates the force balance, with the estimated value of p being about 1.3 MPa. This estimate is admittedly rough, as we have not factored in the complicated geometry of the real system.

Summary and Outlook for the Future

The eruption of Mount St. Helens that began in fall 2004 has presented us with the first-ever opportunity to observe and document emplacement of a lava dome through glacier ice. The eruption has not caused any rapid melting of Crater Glacier, but the effects on the glacier have nonetheless been striking. Dome growth cut the glacier in two and then successively squeezed the two parts. Measurements using both specialized, helicopter-deployed GPS stations and photogrammetrically derived DEMs showed that the two glaciers underwent deformation of an extreme variety, with strain rates of extraordinary magnitude as compared to those in normal alpine temperate glaciers. Moreover, the GPS-derived motion records make clear that Crater Glacier is fundamentally unlike normal alpine glaciers, in that there is no evidence that it slides over its bed. The most reasonable explanation for this anomaly is that meltwater reaching the glacier bed enters the volcano's groundwater system rather than flowing toward the glacier terminus through a drainage network along the bed.

The part of east Crater Glacier that underwent thickening has been thinning since dome growth shifted to the west in April 2005, and normal ice flow has moved mass downstream. Terminus advance is likely to continue unless eruptive processes remove substantial glacier mass. West Crater Glacier is likely to evolve similarly in the short term, with terminus dynamics complicated by the formation of the shear zone shown in figure 20. The pattern of snow accumulation in the crater has been radically perturbed, with heat from the new lava dome locally preventing accumulation. Sufficiently prolonged dome growth could, of course, completely eliminate ice from the crater (and indeed completely eliminate the crater itself). Glaciers at Mount St. Helens come and go, modulated by the style and rhythm of eruptive behavior.

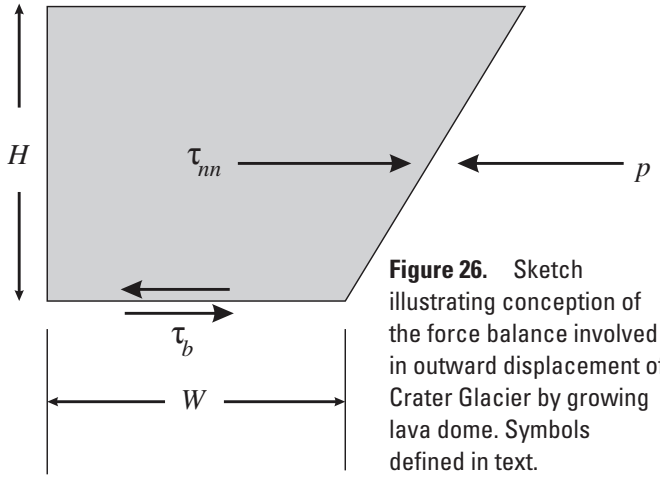

Figure 26. Sketch illustrating conception of the force balance involved in outward displacement of Crater Glacier by growing lava dome. Symbols defined in text.

Acknowledgments

R.M. Iverson and S.P. Anderson made helpful comments on an earlier version of this manuscript. DEMs were prepared by J. Messerich of the U.S. Geological Survey Photogrammetric Lab, Denver, Colorado, using aerial photographs taken by Bergman Photographic Services.

References Cited

Anderson, R.S., Anderson, S.P., MacGregor, K.R., Waddington, E.D., O'Neel, S., Riihimaki, C.A., and Loso, M.G., 2004, Strong feedbacks between hydrology and sliding of a small alpine glacier: Journal of Geophysical Research (Earth Surfaces), v. 109, F03005, 17 p., doi:10.1029/2004JF000120.

Anderson, R.S., Walder, J.S., Anderson, S.P., Trabant, D.C., and Fountain, A.G., 2005, The dynamic response of Kennicott Glacier to the Hidden Creek Lake outburst flood: Annals of Glaciology, v. 40, p. 237–242.

Brugman, M.M., and Meier, M.F., 1981, Response of glaciers to the eruptions of Mount St. Helens, *in* Lipman, P.W., and Mullineaux, D.R., eds., The 1980 eruptions of Mount St. Helens, Washington: U.S. Geological Survey Professional Paper 1250, p. 743–756.

Crandell, D.R., 1987, Deposits of pre-1980 pyroclastic flows and lahars from Mount St. Helens volcano, Washington: U.S. Geological Survey Professional Paper 1444, 91 p.

Fountain, A.G., and Walder, J.S., 1998, Water flow through temperate glaciers: Reviews of Geophysics, v. 36, no. 3, p. 299–328.

Gilbert, J.S., Stasiuk, M.V., Lane, S.J., Adam, C.R., Murphy, M.D., Sparks, R.S.J., and Naranjo, J.A., 1996, Non-explosive, constructional evolution of the ice-filled caldera at Volcán Sollipulli, Chile: Bulletin of Volcanology, v. 58, no. 1, p. 67–83.

Guðmundsson, M.T., Sigmundsson, F., and Björnsson, H., 1997, Ice–volcano interaction of the 1996 Gjálp subglacial eruption, Vatnajökull, Iceland: Nature, v. 389, no. 6654, p. 954–957.

Hallet, B., 1979, A theoretical model of glacial abrasion: Journal of Glaciology, v. 23, no. 89, p. 321–334.

Harper, J.T., Humphrey, N.F., and Greenwood, M.C., 2002, Basal conditions and glacier motion during the winter/spring transition, Worthington Glacier, Alaska, U.S.A.: Journal of Glaciology, v. 48, no. 160, p. 42–50.

Iverson, N.R., and Semmens, D., 1995. Intrusion of ice into porous media by regelation; a mechanism of sediment entrainment by glaciers: Journal of Geophysical Research, v. 100, no. B6, p. 10219–10230.

Kamb, B., Raymond, C.F., Harrison, W.D., Engelhardt, H., Echelmeyer, K.A., Humphrey, N., Brugman, M.M., and Pfeffer, T., 1985, Glacier surge mechanism; 1982–1983 surge of Variegated Glacier, Alaska: Science, v. 227, no. 4686, p. 469–479.

LaHusen, R.G., Swinford, K.J., Logan, M., and Lisowski, M., 2008, Instrumentation in remote and dangerous settings; examples using data from GPS "spider" deployments during the 2004–2005 eruption of Mount St. Helens, Washington, chap. 16 *of* Sherrod, D.R., Scott, W.E., and Stauffer, P.H., eds., A volcano rekindled; the renewed eruption of Mount St. Helens, 2004–2006: U.S. Geological Survey Professional Paper 1750 (this volume).

Major, J.J., and Newhall, C.G., 1989, Snow and ice perturbations during historical volcanic eruptions and the formation of lahars and floods: Bulletin of Volcanology, v. 52, no. 1, p. 1–27.

Mills, H.H., 1992, Post-eruption erosion and deposition in the 1980 crater of Mount St. Helens, Washington, determined from digital maps: Earth Surface Processes and Landforms, v.17, no. 8, p. 739–754.

Murav'ev, Ya.D., and Salamatin, A.N., 1990, Mass balance and thermal regime of a crater glacier at Ushkovskii Volcano: Volcanology and Seismology, v. 11, no. 3, p. 411–424.

Paterson, W.S.B., 1994, The physics of glaciers (3d ed.): Oxford, Pergamon, 480 p.

Philip, J.R., 1980, Thermal fields during regelation: Cold Regions Science and Technology, v. 3, nos. 2–3, p. 193–203.

Price, S.F., and Walder, J.S., 2007, Modeling the dynamic response of a crater glacier to lava-dome emplacement: Mount St. Helens, Washington, U.S.A.: Annals of Glaciology, v. 45, no. 1, p. 21–28, doi:10.3189/172756407782282525.

Raymond, C.F., 1987, How do glaciers surge?: Journal of Geophysical Research, v. 92, no. B9, p. 9121–9134.

Raymond, C., Johannesson, T., Pfeffer, T., and Sharp. M., 1987, Propagation of a glacier surge into stagnant ice: Journal of Geophysical Research, v. 92, no. B9, p. 9037–9049.

Salamatin, A.N., and Murav'ev, Ya.D., 1992, Some results of a study of the physical characteristics of the glacial stratum on the slopes of the Klyuchevskoy volcano: Volcanology and Seismology, v. 13, no. 2, p. 230–240.

Schilling, S.P., Carrara, P.E., Thompson, R.A., and Iwatsubo, E.Y., 2004, Posteruption glacier development within the crater of Mount St. Helens, Washington, USA: Quaternary

Research, v. 61, no. 3, p. 325–329.

Schilling, S.P., Thompson, R.A., Messerich, J.A., and Iwatsubo, E.Y., 2008, Use of digital aerophotogrammetry to determine rates of lava dome growth, Mount St. Helens, Washington, 2004–2005, chap. 8 *of* Sherrod, D.R., Scott, W.E., and Stauffer, P.H., eds., A volcano rekindled; the renewed eruption of Mount St. Helens, 2004–2006: U.S. Geological Survey Professional Paper 1750 (this volume).

Schneider, D.J., Vallance, J.W., Wessels, R.L., Logan, M., and Ramsey, M.S., 2008, Use of thermal infrared imaging for monitoring renewed dome growth at Mount St. Helens, 2004, chap. 17 *of* Sherrod, D.R., Scott, W.E., and Stauffer, P.H., eds., A volcano rekindled; the renewed eruption of Mount St. Helens, 2004–2006: U.S. Geological Survey Professional Paper 1750 (this volume).

Simons, F.S., and Mathewson, D.E., 1955, Geology of Great Sitkin Island, Alaska: U.S. Geological Survey Bulletin 1028–B, 43 p.

Tuffen, H., Gilbert, J., and McGarvie, D., 2001, Products of an effusive subglacial rhyolite eruption; Bláhnúkur, Torfajökull, Iceland: Bulletin of Volcanology, v. 63, nos. 2–3, p. 179–190.

Vallance, J.W., Schneider, D.J., and Schilling, S.P., 2008, Growth of the 2004–2006 lava-dome complex at Mount St. Helens, Washington, chap. 9 *of* Sherrod, D.R., Scott, W.E., and Stauffer, P.H., eds., A volcano rekindled; the renewed eruption of Mount St. Helens, 2004–2006: U.S. Geological Survey Professional Paper 1750 (this volume).

van der Veen, C.J., 1999, Fundamentals of glacier dynamics: Rotterdam, A.A. Balkema, 462 p.

Walder, J.S., LaHusen, R.G., Vallance, J.W., and Schilling, S.P., 2005, Crater glaciers on active volcanoes; hydrological anomalies: Eos (American Geophysical Union Transactions), v. 86, no. 50, p. 521, 528.

Walder, J.S., LaHusen, R.G., Vallance, J.W., and Schilling, S.P., 2007, Emplacement of a silicic lava dome through a crater glacier; Mount St Helens, 2004–06: Annals of Glaciology, v. 45, no. 1, p. 14–20, doi:10.3189/172756407782282426.

Appendix 1. Interstitial Ice in Crater-Floor Rock Debris

As shown by Mills (1992) and noted above, until about 1986, material accumulating on the Mount St. Helens crater floor consisted primarily of rock-avalanche material with interstitial snow. After 1986, the volumetric rate of snow accumulation exceeded the accumulation rate of rock debris. By the time the 2004 eruption began, the crater-fill material was locally as thick as 200 m, and it is hard to envisage that any interstitial snow within the lowermost fill would not have transformed to glacier ice (Paterson, 1994). However, there is reason to believe that some of the deepest fill may in fact be ice free, because interstitial ice within the rock framework will be melted by geothermal heat and not replaced by ice from above. If all heat flux from below causes melting, then the melt rate $\dot{m}$, expressed as thickness per unit time, will be given by the ratio of the geothermal heat flux, q_G, to the energy required to melt a unit volume of ice,

$$\dot{m} = \frac{q_G}{\phi \rho_i L}, \qquad (6)$$

where ϕ is porosity of the avalanche debris, ρ_i is the density of ice, and L is the heat of fusion. If one considers a glacier in a nonvolcanic setting, then taking $\phi = 0$, $L = 3.35 \times 10^5$ J/kg, and $q_G = 0.05$ W/m^2, one finds $\dot{m} \approx 5$ mm/yr. In a volcanic setting, q_G could easily be one hundred times greater (Murav'ev and Salamatin, 1990; Salamatin and Murav'ev, 1992), and taking $\phi \approx 0.4$ for the crater-fill avalanche debris, one finds $\dot{m} \approx 1$ m/yr. Clearly melting can proceed rapidly, although we stress that these estimates for $\dot{m}$ are upper bounds, because ground water could carry away some of the geothermal heat flux.

The rate at which overlying glacier ice can flow into the avalanche debris is very low. The ice intrusion rate V is proportional to the gradient of ice pressure across the debris layer (Iverson and Semmens, 1995):

$$V = K_s P_g, \qquad (7)$$

where P_g is the gradient of ice pressure across the debris layer, and the proportionality constant K_s is analogous to hydraulic conductivity for ground-water flow. The constant K_s can be determined on theoretical grounds (Philip, 1980) in the case that the debris grain size is small enough that ice flow is dominantly by regelation, with plastic creep negligible; experimental results of Iverson and Semmens (1995) support Philip's theory. The crater-fill debris is coarse enough that plastic creep is necessary for the ice to flow through the pore space (Hallet, 1979), so the regelation-only value $K_S \approx 3 \times 10^{-15}$ m^2/Pa·s will give an overestimate of V. The ice pressure gradient P_g obviously depends upon the thickness of the ice-filled debris layer and the pressure of the overlying ice. For present purposes, suppose that the overburden pressure is 1 MPa (corresponding to an ice thickness of about 110 m) and the thickness of the ice-filled debris layer is 10 m. We then find from equation 7 that an upper-bound estimate of V is about 0.01 m/yr. A balance between $\dot{m}$ and V can exist only if the ice-filled debris layer is very thin—a few centimeters at most. We conclude that the ice within the deepest crater fill ought to, over time, melt out and not be replenished. It seems likely that the deepest crater fill will act as an aquifer conveying water along the crater floor toward the glacier terminus.

Appendix 2. Calculating Glacier Volume

The change in total glacier volume within the crater of Mount St. Helens, over the course of the eruption, was determined by GIS methods. Details of the method can be understood with reference to figure 27. The area covered by the glacier before the eruption was broken into three parts: part A1 includes the area within which dome rock was emplaced, and parts A2 and A3 are the east and west glacier arms that were not disrupted directly by dome growth. The glacier volumes in A2 and A3 were determined by differencing DEMs for various dates with the October–November 1986 DEM, the latter representing, as we argued in the main text, approximately the bed of the crater glacier.

As we are only trying to track the change in glacier volume with time, rather than total glacier volume, the exact choice of datum for the bed is not critical. (The ambiguity in determining the bed, upon which we commented in the main text, is thus not a problem.) The glacier volume in A1 is calculated as follows: Using the 1986 DEM as the datum, let the difference between the total volume above this surface at some date τ be denoted by V_τ, and the volume of extruded dome rock within A1 be given by V_d. (The calculation of V_d. is described by Schilling and others, this volume, chap. 8.) The glacier volume within A1 is then $V_\tau - V_d$. This volume is added to the volumes in A2 and A3 to get the total glacier volume. The error in this total volume can be estimated as the total glacier surface area (1.0 km^2) times the root-mean-square error in the elevation-differencing procedure, which we take as 2.5 m. (This value follows from the 2.5 m error on the 1986 DEM, which was produced from a topographic map with contour interval of 5 m, and the 0.1 to 0.2 m error on later DEMs, which were produced directly from aerial photographs.

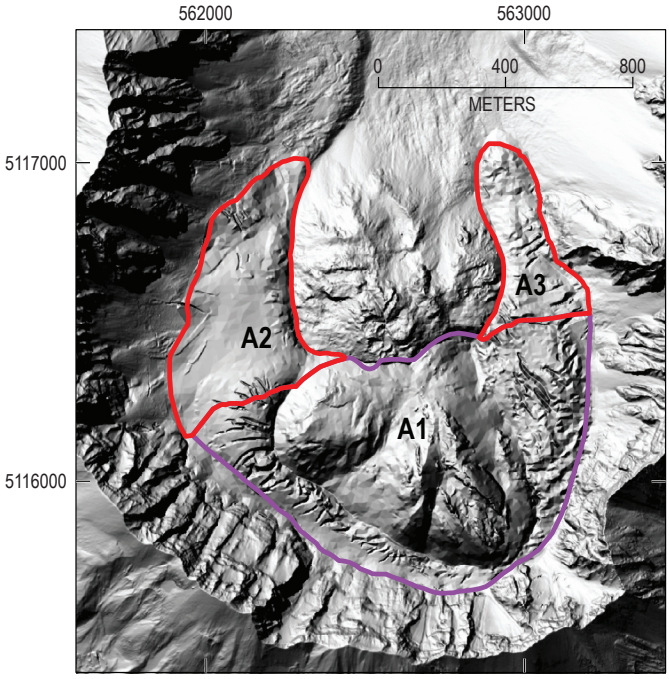

Figure 27. Separation of crater DEM coverages into three sections used in calculating total glacier volume as given in figure 21. Area A1 overlaps new lava dome, whereas areas A2 and A3 correspond to the downstream arms of west Crater Glacier and east Crater Glacier, respectively. Method of volume calculation is described in appendix 2. Background is hillshade-relief map based on DEM of October 24, 2005. Coodinates are UTM zone 10 easting and northing, North America datum 1983.

Appendix 3. Glacier Flow Dynamics

The flow law of ice is an empirical relation between stress and strain rate. For isotropic ice, the flow law is customarily written as the tensor relation (van der Veen, 1999)

$$\tau_{ij} = 2\eta\dot{\varepsilon}_{ij}\,, \tag{8}$$

where τ_{ij} are deviatoric stresses, $\dot{\varepsilon}_{ij}$ are strain rates, and η is an effective viscosity that depends on the overall strain-rate field:

$$\eta = (B/2)\,\dot{\varepsilon}_e^{\,(1/n)-1}\,. \tag{9}$$

B is a material property that depends on temperature, $n \approx 3$ for glacier ice (as compared to $n = 1$ for a Newtonian-viscous fluid like water), and $\dot{\varepsilon}_e$ is the effective strain rate, defined by the relation

$$2\dot{\varepsilon}_e^{\,2} = \dot{\varepsilon}_{xx}^2 + \dot{\varepsilon}_{yy}^2 + \dot{\varepsilon}_{zz}^2 + 2(\dot{\varepsilon}_{xy}^2 + \dot{\varepsilon}_{xz}^2 + \dot{\varepsilon}_{yz}^2)\,. \tag{10}$$

Here x, y, and z are arbitrary orthogonal coordinates. In the simple case of unidirectional slab flow—that is, flow driven by gravity and resisted by drag on the base (see, for example, van der Veen, 1999)—one could choose x as the downglacier coordinate, y as the cross-glacier coordinate, and z as normal to the glacier surface. The only nonzero strain-rate component would then be $\dot{\varepsilon}_{xz}$, in which case $\dot{\varepsilon}_e = |\dot{\varepsilon}_{xz}|$ and the flow law becomes a simple relation between shear stress and shear strain rate,

$$\tau_{xz} = B\,|\dot{\varepsilon}_{xz}|^{(1/n)-1}\dot{\varepsilon}_{xz}\,. \tag{11}$$

We argued in the main text above that the crater glacier probably does not slide over its bed. The average strain rate $\dot{\varepsilon}_{xz}$ may therefore be estimated simply as the surface speed U divided by the glacier thickness H. Taking $U \approx 1$ m/d and $H \approx 150$ m in the part of east Crater Glacier experiencing lateral squeeze (see, for example, station ICY5 on fig. 14), the magnitude of the average strain rate $\dot{\varepsilon}_{xz}$ is then about 6.7×10^{-3}/d, comparable to the magnitude of the lateral strain rate $\dot{\varepsilon}_{yy}$ and vertical strain rate $\dot{\varepsilon}_{zz}$, which, as noted in the main text, averaged about 3×10^{-3}/d over the period of squeezing. The value $\dot{\varepsilon}_e$ is not well approximated by $|\dot{\varepsilon}_{xz}|$ in this case, and the nonzero (and in fact relatively large) values of $\dot{\varepsilon}_{yy}$ and $\dot{\varepsilon}_{zz}$ substantially reduce the effective viscosity (see equations 9 and 10).

In the slab-flow model, shear stress is simply proportional to depth and surface slope; that is, $\tau_{xz} = \rho_i g z \sin\theta$, where θ is surface slope and z increases downward from the glacier surface. One then finds that U depends upon flow ice thickness and slope according to the expression

$$U = \frac{2H}{n+1}\left(\frac{\rho_i g H \sin\theta}{B}\right)^n. \tag{12}$$

With the usual value $n = 3$, the surface speed then varies as H^4.